Interfaces in all-oxide thin-film varactors with highly-conducting SrMoO3 electrodes for microwave applications

Salg, Patrick

(2020)

Interfaces in all-oxide thin-film varactors with highly-conducting $SrMoO_3$ electrodes for microwave applications

Grenzflächen in Volloxid-Dünnschichtvaraktoren mit hochleitenden $SrMoO_3$ Elektroden für Mikrowellen-Anwendungen

Zur Erlangung des akademischen Grades Doktor-Ingenieur (Dr.-Ing.)
genehmigte Dissertation von Patrick Salg aus Erlenbach am Main
Tag der Einreichung: 19. Mai 2020, Tag der Prüfung: 23. Juli 2020

1. Gutachten: Prof. Dr. Lambert Alff
2. Gutachten: Dr.-Ing. Holger Maune
Darmstadt – D 17

TECHNISCHE
UNIVERSITÄT
DARMSTADT

Materials and Earth
Sciences Department
Materialwissenschaft
Dünne Schichten

Interfaces in all-oxide thin-film varactors with highly-conducting $SrMoO_3$ electrodes for microwave applications
Grenzflächen in Volloxid-Dünnschichtvaraktoren mit hochleitenden $SrMoO_3$ Elektroden für Mikrowellen-Anwendungen

Doctoral thesis by Patrick Salg

1. Review: Prof. Dr. Lambert Alff
2. Review: Dr.-Ing. Holger Maune

Date of submission: 19. Mai 2020
Date of thesis defense: 23. Juli 2020

Darmstadt – D 17

Erklärungen laut Promotionsordnung

§8 Abs. 1 lit. c PromO

Ich versichere hiermit, dass die elektronische Version meiner Dissertation mit der schriftlichen Version übereinstimmt.

§8 Abs. 1 lit. d PromO

Ich versichere hiermit, dass zu einem vorherigen Zeitpunkt noch keine Promotion versucht wurde.

§9 Abs. 1 PromO

Ich versichere hiermit, dass die vorliegende Dissertation selbstständig und nur unter Verwendung der angegebenen Quellen verfasst wurde.

§9 Abs. 2 PromO

Die Arbeit hat bisher noch nicht zu Prüfungszwecken gedient.

Darmstadt, 19. Mai 2020

Patrick Salg

Abstract

In this work, the interfaces and growth by pulsed laser deposition of the all-oxide varactor heterostructure was investigated. This all-oxide varactor heterostructure consists of $SrMoO_3/Ba_xSr_{1-x}TiO_3$/Pt/Au layers and has several advantages over thin-film varactors with Pt bottom electrodes such as defect free, epitaxial growth. Furthermore, new interface materials and optimized growth led to an improvement of the all-oxide varactor microwave performance beyond the level of competing state-of-the-art platinum-based technology. A key achievement for this performance increase was the fast and several micrometer thick growth of the bottom electrode $SrMoO_3$. Although grown at a exceptional high rate of 1 μm SMO in only 45 minutes, the bottom electrode exhibits a high conductivity, low defect density, and atomically flat interface to the dielectric layer. The influence of different substrates with varying in-plane lattice constants on the $SrMoO_3$ growth was also investigated, including the industrially relevant substrate silicon. Epitaxial growth has been realized for silicon and a wide range of scandates, proven by reciprocal space maps. In order to unite the the reductive growth conditions of the bottom electrode with the oxidizing background pressure during the growth of the dielectric, a oxygen diffusion barrier is implemented. In order to find the best performing titanate compound, in terms of oxygen diffusion barrier, a novel measurement routine was established utilizing X-ray photoelectron spectroscopy. In addition to comparisons of the different titanate compounds, quantitative diffusion barrier limits for best performing compound, $Ba_{0.5}Sr_{0.5}TiO_3$, such as temperature and background pressure were determined. This enabled the growth of the dielectric at higher oxygen partial pressures leading to a sufficient oxygenation of the dielectric layer and a decrease of the leakage current of several orders of magnitude. The findings were combined in high-performance all-oxide varactor heterostructures both on the $GdScO_3$ and silicon substrates.
In summary, fast and micrometer-thick growth of $SrMoO_3$ and a novel oxygen diffusion barrier were established and could raise the performance of all-oxide varactors and demonstrate the feasibility of this technology for microwave applications.

Zusammenfassung

In dieser Arbeit wurden die Grenzflächen und das Wachstum der Volloxid-Dünnschichtvaraktoren mittels gepulster Laserabscheidung untersucht. Diese Varaktoren bestehen aus $SrMoO_3/Ba_xSr_{1-x}TiO_3/Pt/Au$ Schichten und haben mehrere Vorteile gegenüber Dünnschicht-Varaktoren mit Platin Bodenelektroden wie z.B. defektfreies, epitaktisches Wachstum. Darüber hinaus führten neue Grenzflächenmaterialien und optimiertes Wachstum zu einer Verbesserung der Volloxid-Varaktor Performanz, die das Niveau konkurrierender, hochmoderner Technologie auf Platinbasis übertrifft. Ein Schlüsselerfolg für diese Leistungssteigerung war das schnelle Wachstum mehrerer Mikrometer dicker $SrMoO_3$ Bodenelektroden. Obwohl diese mit einer außergewöhnlich hohen Rate von 1 μm in nur 45 Minuten abgeschieden werden, weisen sie eine hohe Leitfähigkeit und niedrige Defektdichte sowie eine atomar flache Grenzfläche zu der dielektrischen Schicht auf. Der Einfluss verschiedener Substrate mit unterschiedlichen Gitterkonstanten auf das $SrMoO_3$-Wachstum wurde ebenfalls untersucht, einschließlich dem industriell relevanten Substrat Silizium. Epitaktisches Wachstum wurde für Silizium und eine Vielzahl von Skandaten realisiert, was durch Messungen des reziproken Raums nachgewiesen wurde. Um die reduktiven Wachstumsbedingungen der Bodenelektrode mit dem benötigten sauerstoffhaltigen Hintergrunddruck während des Wachstums des Dielektrikums zu vereinen, wird eine Sauerstoffdiffusionsbarriere implementiert. Um die Titanatverbindung mit der besten Sauerstoffdiffusionsbarriere zu finden wurde eine neuartige Messroutine unter Verwendung der Röntgen-Photoelektronenspektroskopie entwickelt. Zusätzlich zu qualitativen Vergleichen der verschiedenen Titanatverbindungen wurden quantitative Diffusionsbarrieregrenzen für die leistungsfähigste Verbindung, $Ba_{0.5}Sr_{0.5}TiO_3$, wie z.B. Temperatur und Hintergrunddruck bestimmt. Dies ermöglichte das Wachstum des Dielektrikums bei höheren Sauerstoffpartialdrücken, was zu einer ausreichenden Oxygenierung der dielektrischen Schicht und zu einer Abnahme des Leckstroms von mehreren Größenordnungen führt. Diese Ergebnisse wurden in hochleistungsfähigen Volloxid-Varaktoren angewendet, sowohl auf dem $GdScO_3$- als auch auf Siliziumsubstraten.
Kurzgefasst konnte ein schnelles und mikrometerdickes Wachstum von $SrMoO_3$ und eine neuartige Sauerstoffdiffusionsbarriere etabliert werden, womit die Performanz von Volloxid-Varaktoren erhöhen werden und die Machbarkeit dieser Technologie für Mikrowellenanwendungen gezeigt werden.

Contents

1 Introduction

With cellphones becoming a mass product in the late 1990s, ferroelectric films were used in a high number of commercial applications including non-volatile memories, also known as ferroelectric random access memories (FRAMs) or microwave electronic components (MEMs) [1]. The approach of using ferroelectric materials for microwave devices can be dated back over fifty years to the 1960s [2]. Microwave dielectrics have also been used for almost half a century in numerous mobile communication devices such as satellite television, radar, Global Position System (GPS) and Wireless Fidelity (WiFi) [3]. Nevertheless, only in the last twenty years intensive research has taken place in this field, due to improvements both in device electronics and material technology. The driving force behind this development is the goal of miniaturizing microwave components and systems using ferroelectric thin-film technology [4]. Current telecommunication evolved substantially with cell phone miniaturization, antenna tuning, high speed data connections with upcoming 5G and internet of things (IoT) technologies [5]. These technological advancements require new approaches and materials, such as highly tunable thin-film dielectrics with high quality factors and low losses.
With the rapid increase in the amount of smartphone and other mobile devices combined with a growing demand for fast data transfer and mobile data demand driven by rise of streaming and cloud-based-storage comes a global bandwidth shortage [6, 7]. Mobile carriers nowadays use the 2G, 3G, 4G and LTE protocols with the frequency spectrum from 700 MHz to 2.6 GHz [6]. With upcoming 5G, which spans from 450 MHz to 6 GHz and WiFi frequencies of 2.4 GHz as well as 5 GHz, smartphones need to be able to operate flawlessly in all of these frequency ranges. In order to combine these requirements with the ongoing miniaturizing, it is not useful to have static filters, which are currently deployed, to match each narrow frequency band. Over a large frequency band, these static filters can not deliver a consistently high performance.

Tunable capacitors, called varactors, can provide the frequency matching for a very broad frequency spectrum. They are a promising candidate to satisfy the steadily growing demand of higher data rates in networks and deliver flexible impedance matching and frequency tuning. Ferroelectric varactors are considered to be employed in phase shifters, delay lines, tunable resonators, filters, and other non-linear devices. The request for space-saving components has driven the development of thin-film materials in a wide range of devices in recent years, including ferroelectric varactors. They have a reduced footprint of the device but require a rather high tuning voltage due to a rough platinum bottom electrode. Platinum bottom electrodes are usually restricted to thickness of around 300 nm due to hillock formation and

delamination [8, 9]. Furthermore, these hillocks prevent an epitaxial and thin dielectric [10]. The dielectrics are typically in the range of 200 – 300 nm to avoid short circuits caused by the hillocks. These thicknesses require tuning voltages above 20 V to achieve a sufficient bias field.

A novel approach to ferroelectric varactors is the concept of all-oxide varactors, which solve the problem of high tuning voltages and have a low power consumption. This opens up the new fields of applications such as mobile communication. The concept of all-oxide varactors is based on the substitution of the metal bottom electrodes with oxide bottom electrodes. Attempts to utilize $SrRuO_3$ as an isostructural bottom electrode were abandoned due to insufficient conductivity of the electrode material [11]. The concept of all-oxide varactors was discontinued until the highest conducting perovskite $SrMoO_3$ revived the concept. The single crystal conductivity surpasses platinum and thin-film conductivities of 20 $\mu\Omega$·cm have been achieved in previous work [12]. In addition to the application field of microelectronics, $SrMoO_3$ is a favorable material for solid oxide fuel cells [13], transparent conductors [14, 15] and plasmonics [16]. The good conductivity in conjunction with a very low lattice mismatch to the dielectric barium-strontium-titanate $Ba_xSr_{1-x}TiO_3$ gives the opportunity for all-oxide varactors to surpass the performance state-of-the-art ferroelectric varactors based on platinum and offers following advantages:

- Inexpensive materials
- High bottom electrode thicknesses above skin depth possible
- Atomically sharp interfaces
- Low defect density in the dielectric due to epitaxial growth

The atomically sharp interfaces in the all-oxide varactor allow dielectrics in the range of 50 nm without short circuits, which in return lowers tuning voltages to the Li-ion battery voltage level (3.7 V) to achieve similar electric fields. One drawback which has to be noted is the volatility of the material $SrMoO_3$. It oxidizes rapidly to $SrMoO_4$, which is insulating and therefore drastically decreases the device performance. Part of this work was the investigation of different intermediate capping layer materials. These suppress oxygen diffusion during the deposition of the dielectric and, thus, preventing $SrMoO_3$ from oxidizing.
Another important factor considering industrial applicability of novel thin-film technology is the choice of substrates. Up until now, research on all-oxide varactors was limited to the substrate $GdScO_3$ [17, 18], which is not feasible for industrial application due to the high cost. Two alternative substrates are sapphire and silicon. Sapphire has low losses and is currently used by competing platinum-based varactor technology. Due to the low bottom electrode thickness of Pt electrodes of around 300 nm in commercially available varactors, which is far below the skin depth, in the field of application of several GHz, a huge part of the RF signal is penetrating into the substrate. Therefore, current varactor technology based on Pt bottom electrodes is fabricated on sapphire substrates.

However, silicon would be the preferred substrate, since it is cheap, can be produced in wafers of 12 inch in diameter and is the most popular substrate in semiconductor industry. In addition, a successful deposition on silicon substrates is required to enable integration of all-oxide varactors into silicon RF circuit technology.

For these reasons, a technology transfer from the lab-scale substrate $GdScO_3$ towards silicon, in combination with unique advantages mentioned above, can establish the all-oxide varactor technology in the RF front end market.

2 Fundamentals

2.1 Dielectric materials

In the presence of an external electric field, positive and negative charges are moved into opposite directions. The response of a solid to such an electric field depends whether charges can move in the solid. In case of metals, electrons can move quasi freely and shield the external field on a very short length scale [19]. In insulators, the electrons can only be shifted slightly from their equilibrium position, causing an electrical polarization [20]. These insulating materials are also called dielectrics [21].

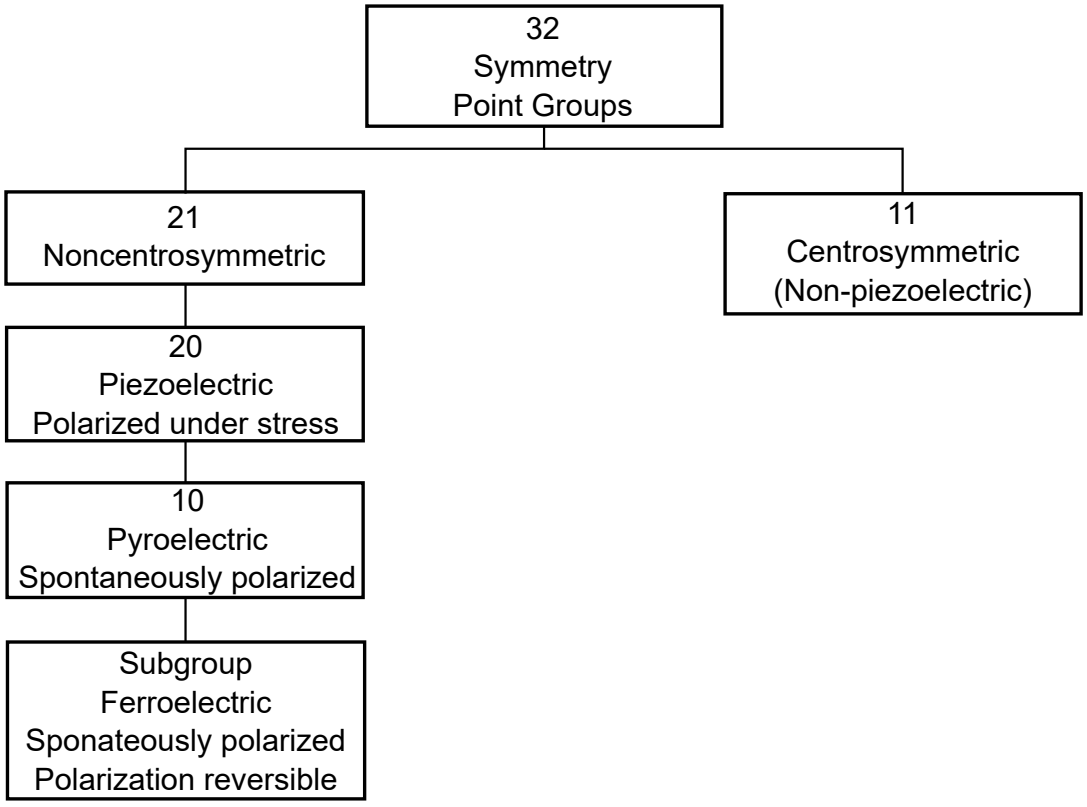

Figure 2.1: Classification of the 32 point groups in non-piezoelectric, piezoelectric, pyroelectric and ferroelectric materials [22].

In crystallography, the symmetry of a crystal is assigned to point groups corresponding the symmetry operations, such that the crystal structure is unchanged after the operation. Depending on the point group dielectrics can be further divided into non-piezoelectric, piezoelectric, pyroelectric and ferroelectric [22], which will be explained in the following.

All crystals can be assigned to one of 32 different point groups (see Figure 2.1), which are based on the seven basic crystal systems, in ascending symmetry: triclinic, monoclinic, orthorombic, tetragonal, rhombohedral (trigonal), hexagonal and cubic [22]. Out of these 32 point groups, 20 exhibit piezoelectric behavior. This means, that an electrical polarisation will arise under mechanical stress on the crystal in a certain direction. Requirement for the piezoelectric effect is the existence of a polar axis. Polar axes can only occur in crystal structures without a structural inversion symmetry. A 180° rotation of the crystal structure perpendicular to the polar axis does not result in the initial state. This can be seen in Figure 2.2 (b), where the polar axis is aligned in the *c*-direction [19].

In piezoelectrica, there exist a subgroup of 10 crystal classes named pyroelectrica. This group is characterized by a permanent polarization within a certain temperature range. The polarization is not a result of stress like in the piezoelectrica, but arises spontaneously and forms permanent dipoles in the crystal and changes with temperature [22].

If a material not only exhibits spontaneous polarization, but the dipoles are also reversible by an electric field, it is called a ferroelectric. Therefore, the ferroelectrics represent a subgroup of the pyrolectrics with the additional necessary requirement of reorientation of the polarization. Ferroelectricity was first discovered in Rochelle salt in 1921 [23]. In analogy to magnetic materials, there also exist ferrielectric and antiferroelectric materials [19].

Ferroelectric materials can be divided into two groups, depending on the type of transition from the para- to ferroelectric phase, namely first-order or second-order transitions. A sudden jump at the Curie-Temperature T_C is assigned to the first-order and a continuous transition is assigned to the second-order. The second-order transition is also called order-disorder transition. This means, that above the transition temperature T_C, the order of the electrical dipole moments is lost, however, the dipoles themselves do not disappear. An example for the second-order transitions, is monopotassium phosphate (KH_2PO_4) [19].

During the first-order transition, also called displacive transition, two sublattices are shifted with respect to each other. Dipol moments emerge due to a displacement of ions. Prominent materials for the first-order transitions are ionic crystals with a perovskite structure (ABO_3), such as barium titanate ($BaTiO_3$). Above the Curie-Temperature $T_C = 383\,\mathrm{K}$, $BaTiO_3$ has a centrosymmetric cubic crystal structure and, thus, $BaTiO_3$ is in the paraelectric phase. Below the Curie-Temperature T_C a first-order phase transition occurs from the cubic into the tetragonal ferroelectric phase [20]. This first-order phase transition is visible in Figure 2.2, where the crystal structure of $BaTiO_3$ is shown in the paraelectric (a) and ferroelectric (b) phase.

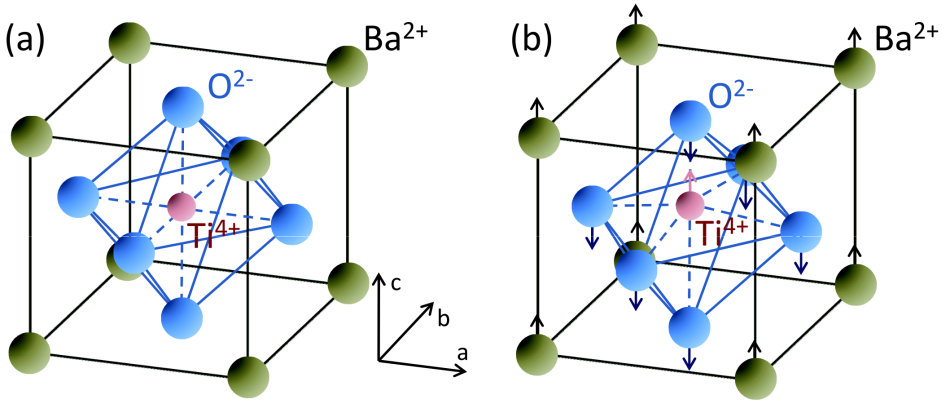

Figure 2.2: Crystal structure of $BaTiO_3$: (a) Above the Curie-Temperature $T_C = 383\,K$, $BaTiO_3$ exhibits a centrosymmetric, cubic crystal structure and is in the paraelectric phase. (b) Below T_C, Ba^{2+} and Ti^{4+} shift upwards and the negatively charged O^{2-} shifts downwards, indicated by the arrows, which leads to a slightly elongated c-axis. The crystal is in a tetragonal structure without inversion symmetry and, thus, with a spontaneous polarization in c-direction [19].

2.2 Polarization and dielectric properties

As described in the previous section, if an electric field $\vec{E}$ is applied to an insulating material it leads to separation of charges and, thus, a polarization $\vec{P}$. Both are related to each other by the electric susceptibility χ_e such that

$$\vec{P} = \varepsilon_0 \chi_e \vec{E}, \tag{2.1}$$

where ε_0 is the electric permittivity in free space ($8.854 \cdot 10^{-12}\,\mathrm{F/m}$). The susceptibility is linked to the relative permittivity ε_r by

$$\chi_e = \varepsilon_r - 1, \tag{2.2}$$

where χ_e and ε_r are 2nd order symmetrical tensors, which become scalar for cubic crystals and amorphous solids [20]. The electric displacement field $\vec{D}$ describes the displacement of charges in a dielectric material in the presence of an electric field $\vec{E}$ and is defined as

$$\vec{D} = \varepsilon_0 \vec{E} + \vec{P} = \varepsilon_0 \varepsilon_r \vec{E}. \tag{2.3}$$

For time-varying electric fields the electric displacement current $\partial \vec{D}/\partial t$ appears in the Maxwell's equations

$$\mathrm{rot}\vec{H} = \vec{j} + \frac{\partial \vec{D}}{\partial t}, \tag{2.4}$$

with the current density $\vec{j}$.

For small field strength of the applied electric field, the resulting polarization of the solid has a linear response. Therefore, $\chi(\omega)$ and $\varepsilon(\omega)$ are linear response functions of the solid to the applied electric field. $\chi(\omega)$ and $\varepsilon(\omega)$ satisfy the Kramers-Kronig-relation [24, 25]. For the dielectric function $\varepsilon = \varepsilon' + \mathrm{i}\varepsilon''$ they read to

$$\varepsilon'(\omega) - 1 = \frac{2}{\pi} \mathscr{P} \int_0^\infty \frac{\omega' \varepsilon''(\omega')}{\omega'^2 - \omega^2} \mathrm{d}\omega', \tag{2.5}$$

$$\varepsilon''(\omega) = -\frac{2\omega}{\pi} \mathscr{P} \int_0^\infty \frac{\varepsilon'(\omega') - 1}{\omega'^2 - \omega^2} \mathrm{d}\omega'. \tag{2.6}$$

Here $\mathscr{P}$ denotes the principal value of the integral. Both equations imply that the real and complex part of the permittivity can be converted into each other, if they are measured with sufficient accuracy. The dielectric function is also connected to optical properties and can be linked to the refractive index n and the extinction coefficient κ with following equation

$$\varepsilon = \varepsilon' + \mathrm{i}\varepsilon'' = (n' + \mathrm{i}\kappa)^2 \tag{2.7}$$

and their components are related by

$$\varepsilon' = n'^2 - \kappa^2 \qquad \text{and} \qquad \varepsilon'' = 2n'\kappa. \tag{2.8}$$

Figure 2.3 shows the dielectric response of an insulating material depending on the frequency of the applied field. The real part of the permittivity can be seen in the upper part and the imaginary part can be seen in the lower part. Depending on the frequency, six different phenomena can be differentiated, which are also numbered in Figure 2.3.

1: For very high frequencies ($\omega > 10^{19}$ Hz) the oscillations are too fast for the polarizable elements of the material to follow the field. Therefore, the material is not polarized and the relative permittivity is close to 1 and the absolute permittivity corresponds to the vacuum permittivity ε_0.

2: When the frequency is below $\omega < 10^{19}$ Hz, the electrons of the deep internal layers close to the nucleus follow the field and shift away from the positively charged nucleus. Absorption at the resonance frequency $\omega_{0\mathrm{p}} = 10^{19}$ Hz occurs.

3: Approaching the optical spectrum, the valence electrons are responsible for the polarization. Two resonance frequencies occur for two different types of valence electrons $\omega_{0\mathrm{e}1}$ and $\omega_{0\mathrm{e}2}$.

4: In the infrared region ($\omega \approx 10^{12}$ Hz) the positive and negative ionic sublattices shift with respect to each other and, thus, contribute to the polarization.

5: At radio and microwave frequencies ($\omega < 10^{10}$ Hz) Debye- or orientation polarization takes place. This effect is a reorientation of existing dipoles such as hydrogen bonds.

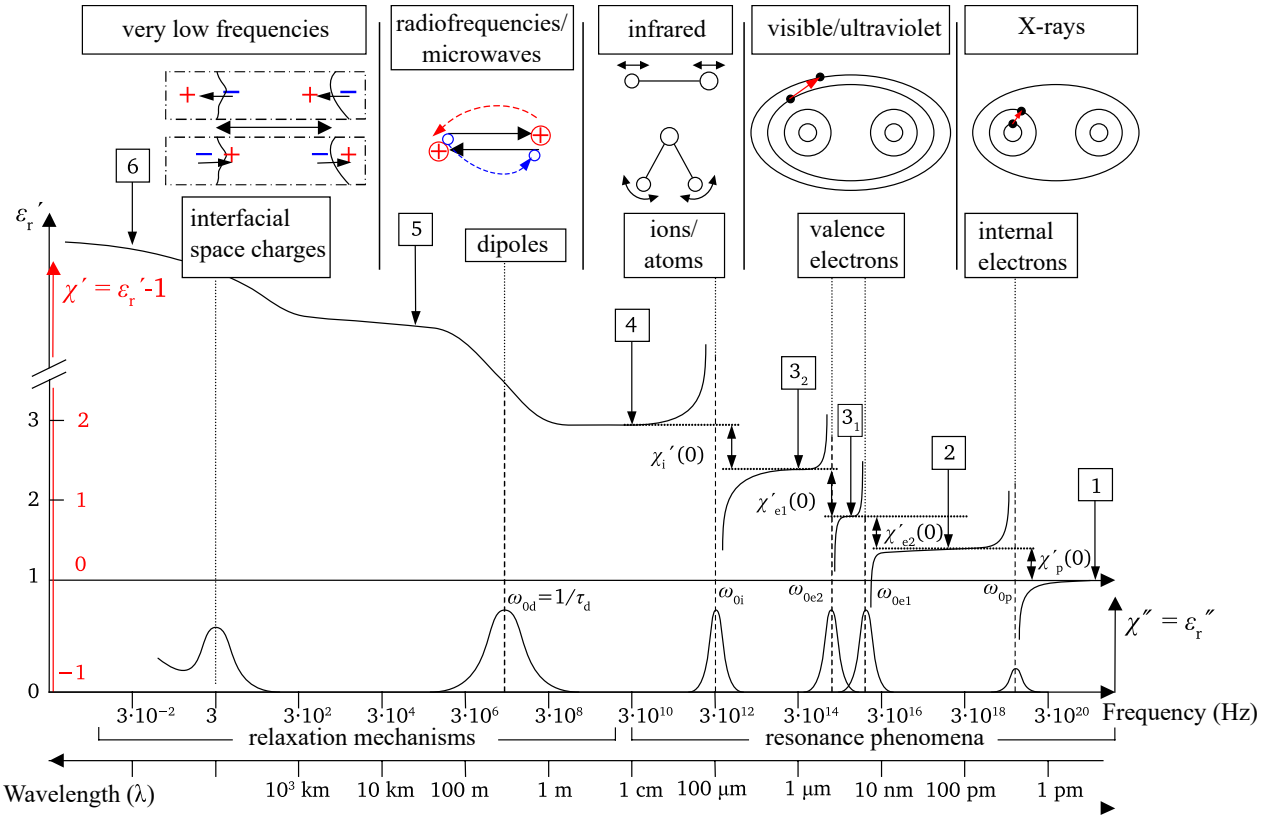

Figure 2.3: Dielectric response function of an insulating material [26, 27].

6: Frequencies below ($\omega < 10^4$ Hz) are low enough to give slow-moving charges such as impurities at grain boundaries or ions and electrons enough time to reach interfaces and form a depletion layer.

2.3 Microwave loss mechanism

Minimizing losses in dielectrics is crucial for commercialization of tunable microwave applications. In recent years, losses of ferroelectrics have been reduced, especially in thin films, due to higher film quality. Microwave losses can be differentiated in the paraelectric phase into intrinsic and extrinsic losses (see Figure 2.4).
Intrinsic losses originate from the interaction of the external electric field with the phonons of the dielectric. Extrinsic losses can be attributed to defects in the crystal. Both intrinsic and extrinsic losses will be briefly discussed in the following section. For more detailed information, see [4, 28, 29]. The total losses of the paraelectric crystal can be described as the sum of all contributing loss mechanisms

$$\tan\delta = \sum_i \tan\delta_i, \tag{2.9}$$

where i denotes the individual loss mechanisms.

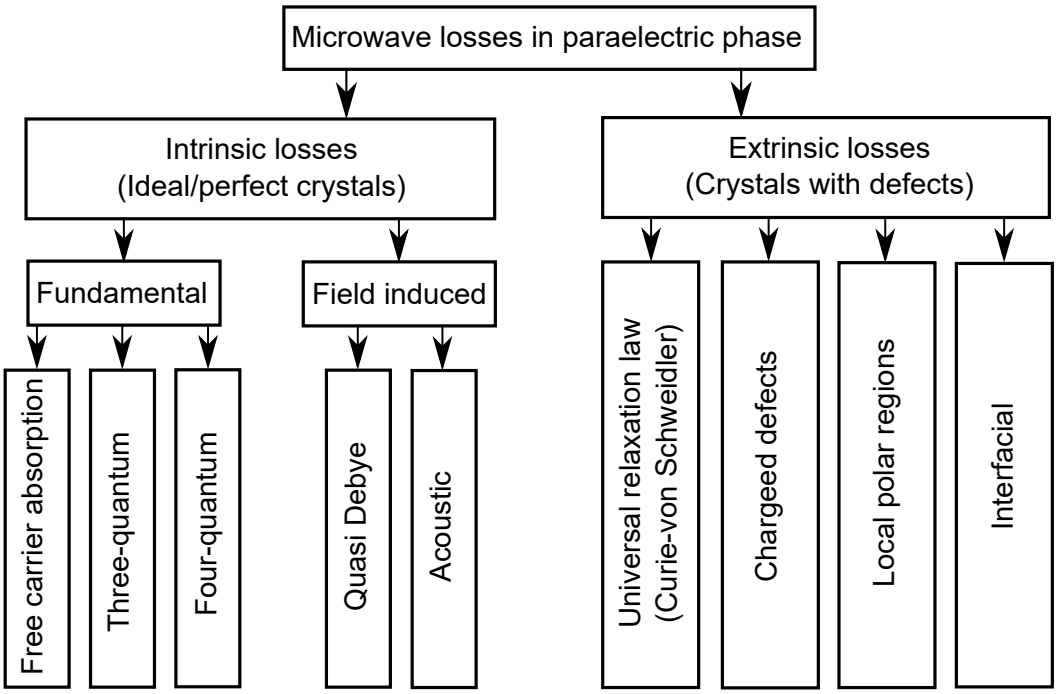

Figure 2.4: Classification of the microwave loss mechanisms in paraelectric dielectrics [28].

2.3.1 Intrinsic losses

As described before, intrinsic losses describe the interactions of the electric field with the phonons of the crystal. The energy quanta of the electromagnetic field $\hbar\omega$ (ω is the frequency of the external field) are absorbed by interactions with thermal phonons of much higher energy. This absorption occurs in the three- and four-quantum mechanism. These processes involve two, and three phonons, respectively. The three-phonon process dominates for popular paraelectrics, such as barium-strontium-titanate, and at room temperature in the microwave region, this process leads to losses of [28]

$$\tan\delta_{\mathrm{ph}} \propto \omega\varepsilon^{3/2}T^2. \tag{2.10}$$

In addition to the discussed fundamental losses, external fields can lead to DC field induced Quasi-Debye and microwave to acoustic transformations. DC and high-power-microwave fields can break the symmetry by shifting the positive and negative charges and induce non-center symmetry. This leads to a polarization of the crystal, which is desired for tunable devices but introduces Quasi-Debye and acoustic losses. Acoustic losses originate due to the electristictive inverse piezoeffect generating acoustic waves.
In an ideal, defect-free paraelectric crystal, where all extrinsic losses are mitigated, the minimum losses of a perfect paraelectric is determined by the electric field induced Quasi-Debye and acoustic losses. In thin films usually losses are dominated by the extrinsic losses, which overlay the intrinsic losses. In high-quality, epitaxial thin films produced in this work, the intrinsic and extrinsic losses are comparable.

2.3.2 Extrinsic losses

Extrinsic losses are associated with defects in the crystal. Depending on the defect density, the extrinsic losses can be much higher than intrinsic losses. The most significant extrinsic losses are associated with

(i) charged defects

(ii) universal-relaxation-law

(iii) Quasi-Debye contribution induced by random-field defects.

Losses due to charged defects contribute essentially in thin-film varactors, like the all-oxide heterostructure in this work. Here, charged defects can be attributed to oxygen vacancies. The Quasi-Debye contribution in centrosymmetric tunable materials can be caused by local polar regions. These may be induced by various defects and structural imperfections [4].

2.4 Perovskites

This work is based on material systems, which belong to the group of perovskites. This material class originates from calcium titanate ($CaTiO_3$) and its crystal structure. The simple perovskites have the formula ABO_3 and consist of two cations A and B as well as an anion O, which is oxygen in this work. The crystal structure for $BaTiO_3$ can be seen in Figure 2.2. The most simple perovskite structure is cubic with the space group $Pm\bar{3}m$ (221).
Perovskites can differ from the cubic lattice structure. This deviation can be approximated by the Goldschmidt tolerance factor τ_{GS}, which reads [30]

$$\tau_{GS} = \frac{r_A + r_0}{\sqrt{2}(r_B + r_0)}, \tag{2.11}$$

where r_A and r_B are the radii of the A- and B-site cation and r_0 is the radius of the oxygen anion. The perovkite is cubic, if τ_{GS} is between 0.95 and 1.04. For decreasing A cation radii, τ_{GS} falls under the threshold value 0.95. This leads to octahedral distortion of the anion octahedra, which was reported by Glazer *et al.* and Sasaki *et al.* [31–33]. For perovskites such as $BaTiO_3$, the Goldschmidt tolerance factor has a value of $\tau_{GS} > 1$ and, thus, the B cation is too small to fill the oxygen octahedral. Hence, below the Curie temperature, the B cation is shifted away from the octahedral middle position leading to a polarization [34].

2.4.1 Barium-strontium-titanate $Ba_xSr_{1-x}TiO_3$

Barium-strontium-titanate $Ba_xSr_{1-x}TiO_3$ (BST) belongs to the group of ferroelectric materials and shows a field dependent permittivity, which is very important for RF circuits and tunable ferroelectric varactors in particular. The tunability states, how much the permittivity changes under the influence of an applied DC field. A detailed introduction will be given in section 2.7. BST is the most studied ferroelectric material in literature. It has a superior tunability, low dielectric loss and is, in addition, lead free [35].
BST is a mixed perovskite of strontium titanate (STO) and barium titanate (BTO). Depending on the ratio of the A-site cations Ba:Sr the value of the Goldschmidt tolerance factor τ_{GS} is changing. With increasing Sr content, the octahedral distortions regress, which is reflected in the value of τ_{GS}, approaching 1.
Depending on the temperature, BST can be ferroelectric or paraelectric and shows a ferroelectric-paraelectric transition at the Curie temperature T_C (see Figure 2.5). The Curie temperature depends on the barium and strontium content in $Ba_xSr_{1-x}TiO_3$ and falls below room temperature for $x < 0.7$ in single crystals [36]. In the ferroelectric phase, the material shows a hysteresis in the electric polarization field due to polarized electric moments. This behavior is used for applications such as non-volatile memories. In the paraelectric phase above T_C the hysteresis vanishes. This absence of the hysteresis is very important for varactors, which is the reason why BST is used in the paraelectric phase for such applications.

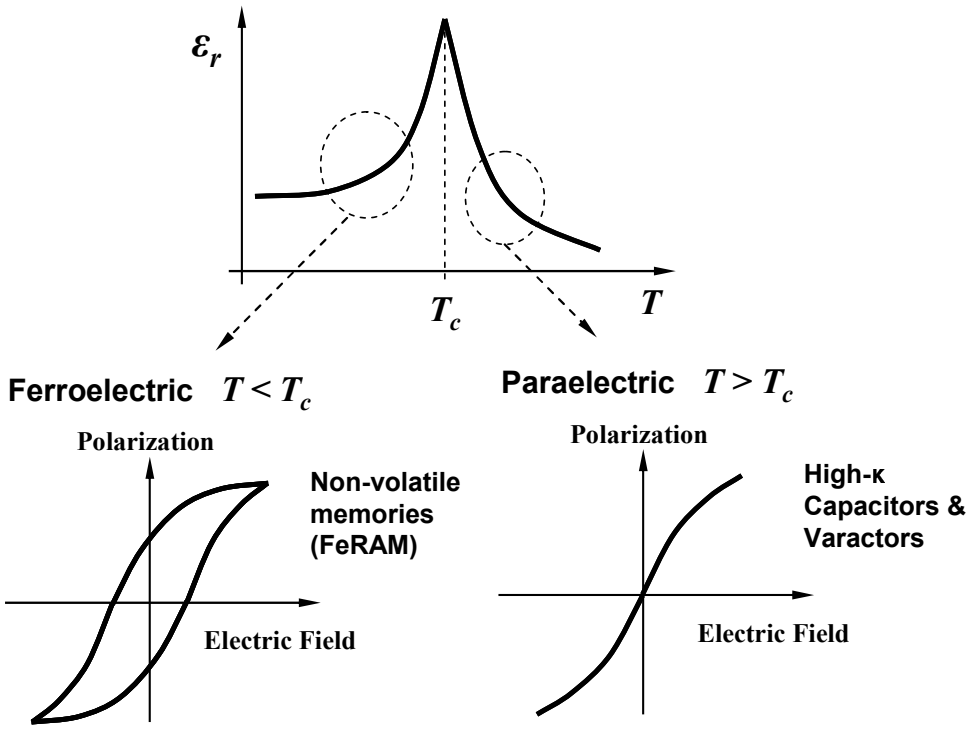

Figure 2.5: Permittivity dependence on the temperature with the ferroelectric-paraelectric transition at the Curie temperature T_C in the upper graph. The bottom two graphs show the hysteresis behavior of the polarization in the ferroelectric phase and polarization behavior in the paraelectric phase [36].

To explain the ferroelectic and paraelectric behavior, it is important to understand the lattice structure. BST, similar to other complex metal oxide ferroelectrics with an ABO_3 formula, is arranged in the perovskite structure (see Figure 2.6). The barium and strontium ions sit on the corners of the unit cell (A-site cation). Both A-site cations are present in the oxidation state Sr^{2+} and Ba^{2+}. The titanium ion is in the middle of the unit cell (B-site cation) with an oxidation state of Ti^{4+}. It is surrounded by oxygen ions (oxidation state O^{2-}) in an octahedral structure. Since barium is bigger than strontium, the lattice constant rises with a higher barium content. The lattice constant of BST can vary from 3.905 Å for pure STO [37] up to the tetragonal BTO with an in-plane lattice constant of $a = 3.994$ Å and an out-of-plane lattice constant of $c = 4.038$ Å [38].
For the paraelectric phase above the Curie temperature, BST shows a cubic structure with the equilibrium position of the titanium ion in the middle of the unit cell. Thus, the crystal has no spontaneous polarization. This is different in the ferroelectric phase. The equilibrium position of the titanium ion is shifted away from the center towards one side of the unit cell and therefore showing spontaneous polarization.

This can also be described by a 1-dimensional oscillator model of the perovskite crystal (see Figure 2.6). The ions are represented by spheres and the bonds between the ions are represented by springs. In the paraelectric phase, the equilibrium position of the positive titanium ion is in the middle (Figure 2.6 (a)), where the free energy has a minimum. By applying an external electric field, the titanium moves away from this middle position and induces an electric dipole. Without the presence of the electric field, the ion returns to the center ($x = 0$). The free energy is described by a parabolic shape ($= kx^2$ with k being the spring constant).
In the ferroelectric phase, the free energy of the crystal has two minima without the presence of an external DC field. Hence, the positive ion is shifted away from the center position in one of these two minima (Figure 2.6 (b)). This leads to the spontaneous polarization. By applying an external DC field, it is possible to switch between both minima. This behavior is exploited, for example, in memory cells [28]. A phenomenological theory based on the expansion of free energy of a ferroelectric crystal as a function of polarization P is given in [28].

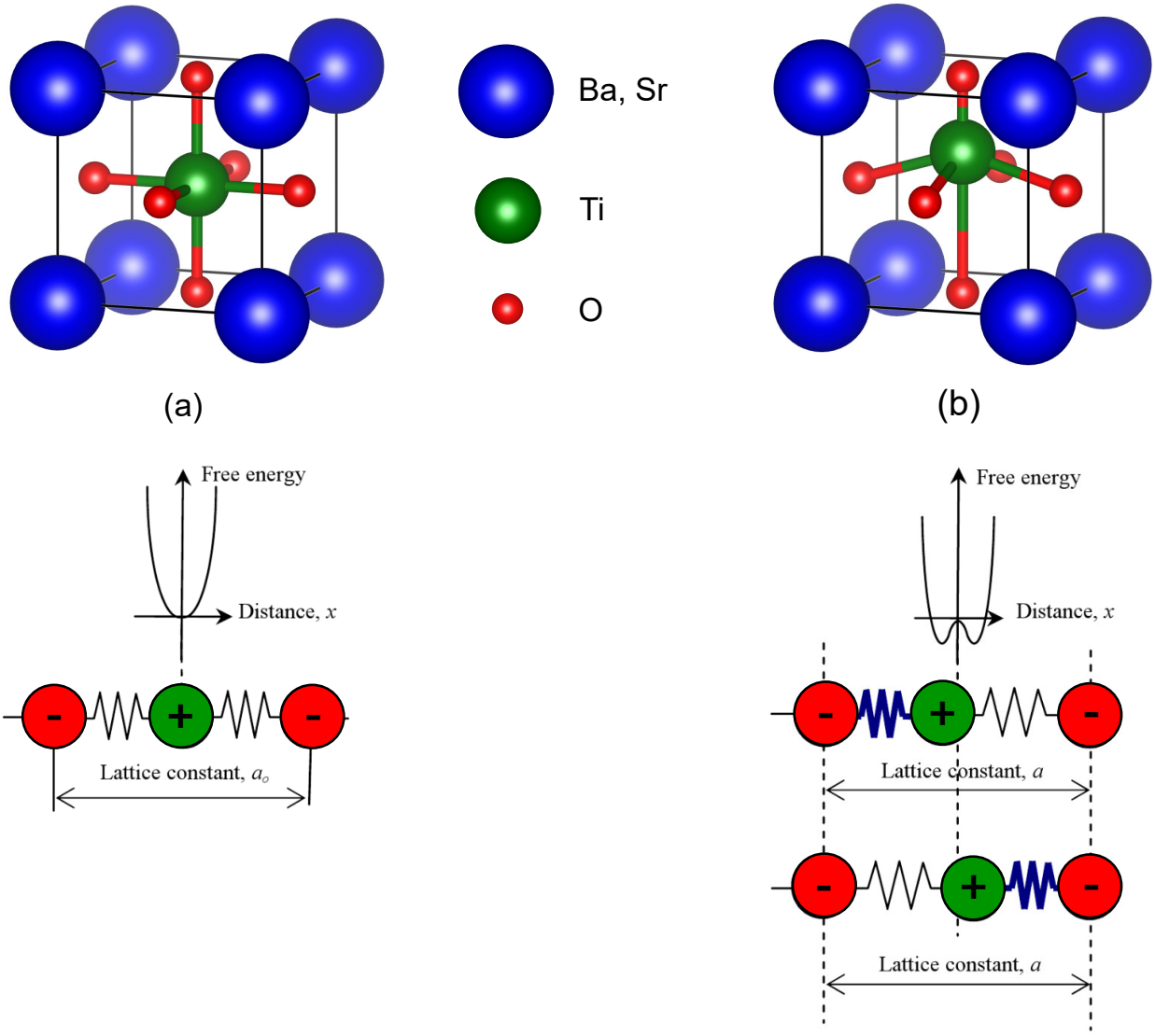

Figure 2.6: Crystal structure of BST in paraelectric phase (a) and ferroelectric phase (b). In the bottom half, the free energy distribution in 1-dimensional unit cells of ABO_3 perovskites is displayed. The spring model shows, how the titanium ion (green) can be shifted away from the middle position towards an oxygen atom (red) [28].

Thin-film BST

Although thin films and their bulk counterparts are chemically the same, the physical properties of thin films can significantly differ from the bulk material [28]. The maximum values of the permittivity of bulk BST samples can be over 60 times higher than comparable thin-film samples. The dielectric constant of thin-film BST is around ($\varepsilon_r \approx 300$) and, therefore, much lower than bulk BST ($\varepsilon_r \approx 20000$). This reduction effect can be explained by smaller grain sizes, cation nonstoichiometry, in-plane stress or interfacial capacitance, acting as a dead-layer [39–42]. This dead-layer effect is more pronounced in very thin films of only several nanometers, were the thickness is comparable to the thickness of the dead-layer. In addition, the temperature dependence of the dielectric constant is drastically reduced in the thin-film as it can be seen in Figure 2.7. There is no obvious ferroelectric-paraelectric phase transition visible for thin films (see Figure 2.7). The maximum in dielectric is shifting with different Ba/Sr ratios in temperature. This allows to tailor the BST composition to have the maximum dielectric constant exactly at the operation temperature area for a possible device. The tunability for thin-film BST requires lower voltages compared to the bulk material [36].

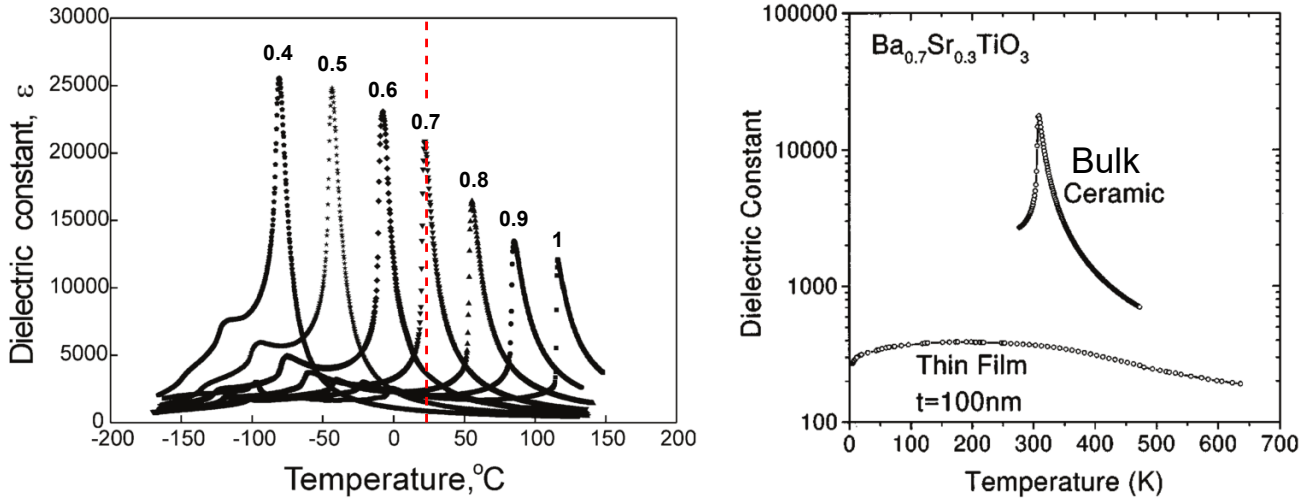

Figure 2.7: (Left) Temperature dependence of the dielectric constant for $Ba_xSr_{1-x}TiO_3$ bulk ceramics sintered at 1450 °C for different Ba/Sr ratios [43]. The red dashed line shows the room temperature. (Right) Dielectric constant of bulk and thin-film $Ba_{0.7}Sr_{0.3}TiO_3$ as a function of temperature [42].

2.4.2 Strontium molybdate $SrMoO_3$

In the past, efforts have been made to develop oxide electronics and implement conducting oxides as electrode material. Promising candidates for oxide bottom electrodes are conducting perovskite oxides such as $SrRuO_3$ [11, 44–48], $La_{0.5}Sr_{0.5}CoO_3$ [49, 50], $La_{0.67}Sr_{0.33}MnO_3$ [51–54] and $LaNiO_3$ [55, 56]. However, all these materials exhibit a resistivity above 100 $\mu\Omega$·cm. Thus, the high frequency losses of such

perovskite materials are too high for applications [12]. Therefore, it was concluded in literature, that conductive oxide electrodes are too resistive for microwave applications [57].
Strontium molybdate $SrMoO_3$ (SMO) single crystals have the lowest resistivity of 5.1 $\mu\Omega$·cm among all known perovskite oxides [58] even outperforming platinum (10.6 $\mu\Omega$·cm). Using the pulsed laser deposition and a growth in reductive conditions it is possible to produce $SrMoO_3$ single crystalline thin films up to 500 nm with a DC resistivity below 20 $\mu\Omega$·cm [59]. The reported bulk value for the *c*-lattice constant is 3.974 Å. [60].

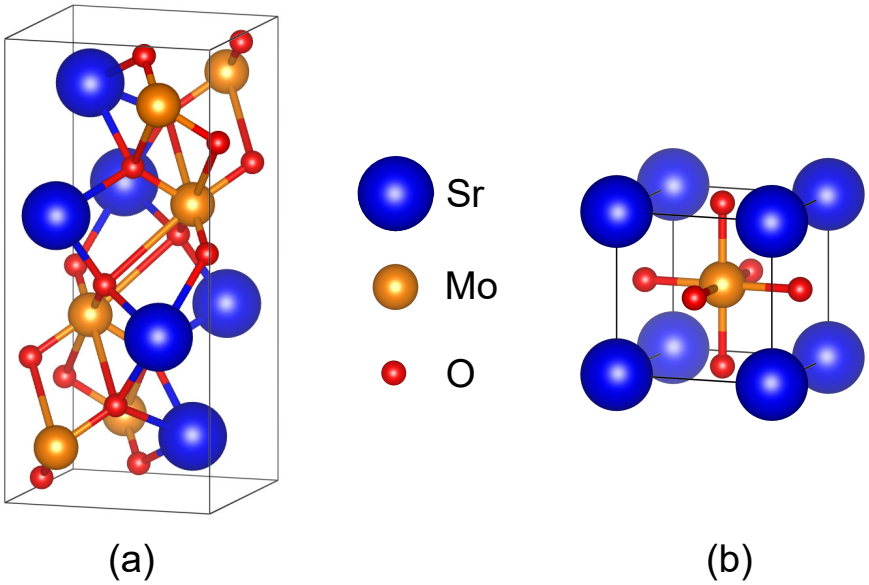

Figure 2.8: (a) Scheelite lattice structure of $SrMoO_4$ used as PLD target and (b) perovskite structure of $SrMoO_3$ after reduction during PLD deposition, utilized as bottom electrodes in oxide electronics.

Starting point for the SMO deposition is a $SrMoO_4$ target. These targets are produced by spark plasma sintering (SPS). $SrMoO_4$ exhibits a scheelite structure (see Figure 2.8). The molybdenum is in the oxidation state Mo^{6+} and, therefore, $SrMoO_4$ is highly insulating. It is stable at atmospheric pressure. The low resistivity of SMO down to $\rho = 20 - 30\,\mu\Omega$·cm [12] relies on Mo being in the thermodynamically unfavorable Mo^{4+} valence state with $4d^2$ (t_{2g}) electronic configuration near the Fermi level [61]. Thus, it is very important to reduce the $SrMoO_4$ target during thin-film growth and to maintain the Mo^{4+} valence state and prevent Mo from oxidizing into Mo^{6+}. This occurs very rapidly and already at very low oxygen background pressures, which becomes evident in the thermodynamic diagram in Figure 2.9.

This oxidation is a big challenge during the production of heterostructures utilizing SMO as bottom electrode material, since its growth is constricted to reductive conditions. It is visible in Figure 2.9 that the SMO growth in vacuum is restricted to a very narrow growth window (below 10^{-7} Torr at 650 °C). An alternative to the growth under vacuum is the growth in reductive background gases such as argon or mixture of hydrogen and argon (2.5 % H_2 + Ar). This has been done in a previous PhD work [17] and H_2 + Ar

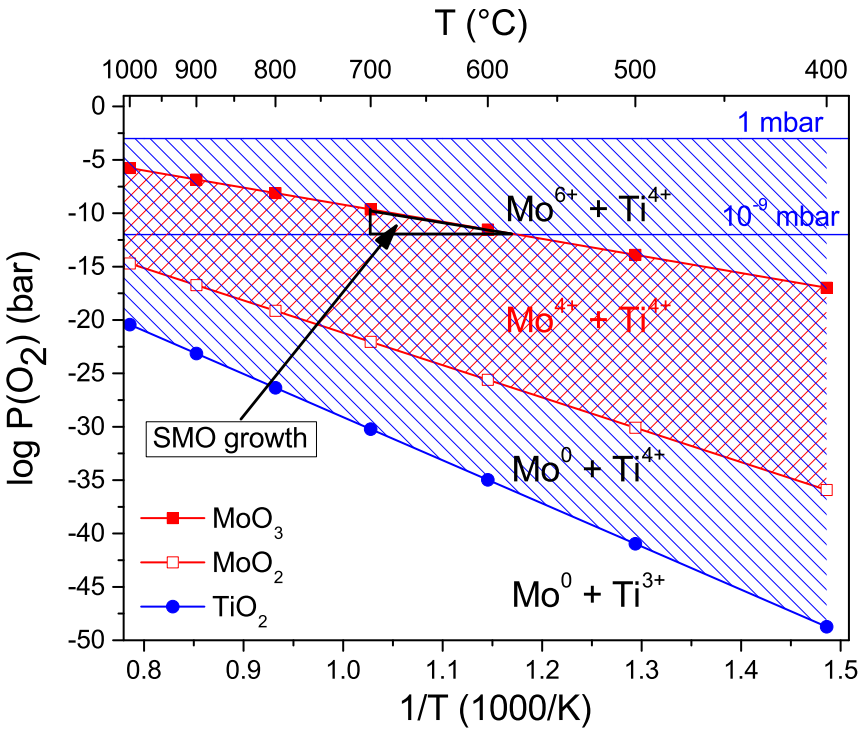

Figure 2.9: Thermodynamic phase diagram of MoO_3, MoO_2, TiO_2. The blue area shows the occurrence of TiO_2 with Ti in 4+ oxidation state as desired in BST. The red area shows the occurrence of MoO_2 with Mo in 4+ oxidation state as desired in $SrMoO_3$. The black triangle shows the narrow growth windows for $SrMoO_3$ in vacuum, which is technically feasible by PLD.

lead to the lowest resistivity values, which might be caused by the additional chemical component of the reduction. However, hydrogen-argon gas mixture has technological drawbacks, such as an unstable gas mixture requiring frequent growth optimizations [17].
It has to be noted, that dielectric materials, such as BST used during this work requires oxidizing growth conditions in order to ensure a sufficient oxygenation of the dielectric. This is of importance, since oxygen vacancies lead to undesired leakage current through the dielectric.
Therefore, in order to realize heterostructures with SMO bottom electrodes and functional oxide materials requiring oxidizing growth conditions, an oxygen diffusion barrier at the interface of the SMO and dielectric is necessary, which should reconcile the two contradictory growth conditions.

2.4.3 Oxygen diffusion barrier

As described in the previous chapter, SMO and BST demand very contradicting growth conditions. Growing both materials in a good quality requires an interlayer acting as an oxygen diffusion barrier. Diffusion can be described by two complementary approaches [62, 63].

Macroscopic approach

The macroscopic approach does not consider matter as atoms. Fick's law describes the material flux of component i through unit area of a reference plane per unit time j_i and reads

$$j_i = -D_i \frac{\partial c_i}{\partial x}, \tag{2.12}$$

where c_i denotes the concentration and D_i the diffusion coefficient of a component i, respectively. This 1-dimensional consideration of Fick's law is usually sufficient considering diffusion along one selected direction. However, it can also easily be generalized into:

$$\vec{j_i} = -\vec{D_i} \nabla c_i \tag{2.13}$$

where c_i is a scalar concentration field and $\vec{D_i}$ is a symmetric second order tensor, which is reduced to a scalar for cubic crystals. Although not visible in the formula (2.13), the driving force for diffusion is not the gradient of concentration, but the gradient in chemical potential ($\nabla \mu_i$) [62].

Microscopic approach

The microscopic approach derives the diffusion coefficient with the mean square displacement of the diffusion species. The derivation of the microscopic definition of diffusion coefficient D_i can be found in [62]. It reads

$$D_i = \frac{1}{6} a^2 Z \Gamma_i, \tag{2.14}$$

with the jump rate Γ_i of the particle to one of its Z neighbors and the distance a to the neighbor sites.

In the present material system, the critical oxygen diffusion is not along the surface, but perpendicular to the surface into the SMO layer. Two different oxygen diffusion processes are present.

1) the gas|solid interface during the growth of BST

2) the solid|solid interface from BST to SMO

Both processes can be supressed by an intermediate oxygen diffusion layer. SMO needs reductive conditions during the growth and oxidizes easily, as visible in the thermodynamic diagram in Figure 2.9. On top of SMO, a thin layer of 5 – 10 unit cells is grown in vacuum, which acts as the oxygen diffusion barrier. Different materials have been investigated in literature with respects to the oxygen diffusion such as $SrZrO_3$, $BaTiO_3$, $SrTiO_3$ and related perovskite oxides [64–66]. However, not only the bulk value needs to be considered, but the strain is also very important [67, 68] (see section 2.6).

2.5 Thin-film growth

Since this work focuses mainly on thin-film deposition and the analysis of the crystal quality, differences of the thin-film growth will be discussed in this section. Technical details of the film deposition will be discussed in section 3.1. There are four distinct types of crystal structures:

- **amorphous**: only short range atomic (ionic) order
- **polycrystalline**: long range atomic (ionic) order in grains but no order between grains
- **textured**: long range atomic (ionic) order in grains and preferential orientation between the grains and the substrate
- **epitaxial**: long range atomic order in grains and orientation relation between grains and substrate, ideally only one orientation

Epitaxial growth is often achieved by growth on single crystal substrates. The epitaxial relation describes the thin films adjusting the orientation to the substrate. Thus, the substrate material and orientation dictates the orientation and structure of the thin films. If a material is grown on a crystalline substrate of the same material the growth is called **homoepitaxy**. If substrate and film are two different materials it is called **heteroepitaxy**.
The short pulse duration of the excimer laser, during the pulsed laser deposition, influences the nucleation and growth process. The mean diffusion time t_D of the ablated atoms is given by [69]

$$t_D = \nu^{-1} \exp\left(\frac{E_A}{k_B T}\right), \tag{2.15}$$

where ν is the attempt frequency for atomistic processes, E_A is the activation energy for diffusion, and k_B is the Boltzmann constant. The mean diffusion time t_D sets the time frame for the nucleation and growth process. For a great number of deposition conditions, t_D exceeds the pulse length. Therefore, the deposition can be seen as instantaneous for each pulse [69]. After each laser pulse there is a relative long time interval with no deposition, depending on the repetition rate. During this duration with no ablation, the atoms which reached the surface can rearrange and successively bond through nucleation [69].
The formation of a thin film has two different stages. The first stage is the nucleation. A schematic overview of the processes on the sample surface during thin-film growth is shown in Figure 2.10. The atoms in the plume arriving on the surface can penetrate, be absorbed, or be reflected from the substrate depending on their kinetic energy. If they are absorbed, they are bound mainly by the Van-der Waals force, which is called physisorption [70] and in this case, surface diffusion is possible. If the atoms form chemical bonds with the substrate it is called chemisorption and diffusion is more difficult. The nucleation starts if atoms shape clusters by forming chemical bonds to each other.

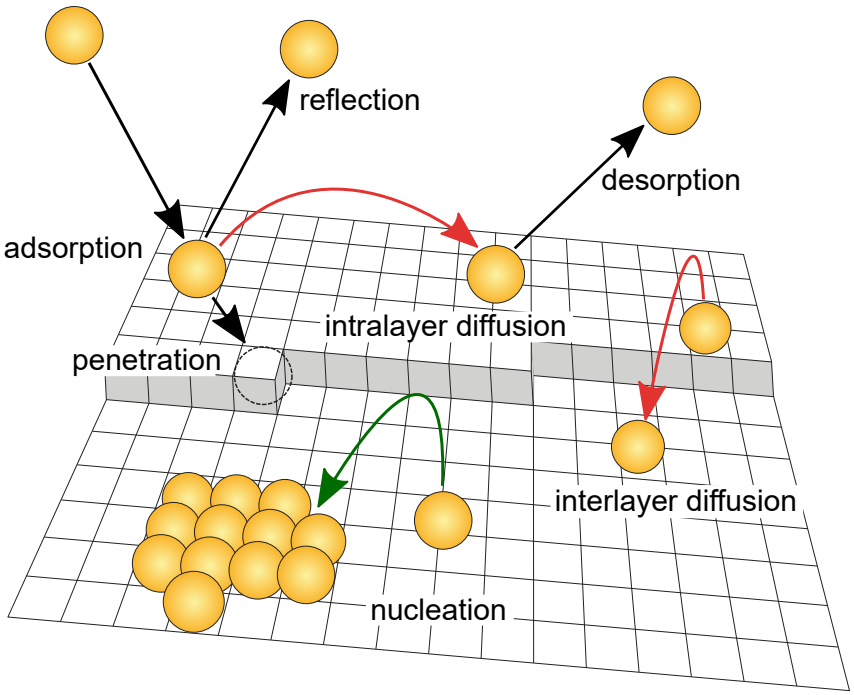

Figure 2.10: Schematic overview of possible processes for particles hitting the surface during thin-film growth [71].

Further growth of the nuclei depends on the surface energy of the substrate γ_S, film γ_F and interface γ_I. The growth of the nuclei can be described by the Young Equation [72]

$$\gamma_S = \gamma_I + \gamma_F \cos\theta, \tag{2.16}$$

where γ_S, γ_I and γ_F are the surface energies and θ is the contact angle. The schematic situation for equation (2.16) can be seen in Figure 2.11. Four different thin-film growth modes are displayed in Figure 2.12 and described in the following.

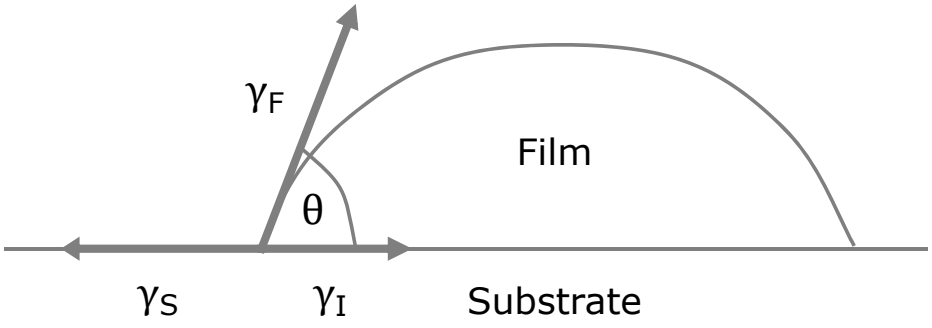

Figure 2.11: Simplified picture of a nucleus growing on a substrate. θ represents the contact angle, γ_F the surface energy of the film, γ_S the surface energy of the substrate and γ_I the interface energy of substrate and film.

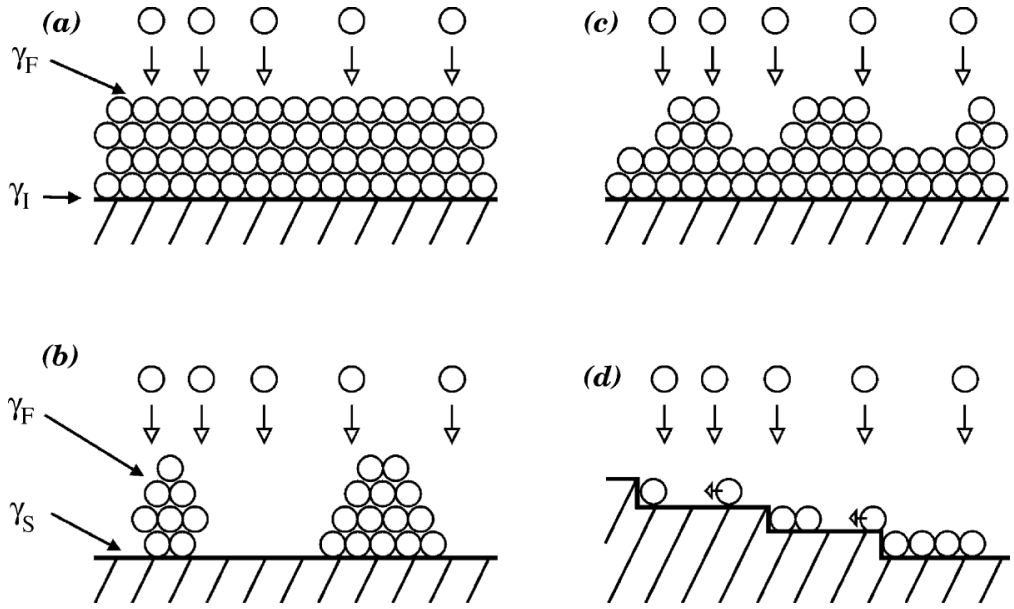

Figure 2.12: Film growth modes: (a) layer-by-layer growth (Frank-Van-der-Merwe), (b) island growth (Volmer-Weber), (c) Stranski-Krastanov, (d) step flow [69].

The **Frank-Van-der-Merwe** or layer-by-layer growth mode is characterized by [71]

$$\gamma_S \geq \gamma_F + \gamma_I. \tag{2.17}$$

The bonding towards the substrate is stronger than between neighboring film atoms. Thus, the substrate gets fully covered by the film, which is called a 2-dimensional or 2D growth. This normally requires a homoepitaxial growth, since there is no misfit energy. The contact angle θ in equation (2.16) is $\theta = 0$, since there are no islands or clusters.

The **Step Flow** belongs to the layer-by-layer growth. The differences between layer-by-layer growth and step flow are determined by a number of kinetic parameters. The most important kinetic parameter is the surface diffusion coefficient D_S of the adatoms which can be expressed as [69]

$$D_S = \nu a^2 \exp\left(-\frac{E_A}{k_B T}\right), \tag{2.18}$$

where E_A is the activation energy for diffusion, ν the attempt frequency, and a the characteristic jump distance. Two different diffusion processes have to be considered in order to differentiate between step flow and layer-by-layer growth. The diffusion of atoms on a terrace, which is called intralayer mass transport, and the diffusion of an atom to a lower terrace (interlayer mass transport). Both diffusion mechanisms are also displayed in Figure 2.10. As shown in Figure 2.12 (d) the process leading to step flow is the intralayer mass transport on vicinal surfaces, which can also be seen as stepped surfaces. If the diffusion length $l_D = \sqrt{D_S \tau}$ is bigger than the width of a terrace step, the mobility of the atoms is high enough to reach the edge of the substrate steps. These steps can be compared to a sink and adatoms diffuse towards them.

Thus, nucleation on the terraces is avoided [69]. To obtain layer-by-layer growth, a high interlayer mass transport is necessary. Atoms deposited on a forming cluster must first reach the bottom of the cluster and then diffuse to a lower layer. It is important to note, that although step flow has the same surface morphology than layer-by-layer growth, it does not show any oscillations while monitored by the reflection high-energy electron diffraction technique which is described in the next section.

For the **Volmer Weber** or island growth mode (see Figure 2.11 (b)) the criterion is:

$$\gamma_S < \gamma_F + \gamma_I \tag{2.19}$$

During this growth mode, the bonding among film atoms is stronger than towards the substrate. Therefore, the film is growing in 3-dimensional (3D) clusters which leads to a very rough surface of the film. For this growth mode, equation (2.16) can be used to determine the contact angle θ, which can have values between $0\,° < \theta < 90\,°$.

In heteroepitaxial growth, the **Stranski-Krastanov** growth mode can occur. This growth mode describes the change from layer-by-layer to island growth. Reason for this change in growth is a lattice mismatch between substrate and film. Due to this mismatch biaxial strain is building up as the film is growing. This results in an elastic energy growing with increasing film thickness. After a certain critical thickness h_c misfit dislocations start forming near the substrate-film interface [69]. These misfit dislocations are introduced to relieve the mismatch strain and, thus, the layer-by-layer growth is switching to island growth mode.

2.6 Strain

Strain is a key factor during thin-film growth and has to be considered during material and substrate choice. Not only does strain directly impact the growth of films, but it also alters the properties of the layers. It has been shown in literature, that ferroelectric thin-film properties can be altered by different values and signs of biaxial strain [73]. Theoretical calculations have shown, that magnetic and electric properties in $SrRuO_3$ thin films affected by the octahedral distortions due to strain can be altered [74]. Electric and ferroelectric properties are very important in the heterostructures during this work. Therefore, the choice of substrate plays a crucial role.

Strain between substrate and film or among two films always occurs if there is a mismatch between the lattice constants of the substrate and film or films in heterostructures. The lattice mismatch is described by [75]

$$\Delta = \frac{\Delta\alpha}{\alpha_{\text{Substrat}}} = \frac{\alpha_{\text{Substrat}} - \alpha_{\text{Film}}}{\alpha_{\text{Substrat}}}, \tag{2.20}$$

where α_{Film} and α_{Substrat} are the lattice constant of the film and and substrate, respectively. For high quality epitaxial films, an excellent substrate quality is essential and the lattice mismatch should be smaller than

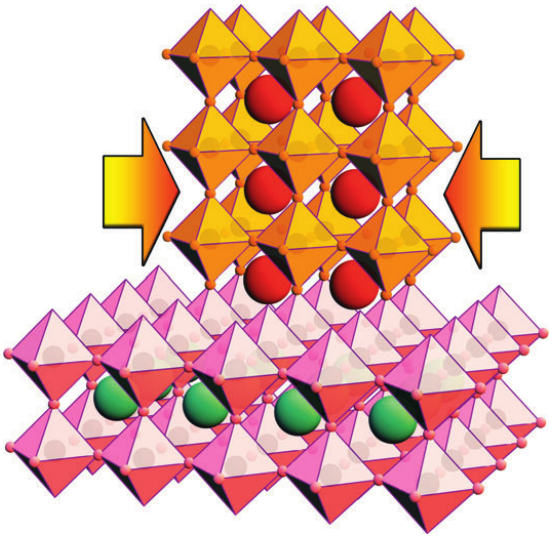

Figure 2.13: Schematic of a fully coherent epitaxial film biaxial strained on the underlying substrate. Both, substrate and film have a perovskite ABO_3 formula [73].

5 %. If $\Delta < 0$ the film is compressively strained in plane, whereas if $\Delta > 0$ the film is tensile strained in-plane. Other reasons than lattice mismatch for strain in crystals can be [28]:

- Temperature – e.g. thermal contraction during cooling after deposition
- Mechanical stress – elastic deformation
- External DC field – piezoelectric and electrostrictive effects

Strain can also impact the oxygen vacancy migration in different materials. This is very important for the oxygen diffusion barrier discussed in the previous section 2.4.3.
In the example of $SrTiO_3$, theoretical strain calculations have shown, that compressive strain up to 6 % can significantly suppress the inter-plane oxygen diffusion normal to the plane of strain, whereas tensile strain increases the diffusion in all directions [67, 68]. At 2 % compressive strain, inter-plane barrier was reported to be increased by 35 – 50 % [68].
Theoretical calculations for BTO predict oxygen vacancy formation energy and migration barrier to be enhanced by compressive strain [76]. Thus, strain engineering by choosing a certain material combinations can increase the oxygen diffusion barrier of a material.
However, strain can also cause lattice defects or small cation nonstoichiometery hindering the comparison with equivalent bulk crystals or theoretical calculations [77]. These defects can in return also lead to a reduction in the oxygen diffusion barrier. Studies during this work investigated different materials as oxygen diffusion barriers. The investigations were carried out by consecutive annealing and measuring XPS. More detailed descriptions will be given in section 4.3.

2.7 Varactors

Current wireless communication is based on a broad radiofrequency spectrum. Therefore, telecommunication devices need to be able to handle data in the broad frequency range. The circuits processing the signals received from the antenna contain inductances and capacitors. In order to capture the whole spectrum with sufficient quality, different values in capacitance are necessary. The impedance of the antenna needs to be adapted to the changes in external circumstances such as, e.g. surrounding metals or other solids. One solution for this demand are so-called switchable antenna tuners. They contain several capacitors with different, but fixed capacitances. Depending on the required frequency to transmit, a particular branch of the antenna tuner is selected. The drawbacks of this approach are a bigger size of the component and that the maximum performance is not always reached, since the possible capacitances have only certain discrete values and can not be changed continuously.
An alternative solution are tunable capacitors, also called varactors. The capacitance of a varactor can be changed by applying an external electric DC field. Varactors are used in tunable filters and switches, voltage controlled oscillators, microwave phase shifters, delay lines, tunable matching networks and other applications [57, 78]. There are currently three different technologies to realize these tunable components, namely semiconductor varactor diodes, RF micro-electro-mechanical systems (MEMS) and ferroelectric thin-film varactors. There has been quite intensive work in the past on thin-film varactors. Most investigations were focused on varactors with platinum bottom electrodes [57, 78–87]. A different approach of varactors utilizing oxide bottom electrodes, mainly $SrRuO_3$, were also the topic of research in the past [11, 45–48] and also, recently, fully optically transparent varactors were produced [88]. However, it was concluded in literature, that oxide bottom electrodes are too resistive for microwave applications [57]. The approach of oxide electrodes and, thus, an epitaxial all-oxide heterostructure was revived by integrating the highest conducting oxide $SrMoO_3$ as the bottom electrode material. The varactor heterostructure in this work, i.e. $SrMoO_3/Ba_xSr_{1-x}TiO_3/Pt/Au$, is called **all-oxide varactor**. It has several advantages over the varactors with Pt bottom electrodes such as:

- Inexpensive materials
- Low surface roughness: high bottom electrode thicknesses above skin depth possible → low losses
- Atomically sharp interfaces → dielectric thicknesses below 50 nm possible
- Low defect density in the dielectric due to epitaxial growth

The device characteristics of the three competing technologies are shown in the Table 2.1. MEMS have on the one hand a high Q value and linearity, but on the other hand a relative slow tuning speed (μs) and high packaging costs. They are also sensitive to environmental conditions such as moisture, temperature and vibrations, possibly hindering the reliability [57].
Semiconductor diodes like GaAs are highly tunable and reliable. They also have a very high Q factor, but only at lower frequencies. The Q factor decreases linearly at higher frequencies. In addition, they are more expensive compared to ferroelectric thin-film varactors [57].

All-oxide varactors further improve the advantages of conventional thin-film varactors, which enables new application fields such as mobile communications. A schematic structure of the all-oxide varactors investigated in this work will be given in section 2.7.1.

Table 2.1: Comparison of the all-oxide varactors reported in this work with different tunable capacitor technologies of semiconductor diodes, RF MEMS and Pt based ferroelectric thin-film varactors (parallel-plate) [28,78,89].

Device characteristics	**Semiconductor diodes**	**RF MEMS**	**Pt-based thin-film varactors**	**All-oxide varactors**
Tuning DC voltage	Low (< 10 V)	High (40 – 100 V)	Low (< 10 V)	Very low (< 3.7 V)
Tuning ratio	> 3:1 (linear range)	> 5:1 (linear range)	≈ 3:1 (linear range)	≈ 4:1 (linear range)
Tuning speed	High (≈ 10 ns)	Low (≈ 10 μs)	High (≈ 10 ns)	High (≈ 10 ns)
Quality factor (Q)	≈ 200 at 1 GHz	> 500 at 1 GHz	≈ 200 at 1 GHz (0 V)	≈ 75 at 1 GHz (0 V)
Switching lifetime	High	Low	High	
Packaging cost	Low	Very high	Low	
Power handling	Poor (≈ 1 W)	Good (< 5 W)	Good (up to 5 W)	
Power consumption	Low (nW – μW)	Low (nW – μW)	Low (nW – μW)	Negligible (< nW)
Breakdown voltage	Low (< 25 V)	Moderate (> 50 V)	Low (< 25 V)	Low (< 25 V)
Linearity	Low	High	High	
Third order intercept (IP3)	Low (≈ +28 dBm)	High (≈ +55 dBm)	High (≈ +55 dBm)	
Integration capability	Very good	Good	Good	Good – Very Good

Five parameters are commonly used to evaluate varactor properties namely loss tangent, quality factor, tunability, relative tunability and commutation quality factor (CQF). Depending on the formula and measurement, these parameters can characterize the individual materials properties or the performance of the whole varactor device. All five parameters will be described in the following, both for description of the ferroelectric material and varactor device properties.

- The **loss tangent** $\tan\delta$ of a ferroelectric material, which is given by the ratio of the imaginary and real parts of the permittivity [57]:

$$\tan\delta(E) = \frac{\varepsilon''(E)}{\varepsilon'(E)} = \frac{\mathrm{Im}(\varepsilon(E))}{\mathrm{Re}(\varepsilon(E))} \tag{2.21}$$

- The losses of a ferroelectric material can also be described with the **quality factor** Q(E) [11, 57]:

$$Q(E) = \frac{1}{\tan\delta(E)} \tag{2.22}$$

  It has to be noted, that this equation represents the quality factor of the ferroelectric material. The quality factors determined by the experimentally measured complex scattering parameters represents the quality factor of the varactor device, which includes the electrode, substrate and additional influences. Taking only the losses of the electrode into account leads to a quality factor representation of the varactor device Q as

$$Q_{\mathrm{device}}(E) = \frac{1}{\omega C R_{\mathrm{ser}}}. \tag{2.23}$$

- The **tunability** n describes the change of permittivity of the ferroelectric material with the electric field [57]:

$$n(E) = \frac{\varepsilon'(0)}{\varepsilon'(E)} \tag{2.24}$$

  In addition, the tunability n can be defined as a device parameter with the change in capacitance with applied electric field:

$$n_{\mathrm{device}}(E) = \frac{C(0)}{C(E)} \tag{2.25}$$

- The **relative tunability** n_r is defined as the change of permittivity with an electric field, divided by the by the permittivity absence of the field [57]:

$$n_r(E) = \frac{\varepsilon'(0) - \varepsilon'(E)}{\varepsilon'(0)} \tag{2.26}$$

Similar to the tunability, the relative tunability n_r can also be defined with the change in capacitance as a device parameter:

$$n_{r,\text{device}}(E) = \frac{C(0) - C(E)}{C(0)} \tag{2.27}$$

- A summarizing figure of merit is the **commutation quality factor (CQF)** [28, 78]. This parameter is used to characterize the device performance

$$\text{CQF}_{\text{device}}(E, f) = \frac{(n(E)-1)^2}{n(E) \cdot \tan\delta_{\text{device}}(0, f) \cdot \tan\delta_{\text{device}}(E, f)} \tag{2.28}$$

$$= Q_{\text{device}}(0, f) \cdot Q_{\text{device}}(E, f) \cdot \frac{(n(E)-1)^2}{n(E)} \tag{2.29}$$

Advancements such as 5G and internet of things (IoT) requires an even more efficient use of the spectrum driving the development of thin-film dielectrics with higher tunability n, quality factor Q and figure of merit CQF [5]. Industrial desired performance properties of BST thin-film varactors are a device loss tangent of $\tan\delta_{\text{device}} < 0.01$ ($Q_{\text{device}} > 100$), as well as a high tunability $n > 2$ [57]. In literature, different requirements for the CQF values are suggested. In [11, 90] a CQF value greater than 2000 and in [78] greater than 5000 is suggested, respectively, for RF/microwave applications.

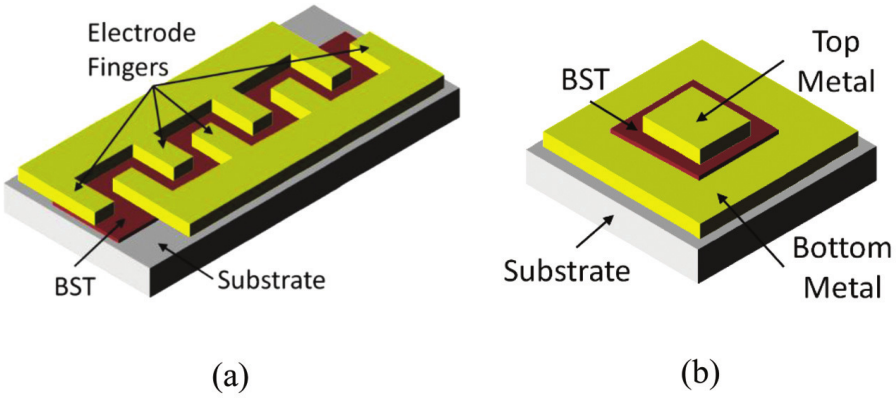

Figure 2.14: Two different varactor layouts: (a) coplanar capacitor, (b) parallel-plate capacitor [78].

There exist two different types of thin-film varactor geometries, namely a coplanar or interdigitated capacitor (IDCs) and a parallel-plate (PP) or metal-insulator-metal (MIM) capacitor (see Figure 2.14). A comparison with advantages of the two different designs can be seen in Table 2.2. For the IDCs, the electric bias field through the dielectric is determined by the gap between the electrodes and can, thus, be controlled by the device design. However, parts of the fields are always confined in the passivation/surrounding air and the field inside the ferroelectric exhibits a rather inhomogeneous distribution especially for small gaps. For

the MIM structure, the field is applied quasi-homogeneous through the dielectric and, thus, it is controlled by the thickness of the dielectric. However, the thickness has to be above a certain threshold, which depends on the roughness of the bottom electrode to avoid short circuits through the dielectric. Usually the thickness of the dielectric is around 300 nm for conventional varactors with Pt bottom electrodes, requiring tuning voltages around 20 V.

Table 2.2: Comparison of the basic properties of coplanar and parallel-plate varactors [4].

Coplanar	**Parallel-plate**
high tuning voltage	small tuning voltage
voltage applied across the gap	voltage applied through thickness
small capacitance	large capacitance
smaller loss contribution of the electrodes	high loss contribution of the electrodes

2.7.1 All-oxide varactor

As already mentioned in the previous section, the concept of **all-oxide varactors** is the substitution of the metallic bottom electrode with the highly conducting perovskite $SrMoO_3$. The complete all-oxide varactor heterostructure consists of the layers $SrMoO_3/Ba_xSr_{1-x}TiO_3/Pt/Au$. $SrMoO_3$ outperforms other perovskites in resistivity (see Figure 2.15) and is located in the same region as metals such as platinum. A second key benefit is, that SMO provides a perfect lattice match for a a wide range of BST compositions. In combination with the right substrate (different scandades such as $GdScO_3$) a heteroepitaxy with all involved lattice mismatches below 0.5 % can be achieved. This enables an epitaxial, defect-free heterostructure with atomically flat interfaces.

A schematic cross section of the heterostructure can be seen in Figure 2.16 (a). The thickness of the STO buffer layer on GSO is about 5 – 10 unit cells and ensures smooth layer-by-layer growth of the SMO [92,93]. The buffer layer prevents the formation of an energetically unstable valence-mismatched interface between GSO and SMO [12] and compensates the octahedral tilts of the GSO [94]. Despite the thickness of only 5 unit cells, the interlayer between SMO and BST prevents SMO from oxidizing during the BST growth and will be further discussed in section 4.3.
The top electrodes (TE) are structured by photolitography with lift-off or ion-beam etching and deposited via DC sputtering. The Pt layer between BST and Au with a thickness of 40 – 80 nm improves the adhesion of Au. Unless stated otherwise,the TE have a circular structure as it can be seen in Figure 2.16 (b). The outer (grounding) pad of the TE has a very large area and, thus, a very large capacitance. Therefore, it can be neglected in comparison to the inner pad ($A_{outer} > \approx 300\, A_{inner}$), yielding the SMO bottom layer as an effective ground for the main capacitance below the center (sourcing) pad [95]. On one 5 x 5 mm^2 single crystal substrate, 36 varactor devices are structured in a 6 x 6 row array as displayed in Figure 2.16 (d).

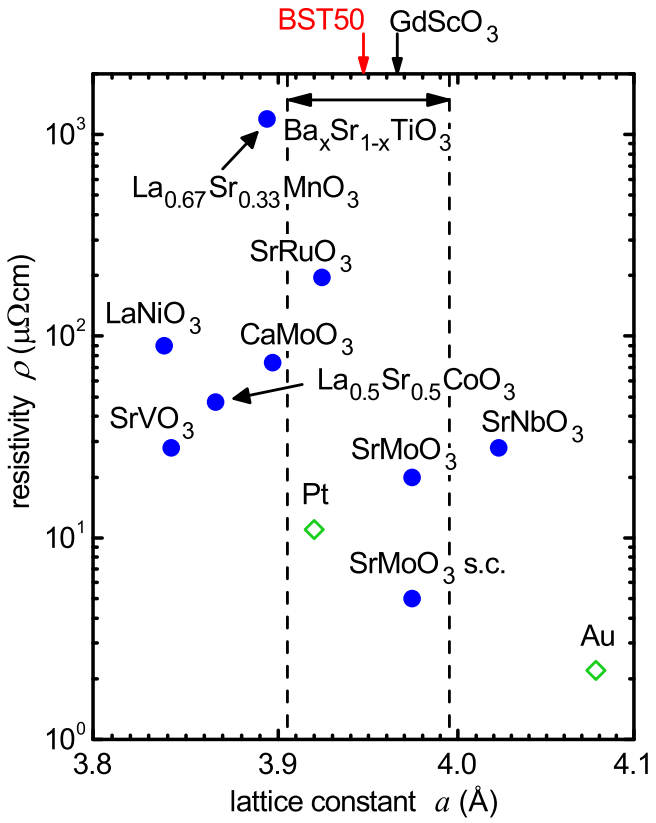

Figure 2.15: Comparison of some common conduction perovskite oxides (filled blue circles) to Au and Pt (green diamonds) with respect to resistivity and lattice parameter. $SrMoO_3$ s.c. denotes the single-crystal value [91].

These 36 varactors differ in dimensions which are specified in Table 2.3. The inner pad d varies from 20 – 60 μm in diameter and the gap $(D - d)$ varies from 20 – 80 μm. The variation in dimensions is designed to allow the extraction of properties such as the resistivity of SMO and BST loss tangent across the whole substrate, assuming the material parameters to be constant across the complete substrate. Each dimension composition exist multiple times for redundancy. Thus, the structure can also be seen as four similar 3 x 3 varactor arrays. The reason for this redundancy is to evaluate a performance divergence across the whole sample and to have a redundancy in individual varactors in case the lithography or lift-off fails for a number of pads.

This varactor heterostructure can be described by the common RLC model (see Figure 2.16 (c)). It consists of a lossy capacitance $C = C(1 - j \cdot \tan\delta)$ representing the dielectric in series with an inductance L_{ser} and resistance R_{ser}, of the electrodes. The energy of the AC field decays exponentially in conductors. If the thickness is lower than three to five times the skin depth, the field penetrates into the substrate, which leads to inaccuracies of the RLC model. Therefore, for thinner electrodes or smaller frequencies, this model has to be extended, which was done for the all-oxide varactors of this work [95, 96].

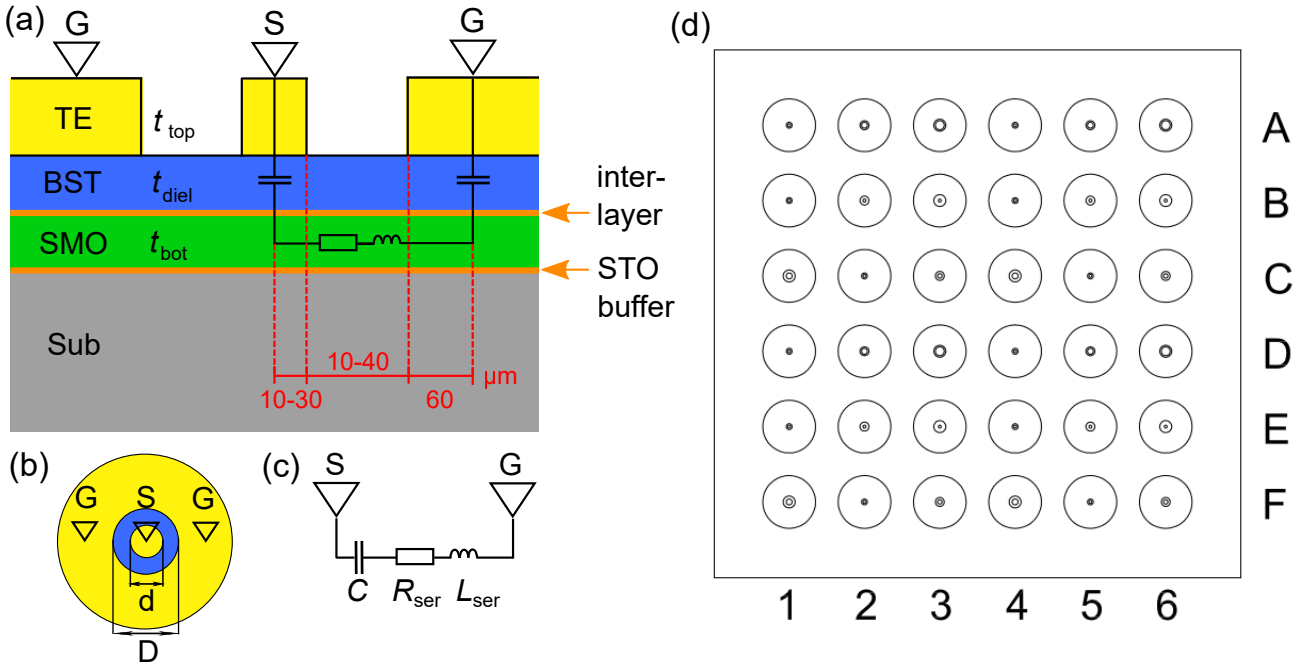

Figure 2.16: (a) Schematic cross section of the all-oxide varactor heterostructure. Buffer- and interlayers between Sub–SMO and SMO–BST 5 – 10 unit cells. The thicknesses of the individual layers were varied between t_{bot} = 500 – 5000 nm, t_{diel} = 50 – 500 nm, t_{top} = 350 – 4000 nm. The top electrodes (TE) consist of a thin Pt layer for adhesion and a thick Au layer for contacting. (b) Top view of the contacts (c) The schematic RLC model (d) Schematic structure of the top electrodes of the 5 x 5 mm^2 photolitographic mask of the circular test structure.

Table 2.3: Dimensions of the pads in Figure 2.16 (d). Three of the 6 lines and 6 rows are redundant and therefore merged in this table.

column	1 & 4		2 & 5		3 & 6	
Row	d (μm)	D (μm)	d (μm)	D (μm)	d (μm)	D (μm)
A & D	20	40	40	60	60	80
B & E	20	40	20	60	20	80
C & F	40	80	20	40	30	60

2.7.2 Conduction mechanism in dielectric films

The leakage current in the varactor originates from conduction through the (insulating) dielectric film. A leakage current needs to be avoided or suppressed as much as possible, since this increases the power consumption of the device and hinders the application as mobile technology. Leakage currents are displayed as a function over applied DC voltage in I-V curves or as as a function over the applied electric field. There are several conduction mechanisms through dielectrics (see Figure 2.17). Conduction mechanisms in dielectrics can be divided in two types: electrode-limited and bulk-limited conduction mechanism. For the electrode-limited mechanism, the barrier height at the electrode-dielectric is the most important factor whereas for bulk-limited mechanism, the trap energy level in dielectric films is important. The most common conduction mechanism in perovskite dielectrics are: Schottky emission, Poole-Frenkel emission and space-charge-limit conduction [97].

The **Schottky emission** is a electrode-limited conduction mechanism. It is also revered to as thermionic emission. If an electron obtains enough energy, for example by thermal activation, the electrons can overcome the barrier height at the metal – dielectric interface and, thus, be injected in the dielectric (see Figure 2.18). This process depends on the barrier height between the electrode and dielectric and, therefore, strongly depends on the interface. In the case of all-oxide varactors, bottom and top electrode have different work functions. This leads to different barrier heights and a potentially asymmetric I-V curve.

Thin dielectrics are also subjected to the bulk controlled **Poole-Frenkel** conduction mechanism. This conduction mechanism is present for higher voltages/fields surpassing the trap energy. Electrons are emitted by thermal excitation from traps into the conduction band of the dielectric (see Figure 2.18). In case of BST films in the all-oxide varactor heterostructure, oxygen vacancies act as internal traps, enhancing the Poole-Frenkel conduction. This depicts a big challenge in the varactor production to fill oxygen vacancies and ensure a sufficient oxygenation of the dielectric, while simultaneously prevent $SrMoO_3$ from oxidizing.

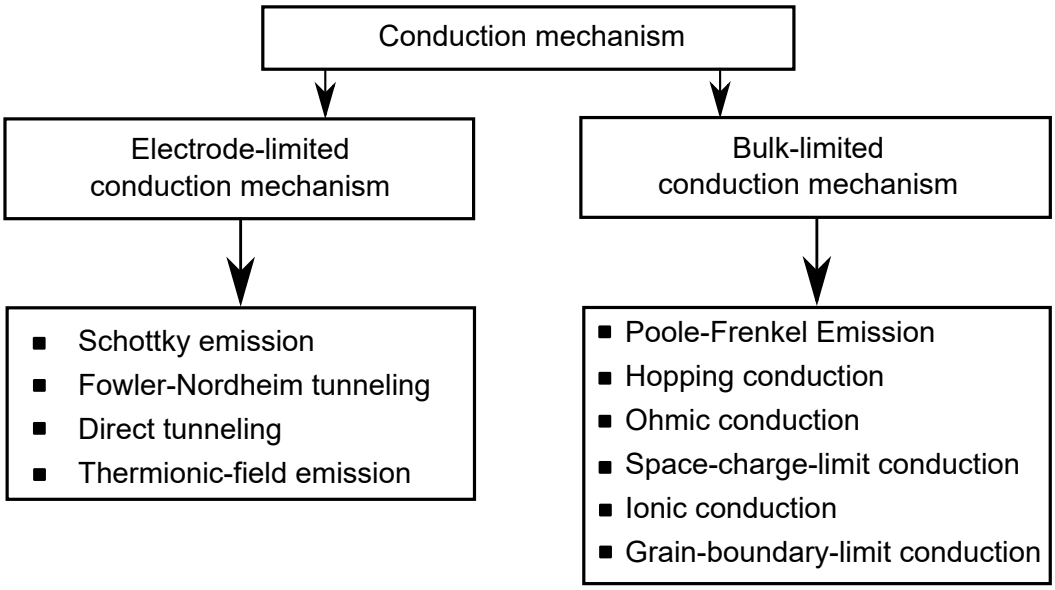

Figure 2.17: Classification of the conduction mechanisms in dielectric films and the separation in to electrode-limited conduction mechanism and bulk-limited conduction mechanism [98].

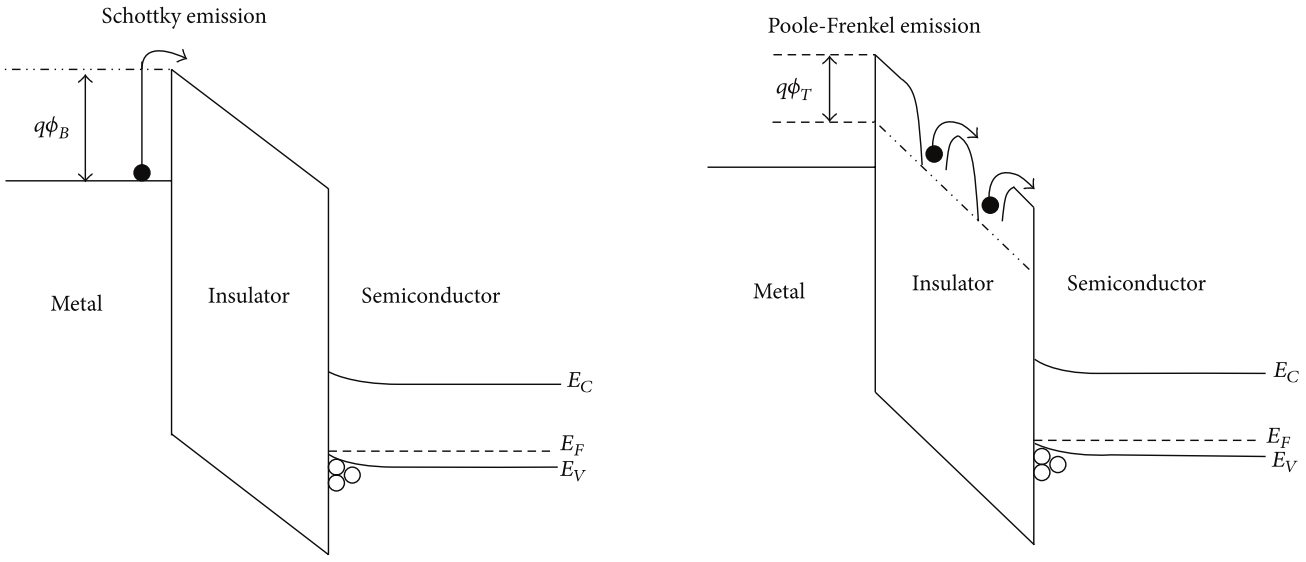

Figure 2.18: Schematic energy band diagram in metal-insulator-semiconductor structures. (Left) Schottky emission and (Right) Poole-Frenkel emission [98]

3 Experimental methods

3.1 Pulsed laser deposition

All films were produced using the pulsed laser deposition (PLD). This method utilizes a pulsed laser beam to ablate material off a target and create a material flux in plasma phase for the film deposition. It has to be distinguished between two different types of extracting atoms from the target. If the laser energy absorbed by the target is low, it results in thermal evaporation of the target. Whereas, if the laser energy is higher than necessary for thermal evaporation, the target material is ablated. Stoichiometric and off-stoichiometric deposition of target material on the selected substrate is feasible, provided that proper growth parameters are chosen.
The ablated material forms a plasma, which is called plume. The particle density distribution of the ablated material is symmetric with respect to the normal of the target surface and depends on the angle between the plume and the surface normal. The particle density D can be expressed with [99]

$$D(\theta) = B \cos^n \theta, \tag{3.1}$$

where B is a constant of the laser energy density, also called fluence, θ is the angle towards the normal of the target and n is dependent on the spot size of the laser on the target. The laser energy density ε is calculated by

$$\varepsilon = \frac{E}{A}, \tag{3.2}$$

where E is the laser energy of the excimer laser on the target and A is the spot size of the excimer laser beam on the target.

A schematic drawing of a PLD system as well as a picture of the used PLD system fabricated by *DCA instruments* are shown in Figure 3.1. The excimer laser at the *DCA* PLD was the model *LEXtra 200* by *Lambda Physik* but it was exchanged during this work with a *Compex 205* laser by *Coherent*. Both lasers are KrF gas excimer lasers, operating at 248 nm and a laser pulse duration time below 30 ns [100]. The importance of short laser pulses is based on the necessity to minimize heat diffusion into the target. The PLD chamber is designed to deposit a film on a substrate with typical size of 5 x 5 mm^2. Up to six different pellets used as PLD targets are installed simultaneously in the motorized target manipulator. The

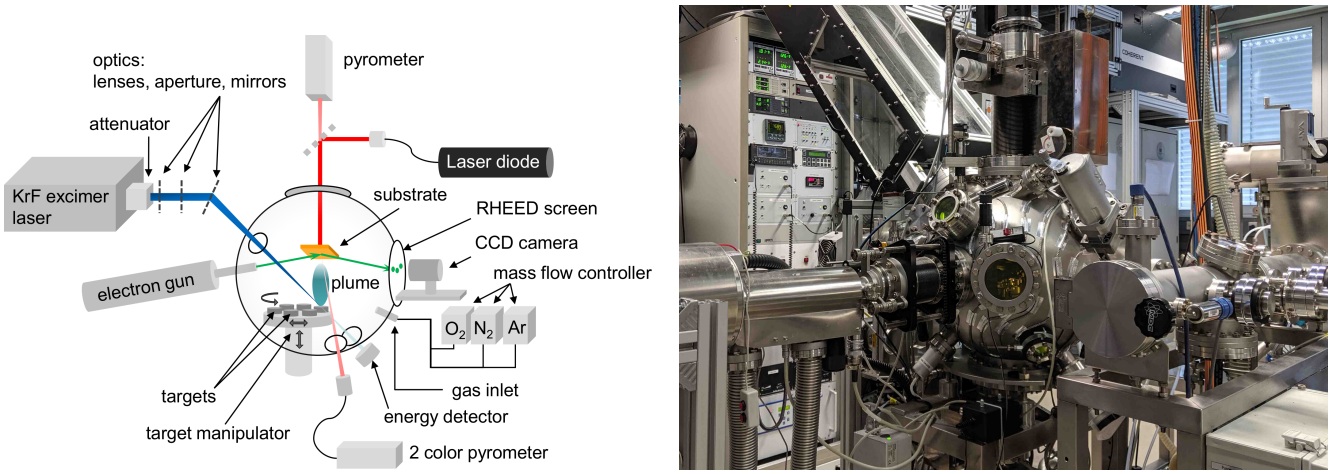

Figure 3.1: (Left) Schematic configuration of the PLD system used to produce the samples during this work [17]. (Right) Picture of the PLD system *PLD 500* from *DCA Instruments*.

manipulator allows to sweep and rotate the target during deposition, to ensure uniform ablation of the target. Both, substrates and targets are loaded via a load-lock using a magnetically coupled transfer arm. The substrate can be heated up to 1000 °C with a heating laser powered by a 140 W laser diode operating at 938 nm. The substrate temperature is controlled by two infrared pyrometers.
The entire system is pumped to ultra-high vacuum with a base pressure below 10^{-8} Torr in the load-lock and 10^{-9} Torr in the chamber. The chamber is also equipped with a gas inlet system including several mass flow control units to regulate the flow of the process gases (oxygen, nitrogen and argon) in the range from 0.3 to 100 sccm.
The PLD is equipped with a 50 kV reflection high-energy electron diffraction (RHEED) system fabricated by *Staib Instruments* allowing *in situ* growth monitoring and surface investigations.

3.2 Reflection high-energy electron diffraction

Reflection high-energy electron diffraction (RHEED) is a powerful method to monitor the surface morphology and growth kinetics *in situ* during deposition. In a typical RHEED system, such as that used during this work, high-energy electrons with 50 keV hit the surface under a grazing incident angle θ of 0.1 – 5° [101, 102]. The absolute value of the wave vector of the incident electrons considering relativistic corrections is given by [103]

$$|\vec{k_0}| = \frac{1}{\hbar}\sqrt{2m_0E + \left(\frac{E}{c}\right)^2}, \tag{3.3}$$

where $\hbar$ is the planck constant divided by 2π and m_0 the rest mass of electrons. For energy of 50 keV used in the RHEED setup during this work, the de-Broglie wave length [21] of the electrons $\lambda = 2\pi/k_0$ is 0.053 Å,

which is smaller than the lattice constants. The penetration depth of electrons with such high energies is several hundreds of nanometers. However, due to the small incident angle, the electrons interact only with the surface (1 – 2 nm). This makes RHEED a very surface sensitive technique [101, 102]. The scattered electrons illuminate a phosphorous screen, showing the diffraction pattern. This diffraction pattern contain information of the surface morphology and growth kinetic.

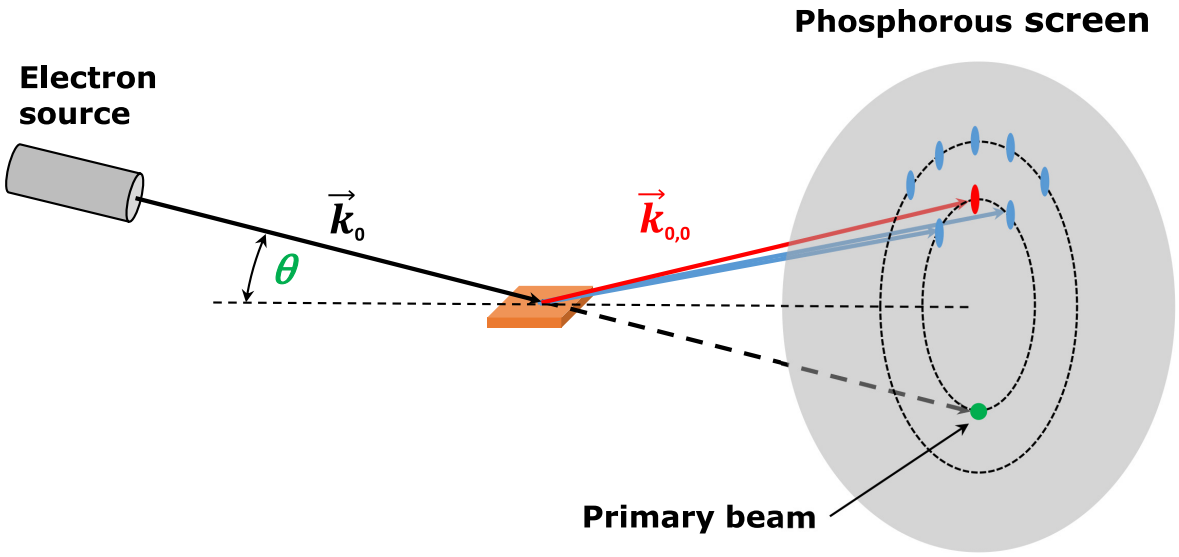

Figure 3.2: Schematic setup during *in situ* RHEED measurement and formation of the RHEED pattern.

The RHEED diffraction pattern also originates from the Laue-condition, similar to the 2θ–ω X-ray diffraction. Hence, only elastic scattering is considered for the RHEED images. Due to the grazing incident angle θ and the low penetration depth of some monolayers, scattering is only considered off a 2-dimensional surface. Therefore, the reciprocal lattice consists of periodic rods perpendicular to the surface (truncation rods). Figure 3.2 shows a schematic construction of the RHEED pattern. Electrons with the wave vector $\vec{k}_0$ hit the sample under the angle θ. The value of k_0 corresponds to the radius of the Ewald-sphere. The scattered electrons hit the phosphorous screen and scattering spots are visible were the Ewald-sphere overlaps with the reciprocal lattice and fulfills the Laue-condition. The scattering spots reside on Laue-circles of n-order. Depending on the surface of the sample, the shape can differ.
Figure 3.3 shows different surfaces and the corresponding RHEED patterns. 2D atomically flat surfaces result in sharp spots at the Laue-circles. For a transition of the atomically flat surface to a a vicinal surface with steps, the spots are vertically broadened and evolve into ellipses. The broadening increases with a higher step density or surface roughness. [17, 104]. Due to the terraces on the surface, the truncation rods are broadened and, thus, the overlap of the Ewald-sphere and the rods in the reciprocal space is larger leading to the ellipses [105]. For a surface with islands, the assumption of a 2-dimensional surface does not hold anymore and the scattering occurs on 3-dimensional clusters. The reciprocal lattice does not consist merely of 2D rods, but a 3D arrangement and therefore, the scattering reflexes do not coincide with the Laue-circles.

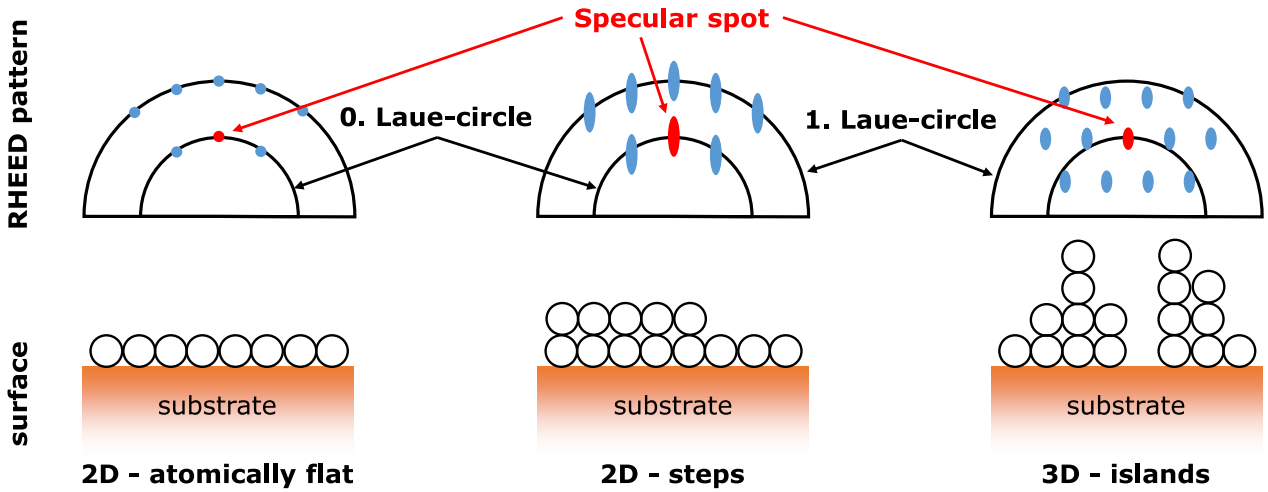

Figure 3.3: Different schematic sample surfaces for several growth modes during thin-film growth with the corresponding RHEED patterns.

In addition to the RHEED pattern, the intensity variation of the spots are monitored over time. If a layer growth in the Frank-Van-der-Merwe growth mode, the intensity of the spots undergoes periodic oscillations. Reason for these oscillations are a change of the surface during growth from a fully-filled with an intensity maximum to a half-filled layer and an intensity minimum. These oscillations allow the determination of thickness and growth rate of a layer. It has to be noted, that in case of the growth mode step flow, although it is a 2D growth mode and the surface morphology looks identical to layer-by-layer growth with 2D steps, no growth oscillations are visible.

3.3 X-ray diffraction

The main and most versatile technique used for characterization of crystalline materials is X-ray diffraction (XRD). Depending on the measurement routine and setup of the system, it is possible to extract a large variety of crystal properties [106]. The system used during this work was a *Rigaku SmartLab*® diffractometer (see Figure 3.3) with CuK_α-radiation. All measurements were performed in the parallel beam geometry. In this geometry, a parabolic multi-layer mirror parallelizes the beam. The beam is still divergent in-plane and the height limitation is confined by a manual slit system. Most measurements were performed with a germanium 2-bounce monochromator. Inside this monochromator, two germanium crystals in (220) orientation are cut 22.6° with respect to the beam. This leads to a measurement resolution below 20 arcsec with this configuration. Further improvement of the resolution can be achieved by using the Ge(220)x2 analyzer crystal.
The probe stage can be moved in the three translation directions x, y, and z (see Figure 3.3). In addition, the stage can also be rotated around the axis, which is perpendicular to the sample surface (angle ϕ) and parallel to the sample surface (angle χ). The measurement plane is defined by the position of the source,

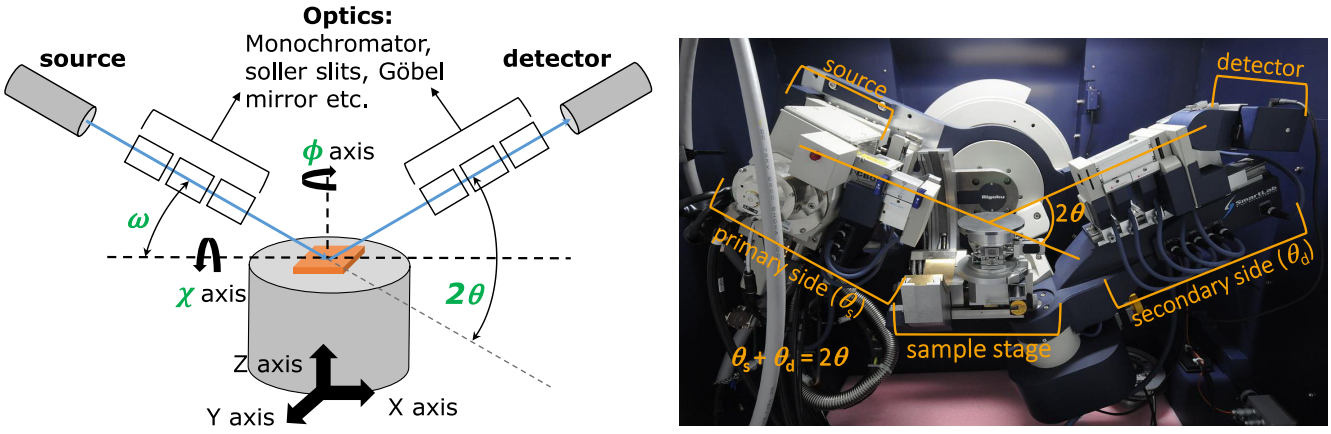

Figure 3.4: (Left) Schematic configuration and degrees of freedom of the X-ray system used to perform characterization in this thesis. (Right) Picture of the Goniometer of a *Rigaku SmartLab®* X-ray diffractometer.

sample and the detector. The sum of the primary side angle θ_s and the secondary (detector) side θ_d is called the diffraction angle 2θ.

Depending on different angles and the orientation of the sample to the source and detector, different sample properties can be extracted by a variety of measurement routines. In the following, the most common routines 2θ–ω, ω-Scan (rocking curve), Reciprocal Space Maps (RSM), X-ray Reflectivity (XRR) and Phi-scans are briefly explained.

2θ–ω X-ray diffraction

The 2θ–ω scan is the most common measurement routine for epitaxial films. It allows the extraction of film orientation, phase, thickness, out-of-plane lattice constant as well as the overall crystal quality [107]. After the sample is aligned with respect to the beam, ω and 2θ are varied in the desired range. As it can be seen in Figure 3.3, ω is the angle between the incident beam and the sample surface. The angle 2θ corresponds to twice the incident angle ω. In case of a symmetric scan, which were performed during this work, ω is equal to θ.

If the Bragg condition is fulfilled or the reflexes in the reciprocal space lie on the Ewald-sphere and fulfill the Laue-condition (see Figure 3.5), constructive interference occurs and a peak is visible in the detected spectrum. If higher orders of a particular hkl-reflex occur in the spectrum, the lattice constant in that direction can be determined with the Nelson-Riley formula [108].
There can be additional peaks or oscillations originating due to interference of coherently diffracted beams on the finite lattice. These peaks are called Laue oscillations and they can be used to determine the thickness

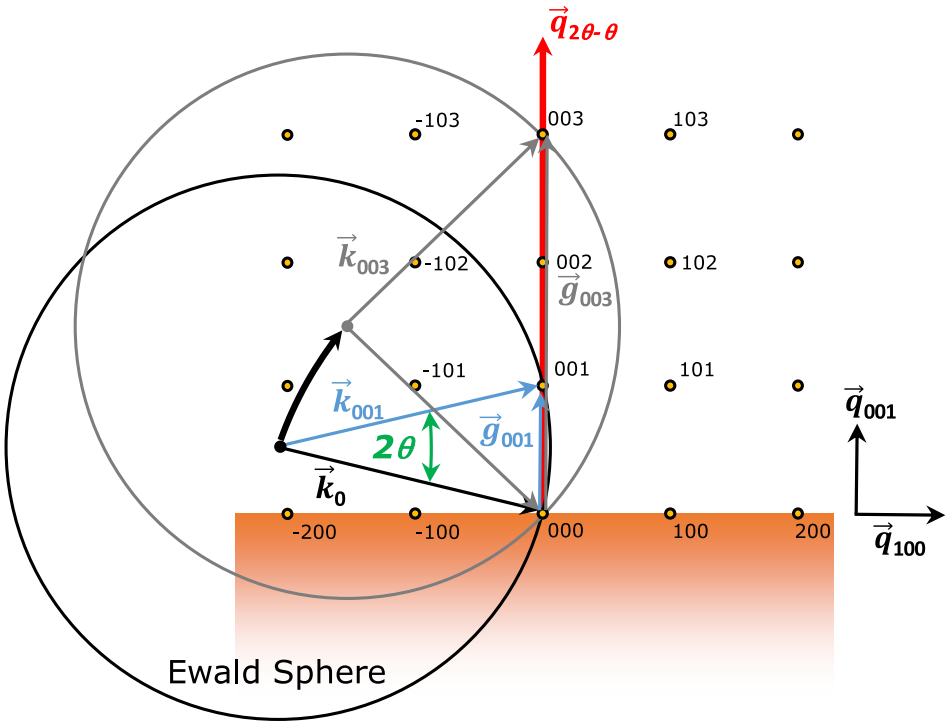

Figure 3.5: Visualization of the reciprocal space map during a $2\theta-\omega$ measurement. $\vec{q}_{100}$ and $\vec{q}_{001}$ represent the [100]- and [001]-directions. The [100]-direction corresponds to the sample surface. The measurement direction is the out-of-plane [001]-direction, represented by $\vec{q}_{2\theta-\theta}$.

t of a film using [109]

$$t = \frac{\lambda}{2[\sin(\theta_i) - \sin(\theta_{i-1})]}, \tag{3.4}$$

where θ_i and θ_{i-1} are the positions of the Laue oscillations and λ is the wave length of the incident X-rays.

ω scan (Rocking curve)

During a rocking curve measurement sequence, the 2θ angle relation between source and detector remains constant. This leads to a diffraction from the same hkl-lattice planes. However, the incident angle ω is varied by $\Delta\omega$. This variation leads to a diffraction at the misaligned lattice planes to the initial one. The measured spectrum is, therefore, a representation of the overall spread of crystal plane orientations, also called mosaicity. A perfect crystal with no or very few misorientations will lead to a very sharp peak. A high mosaicity and dislocations lead to broadening of the rocking curve, since the atomic planes are not perfectly parallel. Therefore, the distribution of preferred orientations can be estimated from the full width at half maximum (FWHM) and the shape of the rocking curve scan [107]. A visualization of the measurement principle can be seen in Figure 3.6.

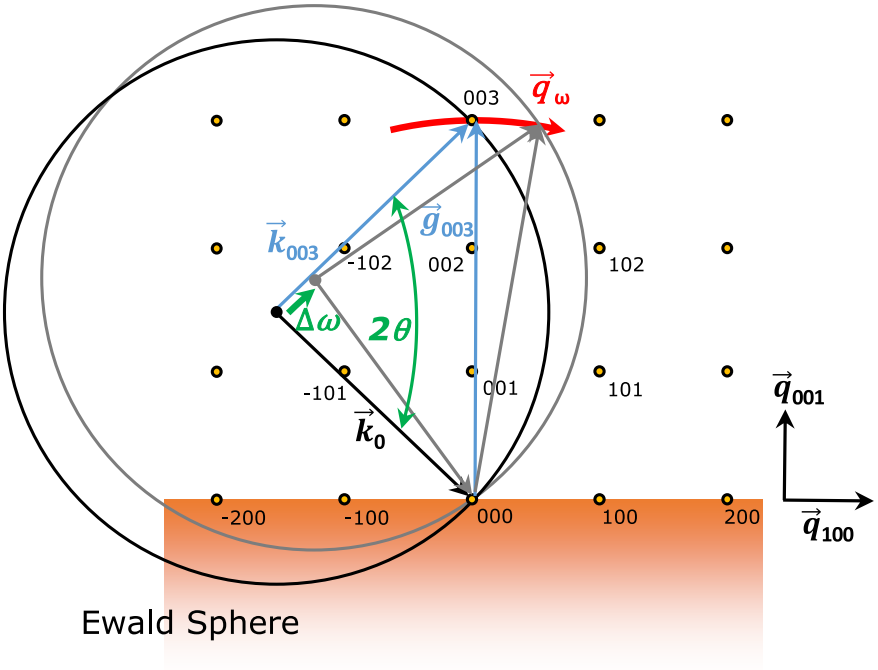

Figure 3.6: Visualization of the reciprocal space map during a rocking curve measurement. $\vec{q}_{100}$ and $\vec{q}_{001}$ represent the [100]- and [001]-directions. The [100]-direction corresponds to the sample surface. The measurement direction is along $\vec{q}_\omega$.

Reciprocal space map

The measurement routines of the 2θ–ω- and ω-scan only reveal information of the out-of-plane sample direction. In order to gain knowledge of the in-plane direction such as distortion/relaxation of the film and determination of the reciprocal space maps (RSM) are a useful measurement routine. The RSM can be interpreted as multiple rocking curve measurements with a varying 2θ angle. Thus, the spread of lattice planes can be directly seen in the RSM as the width of the sample peak. On the basis of Figures 3.5 and 3.6, the measurement directions $\vec{q}_{2\theta-\theta}$ and $\vec{q}_\omega$ define the RSM measurement area in the reciprocal space as it can be seen in Figure 3.7. It has to be noted, that the measured area during a RSM measurement gets distorted the further away from the origin the measured area is chosen. The reason for this is the scattering condition on the Ewald Sphere.

To define the area of the RSM for a given sample, it is important, that all layers of this sample have at least one reflex with an in- and out-of-plane component in this area. The reciprocal space can be simulated for a given layered material heterostructure in the *Rigaku SmartLab® Guidance* software using the Diffraction Space Simulation option. After the measurement, the data is converted with the software *3D Explore* from *Rigaku* and exported in a text file, which can be used for further analyzation and visualization.

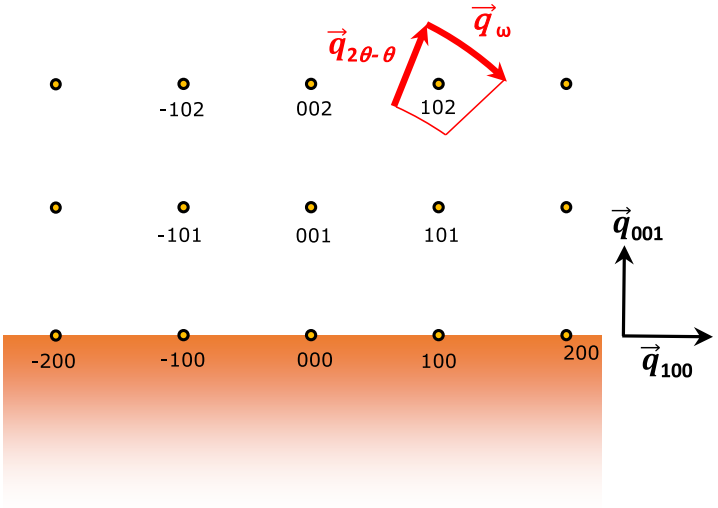

Figure 3.7: Visualization of the area during a reciprocal space map measurement. $\vec{q}_{100}$ and $\vec{q}_{001}$ represent the [100]- and [001]-directions. The [100]-direction corresponds to the sample surface. $\vec{q}_{2\theta-\theta}$ and $\vec{q}_{\omega}$ define the RSM measurement area.

Phi scan and pole figure

Phi scans can extract the preferred orientation of a sample. The 2θ, ω and χ for a particular reflex with out- and in-plane component is set and stay constant for the Phi scan. During the measurement, the sample is rotated by varying φ from $0\,^\circ$ to $360\,^\circ$. In order to measure all layers in a heterostructure and relate the orientation to the substrate, it is important to maintain the physical position of the sample in the spectrometer. The data sets can be plotted over φ to the rotations of the lattice planes.
The Pole figure measurement routine is a sequence of multiple Phi-scans. After each Phi-scan, the angle χ is varied. This leads to a $\varphi - \chi$ map with multiple reflexes.

X-ray reflectivity

Unlike the previous scans, the X-ray reflectivity (XRR) is not a technique to investigate diffraction phenomena, but rather to analyze the X-ray reflection intensity from grazing incident X-ray beams. This method can determine thickness, density and surface morphology or interface roughness [110].
If the incident X-ray beam hits the flat surface under a grazing angle smaller than the limit for total reflection θ_c, the X-rays undergo total reflection. If the incident beam hits the surface under the critical angle θ_c, the X-rays propagate along the sample surface. Above the critical angle θ_c, the X-rays penetrate into the material by refraction and pass through the film onto the substrate.
An example for an XRR graph is displayed in Figure 3.8. Below the critical angle the X-rays are fully reflected. Above θ_c the reflectivity decreases rapidly, proportionally to θ^{-4} [110]. There are several properties which can be extracted from XRR data, namely thickness, density and surface or interface roughness.
As it can be seen in Figure 3.8, the reflectivity oscillates which can be explained as interference of the X-rays

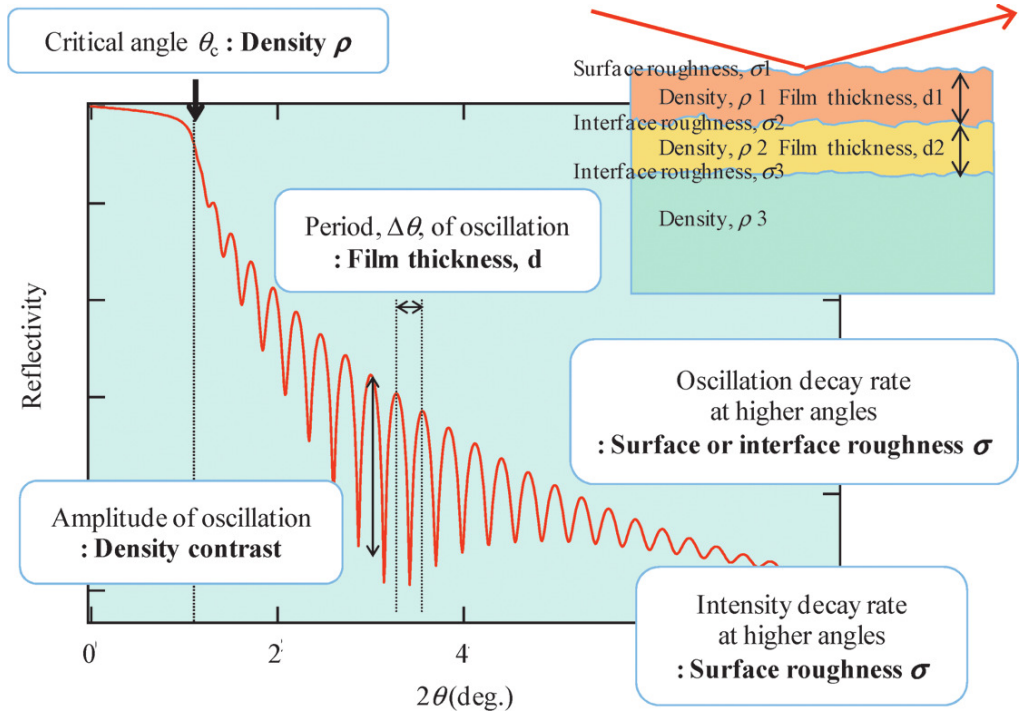

Figure 3.8: Graph of the reflectivity as a function of the the 2θ angle observed in an XRR measurement. The boxes describe which parameters can be extracted from the graph [110].

reflected from the surface of the film and the interface of the film and the substrate. These oscillations are called Kiessig fringes, named by their discoverer Kiessig in 1931 [110]. The period of the oscillations depends on the thickness of the film. Shorter periods of oscillation corresponds to a thicker film. However, the Kiessig fringes are very dependent on the interface quality and can vanish with a very rough interface. The amplitude of the oscillations and the value of the critical angle depend on the density. A higher density results in an higher critical angle as well as a higher amplitude of the oscillations.
An indicator for the surface roughness is the slope of the reflectivity. The interface roughness consists of physical uneven interfaces and transitional boundary layers with continually changes in density [110]. A higher roughness leads to a sharper drop of reflectivity. The interface roughness can be seen in the reflectivity curve by a decrease in amplitude of the Kiessig fringes (see Figure 3.8).

3.4 Photoemission spectroscopy

Photoemission spectroscopy (PES) is a characterization technique used to determine the density of states, oxidation state and chemical composition of a given sample. This measurement technique is based on the photoelectric effect. PES utilizes photons with higher energy than the work function of a certain material. These photons eject electrons, called photoelectrons, from this material. Depending on the energy of the incident photons it can be differentiated between X-ray photoelectron spectroscopy (XPS) and ultraviolet

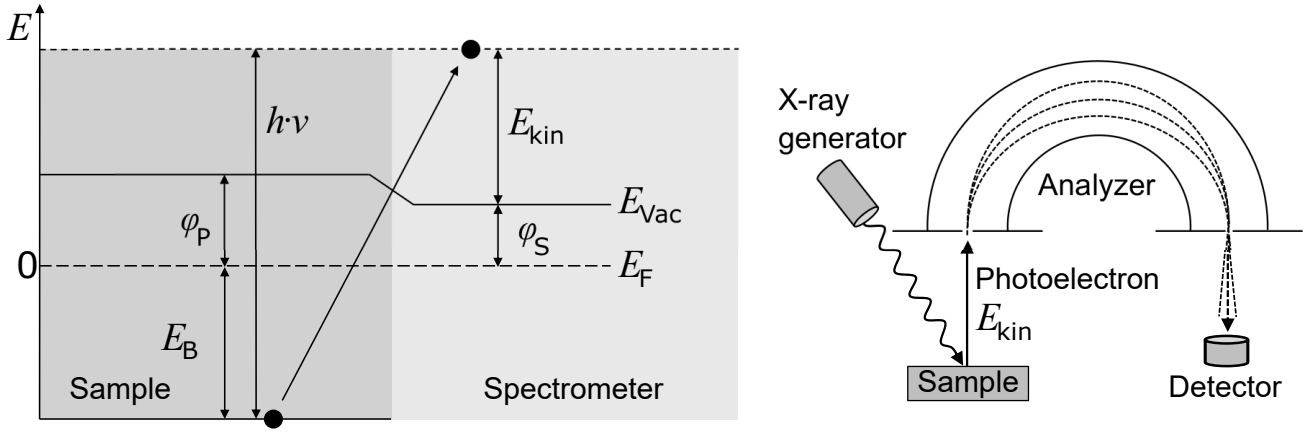

Figure 3.9: (Left) Electronic band structure in an XPS spectrometer with the physical quantities of the incident photon energy $h \cdot \nu$, binding energy E_B, kinetic energy of the photoelectron E_{kin}, vacuum energy E_{Vak}, Fermi energy E_F and the work function of the sample φ_P and the spectrometer φ_S. (Right) Schematic structure of an XPS spectrometer [26].

photoelectron spectroscopy (UPS). The main difference between these two techniques is the penetration depth of the photons caused by the different source energies. The penetration depth for UPS is much smaller, thus, it is highly surface sensitive. In this work only XPS was used to gain more information of the chemical composition deeper inside the material. Although the penetration depth of the XPS is higher than UPS, it is also surface sensitive due to the short mean free path. This is limited by interactions of the electrons with phonons, plasmons or excitons. Hence, it is not save to extrapolate from XPS results certain information for the whole thickness of the sample.
The photoelectrons emitted by the incident photons can be measured dependently on their kinetic energy E_{kin} and can be described with the following equation:

$$E_{kin} = h \cdot \nu - E_B - \varphi_S \tag{3.5}$$

with $h \cdot \nu$ being the energy of the photon, E_B being the binding energy of the electron and φ_S being the work function of the spectrometer. The sample is electrically connected to the spectrometer, leading to a matching of the Fermi energies of the spectrometer and the sample (see Figure 3.9 left). The binding energy of the electron is usually given with respect to the Fermi energy and therefore it is independent of the work function of the sample φ_P. The work function of the spectrometer is measured using a clean metal surface to calibrate the Fermi energy to $E_F = 0\,\text{eV}$.

A schematic structure of an XPS spectrometer is shown in Figure 3.9 (right). Photons produced in an X-ray source are focused as well as monochromatized with a crystal monochromator before hitting the sample surface. The photoelectrons pass an analyzer before reaching the detector. To ensure a long mean free path of the electrons, this process takes place in a ultra-high vacuum. The analyzer consists of two concentric hemispheres with a well defined potential difference. Due to this potential difference only photoelectrons with one specific energy can pass the analyzer. To vary the kinetic energy of the photoelectrons and

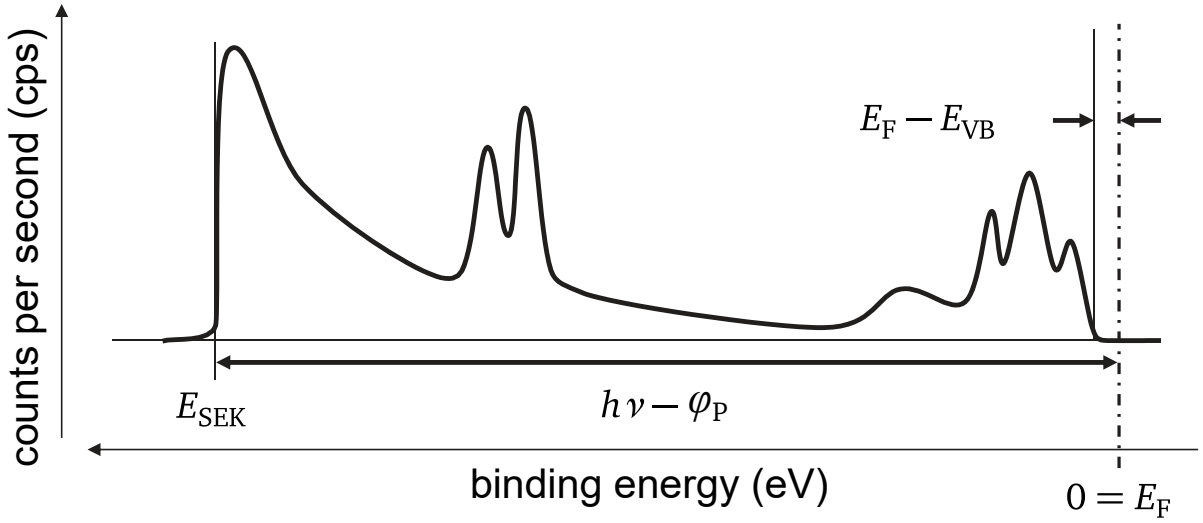

Figure 3.10: X-ray photoelectron spectroscopy of a semiconductor [111]. A shift of the valence band in respect to the Fermi energy leads to a shift of the whole spectrum. A change of the work function φ leads to a change in the position of the secondary electron edge E_{SEK}.

detect the whole range, a deceleration voltage is used before the analyzer. The potential difference of the hemispheres is always constant.
An example for an XP spectrum can be seen in Figure 3.10. The binding energy-axis is typically inverted. The steep drop in intensity on the left side of the spectrum is caused by the secondary electrons. This edge is also used to calculate the work function of a material. The secondary electrons are caused by inelastic scattering and form the background in the spectrum. Above this edge of secondary electrons the kinetic energy of the electrons is zero and they cannot leave the sample. Therefore, the work function can be calculated with:

$$\varphi_P = h \cdot \nu - E_{SEK} \tag{3.6}$$

On the right side the spectrum ends with the valence band, closest to the Fermi level.
The measured spectra can be used to calculate the chemical composition of a sample near the surface. First, the background has to subtracted from the spectrum. For the background correction two different methods are available.

The **Shirley** background, [112]:

$$S(E) = I_2 + \kappa \frac{A2(E)}{(A1(E) + A2(E))} \tag{3.7}$$

This algorithm calculates the background $S(E)$ in a certain energy range using two regions $A1$ and $A2$. The variable I_2 is the intensity of the end of the energy range and κ is the step in energy, typically equal to

$(I_1 - I_2)$ where I_1 is the intensity at the beginning of the energy range. This is an iterative algorithm, since the areas $A1$ and $A2$ are calculated respective to the background $S(E)$ and with each calculation step the background and therefore the areas $A1$ and $A2$ are adjusted.

The **Tougaard** background, [113]:

$$T(E) = \int_E^\infty F(E' - E)S(E')dE' \tag{3.8}$$

The Tougaard algorithm convolutes an energy loss cross section $F(E)$ and the measured spectrum $S(E)$. The energy loss cross section represents the probability of an electron at an energy E undergoing a loss event and therefore contributing to the background. The universal cross section used in the program *CasaXPS* is described by

$$F(E) = \frac{B \cdot E}{(C + E^2)^2}, \tag{3.9}$$

where B is a parameter adjusted by the program *CasaXPS* to match the background with the data at the region limits.

After the background correction, the raw area under the spectrum for all elements is calculated. This area is divided by a tabulated element dependent *Relative Sensitivity Factor* (RSF). Hence, the concentration of an element c_x in the sample can be calculated using following equation [26]:

$$c_x = \frac{I_x/RSF_x}{\sum_i I_i/RSF_i} \tag{3.10}$$

The XPS measurements were performed at the *DAISY-BAT (**DA**rmstadt's **I**ntegrated **SY**stem for **BA**Ttery research)* XPS system. This spectrometer is a *PHI Versaprobe 5000*, which allows angle dependent XPS and UPS measurements. It is connected to DAISY-BAT PLD via a distribution chamber. This enables *in situ* sample transfer from the PLD to the XPS and vice versa. The radiation used for the experiments was monochromatic AlK_α ($h\nu = 1486.6\,\text{eV}$). The measurements were performed at room temperature and under ultra-high vacuum of $3.8{\cdot}10^{-9}$ Torr. The detector was set in at angle of 75 ° towards the substrate, which leads to an information depth of $\approx 5 - 8\,\text{nm}$.

3.5 Electrical characterization

Evaluation of the electrical performance was done by determining the electrical resistivity ρ of the bottom electrode material SMO as well as measuring the high frequency properties of the varactor heterostructure.

Determination of the electrical resistivity

The most frequently used geometry to determine the electrical resistivity was the four-bar geometry (see Figure 3.11). Top contacts are applied by sputtering gold through a shadow mask on the sample. The sample is contacted in the measuring stick by applying a current on the outer electrodes and measuring the voltage at the inner electrodes. The resistivity is calculated from the resistance through a certain cross section per length. In present setup, the resistivity is determined by

$$\rho = R\frac{d \cdot l}{b} = \frac{U \cdot d \cdot l}{I \cdot b}, \tag{3.11}$$

where R is the resistance, U is the voltage, I is the current, d is the thickness, b is the distance and l is the length. To eliminate the impact of the thickness of a given sample and for better comparison, the property of the sheet resistance $\rho_\square$ is introduced:

$$\rho_\square = \frac{\rho}{d} \tag{3.12}$$

The unit of $\rho_\square$ is $\Omega/\square$ where $\square$ is the unit area and has no dimension.

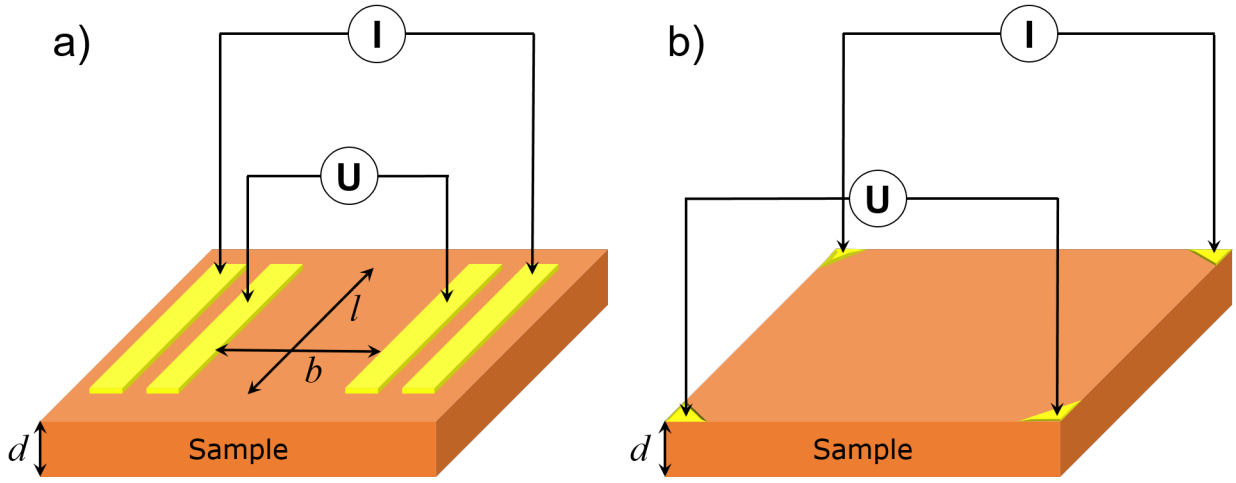

Figure 3.11: Two different geometries for the measurement of the electrical resistivity. a) four-bar geometry and b) Van-der-Pauw geometry.

The Van-der-Pauw geometry was used during Hall measurements, where in addition to the resistivity also charge carrier density and mobility can be determined. The contact is ensured by spring loaded pins,

touching the electrodes at the corner.
Both measurements can also be done temperature dependent. Further information for both geometries and the setup devices including temperate dependent measurements can be found in [17].

Impedance analyzer

The microwave performance of the varactors were measured in the frequency range from 1 MHz to 3 GHz with an impedance analyzer. During impedance spectroscopy the sample is exposed to an alternating electrical field and the resulting current as well as the phase shift to the applied field are measured. With current and applied voltage, the impedance can be calculated as a complex resistance Z. From that, the effective capacitance and quality factor can be calculated as

$$C_{\text{eff}} = -\frac{1}{2\pi f \,\text{Im}(Z)} \tag{3.13}$$

$$Q = -\frac{\text{Im}(Z)}{\text{Re}(Z)}, \tag{3.14}$$

where f is the frequency of the alternating electrical field. The parallel-plate MIM structure design of the varactors used in this work (see Figure 2.16 in section 2.7.1) has a large-area bottom electrode compared to the small circular contact electrodes and small layer thickness d compared to the radius r of the contact electrodes. With the real part $R = \text{Re}(Z)$ and imaginary part $I = \text{Im}(Z)$ the permittivity ε depending on f can be calculated:

$$\varepsilon = \varepsilon' + i\varepsilon'' \tag{3.15}$$

$$\varepsilon' = \frac{I}{R^2 + I^2} \cdot \frac{d}{2\pi f \,\varepsilon_0 \pi r^2} \tag{3.16}$$

$$\varepsilon'' = \frac{R}{R^2 + I^2} \cdot \frac{d}{2\pi f \,\varepsilon_0 \pi r^2}. \tag{3.17}$$

This determination of the permittivity loses accuracy until the limit of the impedance analyzer around 3 GHz, because then the losses of the electrodes can not be neglected for frequencies approaching the impedance analyzer limit.
In the complex impedance plane, the x-axis represents $\text{Re}(Z)$, which can be attributed to a resistance. The y-axis represents $\text{Im}(Z)$, which is is attributed to an inductance or capacitance, depending on the sign. (inductance: positive, capacitance: negative) The varactor is a capacitor and, thus, a perfect varactor without losses would solely have a contribution on the y-axis. In reality, all varactors have losses, acting as resistance. Thus, the losses can be attributed to the part of the x-axis and be calculated by $\tan\delta$.

Vector network analyzer

In the frequency range from 300 kHz to 20 GHz, the vector network analyzer (VNA) *Keysight E5071C* is used to measure the microwave performance. Although the lower limit is specified to be 300 kHz, the accuracy for the quality factor is not sufficient in this range. Therefore, the VNA is deployed from 300 MHz to 20 GHz.
Instead of directly measuring the impedance, the vector network analyzers measures the reflected and transmitted portions of a wave transmitted to the device under test (DUT). This measured complex scattering parameter can be described by a matrix and links the incoming signal (a_1 and a_2) to the outgoing signal (b_1 and b_2), where the subscript indexes the port.

$$\begin{bmatrix} b_1 \\ b_2 \end{bmatrix} = \begin{pmatrix} s_{11} & s_{12} \\ s_{21} & s_{22} \end{pmatrix} \begin{bmatrix} a_1 \\ a_2 \end{bmatrix} \tag{3.18}$$

For multiple subscripts such as S_{21} the first subscript indexes the output port and the second subscript indexes the input port. The varactors are characterized in reflection. The impedance is determined by:

$$Z_{\mathrm{DUT}} = Z_{\mathrm{ref}} \frac{1 + S_{11}}{1 - S_{11}} \tag{3.19}$$

3.6 Ion beam etching

Ion Beam Etching (or milling) (IBE) utilizes ions to remove material from a sample. If the sample is patterned with a mask beforehand, it can be used for structuring e.g. the top electrodes. IBE provides high precision structuring and clean edges.
During this work a *MANTIS* ion beam etching system has been used. It is connected with a transfer tunnel to the *DCA* PLD and allows an *in situ* sample transfer. The ion source uses RF excitation of Ar ions, which are accelerated to the energy of 500 eV. The mean free path of the ions is longer than the chamber dimensions due to the low background pressure of $1{\cdot}10^{-4}$ mbar. The Ar ion beam has a diameter of 40 mm and provides homogeneous etching for samples with a size up to 10 x 10 μm^2. The system is equipped with a *HIDEN ANALYTICAL* quadrupole mass spectrometer. This allows an *in situ* monitoring of the currently etched material. It enables a precise calibration of the etch rate and etch stop at a desired interface. For longer etch processes, the sample stage can be cooled with liquid nitrogen.
IBE was used during this work for structuring the top electrodes in case of very thick Au top electrodes, which does not allow lift-off or removal of a gold seed layer in case of galvanic growth. Another use case was the structuring during the production of the surface mount device component, which will be discusses in section 4.5.

3.7 Photolitography

Before the electrical characterization of the all-oxide varactors can be done, top contacts need to be applied, completing the MIM-structure. After the PLD deposition, the top layer of the heterostructure is BST. All non-destructive materials characterizations such as XRD, XPS, or microscopy (laser microscopy, scanning electron microscopy or atomic force microscopy) were done before further processing of the samples.

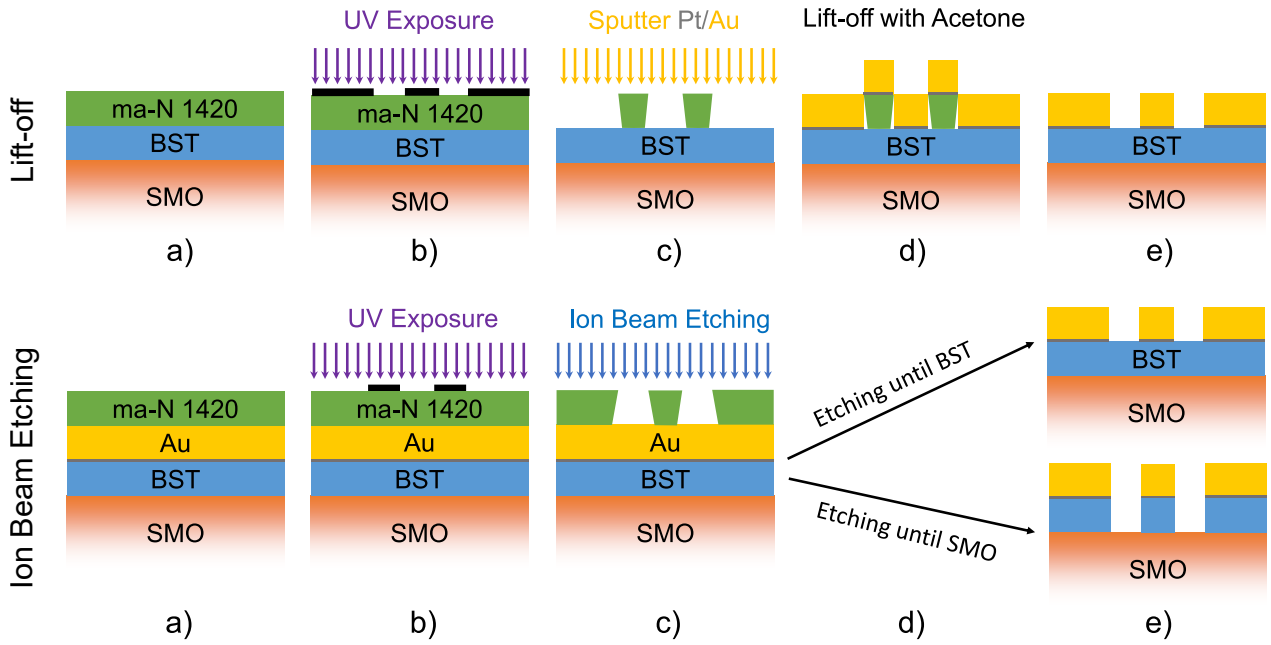

Figure 3.12: Procedure of the photolitography used for structuring top electrodes of all-oxide varactors. The first row shows the steps during lift-off structuring and the lower row shows the steps for structuring with Ion Beam Etching.

The processing was done in the inhouse clean room. The backsides of the samples were cleaned from all residual silver glue, to ensure a good vacuum contact during spin coating. The photolitography sequence can be seen in Figure 3.12. Two patterning techniques can be applied. The lift-off technique (upper row Figure 3.12) and IBE (lower row Figure 3.12). In the lift-off technique, the BST surface is covered with photoresist and patterned. Then, top contacts are applied, which are partially removed by acetone in the lift-off process. In contrast, during the IBE patterning top contacts are directly sputtered on the BST surface and then photolitography is done. Afterwards, etching removes the undesired gold areas by bombarding the sample with argon ions. Etching can be monitored with a *HIDEN analytical* spectrometer enabling a precise etch control and stopping at each interface. Additionally, the IBE patterning technique allows *in situ* deposition of the top contacts, which guarantees a good interface.
Both techniques start by spin coating a photoresist, which was the negative resist ma-N 1420 from *Microresist*. It was applied by spincoating with 3000 rpm resulting in a thickness of 2 μm. Due to the centripetal force during spin coating the photoresist builds up at the edges and corners (edge bead). This accumulation might lead to contacting problems during exposure in the mask aligner. Thus, the edge bead is removed

from the corners with a thin rectangular cover glas. Afterwards, the resist is soft baked at 105 °C for two minutes on the heating plate to reduce the remaining solvent concentration.
Structuring of the photoresist is done in the mask aligner (*MJB4* from *Süss MicroTec*). This device is equipped with a microscope and is used to align the glas mask exactly over the substrate and bringing both into contact. A Hg-lamp containing the emission lines g-line ($\lambda = 436\,\text{nm}$), h-line ($\lambda = 405\,\text{nm}$), i-line ($\lambda = 365\,\text{nm}$) exposes the sample with UV light. This UV exposure leads, in case of negative resist, to a hardening. After the exposure, the sample is submerged in the corresponding developer only leaving behind the hardened parts of the photoresist. The surface is cleaned finally by O_2 plasma etching.
After a final quality control with the microscope, the Pt/Au contacts are sputtered and then the resist is stripped by acetone leaving behind the final structure. In case of the IBE routine, the samples are directly processed by IBE and etched until the desired layer.
In summary, the IBE routine is to be favored, since it allows *in situ* electrodes and produces finer structures.

3.8 Scanning electron microscopy

High resolution scanning electron microscopy (SEM) was used to investigate and analyze the microstructure and topological features of the samples. In contrast to optical microscopy, SEM utilizes an electron beam (1 – 30 keV), which enables a resolution below 1 nm. This electron beam is focused and deflected on the sample by a variety of electromagnetic lenses. The beam path and sample chamber is in high vacuum to avoid electron scattering with a background gas particles. A convergent electron beam is scanned across the sample, interacting with the surface of the sample, ejecting high and low energetic electrons and characteristic X-ray radiation, which are detected and processed to form an image.
Depending on the applied voltage, the energy of the electron beam can be commonly varied from 1 – 30 keV, which affects the penetration depth of the incident electron beam. In case for the material SMO, at 30 keV, the penetration depth of the incident electron beam is around 2 μm.
In this work, a *Philips XL30* SEM and *dual beam Jeol SEM/FIB JIB-4600F* were used. Both systems are equipped with an *Oxford Instruments* energy dispersive X-ray detector (EDS). For imaging, detection of low-energy electrons ($< 50\,\text{eV}$) by the secondary electron detector (SE) was used.

3.9 Scanning transmission electron microscopy

The varactor heterostructures were investigated by scanning transmission electron microscopy (STEM) in order to get atomic resolution images of the cross section of the heterostructure and all interfaces. These measurements were done in collaboration with the group of Dr. Leopoldo Molina-Luna.
The samples have to be prepared for measurement in the STEM. A thin lamella ($< 100\,\text{nm}$ thickness) has to be cut from each sample. The cross-sectional cuts of the samples were done using a SEM/FIB *dual beam Jeol JIB-4600F* focused ion beam (FIB) with a gallium ion source. An atomic resolution microscope (ARM)

Jeol 200 F TEM with Cs corrector was used in this work for taking the atomic resolution images in STEM mode. The microscope was operated at 200 keV and the images were acquired using a high-angle annular dark-field (HAADF) detector. HAADF images use highly deflected elastically scattered electrons, which interact with the atom nuclei, therefore, they contain information about the average density (Z-contrast) of the imaged atoms.

3.10 Atomic force microscopy

The atomic force microscopy (AFM) is a powerful tool to measure and characterize surfaces. It uses a small tip, which is attached at the end of a cantilever. The tip is scanned across the sample usually in an area of 5 x 5 μm^2 – 20 x 20 μm^2. The sharp tip reacts to the forces of the sample surface (e.g., attractive, repulsive, magnetic, electrostatic, van der Waals) and the cantilever is bent (see Figure 3.13). The reaction of the cantilever is measured by a reflection of a laser beam from the cantilever on a photodiode. By tracking the reaction of the probe tip, a 3-dimensional map of the sample surface can be generated. This allows a height resolution in the range of 0.1 nm – 0.5 μm.
The images for this work were created in the tapping mode at the *Cypher AFM* from *Asylum Research*. During tapping mode, the cantilever with the tip is driven by the piezo oscillator near its resonance frequency (200 – 300 kHz). The tip is only in contact with the surface during oscillations of the cantilever, which eliminates lateral shear forces [114].

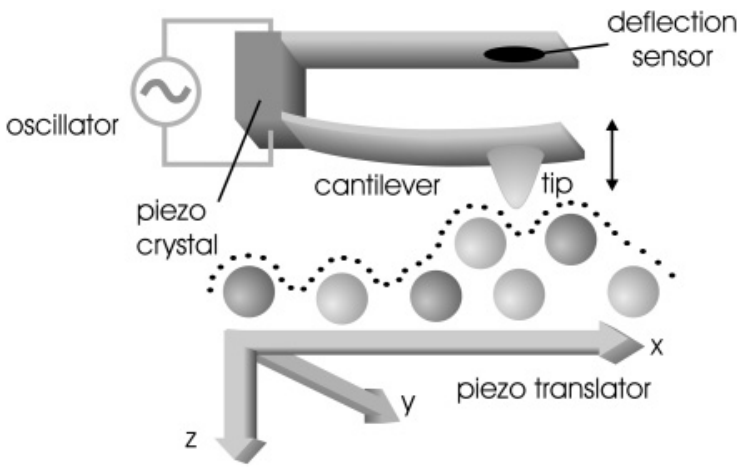

Figure 3.13: The schematic principle of AFM. The sample, represented by the circles is scanned by the cantilever and tip [114]. The piezo crystal driven by the oscillator is used during the tapping mode.

4 Results and discussion

In this chapter, results will be presented and discussed in 6 different sections. It is structured in a way that all layers and interfaces of the all-oxide thin-film heterostructure will be discussed successively, starting from the substrate towards the top contacts. In **section 4.1** the influence of different substrates, leading to different strain values, on the SMO growth has been investigated. In addition, a feasibility of the transition to an industrially relevant silicon substrate has been investigated. **Section 4.2** describes the growth of several μm thick SMO. Both, the crystal structure, as well as the influence on microwave properties of the all-oxide varactors are discussed. In **section 4.3** the search for an effective oxygen diffusion barrier material between SMO and BST utilizing a novel XPS measurement routine are presented. The **sections 4.4** and **4.5** cover the BST composition and development of a novel component design. In the final **section 4.6**, all-oxide varactors grown on silicon as well as high-performance all-oxide varactors on $GdScO_3$ will be demonstrated and compared to commercial state-of-the-art platinum-based varactors.

4.1 Substrate

During this work, all-oxide varactor heterostructures have been grown on different substrates and their influence on the growth and crystal structure has been investigated and will be discussed in this section. The different substrates introduce different strain values to the SMO and their applicability in future industrial depositions vary widely. A fast growth established on substrate $GdScO_3$ will be presented followed by the influence of strain from different scandate substrates. In the end of the section, growth on silicon covered by an STO buffer layer will be presented.

4.1.1 Fast SMO growth on $GdScO_3$

Single crystalline gadolinium scandium oxide, $GdScO_3$ (GSO) in (110) orientation, has been used in previous works as a substrate for extensive SMO growth optimizations [17] and for all-oxide varactor heterostructure depositions [18]. However, the growth has always been limited to fairly low laser repetition rates of 4 Hz and the thicknesses never exceeded several hundreds of nanometers. To obtain outstanding microwave performance for the all-oxide varactors, a thick bottom electrode is of importance while maintaining a high

conductivity. A faster growth rate can be achieved by increasing the laser spot size, laser energy density, and the repetition rate. However, the laser spot size can not be increased sufficiently without becoming inhomogeneous. In addition, the laser can not provide the necessary energy for large spot sizes. Increasing the fluence was also not an option, since higher laser energy densities lead to higher SMO resistivities. This trend of low resistivities and small lattice constants at low laser energy densities has been observed in literature for SMO [17] and STO [77, 115–117]. For these reasons, the growth has been optimized for higher excimer laser repetition rates of up to 20 Hz to achieve SMO thicknesses of several micrometer in a feasible time frame.

The lattice parameters of 5 x 5 mm^2 single crystal GSO substrates are $a = 5.48$ Å, $b = 5.75$ Å, $c = 7.93$ Å [118], which lead to a pseudocubic lattice parameter of ($a_{pc} \approx \frac{a_0}{\sqrt{2}} \approx \frac{b_0}{\sqrt{2}} \approx \frac{c_0}{2}$ [119]) $c_{pc} = 3.966$ Å and a lattice mismatch of only $\Delta = 0.18$ % of its pseudocubic lattice parameter of $a^* = 3.967$ Å with that of $SrMoO_3$ ($a(SrMoO_3) = 3.974$ Å) [60]. A five unit cell buffer layer of $SrTiO_3$ has been grown prior to $SrMoO_3$ films to ensure smooth layer-by-layer growth [92, 93].
Starting with the growth parameters from [17], several optimization studies have been carried out, including the variation of temperature, fluence, pressure and gas flow. The first achievement was a repetition rate of 10 Hz, which was the limit of the *Lambda Physik LEXtra* excimer laser at the *DCA* PLD. The $2\theta - \theta$ XRD scan near the SMO 002 reflex (see Figure 4.1) shows pronounced Laue oscillations indicating the high crystalline quality of the SMO layer. The Laue oscillations have been used to determine the thickness, which yielded 144 ± 2 nm. The out-of-plane lattice constant exhibits a value of $c = 3.990$ Å (determined by the Nelson-Riley formula). Taking into account a Poisson ratio of 0.271 [120], the expected *c*-lattice constant for a fully strained SMO on GSO is 3.977 Å as compared to the theoretical bulk value of 3.974 Å. The repetition rate of 10 Hz could substantially increase the growth rate to 8.6 nm/min in comparison to previous work from [17, 18] with growth rates of 4.7 nm/min and 6 nm/min, respectively. However, to this point of time, further increase in repetition rate was not possible, due to limitations of the excimer laser.
This changed with the purchase of a *COMPex 205* excimer laser from *Coherent* in January 2019. The repetition rate could be further increased and new optimization experiments have been performed. After installation and alignment, the previous SMO thin-film quality was reproduced before new attempts to further increase the repetition rate have been made. The SMO growth parameters for different laser repetition rates, as well as the corresponding growth rates are shown in Table 4.1. The growth temperature for all laser repetition rates was 630 °C and the fluence was 0.92 J/cm^2. It has to be noted that the substrate-to-target distance was decreased due to a change in the beam path based on the optics alignment of the new laser. In addition, the lowest spot size is bigger (3 mm^2) compared to 2.3 mm^2 of the previous setup. Therefore, the background pressure had to be increased to achieve the same reduction with the higher ablation rates. $2\theta - \theta$ XRD scan near the SMO 002 reflections of SMO films produced with the new laser and the corresponding resistivities, determined in the four-bar geometry, can be seen in Figure 4.1. The dashed line indicates the theoretical peak position of a fully strained SMO on GSO ($c = 3.977$ Å [60]) taking into account the Poisson ratio of 0.271 [120]. All samples grown with the new laser are between 290 – 350 nm thick and have excellent crystalline quality shown by Laue oscillation.

It is evident that with an argon background pressure of 30 mTorr the SMO 002 reflex produced with the new excimer laser is shifted towards lower angles due to a larger out-of-plane lattice constant of $c = 4.009$ Å compared to the sample produced by the old laser with the same growth conditions. This confirms that the growth conditions are not reductive enough due to the smaller substrate-to-target distance and higher material flux due to the larger laser spot size.
This is also reflected in the higher resistivity of 45 $\mu\Omega$·cm, which is correlated to larger out-of-plane lattice constants, which has been reported before [17]. The reason for this change in conductivity and lattice constant is off-stoichiometry. This has been reported in literature for STO [77, 115, 116]. The cation stoichiometry can be altered by adjusting the background pressure, whereas the gas flow changes the reduction of the background gas. This impacts the anion stoichiometry, directly affecting the oxidation state of Mo and therefore the conductivity [17].
By increasing the background pressure and flow simultaneously to the repetition rate, the SMO out-of-plane lattice constant could be adjusted towards the theoretical value of a fully strained SMO on GSO of 3.977 Å (dashed line in Figure 4.1) and the resistivity could be lowered significantly. The background pressure of 50 mTorr in combination with an argon flow of 30 sccm leads to the correct stoichiometry and reduction for 20 Hz laser repetition rate. The resulting SMO film has an out-of-plane lattice constant of 3.992 Å and a resistivity of 31 $\mu\Omega$·cm. 15 000 excimer laser pulses were necessary to achieve a thickness of 300 nm. This translates to a growth rate of 24 nm/min.
The successful SMO optimizations on GSO with the new laser yielded a repetition rate of 20 Hz combined with the conditions in Table 4.1 and enable a growth of 1 μm SMO in only 45 minutes with resistivities of 31 $\mu\Omega$·cm. This allows thick bottom electrodes for all-oxide varactors and will be discussed in section 4.2.

Table 4.1: Growth parameters of SMO on GSO substrates for different laser repetition rates. The growth temperature for all laser repetition rates was 630 °C and the fluence was 0.92 J/cm^2. The parameters were optimized to achieve a high growth rate in combination with a low resistivity.

Frequency (Hz)	Pressure (mTorr)	Flow (sccm)	Growth rate (nm/min)	Resistivity ($\mu\Omega$·cm)
10 old laser	30	15	8.6	
10 new laser	40	20	12	39
15	45	25	19.2	32
20	50	30	24	31

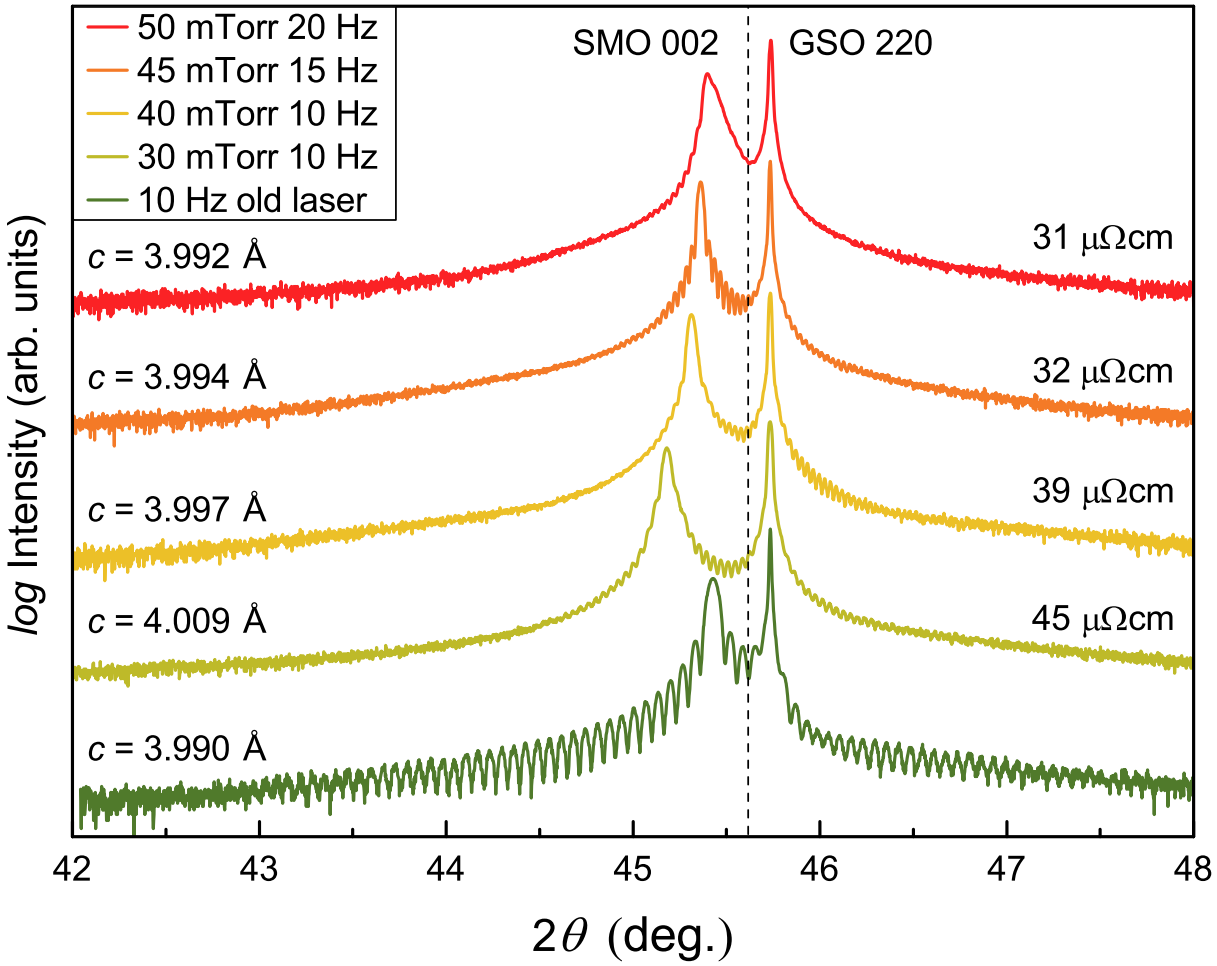

Figure 4.1: High resolution $2\theta - \theta$ scan of the SMO 002 reflections. The dashed line indicates the theoretical out-of-plane peak position of a fully strained SMO on GSO. The resistivity values were determined in the four-bar geometry and the lattice constants were determined by Nelson-Riley formula. The SMO peak shifts towards higher angles by increasing the background pressure and laser repetition rate towards the bulk value.
The resistivity value for the 10 Hz sample produced by the old laser was not determined and could not be remeasured due to SMO degradation over time.

4.1.2 SMO growth on different scandates $XScO_3$ (X = Dy, Tb, Gd, Sm, Nd)

In order to investigate the influence of strain on the growth of SMO and especially on the cation stoichiometry, different scandate substrates with varying in-plane lattice constants were chosen. Namely, dysprosium scandate $DyScO_3$ (DSO), terbium scandate $TbScO_3$ (TSO), gadolinium scandate $GdScO_3$ (GSO), samarium scandate $SmScO_3$ (SSO), and neodymium scandate $NdScO_3$ (NSO). With this substrate variety, a change in in-plane lattice constant from $\Delta(\text{NSO} - \text{DSO}) = 0.068\,\text{Å}$ can be achieved. All substrates are 5 x 5 mm^2 single crystals, orthorhombic and cut in the (110) orientation. This leads to a pseudocubic in-plane lattice constant. The important parameter determining the strain is the pseudocubic in-plane lattice constant calculated by $0.5{\cdot}\sqrt{a^2+b^2}$. The lattice constants of all substrates, including the pseudocubic ones, can be seen in Table 4.2. Due to the different in-plane lattice constants of the substrates, SMO is exposed to different amounts of tensile and compressive strains. The hypothesis of the SMO growth mode is, that the material self adjusts the cation stoichiometry to accommodate the strain and overcome the critical thickness. This leads to the ability of SMO to grow up to several micrometer (see section 4.2) without any relaxation. However, different amounts of strain might affect the resistivity of SMO due to additional scattering centers which have their origin in cation off-stoichiometry or defects.

Table 4.2: Lattice constants of different scandate substrates and their pseudocubic lattice constant for the (110) orientation used during this work [118].

Crystal	a (Å)	b (Å)	c (Å)	$0.5{\cdot}\sqrt{a^2+b^2}$ (Å)	$0.5{\cdot}c$ (Å)
$DyScO_3$	5.440	5.717	7.903	3.946	3.952
$TbScO_3$	5.466	5.731	7.917	3.960	3.959
$GdScO_3$	5.480	5.746	7.932	3.970	3.966
$SmScO_3$	5.527	5.758	7.965	3.991	3.983
$NdScO_3$	5.575	5.776	8.003	4.014	4.002

All samples on the scandate substrates have been grown with a laser repetition rate of 20 Hz and the corresponding growth parameters in Table 4.1. Optimizations for each individual substrate have not been done in order to make sure possible shifts in stoichiometry or growth are related to strain and not due to changed growth conditions. A five unit cell buffer layer of $SrTiO_3$ has been grown on the substrates prior to $SrMoO_3$ films to ensure smooth layer-by-layer growth [92, 93]. To protect the SMO layer from degradation over time and to ensure subsequent FIB preparation without any loss in film quality, all $SrMoO_3$ layers were capped with a 10 unit cell thick layer of $SrTiO_3$.

Figure 4.2 shows a high resolution $2\theta - \theta$ scan of the SMO 002 reflections of all SMO samples on the different scandate substrates. All films have a thickness of around 620 – 660 nm. The samples have been grown with high thicknesses, in order to examine possible relaxations of the SMO layer for higher lattice mismatches or if the SMO continues to grow strained.

The SMO layers on TSO, GSO and SSO exhibit Laue oscillations, which have a very small period due to

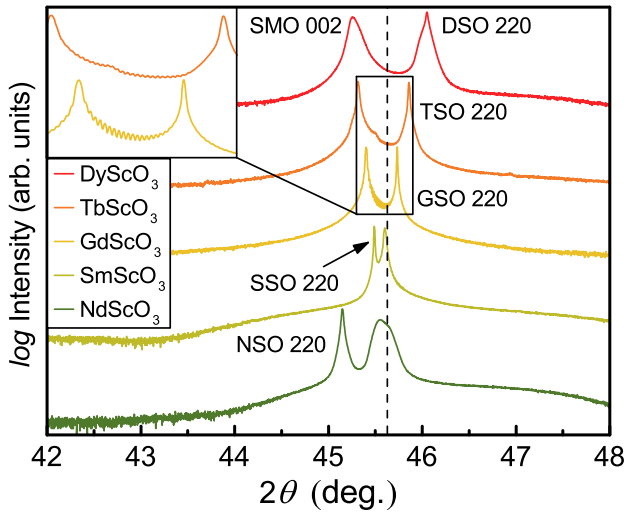

Figure 4.2: High resolution $2\theta-\theta$ scan of the SMO 002 reflections on the different scandate substrates. The dashed line indicates the theoretical peak position of bulk SMO. The inset shows the Laue oscillations for the SMO layers on TSO and GSO.

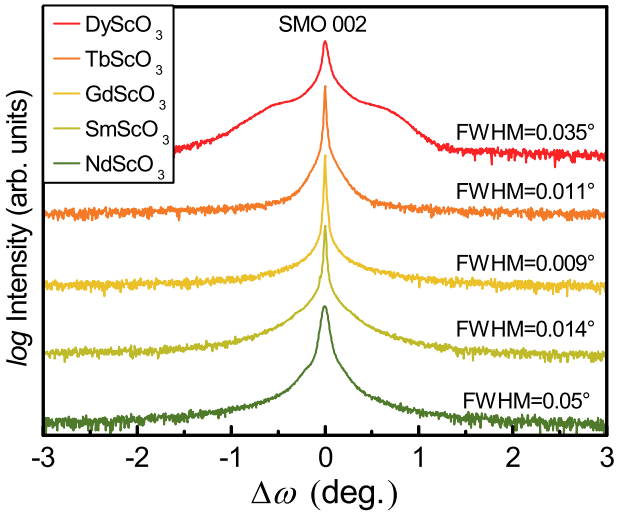

Figure 4.3: Rocking curve measurements of the SMO 002 reflections on the different scandates. Coinciding with the broader peak in the $2\theta-\theta$ scan, the FWHM of the rocking curves for SMO on DSO and NSO are broader.

the high thickness. Thus, they are only visible under high magnification of the spectra (see the inset in Figure 4.2). All thicknesses have been determined using these Laue oscillations and can be seen in Table 4.3. The absence of Laue oscillations for the SMO on DSO and NSO makes it difficult to determine the precise thickness, which is why an approximate value is given, based on the same amount of laser pulses and laser energy density as the other samples and extrapolation of RHEED intensity oscillations.

The substrate peak position shifts in the $2\theta-\theta$ scan from $DyScO_3$, $TbcO_3$, $GdScO_3$, $SmScO_3$, $NdScO_3$ towards lower angles due to the increasing lattice constants (see Table 4.3). Note, that the $2\theta-\theta$ is only dependent on the out-of-plane lattice constant. However, the in-plane lattice constant behave similarly as shown in the RSM measurements (Figure 4.4). The substrate peak of DSO appears extraordinarily broad. X-ray diffraction of this exact substrate was measured before deposition and the results are visible in Figure 6.1 in the Appendix. The broadening appears after deposition and might be related to the annealing of the substrate or overlapping of a different phase. An XRD alignment issue can most certainly be excluded, since the sample alignment angle as in the measurement of the blank sample before deposition was used and the measurement was repeated several times.

The SMO $2\theta-\theta$ 002 peaks on DSO and NSO are very broad with a FWHM values of 0.08° and 0.13°, respectively, whereas the SMO 002 peaks on the other substrates exhibit FWHM values of 0.02° ± 0.003°. This divergence of crystal quality to the other SMO layers is also evident in the rocking curves (see Figure 4.3). The rocking curves of the SMO layers on DSO and NSO have a larger FWHM of 0.035° and 0.05°, respectively, indicating a higher spread in lattice planes. Both layers exhibit a distinct second component underlying

Table 4.3: Thicknesses, out-of-plane lattice constants c_{SMO} of SMO, in-plane lattice constants a_{Subs} of the substrates displayed in Figure 4.2, resulting lattice mismatch, and theoretical out-of-plane lattice constants $c_{SMO\ Poisson}$ of SMO taking into account the Poisson ratio 0.271 [120]. The in-plane lattice constant of the substrate and SMO film are identical due to strained growth. Thicknesses were determined using Laue oscillations, out-of-plane lattice constants using Nelson-Riley-Plots and in-plane lattice constants from RSM (see Figure 4.4).

Substrate	SMO thickness (nm)	c_{SMO} (Å)	a_{Subs} exp (Å)	lattice mismatch (Å)	$c_{SMO\ Poisson}$ (Å)
$DyScO_3$	≈ 650	4.003	3.949	-0.025	3.981
$TbScO_3$	621	3.998	3.958	-0.016	3.978
$GdScO_3$	657	3.992	3.964	-0.010	3.977
$SmScO_3$	664	3.977	3.985	0.011	3.971
$NdScO_3$	≈ 650	3.978	4.009	0.035	3.965

the main peak. The FWHM values do not include these broad components since they appear below half of the main intensity. The origin of this second component is diffusive scattering on defects such as dislocations [121, 122], which arise due to the larger amount of strain on these substrates. The SMO on TSO, GSO, and SSO exhibit an excellent crystal quality with low mosaicity as indicated by the small FWHM values of 0.009° to 0.014°. These values are near the resolution limit of the used optics of the X-ray diffractometer.
SMO, being in-plane locked to the substrate, has different out-of-plane lattice constants for varying substrates. With smaller in-plane lattice constants, the unit cell expands out-of-plane according to the Poisson ratio. Both experimental and theoretical out-of-plane lattice constants of a fully strained SMO, according to the Poisson ratio of 0.271 [120], can be seen in Table 4.3. This experimental values c_{SMO} follow the overall trend of $c_{SMO\ Poisson}$, except the SMO on NSO. The out-of-plane lattice constants c_{SMO} shrink from $c(\mathrm{DSO}) = 4.003\,\text{Å}$ to $c(\mathrm{SSO}) = 3.977\,\text{Å}$. The value $c(\mathrm{NSO}) = 3.978\,\text{Å}$ does not follow the trend, which might be caused by an in-plane relaxation of the film due to the large tensile strain.

A confirmation that SMO is in fact in-plane locked to the substrate can be seen in Figure 4.4. Note, that for all RSM measurements, the same color gradient is applied. All samples, except for SMO on NSO, grow in-plane locked with thicknesses over 600 nm and do not relax. The RSM data coincides with the results of the $2\theta-\theta$ scan and rocking curves in terms of peak broadening, mosaicity and lattice constants. The spread in the in-plane wave vector Q_x follows the FWHM values and shape of the rocking curve measurements confirming a higher mosaicity and second component due to diffusive scattering for SMO on DSO and NSO. The SMO layers on TSO, GSO, and SSO are strained to the substrate and do not show a large spread in lattice planes. SMO on DSO is still strained, however the crystalline quality is impaired compared to the layers on TSO, GSO, and SSO. It is also visible, that the DSO substrate peak is broader than the other substrates as also visible in the $2\theta-\theta$ scan. The out-of-plane lattice constants determined by the RSM values coincide by ± 0.001 Å to the values in Table 4.3 determined by the Nelson-Riley-Plot.
The RSM of SMO on NSO explains, why the out of-of-plane lattice constant of SMO for this sample does

not follow the overall trend of this series, which suggests it to be smaller than the one for SMO on SSO. SMO grows relaxed on NSO with an in-plane lattice constant of $a = 3.996$ Å and $c = 3.977$ Å. Seemingly, a compressive lattice mismatch of -0.025 Å in case of DSO and tensile lattice mismatch of 0.035 Å in case of NSO are too high for SMO to grow in-plane locked without defects such as dislocations. The underlying growth mechanism accommodating this strain for a thickness of several micrometer on different scandates will be further investigated by TEM.

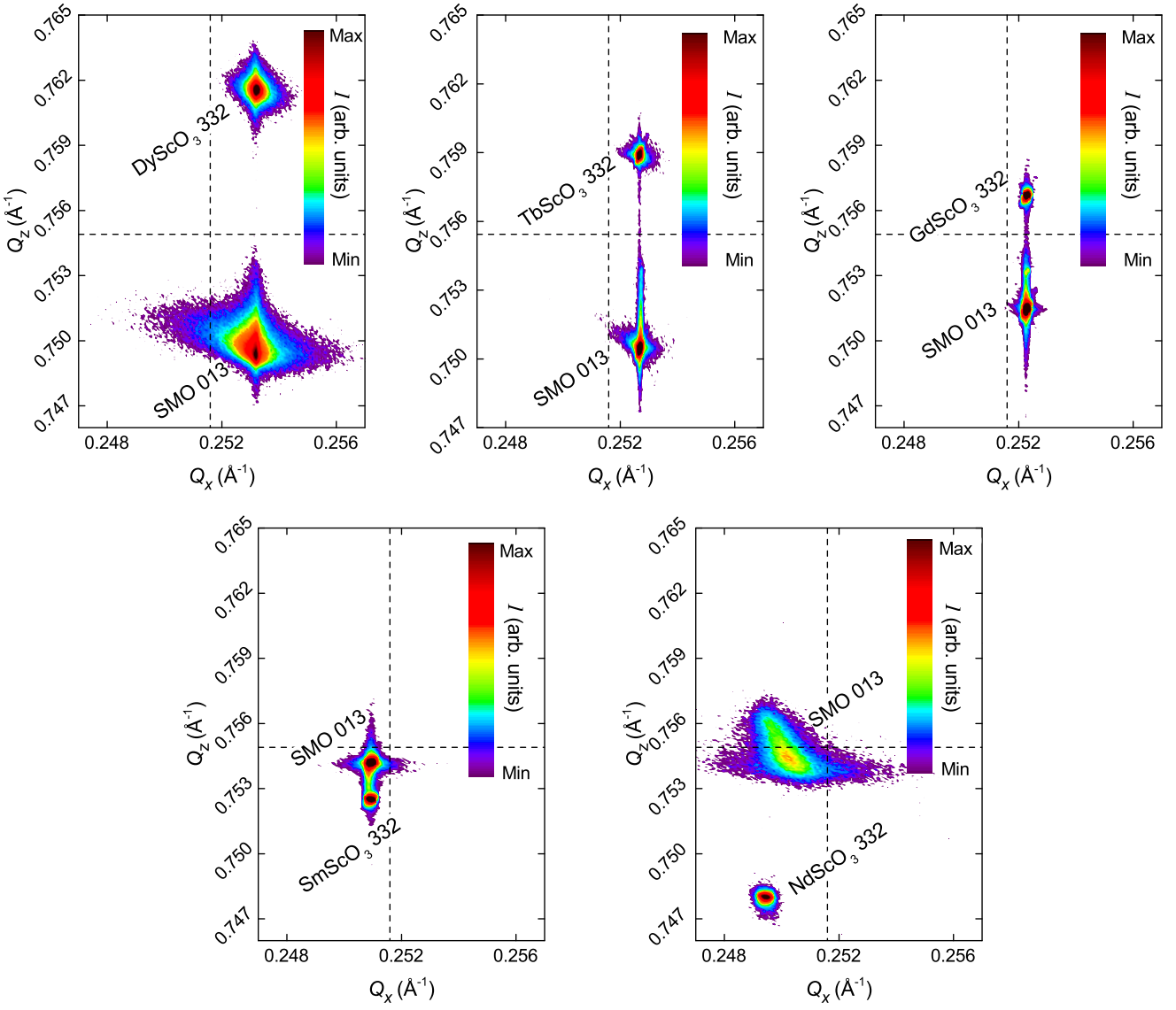

Figure 4.4: Reciprocal space maps of SMO layers grown on different scandate substrates. From top left to bottom right: $DyScO_3$, $TbScO_3$, $GdScO_3$, $SmScO_3$, and $NdScO_3$. The dashed lines indicate the in- and out-of-plane positions of bulk SMO in the reciprocal space map. All SMO layers, except on NSO, grow in-plane locked.

After the influence of different substrates was investigated with respect to strained or relaxed growth, a second study was carried out to check the influence of strain on the SMO conductivity. This could not be done on the first set of samples, since these were capped with a 10 unit cell layer of STO to prevent SMO degradation until FIB preparation can be done. Unfortunately, this capping layer rules out electrical measurements.

For this reason, a new set of of samples has been grown with a SMO thickness of 69 – 77 nm. These samples were not covered by an STO capping layer. Figure 4.5 shows a high resolution $2\theta - \theta$ scan of the SMO 002 reflections of all SMO samples in this series. The XRD scan reveals a discrepancy in sample quality. The SMO 002 peak on the DSO is broadened as compared to the other films, which falls in line with the results from the RSM measurements (Figure 4.4) and $2\theta - \theta$ scans from the thicker samples in Figure 4.2. SMO on NSO and TSO are better than layer on DSO, however, as compared to the SMO quality on GSO and SSO, the peaks appear broadened and the Laue oscillations are not as pronounced.
The resistivity values in Figure 4.6 confirm the trend from the XRD $2\theta - \theta$ scan. Note that the y-axis is interrupted and the two regimes do not have the same scaling. The SMO layer on DSO has a room temperature resistivity of 736 $\mu\Omega$·cm, which is one order of magnitude higher than the other room temperature SMO resistivities (see Figure 4.6). Thus, it can be concluded that this sample is defect enriched hindering the conductivity. However, possibly this drastic increase might also be amplified by an error such as a bad interface from the gold contacts to SMO.
The reduction from resistivity of the SMO layer on TSO → GSO → SSO follows the decrease in out-of-plane lattice constant towards the bulk lattice constant. This coincides with the findings of section 4.1.1 and [17]. The increased resistivity on NSO can be traced back to the lower crystal quality of the SMO layer. The best SMO room temperature resistivity during this study was achieved on SSO with a value of 34 $\mu\Omega$·cm.

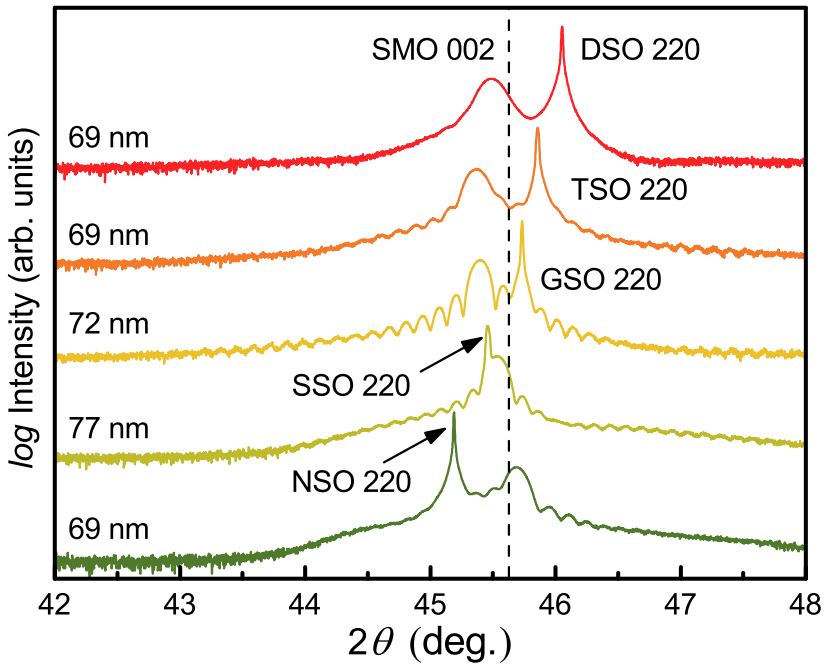

Figure 4.5: High resolution $2\theta - \theta$ scan of the SMO 002 reflections on the different scandate substrates. The dashed line indicates the theoretical peak position of bulk SMO. These samples were used to determine the resistivity. Thickness of the samples were determined by Laue oscillations.

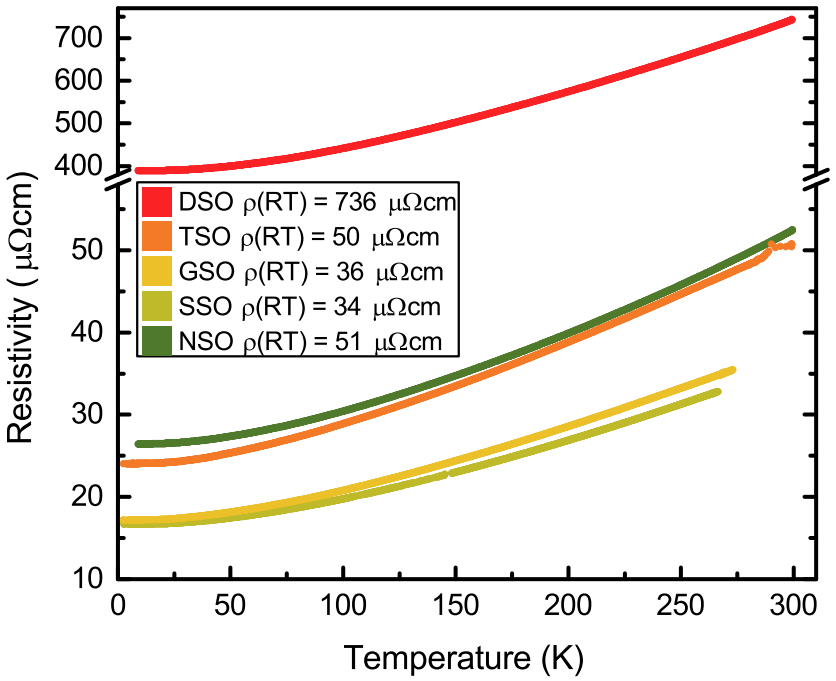

Figure 4.6: Resistivity over temperature of SMO grown on different scandates, including the room temperature values. The resistivity was determined in the four-bar geometry. The thickness of the samples can be seen in the (left) Figure 4.5 and varies from 69 – 77 nm.

4.1.3 Silicon covered with an STO layer

Since the industrial applicability of GSO and other scandate substrates is limited due to the high price and the scarceness of big wafers, it is highly important for the all-oxide varactor technology to substitute GSO with a more industrially relevant substrate in order to accomplish the transition from the lab scale proof-of-concept towards industrial production. The most widespread substrate in industry is silicon. It is cheap and can be produced up to 12 inch wafers. In addition, successful SMO deposition might open up the possibility of all-oxide varactors in integrated RF circuits.
However, the epitaxial growth directly on silicon is very difficult. The silicon substrates need to be treated before deposition to remove the amorphous SiO_2 layer. This can be done either by Hydrofluoric acid treatment or an *in situ* cleaning process by heating the substrates to break the SiO_2 bonds [123]. This procedure has been done in the *DCA* PLD and works very well (see Figure 6.2 in the Appendix). However, cleaned silicon again forms very rapidly a SiO_2 layer when exposed to oxygen. This already occurs for perovskite depositions by PLD in ultra-high vacuum, since the oxygen in the target is enough to form an amorphous SiO_2 layer. This amorphous oxide layer leads to a loss of epitaxy for subsequent layers.
A first alternative are commercially available silicon substrates coated with an STO layer by the manufacturer. On these substrates the feasibility of an epitaxial all-oxide heterostructure should be demonstrated. The substrates were provided from *Crystec* and have dimensions of 10 x 10 mm^2. Prior to usage of the substrate, they were cut to 5 x 5 mm^2 dimensions. This was done by cleaving the backside of the substrate with a diamond pen and then breaking it, which created a clean breaking edge.
The silicon substrates are (100)-oriented and have an out-of-plane lattice constant of 5.430 Å [124]. The STO layer on the substrate is (001)-oriented. The STO out-of-plane lattice constant was calculated from the measured XRD $2\theta - \theta$ scan (see Figure 4.11 (a)), using the Nelson-Riley formula and has a value of $c = 3.898$ Å. A Phi-scan (see Figure 4.7), measured on a varactor heterostructure, showed that the STO is rotated 45° around the Si surface normal [001] axis. Thus, the diagonal of the STO unit cell lies over the edge of the silicon unit cell (see Figure 4.8), which leads to a fairly small lattice mismatch of $\approx 1.7\%$. This is also reported in literature [125]. SMO and STO are well aligned on top of each other. The results of an XRR measurement of a blank substrate can be seen in Figure 4.9. The oscillations originate from the STO layer. The thickness of the STO layer was determined by fitting of the XRR curve using *RCRefSim* software [126] and can be calculated to 97 nm. The RHEED surface image of the preapplied STO layer can be seen in Figure 4.10. The streaky pattern indicates an epitaxial, 2-dimensional STO growth.

The same growth conditions for SMO have been used for these substrates, as for SMO on GSO substrates (see Table 4.1). Despite the STO buffer layer with a thickness of 97 nm on the silicon, still a five-unit-cells-thick STO buffer layer has been grown by PLD prior to SMO in order to ensure a high quality buffer layer and good interface between STO and SMO. On top of this buffer layer, a 96 nm thick SMO layer has been grown at 30 mTorr Ar background pressure and 10 Hz repetition rate. The SMO was then capped with a 10 unit cell STO layer to prevent SMO oxidation. The XRD $2\theta - \theta$ full scan of this sample can be seen in Figure 4.11 (a). It shows no additional phases. The high resolution scan of the SMO 002 reflex (see Figure 4.11 (b)) exhibits Laue oscillations evidence for the good crystal quality of the SMO layer. These

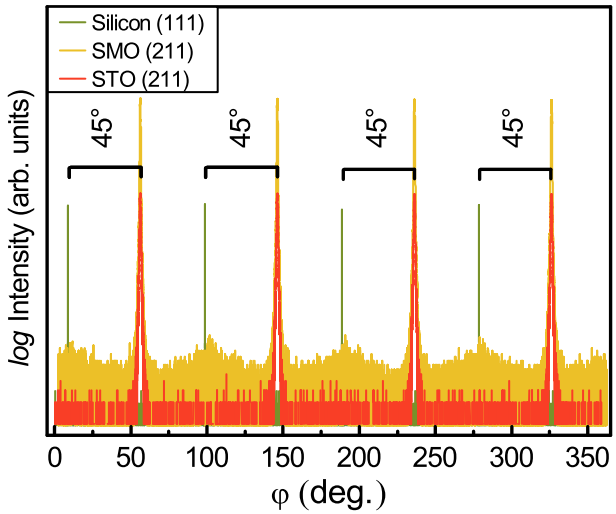

Figure 4.7: Phi-scan of a SMO film grown on a silicon substrate covered with an STO layer. It can be seen that the STO is 45° rotated with respect to the silicon. SMO and silicon are well aligned.

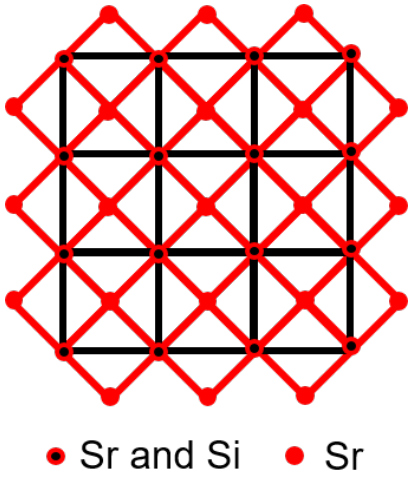

Figure 4.8: Schematic top view of the silicon unit cell (black) and the 45° rotated unit cell of STO on top (red). Black/red dots mark the positions of Sr and Si atoms and red dots mark the positions of Sr.

Laue oscillations were used to determine the SMO film thickness. The out-of-plane lattice constants were determined using Nelson-Riley-Plots and are $c(\mathrm{STO}) = 3.898\,\text{Å}$ and $c(\mathrm{SMO}) = 3.977\,\text{Å}$. Taking into account the Poisson ratio of STO 0.238 [127] and SMO 0.271 [120], the theoretical out-of-plane lattice constants are c_{Poisson} (STO) $= 3.900\,\text{Å}$ and c_{Poisson} (SMO) $= 3.986\,\text{Å}$, which agree with the experimental values. The peaks out-of-plane are matched in the following: STO(001)||Si(001), whereas in-plane, STO is 45° rotated meaning STO(110)||Si(100).
To confirm the in-plane strained epitaxial growth on this substrate also for thicker SMO films, another sample was grown with a thickness of around 600 nm (see Figure 4.11(b)). This sample has been produced with the new excimer laser and a repetition rate of 20 Hz. The SMO layer in this sample does not shows Laue oscillation which makes a precise thickness determination difficult. This is the reason, why only an approximate value is given, based on the same amount of laser pulses and laser energy density as the other samples and extrapolation of RHEED intensity oscillations. The out-of-plane lattice constants are $c(\mathrm{STO}) = 3.901\,\text{Å}$ and $c(\mathrm{SMO}) = 3.982\,\text{Å}$. Both values are in very close agreement with the theoretical out-of-plane positions c_{Poisson} of strained STO and SMO according to the Poisson ratios (Table 4.4).

A reciprocal space map of this sample can be seen in Figure 4.12. It is clearly visible that the STO 114 and SMO 114 peaks are strained to the silicon 026 substrate peak. The background reflex around SMO 114 originates from the Au 331 peak. The sample was coated with an Au layer for FIB preparation prior to the RSM measurement. The RSM allows the determination of the in- and out-of-plane lattice constants, shown in Table 4.4. Although, the whole heterostructure is in-plane locked, the lattice constants of silicon and STO/SMO differ. This can be explained by the 45° rotation of STO around the Si surface normal [001] axis. Over this diagonal of the Si unit cell two STO unit cells are located. The lattice mismatch of SMO to

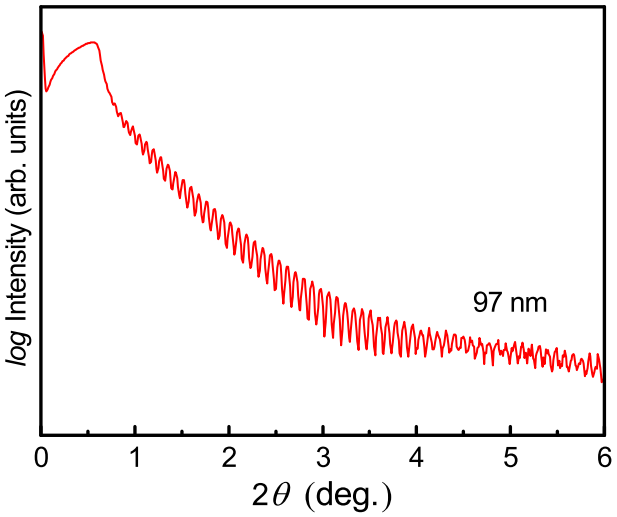

Figure 4.9: XRR of a blank silicon substrate covered with an STO layer. The oscillations originate from the STO layer and confirm a thickness of 97 nm.

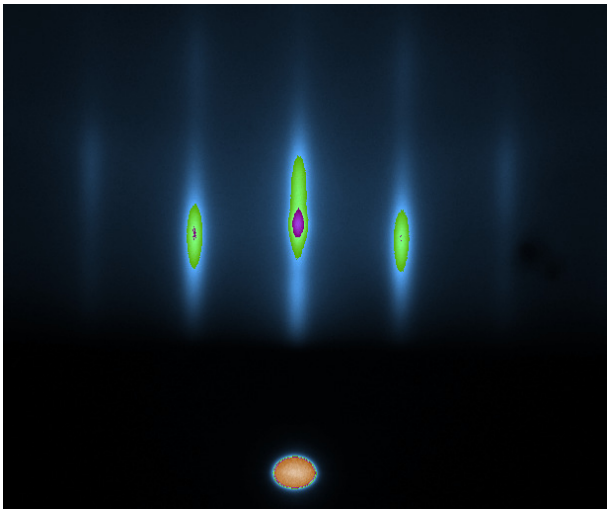

Figure 4.10: Streaky RHEED surface images of a silicon substrate with a preapplied STO buffer layer.

Table 4.4: Lattice constants of the STO/SMO heterostructure on silicon substrates coated with an STO layer showed in the RSM (see Figure 4.12). c_{Poisson} is the theoretical lattice constant according to the Poisson ratios.

Layer	out-of-plane c (Å)	in-plane a (Å)	c_{Poisson} (Å)
Silicon	5.441	5.556	
STO_3	3.901	3.928	3.900
SMO_3	3.982	3.928	3.986

the underlying STO, which is rotated by 45° with respect to Si, is $\Delta = -0.046\,\text{Å} = -1.2\%$. The dashed line in Figure 4.12 indicates the theoretical out-of-plane positions of fully strained SMO taking into account the Poisson ratio.

Although the XRD results suggest a good crystal quality of SMO on Si substrates, in order to deploy SMO as a bottom electrode in the varactor heterostructure, the resistivity has to be low. This has been verified by four-bar resistivity measurements. A 70 nm thick SMO layer on silicon substrates with an STO buffer layer has been grown with the same conditions and amount of shots as the samples in Figure 4.5. RHEED surface images indicate a mixture of 2D and 3D growth (see Figure 4.13). In addition, the SMO 002 reflex is slightly broadened in the $2\theta - \theta$ scan in Figure 4.13 as compared to previous SMO layers on Si. The four-bar resistivity results can be seen in Figure 4.14 and the room temperature resistivity for this sample is 48 $\mu\Omega$·cm, which is a good value for a SMO layer with this quality. Further small optimizations can lower the resistivity values in the same range as achieved on GSO.
After an epitaxial SMO growth on Si substrates has been established and a sufficient resistivity was realized,

the next step was to grow the complete varactor heterostructure on silicon substrates. The results of crystal structure and microwave performance of these devices will be discussed in section 4.6.2.

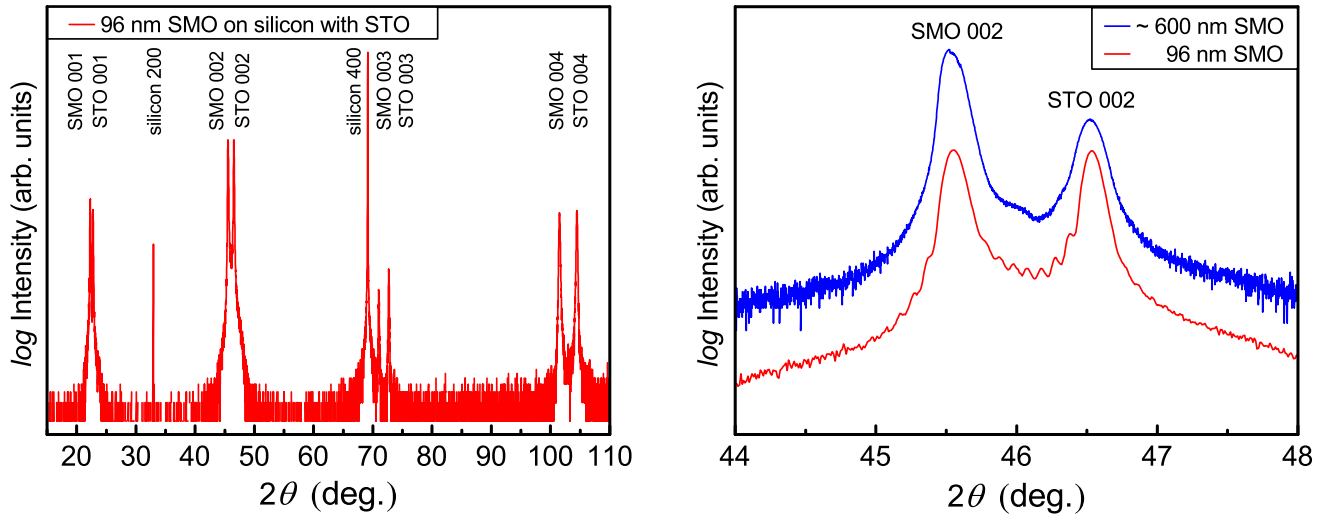

(a) $2\theta - \theta$ full scan

(b) $2\theta - \theta$ SMO 002

Figure 4.11: (a) $2\theta - \theta$ full scan of a 96 nm thick SMO layer on silicon substrate covered with an STO layer. (b) $2\theta - \theta$ scan of two SMO samples around the SMO (002) peak on silicon substrate covered with an STO layer. The SMO layer with 96 nm has similar intensity to the STO peak which is in the same thickness regime and exhibits Laue oscillations.

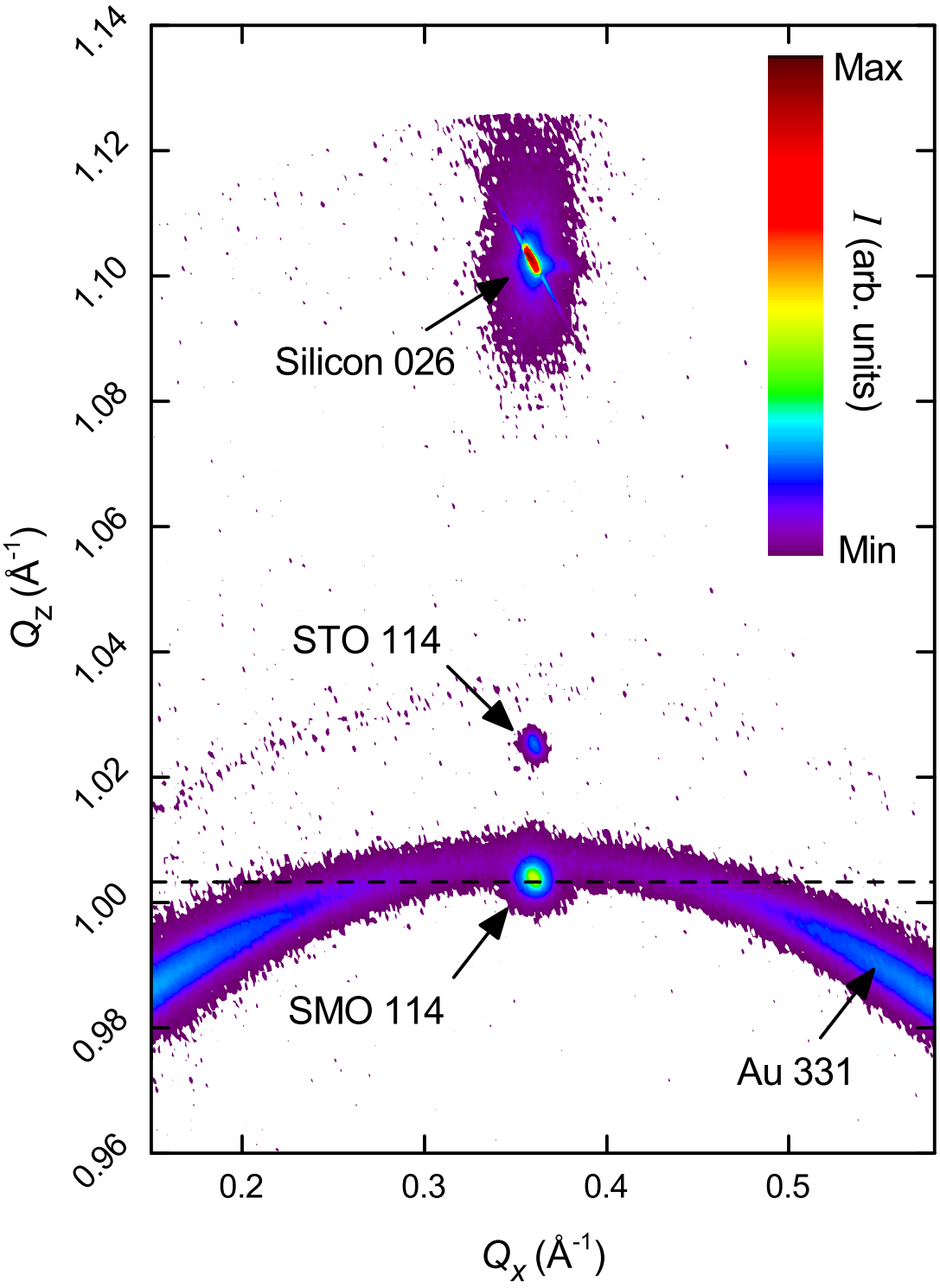

Figure 4.12: Reciprocal Space Map of a 600 nm thick SMO layer on a silicon substrate covered with an STO layer. STO 114 and SMO 114 peak are in-plane strained to the silicon 026 substrate peak. The background reflex around SMO 114 originates from the Au 331 peak. The dashed line indicates the theoretical out-of-plane positions of fully strained SMO taking into account the Poisson ratio.

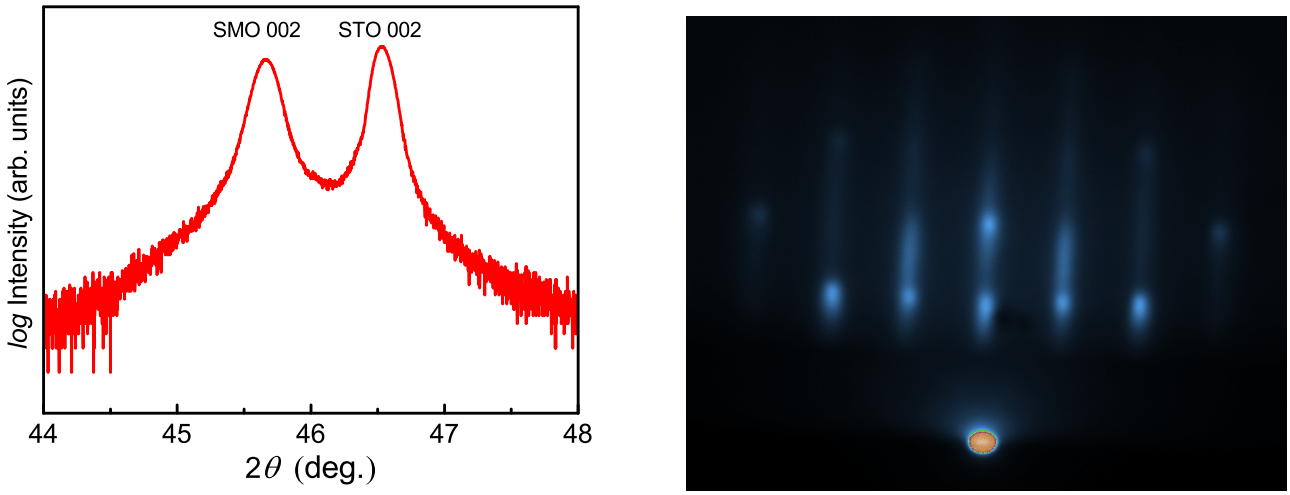

Figure 4.13: (Left) High resolution $2\theta - \theta$ scan of the SMO 002 reflex on silicon substrate covered with an STO layer. This sample has been used to determine the resistivity. (Right) RHEED surface image halfway through the SMO layer. The surface reflects a mixture of 2D and 3D growth.

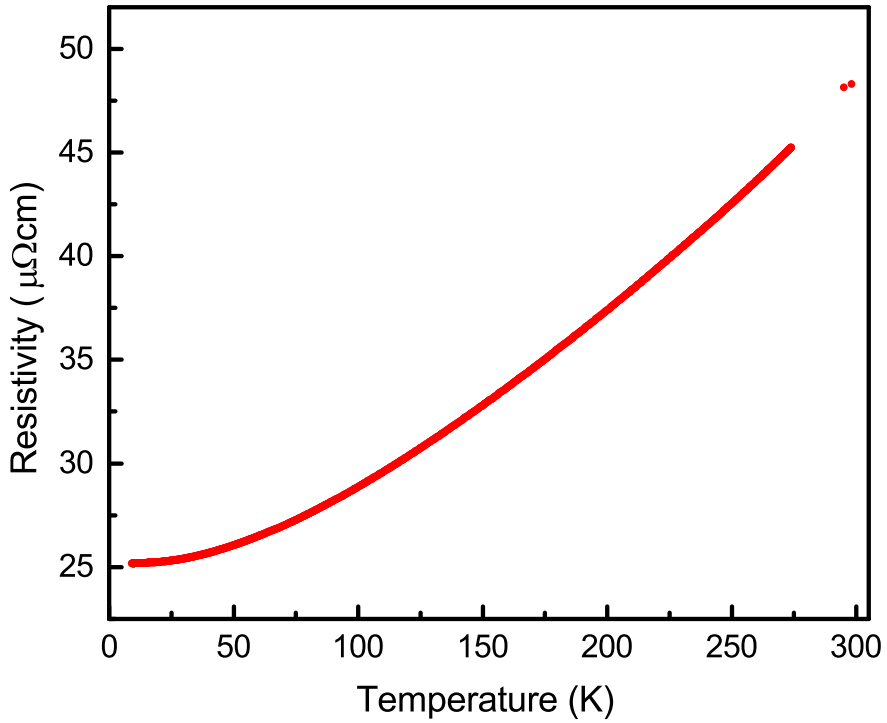

Figure 4.14: Resistivity over temperature of SMO grown on silicon substrate covered with an STO layer. The resistivity was determined in the four-bar geometry. The thickness of the particular sample is 70 nm.

4.2 Growth of several micrometer-thick SMO films

Since a thick bottom electrode is indispensable for the microwave performance of varactors, emphasis was put on accelerating the SMO growth and achieving epitaxial bottom electrodes with thicknesses in the range of several micrometer. As already mentioned in section 4.1.1, the laser repetition rate was increased to 20 Hz enabling the growth of several micrometer thick samples in a reasonable time span. The growth of thick samples will be discussed in detail in this section.
The increase of the bottom electrode thickness has two beneficial influences on the varactor performance. On the one hand, the series resistance can be lowered and on the other hand the bottom electrode exceeds the skin depth. The skin effect leads to a accumulation of an alternating electric current near the surface of a conductor. This effect increases for higher frequencies and the skin depth δ can be described by [57]

$$\delta = \sqrt{\frac{2\rho}{\omega\mu}}, \tag{4.1}$$

where ρ is the resistivity, ω is the angular frequency and μ is the material permeability. In section 4.1.1, the SMO resistivity was optimized to 31 $\mu\Omega$·cm. For the assessment of the skin depths (see Table 4.5) a resistivity of 40 $\mu\Omega$·cm was estimated, which is realistic for thicker SMO layers in the micrometer range as used in the all-oxide varactors. Thus, the calculated skin depths might deviate slightly depending on the achieved SMO resistivity.

Table 4.5: Skin depth in SMO for varactor heterostructures with a SMO resistivity of 40 $\mu\Omega$·cm

Frequency (GHz)	0.45	1	2.7	4	6	8
Skin depth (μm)	15.0	10.1	6.1	5.0	4.1	3.6

Table 4.5 shows that the skin depth is as large as 15 μm for 450 MHz and decreases for increasing frequency. This shows that the dissipation of the field in the conductor is greater, for higher frequencies. For the 5G frequency spectrum from 450 MHz to 6 GHz, the skin depth varies from 15 μm to 4.1 μm. However, it is not sufficient to match the desired skin depth with the electrode thickness. The electrodes in microwave devices should ideally be thicker than three to five times the skin depth [57]. Otherwise, the high current densities increase the Ohmic losses. If the skin depth surpasses the thickness of the electrode, the field can not decay completely inside the bottom electrode and penetrates into the substrate. This leads to a contribution to the total losses due to the free carrier absorption [128]. These losses due to electrodes thinner than the skin depth were modeled in detail for the present all-oxide varactor heterostructure in [95, 129], using a novel analytical model derived from the common RLC model.
A second benefit of thicker bottom electrodes is the lower series resistance of the bottom electrode, which leads to an increase in the quality factor. This is directly visible in equation (2.23) in section 2.7, where $Q = 1/\omega C R_{\mathrm{ser}}$. With increasing thickness, R_{ser} becomes smaller, resulting in an overall higher Q of the varactors. This increase can be seen in Figure 4.15, where the impact of different SMO thicknesses on

the quality factor was simulated by a 3D EM model using CST Studio Suite by M.Sc. D. Walk. For these simulations, a dielectric thickness of 85 nm, relative permittivity of 330, and SMO resistivity of 40 $\mu\Omega$·cm were estimated as fixed conditions.

For the frequency range up to MHz, the losses are dominated by the dielectric. The losses due to charged defects of the dielectric mainly contribute to the total loss up to 500 MHz. At higher frequencies, the losses are dominated by the electrode series resistance [11].
This behavior can be seen in Figure 4.16 (left). At lower frequencies, the series resistance R_{ser} and inductance L can be neglected and the resulting impedance can be described by a parallel connection of the losses of the dielectric R_{diel} and the capacitance. Therefore, the quality factors Q can be described in this case by $Q = \omega C R_{\mathrm{diel}}$. For higher frequencies, series resistance and inductance can not be neglected and the quality factor follows equation (2.23). The quality factor decays proportional to ω^{-1} and reduces to 0 at the series resonance frequency of the capacitance with its electrode's inductance. More in-depth information regarding the modeling can be found in [130].
The simulated data of the all-oxide varactors in Figure 4.16 (right) follows the overall trend of the 10 pF capacitor (left) in the displayed frequency range. The resonance frequency f_0 can be described by

$$\lim_{R_P \to \infty} f_0 = \frac{1}{2\pi\sqrt{LC}}. \tag{4.2}$$

The dependence of the resonance frequency f_0 on the inductance is the reason, why the resonance frequency is not reached until 12 GHz for the simulated all-oxide varactors. Although the capacitance for both, the simulated data for the all-oxide varactors and the 10 pF capacitor are comparable, the inductance varies, leading to the shifted resonance frequency.
It has to be noted that these simulation of the all-oxide varactors should only visualize the dependency of the quality factor on the SMO thickness. The simulated data might deviate from the experimental real device Q, since several factors such as thickness of dielectric and top electrode were predefined and kept fixed.
The quality factor can also be increased by lowering the capacitance C. The capacitance for a parallel-plate varactor is defined by $C = \varepsilon_0 \varepsilon_r A/d$. This formula suggests, that decreasing the capacitance can be achieved by lowering permittivity ε_r or increasing the thickness of the dielectric. However, both of these possibilities come with drawbacks. Lowering the permittivity would generally lower the achievable tunability and increasing the thickness would require a higher tuning voltage, which would negate the unique benefit of the all-oxide varactor of tuning voltages in the ion battery regime.
Decreasing the lateral area of the varactor is, in addition to a thicker bottom electrode, the second measure without drawbacks to increase the quality factor. This change in the design of the varactor device will be discussed in section 4.5.

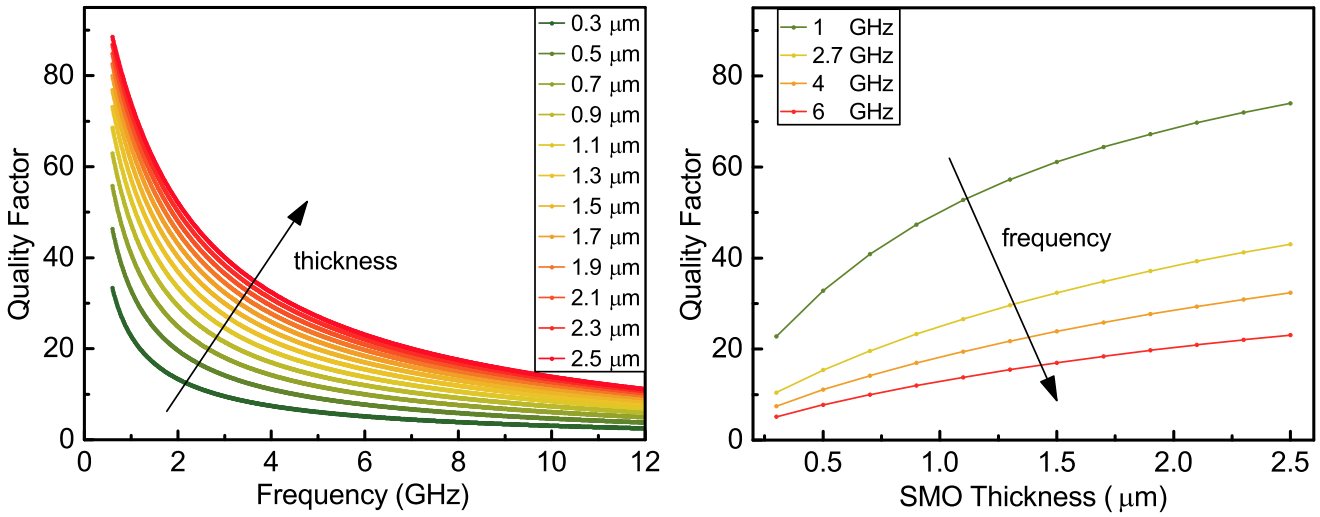

Figure 4.15: Simulation of the quality factor for all-oxide varactor heterostructures with different SMO thicknesses. (Left) Q-factor over frequency for different SMO thicknesses from 300 nm to 2.5 μm. (Right) Q-factor over SMO thickness for frequencies of 1, 2.7, 4 and 6 GHz.

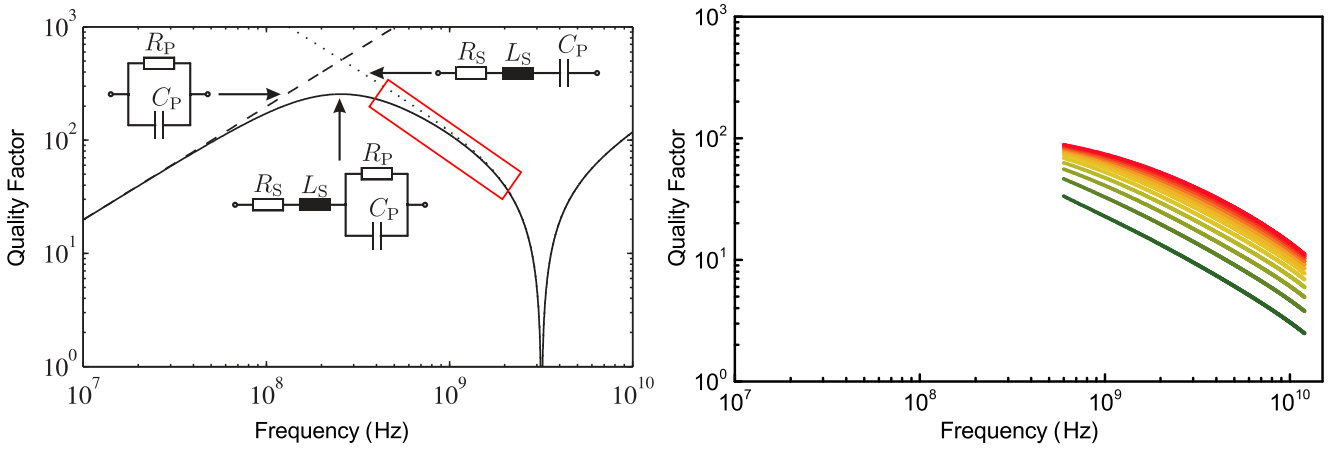

Figure 4.16: (Left) Quality factor of a 10 pF capacitor over the frequency, adapted from [130]. The red square visualizes the frequency range, which is relevant for the all-oxide varactors. (Right) Quality factor of an all-oxide varactor heterostructure for different SMO thicknesses. Both graphs are plotted over the same frequency range.

4.2.1 Crystal structure of micrometer-thick SMO films

A first attempt of scaling up the thickness of SMO on GSO substrates was performed in early 2017. This was carried out with the *LEXtra* excimer laser under the old growth conditions (see Table 4.1). A set of four all-oxide heterostructures was produced with a varying SMO thickness from 420 – 2800 nm and a BST thickness of 61 – 70 nm. Thicknesses were determined by XRD $2\theta - \theta$ Laue oscillations or, in case of the SMO thickness of 2800 nm, which is beyond the resolution limit, by RHEED intensity oscillations. For this reason, the determined value has an error of ± 50 nm since the thickness value was extrapolated by RHEED intensity oscillations for the first 30 unit cells.
Results of XRD $2\theta - \theta$ scans from these GSO/SMO/BST heterostructures with STO buffer layers can be seen in Figure 4.17. The out-of-plane lattice constants for all four samples are also coinciding. The values were determined via the Nelson-Riley Plot to be $c(\mathrm{SMO}) = 3.989 \pm 0.03$ Å and $c(\mathrm{BST}) = 3.984 \pm 0.03$ Å. All BST layer thicknesses differ by less than 10 nm and show very pronounced Laue oscillations over several degrees. SMO Laue oscillations can be seen for thicknesses up to 1380 nm (see inset in Figure 4.17 (right)), which is near the resolution limit of the *Rigaku SmartLab*® X-ray diffractometer and could only be achieved with an additional Ge(220)x2 analyzer at the detector side. In case of the sample with 420 nm SMO, the corresponding SMO Laue oscillations are also visible for several degrees and form a superposition with the BST Laue oscillations.
Rocking curve measurements of the SMO 002 reflections were performed on this series of samples and the results can be seen in Figure 4.18. It has to be noted that the rocking curves for the samples with 1380 nm and 2800 nm have been measured with the Ge(220)x2 analyzer at the detector side. All samples have very low mosaicity as indicated by the sharp rocking curves and low FWHM values of 0.003° – 0.012° (see Figure 4.18). The rocking curves of 1380 nm and 2800 nm thick SMO show a diffusive background due to the higher number of defects based on the increase thickness of the SMO layer [121, 122]. The rocking curve measurement of the 671 nm thick SMO layer shows an additional peak at 0.027 ° which can be assigned as a tail of the BST 002 reflex. The FWHM values decreases with increasing SMO thickness until 1380 nm and slightly increases to the 2800 nm thick sample. Generally, the FWHM are near the resolution limit of the X-ray diffractometer and in the same range as the GSO substrate.

To confirm that 2.8 μm thick SMO is still in-plane locked to the substrate and not relaxed, a RSM measurement was performed (see Figure 4.18 (right)). It is clearly visible, that the SMO continues to grow in-plane locked to the GSO substrate, even after several micrometer and provides a good surface for the subsequent BST layer, which is also in-plane locked to the layers underneath.

Based on these XRD results, an unlimited increase in SMO thickness seems possible, while still maintaining strained, epitaxial relation. In the later section 4.6.1, a working and high performance varactor with over 5 μm SMO bottom electrode will be presented.

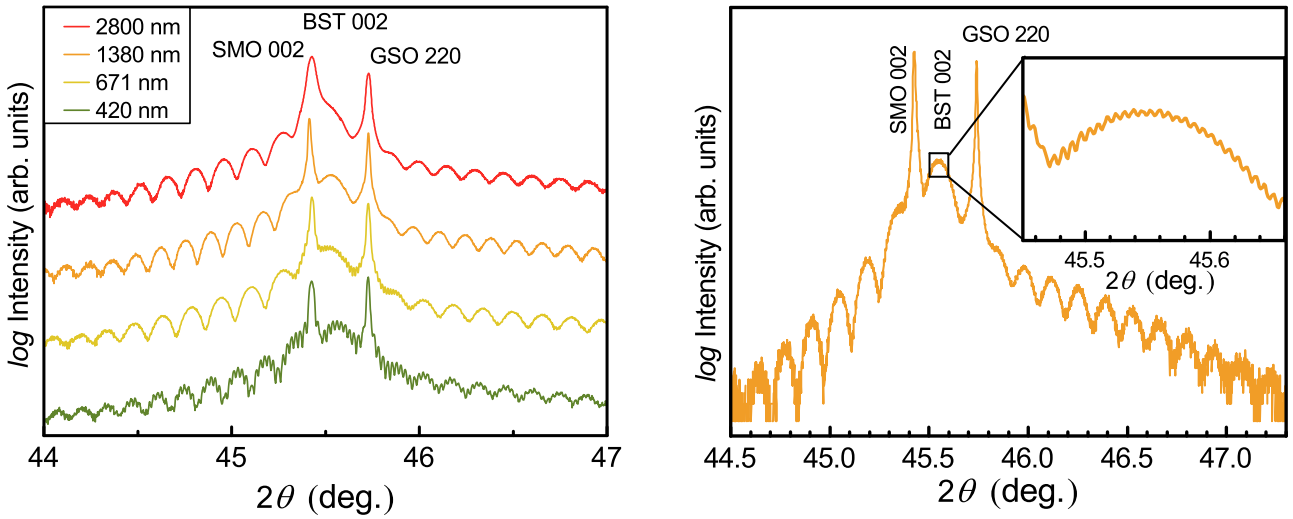

Figure 4.17: (Left) $2\theta-\theta$ scan around the SMO 002 reflections with different thickness of 420 – 2800 nm from a study early 2017. (Right) High resolution scan with the Ge(220)x2 analyzer at the detector side of the SMO sample from the left graph with a film thickness of 1380 nm. The inset shows the SMO Laue oscillations on top of the BST 002 peak.

Defects in thick SMO layers

Further inspection of the surface of varactor heterostructure, with micrometer-thick SMO bottom electrodes, revealed defects, already visible in the optical microscope under low magnification (see Figure 4.19 (left)). The surface depicted in these figures are the BST layer of the varactor. However, the origin of these structures originate in the SMO, which is shown by further inspections. These structures only appear for SMO beyond a thickness of $\approx 1\mu$m. The defects appear in clusters of higher densities across the 5 x 5 mm^2 sample. These clusters have an elongated, elliptical appearance and are aligned parallel to each other. One theory, which links these clusters to insufficient substrate cleaning, could be disproven, since the defects also appear after cleaning the substrates with an established cleaning routine. With a higher magnification (see Figure 4.19 (right)), the defects can be divided into two different shapes:

i) rectangular

ii) star/butterfly shaped

To get a more precise picture of the SMO surface, another 5 μm varactor sample was measured by SEM. However, this sample was already structured and patterned using ion beam etching. Therefore, the area not covered by the gold contacts, was etched down to SMO. For this reason, the measured surface is not BST, but SMO. It also has to be noted, that although both varactors with 5 μm SMO show these defects, the microwave performance is not compromised and the varactors still function as desired.

The SEM images (see Figure 4.20) were taken in the center region of the sample at 10 kV acceleration voltage to minimize the interaction volume and be as surface sensitive as possible. The SEM images coincide

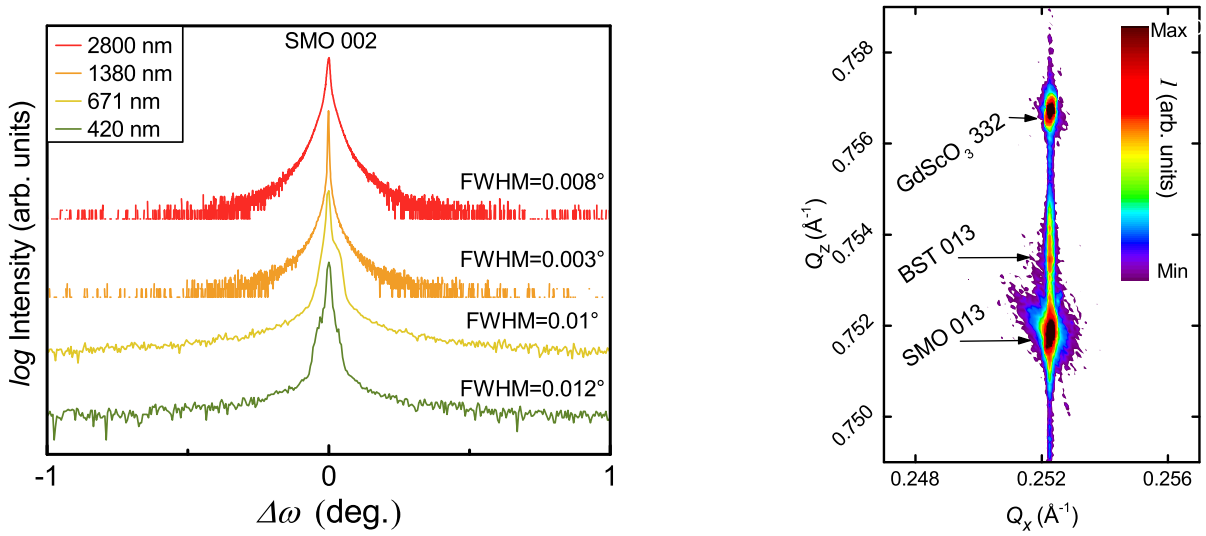

Figure 4.18: (Left) Rocking Curve Measurements of the SMO (002) reflex with different thickness from a study early 2017. (Right) Reciprocal space map of an all-oxide heterostructure with 2800 nm SMO.

with the optical microscope image of Figure 4.19. This proves, that the defects do not originate in the BST, since the BST layer of this sample was etched by IBE. The picture of the rectangular defect (Figure 4.20) has a high spot in the middle indicated by the increased brightness. This high spot in square shape is surrounded by a trench lower than the overall sample surface. The star/butterfly shaped defect has the high point at the edge of the defect and a hole in the middle.

The height profile of these two types of defects was also investigated by atomic force microscopy (AFM). The corresponding profiles can be seen in Figure 4.21. The AFM results confirm the interpretation of the SEM images. The high point in the square defect is 197 nm high, whereas the trench has a depth of 215 nm (see Figure 6.3 in the Appendix). The high point at the edge of the star/butterfly shaped defect has a height of 143 nm and the depth in the middle is 328 nm (see Figure 6.3 in the Appendix).

In addition to the AFM measurements of the SMO surface, etched by IBE, this sample was also measured by AFM directly after growth. Therefore, the measured surface is the dielectric BST. The resulting AFM images can be seen in Figure 4.22. The 3D image of a 20 x 20 μm^2 area (Figure 4.22 (left)) shows the same rectangular and star/butterfly shaped defects. This validates, that the defects do not have their origin in the IBE process, but arise during growth. In addition to these two types of defects, the surface shows an additional structure similar to grain boundaries. A finer scan of a 5 x 5 μm^2 area (Figure 4.22 (right)) shows a height difference from top to valley of 3.5 nm. The RMSR (Root Mean Square Roughness) equals RMSR = 0.2 nm (between the grains) and RMSR = 0.5 nm (over the grain boundaries), both for 5 x 5 μm^2 measurement area. These grain boundary structures were not visible in the previous AFM and SEM images, since the originate in the BST and are very thin. For these reasons, they were etched by IBE and are not visible anymore.

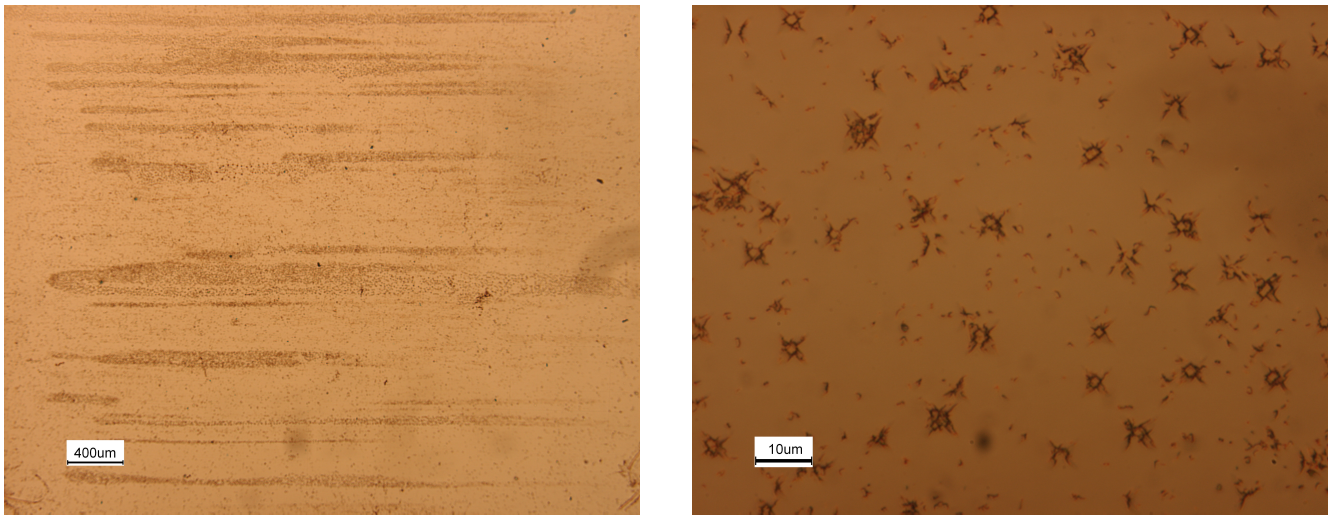

Figure 4.19: (Left) Low magnification microscope image of the BST surface of a varactor heterostructure before structuring by photolithography with 5 μm SMO bottom electrode. Areas with high and low density of defects are visible. (Right) High magnification image of the same varactor heterostructure. Two types of defects, rectangular and star/butterfly shape are visible.

To clarify the origin of the defects, a FIB lamella was cut through two rectangular shaped defects (see Figure 6.4 in the Appendix for the lateral alignment). This lamella was cut on the same varactor sample with 5 μm SMO, which was investigated in the previous SEM and AFM images. An image of the lamella can be seen in Figure 4.23. Before cutting the FIB lamella, a platinum layer is deposited on the sample surface to protect the sample. This layer is visible as a bright layer on top of SMO. The red line at the SMO – Pt interface outline the shape of the rectangular defect. The trench and square high point are clearly visible. For both defects, a black line is visible at its boarder. This line continues in a cone shape deep into the SMO. This black line might be a crack through the SMO caused by a dislocation. Further TEM images will clarify the origin and exact type of crack. The origin of the defect is visualized by a red dot. It appears for the SMO thickness range 600 – 1200 nm.

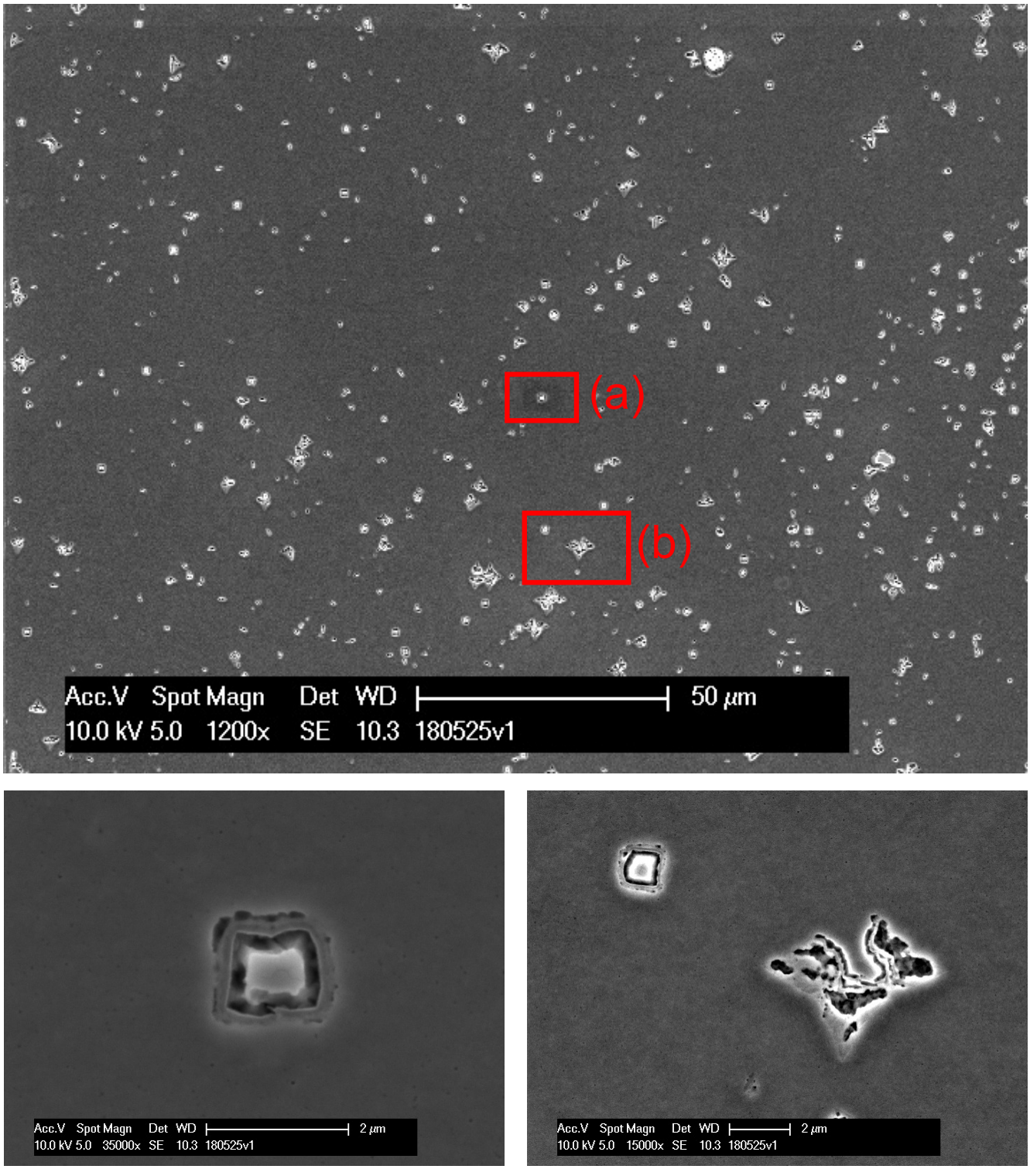

Figure 4.20: Upper Image: SEM image of the SMO surface with a thickness of 5 μm. The rectangular defect (a) and star/butterfly shaped defect (b) are shown in the higher magnification below. Bottom left: rectangular defect (a) with diameter of 1 μm. Bottom right: Both rectangular and star/butterfly shaped defects from (b).

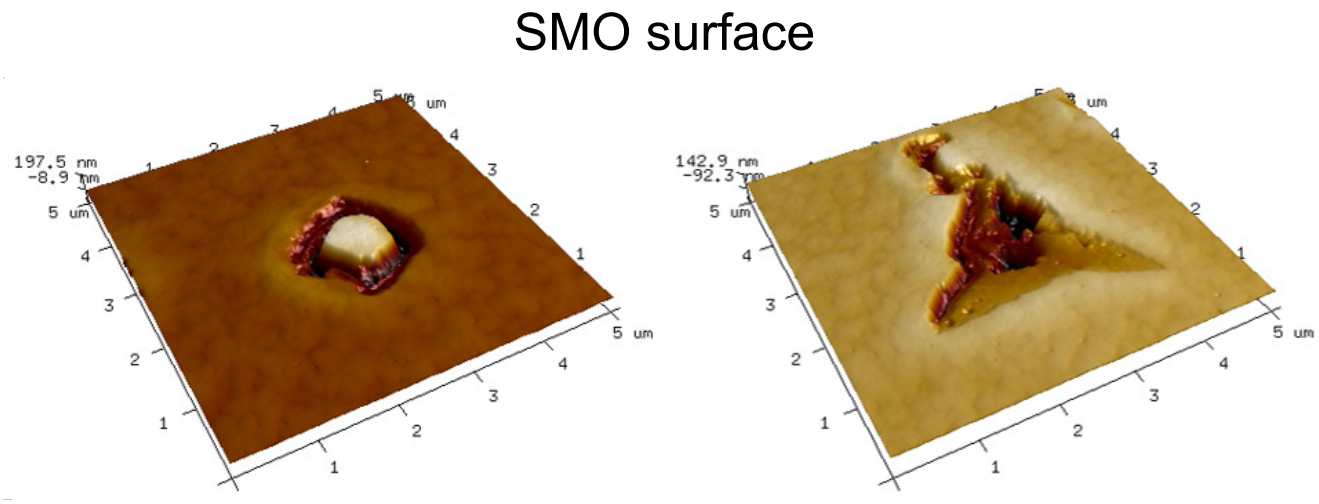

Figure 4.21: SMO surface of a varactor with 5 μm SMO bottom electrode after IBE. (Left) 3D AFM depth profile of the rectangular defect. (Right) 3D AFM depth profile of the star/butterfly shaped defect.

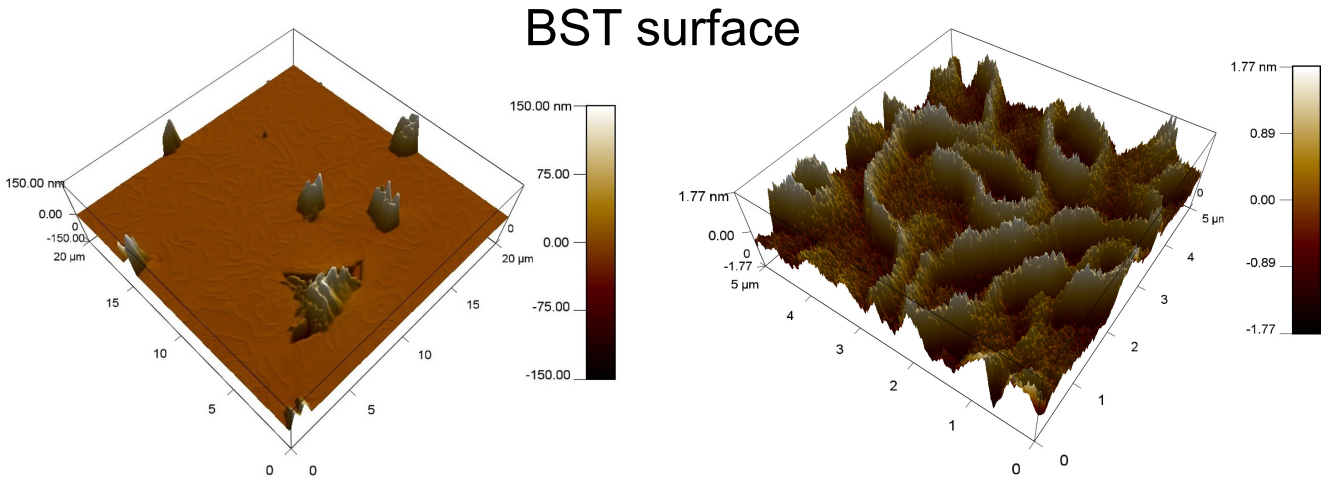

Figure 4.22: BST surface of a varactor with 5 μm SMO bottom electrode. (Left) 3D AFM depth profile of the defects on the surface. The same defects from Figure 4.20 are visible. (Right) 3D AFM depth profile of the same varactor surface on a section with no defects. The surface shows structures with RMSR (Root Mean Square Roughness) of RMSR = 0.5 nm over the grain boundaries. They are also visible in the left image.

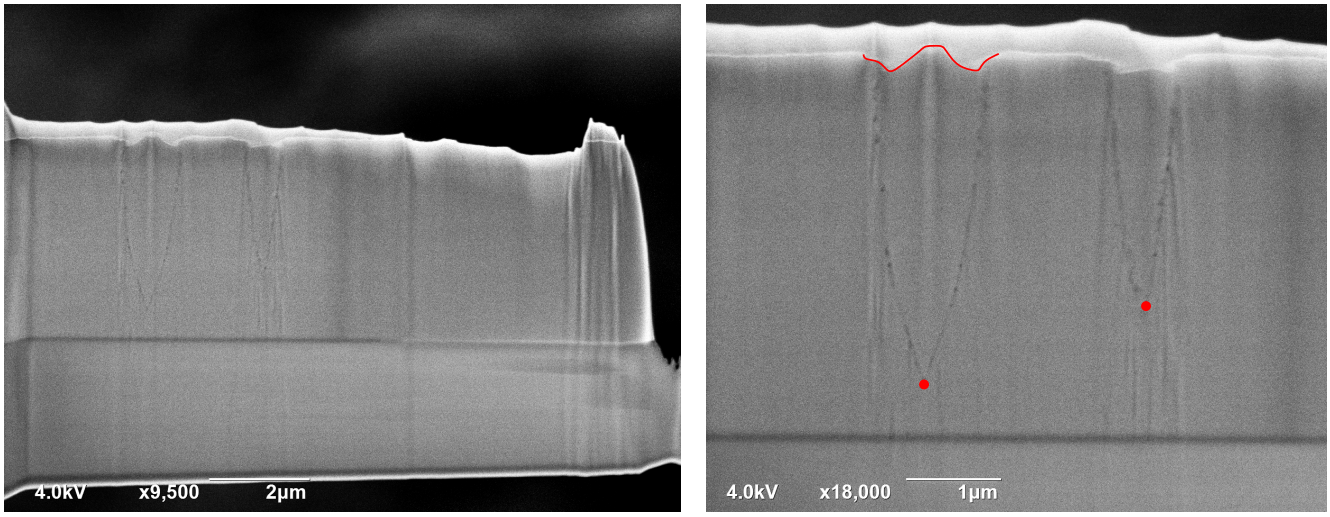

Figure 4.23: (Left) SEM image of a FIB lamella through two square shaped defects. (Right) Higher magnification SEM image of the two defects. The bright top layer is a protective platinum layer. The red line indicates the defect. The trench and top part are clearly visible. Through the 5 μm SMO layer a clear cone shaped crack is visible. The origin, indicated by a red dot is several hundred nanometer above the substrate.

4.2.2 Microwave results for varactors with micrometer-thick SMO bottom electrodes

After the heterostructures with varying SMO thickness presented in the previous section (see Figure 4.17) were fully characterized by XRD, top electrodes were structured by photolithography, sputtering, and lift-off process. The microwave performance of the resulting 36 varactor devices of each sample were determined by VNA and impedance analyzer. The microwave properties are shown in Figure 4.24. The values for each sample are averaged over all varactor devices with 20 μm inner pad diameter. All microwave properties are plotted over the bias field V/μm. This field is calculated with the applied DC bias and the thickness of the dielectric BST layer, which is 61 – 70 nm for these samples. This way of displaying the data has been chosen to better compare the samples, since the DC field is important to achieve the polarization of the BST layer and, thus, change in permittivity and tunability. The voltage can be recalculated from the BST thickness in Figure 4.17 and is around 6.5 V for 100 V/μm.
Judging from the XRD results in Figure 4.17 one would expect very reproducible microwave performance, since the SMO and BST have very similar positions in the $2\theta - \theta$ peak positions. However, the microwave results of the samples vary considerably. The devices are not symmetrically tunable and show a very high leakage current. The varactors are only tunable for negative bias voltages and the measurements abort for positive bias fields around 50 V/μm (around 3 V). All samples have a tunability of almost 60 % for negative bias fields of -100 V/μm (around -6.5 V). The permittivity shows a spread over all samples from maximum values of 450 down to 250, although the crystalline quality of the BST indicated by Laue oscillations and 002 peak positions is almost identical for all samples (see Figure 4.17).

The measurements were aborted at positive bias fields around 50 V/μm due to a too high leakage current through the dielectric. The measurement setup is equipped with a current compliance limit of 1 mA. If this limit is reached, the measurement is aborted to protect the dielectric from being burned by the high leakage current. Generally, leakage currents are caused by electrode or bulk-limited conduction mechanism (see section 2.7.2). In this case, the leakage current is caused by oxygen vacancies in the dielectric BST layer. The samples of this series were grown before investigations on oxygen diffusion barriers and BST optimized deposition conditions have been done. For these reasons, the BST was deposited at low oxygen partial pressure of 1.5 mTorr to prevent SMO oxidation, causing the oxygen vacancies. The leakage current density in Figure 4.24 has maximum values for negative bias fields of -100 V/μm of around J(leak): 10^6 A/m^2.

The high leakage current prohibits investigations of the SMO thickness on the microwave properties, primarily on the quality factor. No trend following the SMO thickness is visible in the quality factor. This is caused by the widely varying permittivity, which changes the overall capacitance C and, thus, the quality factor $Q = 1/\omega C R_{\mathrm{ser}}$. The conclusion of this study is that high crystalline quality does not necessarily lead to good microwave performance. The high leakage current reduces the overall functionality of the varactors and lead to unpredictable behavior.

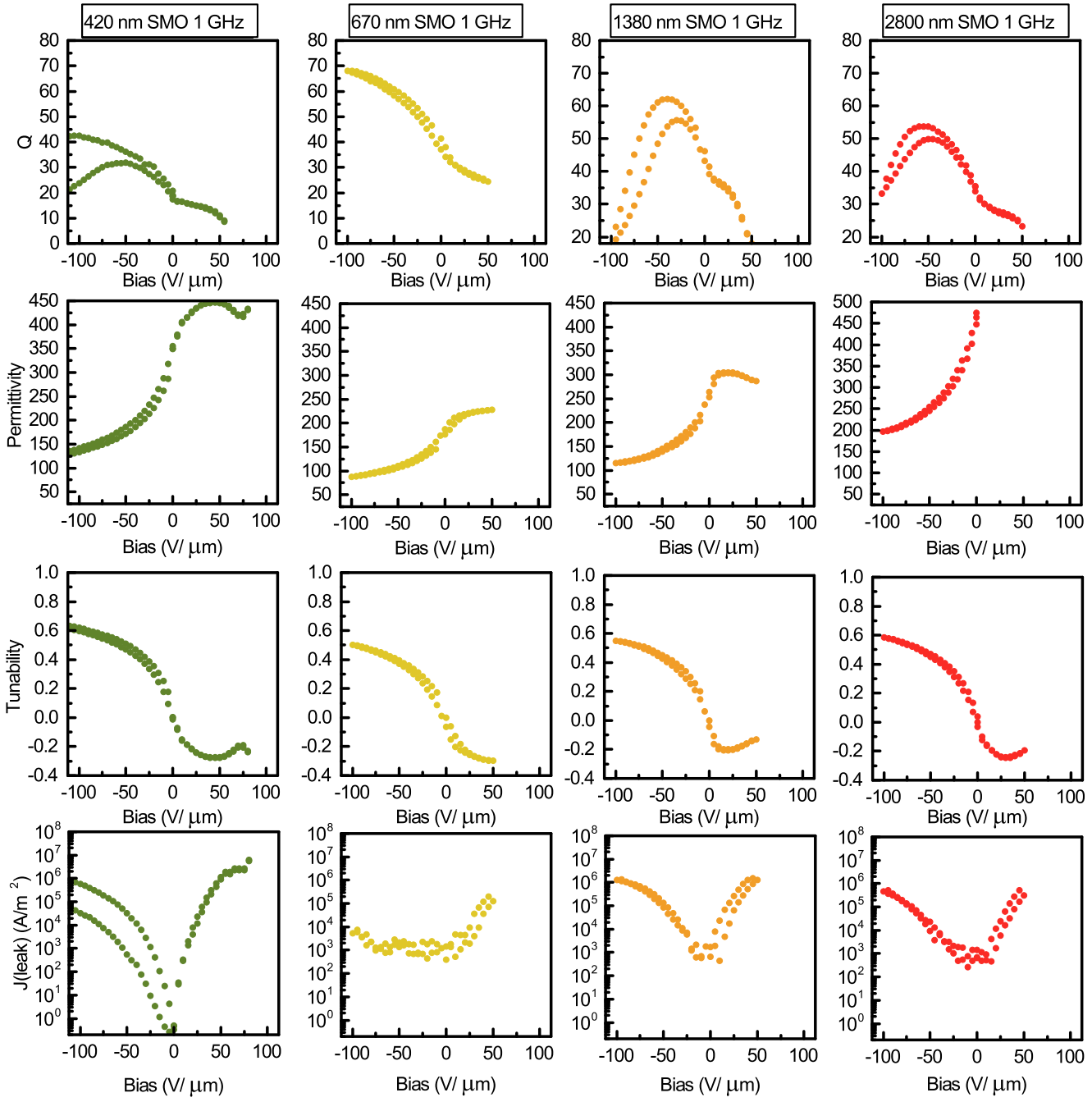

Figure 4.24: Microwave properties of varactors with different SMO thickness from a study early 2017. It is evident that the microwave properties are not as expected due to high leakage current. The values are averaged over all varactors with a 20 μm inner pad diameter on one sample.

After the problem of the high BST leakage current was solved (see section 4.3 and 4.4), a new set of samples was produced. Results of XRD $2\theta - \theta$ scans can be seen in Figure 4.25. The SMO 002 peak reflections coincide for all samples at 45.415 ± 0.005 ° leading to a *c*-lattice constant of 3.990 ± 0.001 Å. In addition, the SMO layers show Laue oscillation until the sample with a thickness of 958 nm, approaching the resolution limit of the XRD. The SMO thicknesses were determined by Laue oscillations and in case of the absence of Laue oscillations for the SMO layer with 2000 nm the thickness was extrapolated by the RHEED growth oscillations. Therefore, this value has an error of ± 50 nm. The SMO layers were grown from 243 – 2000 nm with a number of 16 250, 33 000, 60 000, and 130 000 excimer laser pulses respectively.

The BST peak is shifted towards lower angles compared to the previous set samples with varying SMO thickness due to a higher out-of-plane lattice constant. The *c*-lattice constants are 4.009 ± 0.008 Å. Usually one would expect a smaller out-of-plane lattice constant with a filling of the oxygen vacancies, since the cation repulsion is suppressed by the oxygen ion. However, this shift might be caused by a change in the cation stoichiometry, since the different mass of the atoms lead to different scattering and mean free paths with higher background pressures. All BST layers were grown with 7 500 excimer laser pulses and an oxygen background pressure of 15 mTorr. This leads to a thickness of 85 ± 3 nm determined by Laue and RHEED intensity oscillations. All layer are in-plane locked to the GSO substrate and only differ in out-of-plane lattice constant, proven by the reciprocal space map for the sample with a 2 μm SMO bottom electrode (see Figure 4.25 (right)).

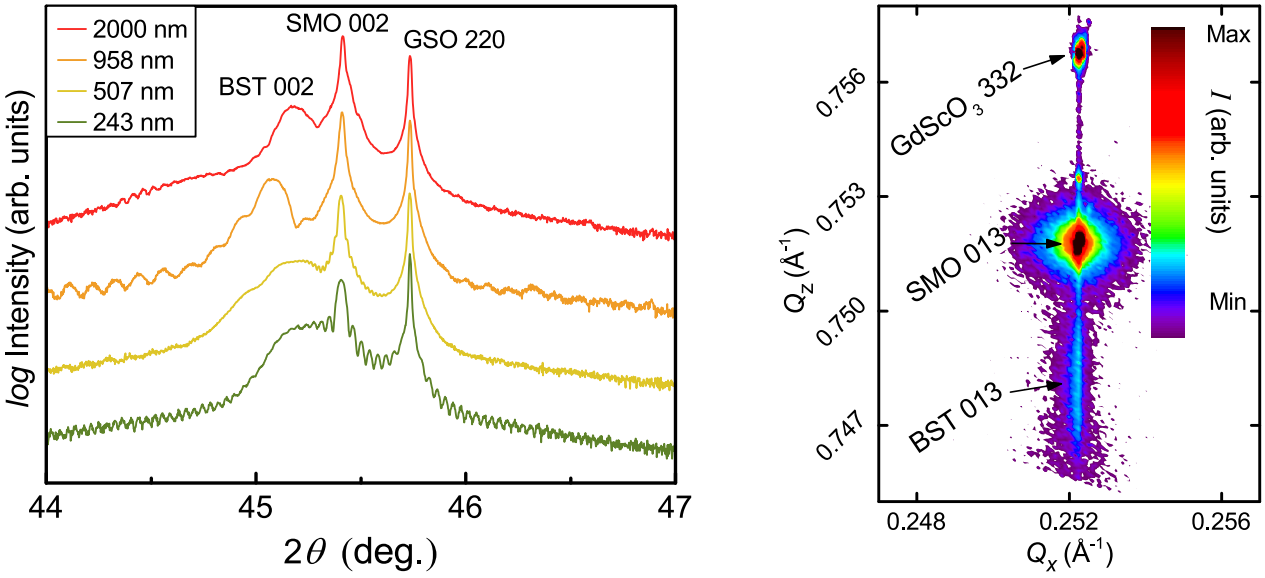

Figure 4.25: (Left) $2\theta - \theta$ scan of the SMO 002 reflections with different thickness of 243 – 2000 nm after the high BST leakage current was solved. (Right) Reciprocal space map of the varactor heterostructure with 2 μm of SMO.

The RHEED surface images taken after each layer (see Figure 4.26) during the heterostructure deposition confirms a layer-by-layer growth for all layers until the end of the heterostructure. The pattern remains consistent throughout the deposition indicating a 2-dimensional layer-by-layer growth. Furthermore, no oxidation of the SMO is visible during the BST deposition with increased background pressure. It has previously been observed that $Mo^{4+} \rightarrow Mo^{6+}$ oxidation caused by a too high oxygen background pressure leads to a roughening of the interface shown by a 3-dimensional island RHEED pattern [131].

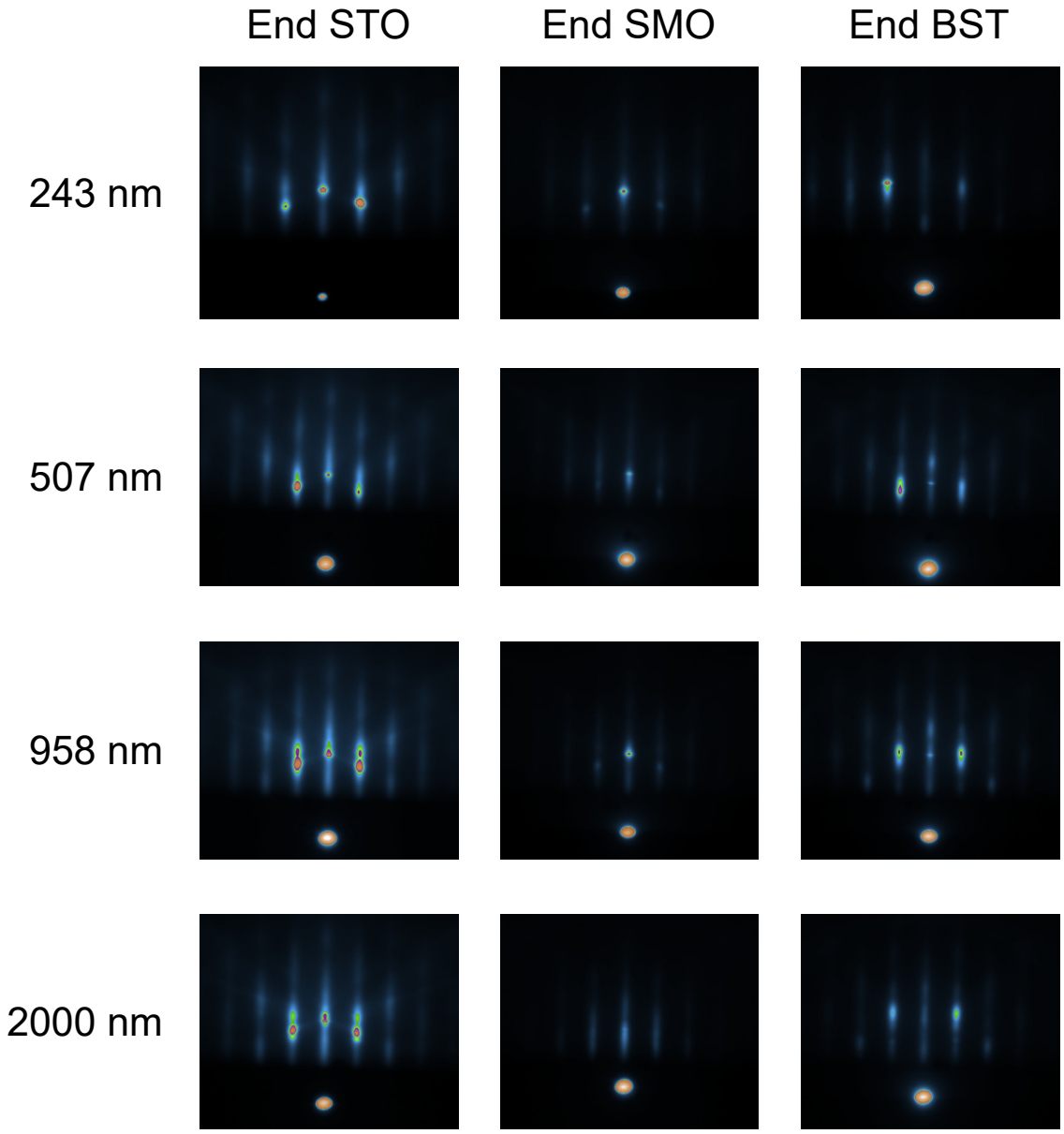

Figure 4.26: RHEED surface images for all four samples displaying the end of of the STO buffer layer, SMO layer and dielectric BST, which is also the final surface of the samples.

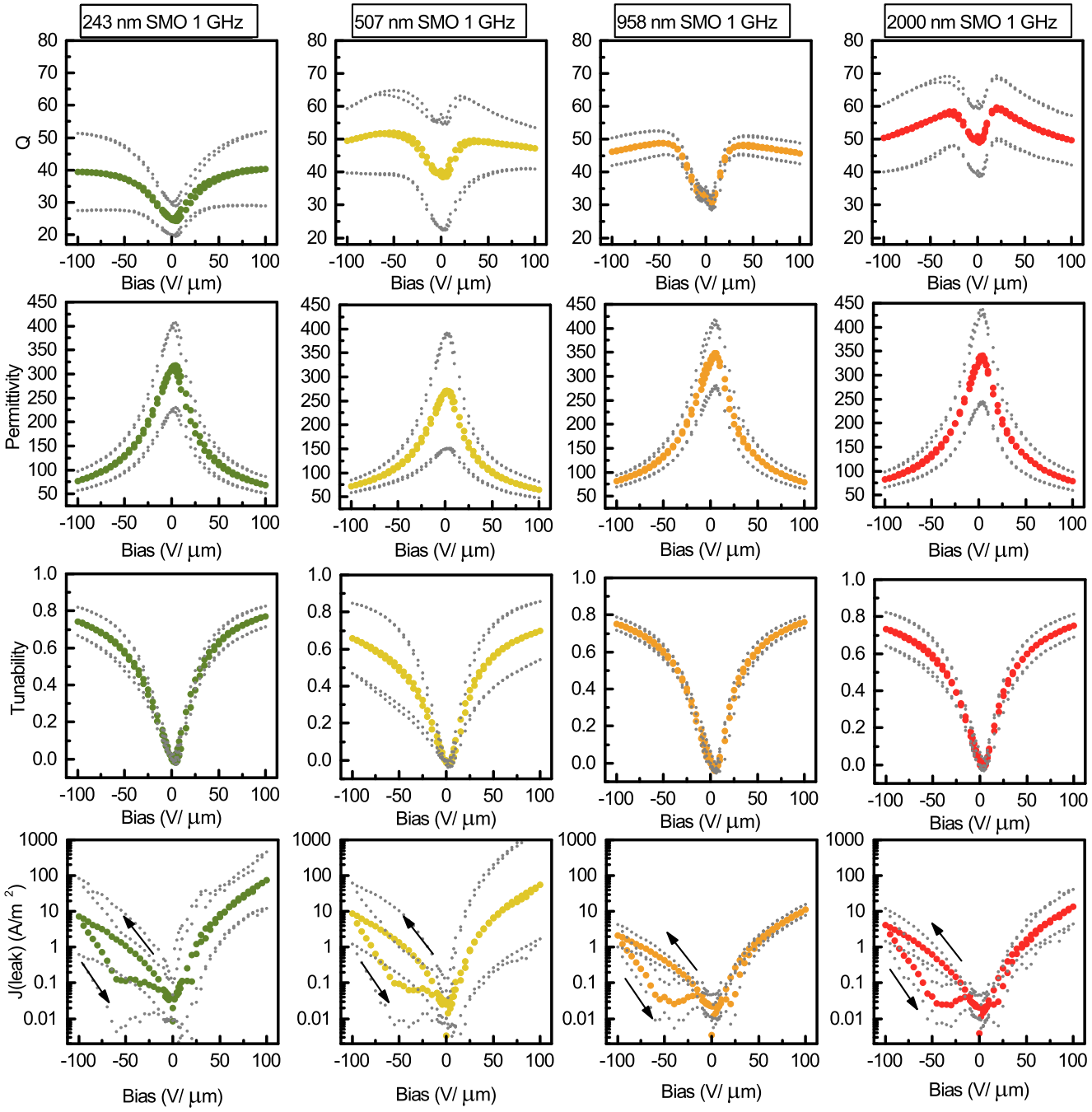

Figure 4.27: Microwave properties of varactors with different SMO thickness of 243 – 2000 nm after the high BST leakage current was solved. The values averaged over all varactors with a 20 μm inner pad diameter. The gray dots indicate the minimum and maximum values and the colored dots shows the averaged values over all measured devices.

After X-ray characterization, top electrodes have been deposited utilizing photolithography, sputtering and lift-off process. The microwave performance of the resulting 36 varactor devices of each sample have been measured with a VNA and an impedance analyzer. The results are displayed in Figure 4.27. The properties are plotted over the bias field V/μm. The voltage can be recalculated from the BST thicknesses in Figure 4.25 and is around 8.5 V for 100 V/μm.
All varactor devices perform as expected and are symmetrically tunable in both bias directions over the whole range until ± 100 V/μm. The optimized growth conditions with the increased oxygen background pressure of 15 mTorr lead to a decrease in leakage current of five orders of magnitude from the current compliance 10^6 A/m^2 down to 10 A/m^2, proving a higher oxygenation of the dielectric BST. The leakage current behavior is different for negative and positive bias voltages. Reason for this are the two varying interface materials Pt – BST and SMO – BST. The differing work functions of Pt (5.3 – 5.7 eV) [132, 133] and SMO (4.1 eV) [17] lead to a different charge injection. Charge injection at the interface occurs, in particular, for small barrier heights at the interface. For the Pt – BST interface, a barrier height of 1 eV has been reported [134]. Considering a BST electronegativity of ≈ 3.9 eV [135] and the difference in work function between SMO and Pt, it is evident that the barrier height is considerably smaller for the SMO – BST interface, in the range of 0.1 eV. Positive biasing injects charges through the SMO – BST interface and due to the lower barrier height, the leakage current is higher in this case.
The hysteresis for negative bias voltages might be explained by the filling of traps with the first increase in bias voltage, leading to a higher measured leakage current. Note that the leakage current is measured at the current source of the measurement device, thus, a filling of traps leads to an increase in measured leakage current. When decreasing the voltage again, the traps are already filled, hence, the drain of current and measured leakage current is smaller.
For the samples with 243 nm, 958 nm and 2000 nm SMO, the tunability is around 0.75 ± 0.02. Only the sample with 507 nm differs with an averaged value of 0.66. In addition, this sample shows the largest spread of values across all measured varactor devices. A similar trend is visible for the permittivity, since both, tunability and permittivity are generally connected. The samples with 243 nm, 958 nm and 2000 nm SMO have a BST relative permittivity at 0 V bias of 340 ± 20. The averaged permittivity of the sample with 507 nm SMO is lowered to 270 also explaining the lower tunability. Reason for this decreased permittivity might be slight deviations in the BST stoichiometry due to fluctuations during the deposition process. As expected, the values of leakage current, tunability, and permittivity should be independent of the SMO thickness, since they are a property of the dielectric layer and the BST has the same thickness and composition in all samples.
However, with increasing SMO thickness, the quality factor is also expected to be increased as shown in the simulated data for the Q-factor in Figure 4.15 due to a reduction of the series resistance R_{ser}. This expected behavior can be seen in the experimental data in Figure 4.27. It has to be noted that the increased value for the sample with 507 nm SMO is based on the lowered permittivity leading to a smaller capacitance and quality factor, since Q is invers proportional to C for higher frequencies: $Q = 1/\omega C R_{\mathrm{ser}}$.
The experimental values for $Q(0\,\mathrm{V})$ averaged over all varactors with 20 μm inner diameter as well as individual varactors are displayed for 1 GHz and 2.7 GHz depending on the SMO thickness in Figure 4.28,

in addition to 3D EM simulated values of the quality factor. The individual varactors were chosen to have a relative permittivity close to 330 and an inner pad diameter of 20 μm. This should ensure, that a change in dielectric permittivity does not impact the Q-factor and the fixed conditions of the simulations are matched accurately. As already mentioned, the averaged quality factor for 507 nm thick SMO has to be excluded from this series due to the lowered permittivity. However, the value for the individual varactor does coincide with the simulated data. The 243 nm thin sample does also fit to the simulated data. For the SMO layers with 958 nm and 2000 nm, the experimental Q-values are increasing, however, slower than the simulated data. For these simulations, a BST dielectric thickness of 85 nm, relative permittivity of 330, dielectric loss tangent of $\tan\delta = 0.008$, and SMO resistivity of 40 $\mu\Omega$·cm were estimated as fixed conditions. This lowered experimental Q-factors suggest a higher SMO resistivity than the assumed 40 $\mu\Omega$·cm. Fitting of the experimental data with a highly accurate analytical model [95] yielded SMO resitivities of 55 $\mu\Omega$·cm for 958 nm SMO and 56 $\mu\Omega$·cm for 2000 nm SMO. These higher resistivities explain the lowered experimental values, which fall short compared to the simulated values.
However, this study showed that by increasing the SMO thickness, the Q-factor can be increased. No visible threshold for the SMO thickness has been found during this thesis. This suggest that an increase in SMO thickness beyond 10 μm and the skin depth at 1 GHz is possible. This can further increase the performance edge of all-oxide varactors over state-of-the-art platinum varactors.

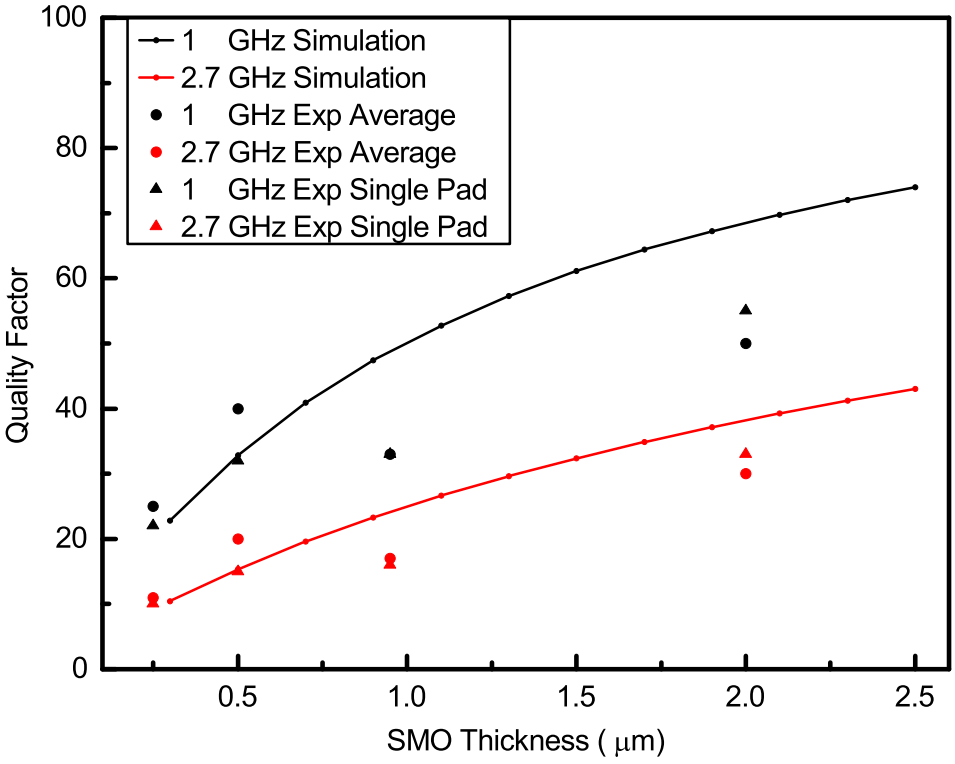

Figure 4.28: Simulated Q-factors over SMO thickness for frequencies of 1 and 2.7 GHz (solid lines) as well as the experimental data for the same frequencies averaged over all varactors with a 20 μm inner pad diameter and individual varactor pads with 20 μm inner pad diameter and a BST permittivity of 330.

4.3 SMO – BST interface: Oxygen diffusion barrier

The high conductivity of $SrMoO_3$ relies on the Mo cation in the thermodynamically unfavorable Mo^{4+} valence state with the $4d^2$ (t_{2g}) electronic configuration near the Fermi level [61]. In order to prevent $Mo^{4+} \rightarrow Mo^{6+}$ oxidation (leading to formation of the electrically insulating $SrMoO_4$ phase), a highly reductive atmosphere is required for the growth of $SrMoO_3$, which is incompatible with the relatively high oxygen pressure typically used for the thin-film growth of functional oxide materials, such as BST. The dielectric BST requires a high oxygen partial pressure in order to minimize oxygen vacancies and suppress the leakage current in the final varactor device. Literature reports suggest a partial oxygen background pressure of 75 mTorr [136]. For this reason, the reductive growth conditions of $SrMoO_3$ present a major obstacle for the production of thin-film heterostructures with $SrMoO_3$ electrodes. The obstacle can be overcome if the $SrMoO_3$ film is capped by a thin layer of a material which minimizes oxygen diffusion between BST and $SrMoO_3$ and, thus, prevents $Mo^{4+} \rightarrow Mo^{6+}$ oxidation.
In general, the transport of oxygen ions plays a central role in applications of oxide materials. Oxygen diffusion has previously been intensively studied based on sophisticated positron beam annihilation or oxygen tracer experiments [65, 66, 137–141]. For heterostructures with $SrMoO_3$, oxygen diffusion through the capping layers can be indirectly, yet still accurately, analyzed by monitoring the Mo valence state using X-ray photoelectron spectroscopy (XPS) [142, 143].

Here, a similar measurement routine has been utilized and the Mo oxidation state in $SrMoO_3$ has been monitored by XPS to compare oxygen diffusion through $Ba_{0.5}Sr_{0.5}TiO_3$ and two other capping layers, namely $SrTiO_3$ (STO) and $BaTiO_3$ (BTO). An oxidation limit for the growth of functional BST on top of $SrMoO_3$ is determined from the rise of the Mo^{6+} oxidation state for each capping material [143].
The capping materials were selected according to the following criteria:

i) perovskite structure with a low mismatch of the lattice parameters between the capping material $SrMoO_3$ and the $GdScO_3$ substrate

ii) consistency of the oxidation states of their cations with the formula $A^{II}B^{IV}O_3$ to prevent formation of an energetically unstable valence-mismatched interface with $SrMoO_3$ [12]

Accordingly, perovskite titanates with Sr and Ba at the *A*-site were selected as the capping materials, i.e. $SrTiO_3$ with a lattice parameter of 3.905 Å [37] ($\Delta = -1.56\,\%$ to $GdScO_3$), $BaTiO_3$ with an in-plane lattice parameter of 3.994 Å [38] ($\Delta = 0.68\,\%$), and $Ba_{0.5}Sr_{0.5}TiO_3$ with a lattice parameter of 3.947 Å [144] ($\Delta = -0.5\,\%$).
The heterostructures were grown on (110) $GdScO_3$ 5 x 5 mm^2 single crystal substrates. A ceramic $SrMoO_4$ pellet, produced by spark plasma sintering, was used as a PLD target for $SrMoO_3$ thin films. Stoichiometric ceramic pellets were used for the growth of the correspondent capping layers. The KrF excimer laser in the *DCA* PLD was operated during the $SrMoO_3$ deposition with a fluence of 0.9 J/cm^2. In order to provide an effective reduction of $SrMoO_4$ to $SrMoO_3$ during the film growth, the PLD chamber was filled with 30 mTorr of argon background gas supplied at a flow of 15 sccm. The substrates were kept at a temperature

of 630 °C. The thickness of the $SrMoO_3$ layer in all samples was 33 ± 2 nm. A buffer layer of 5 – 7 unit cells of $SrTiO_3$ was grown on $GdScO_3$ substrate prior to $SrMoO_3$ films to ensure smooth layer-by-layer growth [92, 93].
All capping materials with a thickness of 6 unit cells were grown with a fluence of 0.6 J/cm^2. The depositions of the capping layers were performed in vacuum, specifically at a base pressure of $4{\cdot}10^{-8}$ Torr in the PLD chamber. The growth of the entire heterostructure was monitored *in situ* using a RHEED system. The roughness of the layers was determined via the fitting of the XRR curves using *RCRefSim* software [126]. XPS was utilized to trace the Mo valence state in $SrMoO_3$ through the capping layer after annealing of the samples in oxygen. This method allows an indirect quantification of the oxygen diffusion through the capping layer as the ratio of Mo^{4+}: Mo^{6+}. This indicates the amount of Mo oxidized from the initial state ($Mo^{4+} \rightarrow Mo^{6+}$). XPS measurements were carried out with a *PHI Versaprobe 5000* spectrometer using monochromatic Al Kα radiation at the take-off angle of $\varphi = 75°$ to record Mo 3*d* emission from the underlying $SrMoO_3$ through the thin capping layers. Binding energies for all recorded spectra were measured with a precision of ± 0.1 eV.

The sequence of the XPS measurements can be seen in Figure 4.29. First, as-grown heterostructures with $SrTiO_3$, $BaTiO_3$, and $Ba_{0.5}Sr_{0.5}TiO_3$ capping layers were mounted together onto one sample holder and the Mo 3*d* and valence band emissions were measured by XPS. After measuring each sample, the sample holder was transferred *in situ* into an annealing chamber where the samples were annealed in oxygen. The XPS measurements of each sample were repeated after each annealing step and the increase in Mo^{6+} due to a thicker oxidized $SrMoO_4$ layer can be determined.

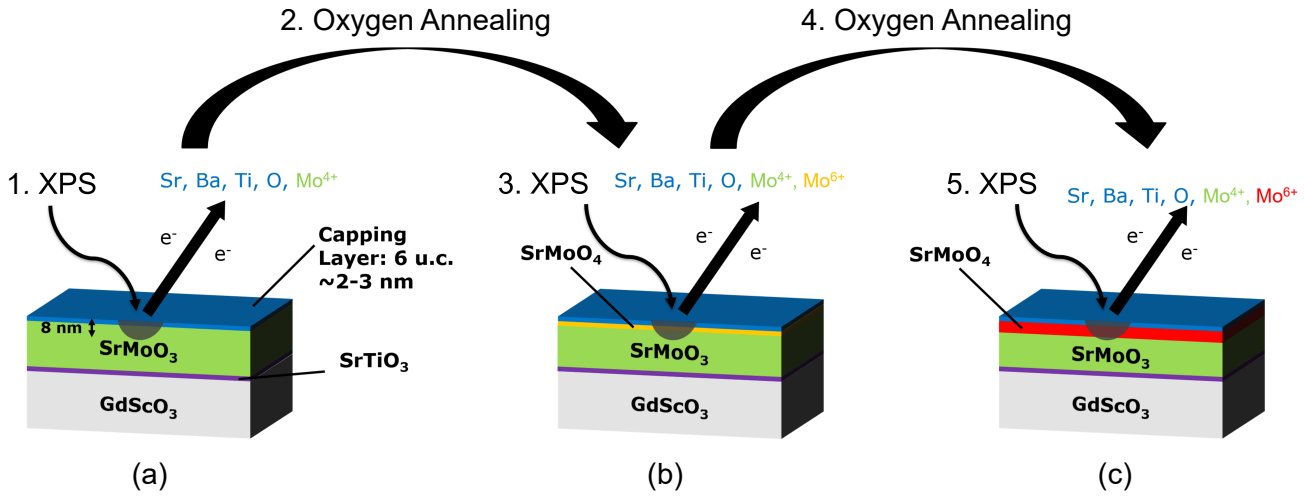

Figure 4.29: Annealing procedure used to evaluate oxygen diffusion through different capping layers. All transferring was done *in situ*. (a) All as-grown samples were mounted on one holder and measured in the XPS. After successive annealing steps, the samples were measured again in the XPS and increasing contribution of Mo^{6+} due to a thicker oxidized $SrMoO_4$ layer can be observed during measurements (b) and (c).

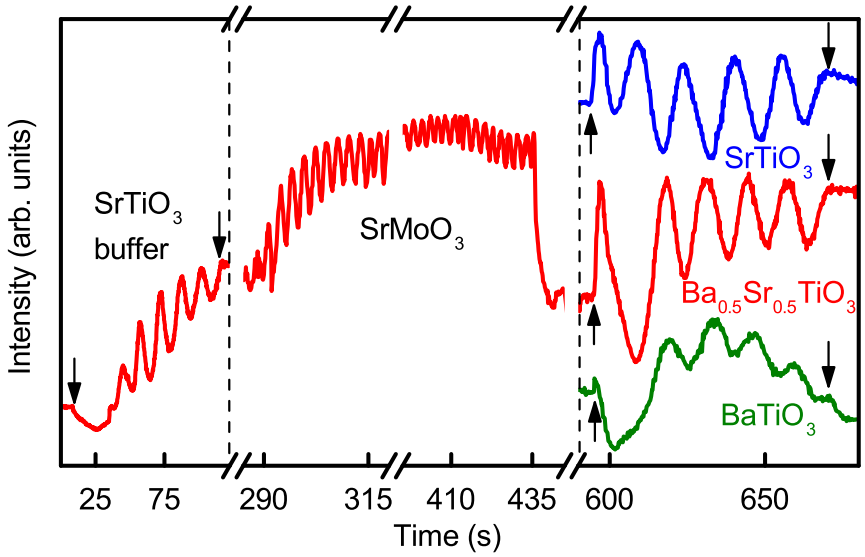

Figure 4.30: Time variations of the RHEED specular spot intensity during the growth of the heterostructures for a 6 – 8 unit-cells-thick $SrTiO_3$ buffer layer (left side), the $SrMoO_3$ film (middle), and the $SrTiO_3$, $Ba_{0.5}Sr_{0.5}TiO_3$, or $BaTiO_3$ capping layers (right side). The intensity variations for the $SrTiO_3$ buffer layer and the $SrMoO_3$ film are shown for the sample capped with $Ba_{0.5}Sr_{0.5}TiO_3$. Dashed lines indicate interfaces between different layers of the heterostructures. The arrows denote the start and stop moments for the depositions of the $SrTiO_3$ buffer layers and the capping films. The RHEED intensity oscillations are observed throughout the growth of the complete $SrMoO_3$ film thickness and are shown only at the beginning and directly before the end of the $SrMoO_3$ deposition.

The time dependence of the RHEED specular spot intensity recorded during the growth of the heterostructures is shown in Figure 4.30. The growth oscillations are clearly visible for all layers indicating their high quality layer-by-layer growth and make a precise deposition with a thickness control in the unit cell scale possible.

The XRD out-of-plane 2θ–θ scan of the as-grown sample before annealing shows c-axis orientation of the heterostructure similar to previously reported results [12, 142]. High crystal quality for all as-grown samples is indicated by the pronounced and distinct Laue oscillations assigned to the $SrMoO_3$ layer (see Figure 4.31 (a)). The period of the oscillations yields 33 ± 2 nm $SrMoO_3$ film thickness, which is independently confirmed by the RHEED, XRD, and X-ray reflectivity (XRR) data (see Figure 4.30 and inset in Figure 4.31 (a), respectively). The surface roughness of the capping layers (R_s) and the roughness of their interface with $SrMoO_3$ (R_{int}), extracted from the fitting of the XRR curves, are given in Table 4.6. The values of both R_s and R_{int} for the samples with $SrTiO_3$ and $Ba_{0.5}Sr_{0.5}TiO_3$ capping layers are smaller than those for the $BaTiO_3$-capped sample (see Table 4.6). The XRD pattern of the $BaTiO_3$-capped sample shows an asymmetric 002 $SrMoO_3$ peak shape with a higher intensity shifted towards the lower 2θ angles. One reason for this is the larger out-of-plane lattice parameter of $BaTiO_3$ as compared to $SrMoO_3$. For the sample capped with $SrTiO_3$, a small out-of-plane lattice parameter of the $SrTiO_3$ capping layer results in the asymmetrical high intensity of the XRD pattern at higher 2θ angles.

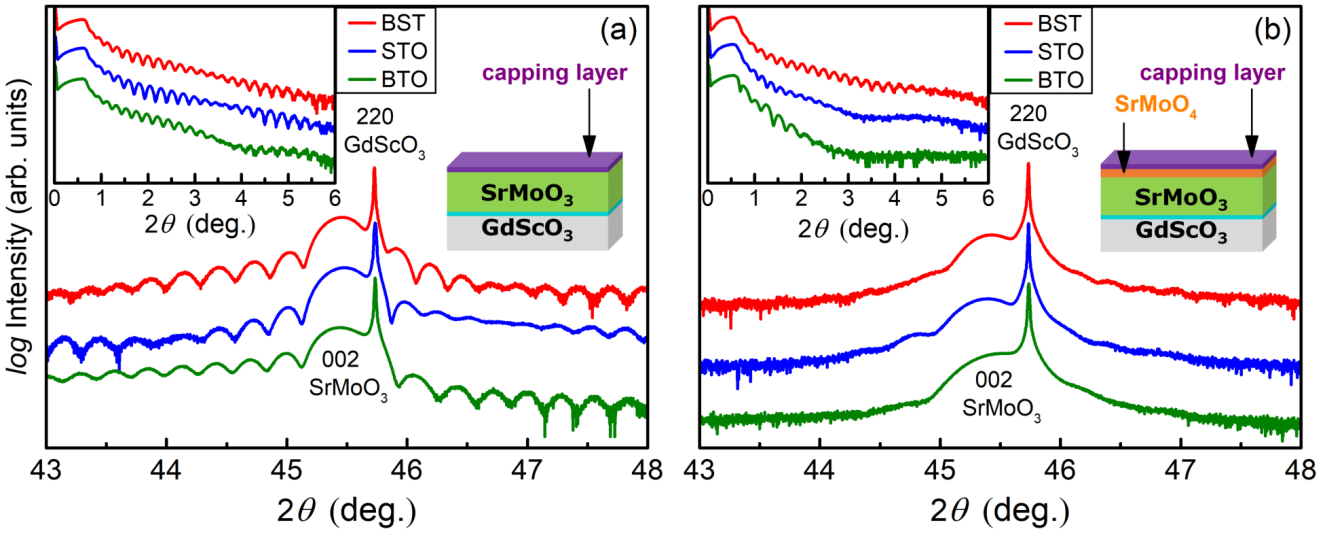

Figure 4.31: $2\theta-\theta$ XRD patterns around the 002 reflections of $SrMoO_3$ for the (a) as-grown heterostructures (b) after their annealing in oxygen for 2 minutes at 630 °C and 10 mTorr. Left insets show X-ray reflectivity curves for the heterostructures which are schematically depicted in the corresponding right insets. Surface oxidation of the annealed $SrMoO_3$ films is highlighted in orange.

After the annealing of the samples for 2 minutes at 630 °C in oxygen atmosphere at 10 mTorr, a significant difference between the samples arises. The 2θ–θ scan in Figure 4.31 (b) shows a spread in their crystal quality. The $SrTiO_3$- and $Ba_{0.5}Sr_{0.5}TiO_3$-capped samples still maintain low intensity Laue oscillations and a high $SrMoO_3$ peak intensity after the annealing step. However, the observed $SrMoO_3$ peak of the $BaTiO_3$-capped sample has low intensity and shows no Laue oscillations, indicating degraded $SrMoO_3$ crystal structure as a result of its oxidation during the annealing. Moreover, for all samples, a significant roughening can be observed due to a surface oxidation of $SrMoO_3$ to $SrMoO_4$, resulting in a bad interface. This is confirmed by the XRR fitting, which yields the best matching with a 3–5 nm thick $SrMoO_4$ surface layer (see right inset in Figure 4.31 (b)). After the first annealing step, both R_{int} and R_s are increased up to 0.7 – 0.9 nm for the $SrTiO_3$- and $Ba_{0.5}Sr_{0.5}TiO_3$-capped samples and even further up to 1.4 nm for the $BaTiO_3$-capped sample. Note that the roughness values for the $SrTiO_3$-capped sample increase more than those for the $Ba_{0.5}Sr_{0.5}TiO_3$-capped one.

Table 4.6: Surface roughness of the capping layers (R_s) and the roughness of their interface with $SrMoO_3$ (R_{int}) for the as-grown and annealed heterostructures with different capping layer materials.

	$SrTiO_3$	$Ba_{0.5}Sr_{0.5}TiO_3$	$BaTiO_3$
as-grown R_s	0.5 nm	0.5 nm	0.6 nm
as-grown R_{int}	0.2 nm	0.2 nm	0.4 nm
annealed R_s	0.9 nm	0.7 nm	1.4 nm
annealed R_{int}	0.9 nm	0.8 nm	1.4 nm

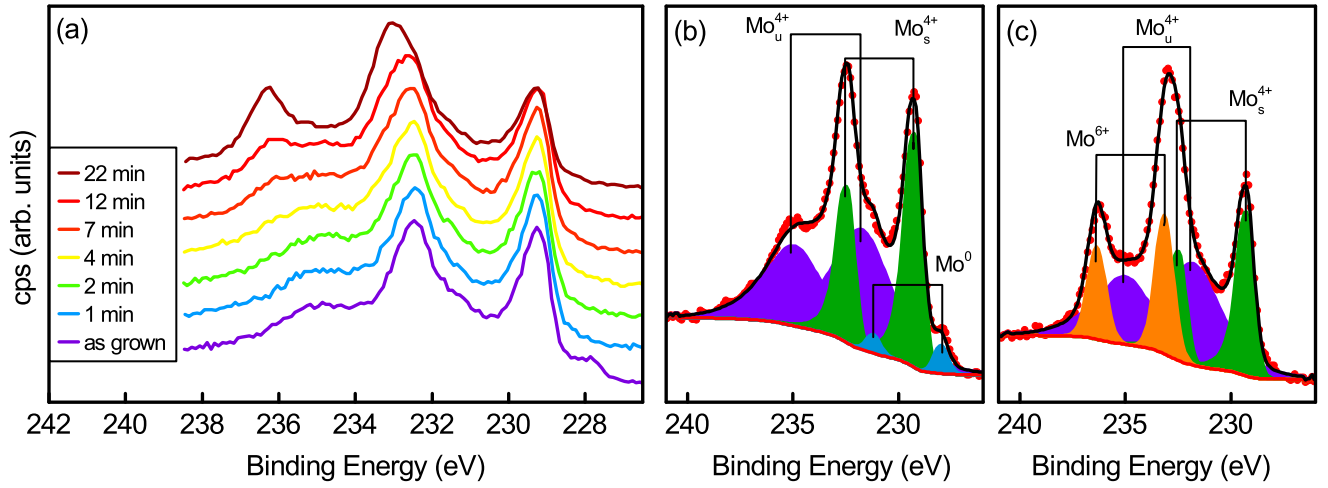

Figure 4.32: (a) Mo 3*d* spectra of a $SrMoO_3$ sample capped with 6 unit cells $Ba_{0.5}Sr_{0.5}TiO_3$ for different annealing times at 630 °C with 1 mTorr background pressure and 1 sccm flow of oxygen. Fitting of the Mo 3*d* spectra for (b) non-oxidized and (c) oxidized heterostructures using a combination of the peaks for metallic Mo^0, fully oxidized Mo^{6+}, and screened (subscript "s") and unscreened (subscript "u") Mo^{4+} [142,145].

The Mo 3*d* spectra recorded after each annealing step are shown in Figure 4.32 (a) for the heterostructure with the $Ba_{0.5}Sr_{0.5}TiO_3$ capping layer. Screening effects in conducting transition metal oxides lead to a splitting of the core peaks of the transition metals and an occurrence of so-called screened satellite sharp peaks at low binding energies, whereas the unscreened peaks at high binding energies appear broadened [145]. For this reason, the observed Mo 3*d* spectra of the heterostructures were fitted with a superposition of two sharp peak doublets related to Mo^{6+} ($3d_{5/2} = 233.0$ eV and $3d_{3/2} = 236.2$ eV) and the screened peaks of Mo^{4+} ($3d_{5/2} = 229.3$ eV and $3d_{3/2} = 232.5$ eV), as well as a broad doublet of the unscreened peaks of Mo^{4+} ($3d_{5/2} = 231.8$ eV and $3d_{3/2} = 235.0$ eV) in agreement with Ref. [142, 145] (see Figure 4.32 (b) and (c)). In addition, the as-grown samples exhibit a metallic Mo^0 contribution at 227.9 eV [59]. For all the doublets, the spin-orbit splitting between the peaks of $\Delta E = 3.2$ eV is nearly identical.

The extracted amount of Mo^{4+} for the heterostructures with different capping materials, normalized by the sum of Mo^{4+} and Mo^{6+}, is shown in Figure 4.33. The Mo^0 component of 3.0 % is present only in the as-grown samples and vanishes after the first annealing step. For this reason, this component is not included in the quantitative analysis. The amount of Mo^{4+} in the as-grown samples shown in Figure 4.33 is 99.5 %. The first two annealing steps lead to only minor formation of Mo^{6+}. After the third annealing step (total annealing time of 4 minutes), the Mo^{4+} percentage in the $BaTiO_3$-capped sample decreases drastically to 78 %, whereas in the other two samples, it remains at approximately 95 %. Aside from the steep initial oxidation of the $BaTiO_3$-capped sample, all the samples exhibit almost linear oxidation with time. After the 6th annealing step (22 minutes), $Ba_{0.5}Sr_{0.5}TiO_3$ emerges as the material with the highest oxygen diffusion barrier of the three titanates, still having 75 % of Mo^{4+}.

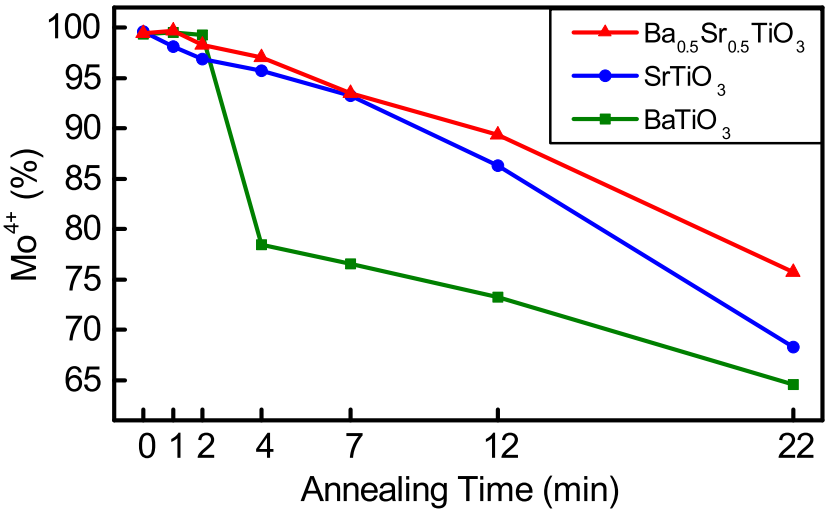

Figure 4.33: The relative intensity of the Mo^{4+} 3*d* emission in $SrMoO_3$ capped with $SrTiO_3$, $Ba_{0.5}Sr_{0.5}TiO_3$, and $BaTiO_3$, depending on the annealing time. The annealing was performed at 630 °C in oxygen atmosphere at 1 mTorr and 1 sccm. The intensity is normalized by the total intensity from the Mo^{4+} and Mo^{6+} components. A small contribution from Mo^0 for the as-grown heterostructures is neglected.

The extracted amount of Mo^{4+} for the heterostructures with different capping materials, normalized by the sum of Mo^{4+} and Mo^{6+}, is shown in Figure 4.33. The Mo^0 component of 3.0 % is present only in the as-grown samples and vanishes after the first annealing step. For this reason, this component is not included in the quantitative analysis and the amount of Mo^{4+} in the as-grown samples shown in Figure 4.33 is 99.5 %. The first two annealing steps lead to only minor formation of Mo^{6+}. After the third annealing step (total annealing time of 4 minutes), the Mo^{4+} percentage in the $BaTiO_3$-capped sample decreases drastically to 78 %, whereas in the other two samples, it remains at approximately 95 %. Aside from the steep initial oxidation of the $BaTiO_3$-capped sample, all the samples exhibit almost linear oxidation with time. After the 6th annealing step (22 minutes), $Ba_{0.5}Sr_{0.5}TiO_3$ emerges as the material with the highest oxygen diffusion barrier of the three titanates, still having 75 % of Mo^{4+}.

In general, oxygen diffusion in perovskite oxide materials depends on the stability of the oxidation state of the *B*-site cation. It has been previously shown, that transition metals with low electronegativity form stable ionic bonds with oxygen. Titanium, with an electronegativity of 1.54, is considered a good candidate for high oxygen barrier perovskite materials [139–141]. As titanium is present at the *B*-sites of all three chosen capping materials, it is not surprising that they have similar bulk oxygen diffusion coefficients [65, 66]. Thus, the observed differences in oxygen diffusion in these materials are likely related to their crystal- and microstructure.

The results of the initial theoretical calculations suggested that in-plane compressive strain of $SrTiO_3$ films up to 6 % should significantly suppress the inter-plane oxygen diffusion, whereas in-plane tensile strain should increase the oxygen diffusion in all crystallographic directions [67, 68]. For $SrTiO_3$ films compressively strained by 2 %, this theory predicts an increase in the inter-plane oxygen diffusion barrier

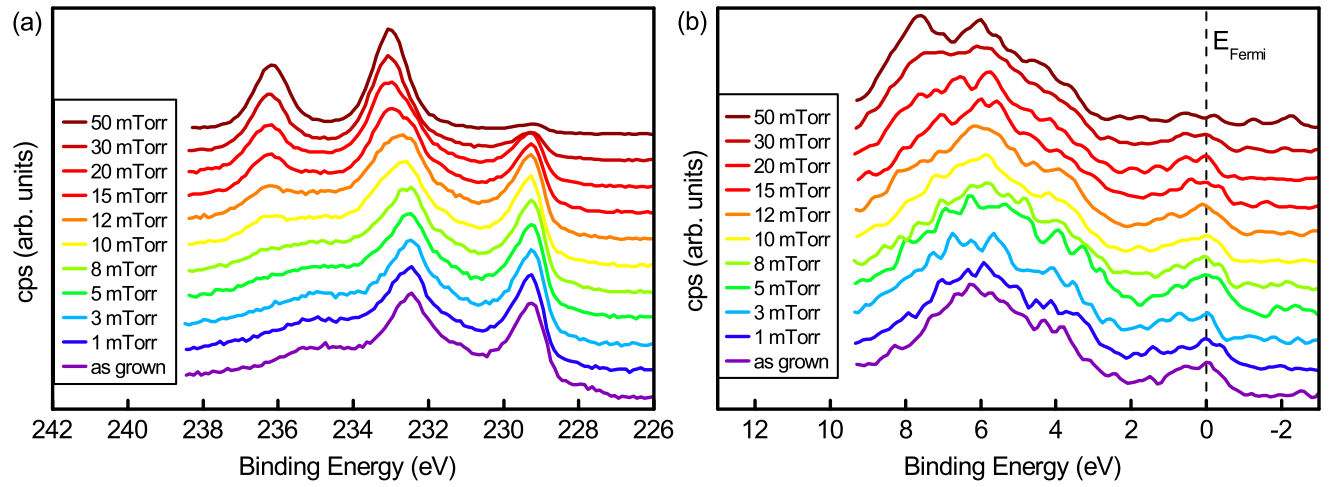

Figure 4.34: XPS spectra for the $SrMoO_3$ sample capped with 6 unit cells of $Ba_{0.5}Sr_{0.5}TiO_3$ during the pressure study (a) Mo 3*d* spectra. The contribution of the 4+ valence state decreases with an increase in oxygen pressure. The green dashed line shows the position of the Mo^{4+} $3d_{5/2}$ and Mo^{4+} $3d_{3/2}$ peaks and the black dashed lines show the positions of the Mo^{6+} $3d_{5/2}$ and Mo^{6+} $3d_{3/2}$, (b) Spectra of the valence state. The density of states at the Fermi level (represented by the dashed line) decreases with a higher background pressure and indicate the transition from conducting $SrMoO_3$ to insulating $SrMoO_4$.

by 35–50 % [68]. However, theoretical calculations assume perfect microstructure and do not consider defects or change in microstructure due to strain.

The observed faster oxidation of the $SrMoO_3$ film capped with $BaTiO_3$ (see Figure 4.33) indicates faster diffusion of oxygen ions in the compressively strained $BaTiO_3$ film as compared to the other investigated titanites, which does not comply with the aforementioned theoretical predictions [76]. This result can be qualitatively explained, in that the as-grown $BaTiO_3$-capped sample before the annealing was rough as compared to the other investigated samples (see Table 4.6). The rough microstructure leads to the formation of multiple grain boundaries which serve as channels for the diffusion of oxygen ions. For the other two samples capped with $SrTiO_3$ and $Ba_{0.5}Sr_{0.5}TiO_3$, similar $SrMoO_3$ oxidation rates are observed for the initial annealing steps approximately up to the total annealing time of 7 min (Figure 4.33). This observation is in line with the similar roughness values measured for these two samples (see Table 4.6). However, the larger strain value for the $SrTiO_3$ film, as compared to the $Ba_{0.5}Sr_{0.5}TiO_3$, probably leads to the faster accumulation of defects and faster degradation of the microstructure. As a result, for an annealing time longer than 7 min, the oxidation of the $SrMoO_3$ film proceeds more quickly for the $SrTiO_3$-capped sample. For these reasons, the $Ba_{0.5}Sr_{0.5}TiO_3$ film is the most effective capping among the investigated materials.

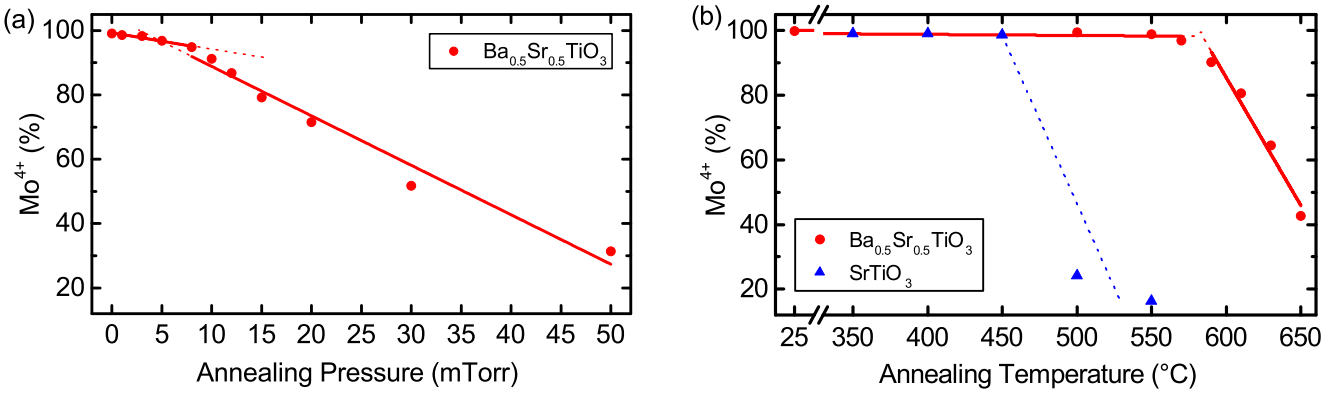

Figure 4.35: (a) The relative intensity of the Mo^{4+} 3*d* emission in $SrMoO_3$ capped with $Ba_{0.5}Sr_{0.5}TiO_3$ over the different annealing steps with increasing background pressure at an annealing temperature of 630 °C for 2 minutes. The annealing process can be divided into a low and high pressure regime. For both, a linear fitting was done and the dashed lines are an extension as a visual guidance.
(b) The relative intensity of the Mo^{4+} 3*d* emission in $SrMoO_3$ capped with $Ba_{0.5}Sr_{0.5}TiO_3$ over the different annealing steps with increasing temperature and a constant annealing pressure and time. In case of $Ba_{0.5}Sr_{0.5}TiO_3$, the pressure was 10 mTorr and annealing time 2 minutes. The annealing process can be divided into a low and high temperature regime. For both a linear fitting was done and the dashed lines are an extension as a visual guidance. In addition, values for $SrTiO_3$ are shown, but for pressures of 100 mTorr and annealing times of 5 minutes. The threshold manifests at lower temperatures of 450 °C and the dashed line a visual guidance. However, the overall temperature dependence is similar for both materials.

$Ba_{0.5}Sr_{0.5}TiO_3$ capping was chosen for further experiments to determine the quantitative limits of oxygen diffusion in the heterostructures. The effect of oxygen pressure was investigated using a sample with 6 unit cells of $Ba_{0.5}Sr_{0.5}TiO_3$ capping. The sample was consecutively annealed in steps of 2 minutes each at 630 °C. For each consecutive step, the oxygen background pressure was increased from 1 mTorr up to 50 mTorr. Valence band and Mo 3*d* emissions were measured after each annealing step. The Mo^{6+} $3d_{3/2}$ peak at 236.2 eV appears at pressures above 10 mTorr, indicating the start of the $SrMoO_3$ oxidation (Figure 4.34 (a)). The intensity of this peak increases with pressure. Moreover, the screened Mo^{4+} $3d_{3/2}$ peak at 232.5 eV peak broadens with annealing and its intensity shifts towards the Mo^{6+} $3d_{5/2}$ peak at 233.0 eV. Meanwhile, the Mo^0 contribution has already vanished after the first annealing.
The valence band spectrum of the as-grown sample shows states at the Fermi level due to the $4d^2$ (t_{2g}) electronic configuration of $SrMoO_3$ (Figure 4.34 (b)). The spectral intensity at the Fermi level decreases at high annealing pressures and vanishes completely above 30 mTorr, confirming the formation of insulating $SrMoO_4$.

The normalized amount of Mo^{4+} derived from the fitting of the XPS spectra can be seen in Figure 4.35 (a). Up to 8 mTorr, the $SrMoO_3$ oxidation is a slow linear function of pressure, resulting in a decrease of the number of Mo^{4+} cations by 0.5 % per mTorr. Above 8 mTorr, the linear oxidation with pressure is preserved, however, with significantly higher rate of 1.5 % per mTorr. Thus, up to an oxygen pressure of 8 mTorr

at 630 °C, $Ba_{0.5}Sr_{0.5}TiO_3$ capping serves as an efficient oxygen barrier. Above this pressure, the $SrMoO_3$ deteriorates and an insulating $SrMoO_4$ layer is formed.
Because oxygen diffusion is a function of both pressure and temperature, the impact of temperature on the oxygen diffusion through the $Ba_{0.5}Sr_{0.5}TiO_3$ was investigated. For this purpose, a similar heterostructure comprised of an $SrMoO_3$ film capped with 6 unit cells of $Ba_{0.5}Sr_{0.5}TiO_3$ was annealed in steps of 2 minutes at the annealing temperatures, increasing from 500 up to 650 °C. During the annealing, the oxygen pressure and flow were kept at 10 mTorr and 4 sccm, respectively. Photoelectron spectra were measured after each annealing step. The amount of the Mo^{4+} as a function of the annealing temperature is shown in Figure 4.35 (b). The $SrMoO_3$ oxidation exhibits different rates below and above 580 °C. Only minor oxidation occurs below 580 °C, with approximately 97 % Mo^{4+} cations still present. Above 590 °C, the oxidation rate is vastly increased up to 0.8 % per Kelvin. Thus, the growth parameter window for the heterostructure with $Ba_{0.5}Sr_{0.5}TiO_3$ capping layer extends up to 580 °C at 10 mTorr of oxygen.
Figure 4.35 (b) shows the data for an $SrMoO_3$ sample capped with 10 unit cells of $SrTiO_3$, which was consecutively annealed for 5 minutes at 100 mTorr. The behavior in this case is very similar with almost no oxidation below 450 °C and after the annealing step at 500 °C, a drastic oxidation to 25 % Mo^{4+} occurs.
In general, oxygen diffusion in heterostructures is affected by three important factors. Firstly, the chemical potential, which is due to the oxygen concentration gradient between the sample and the surrounding gas phase. Secondly, the activation energy necessary to fill the oxygen vacancies in the capping layer. The concentration gradient is pressure dependent, whereas the activation is temperature dependent. These two factors determine the oxygen diffusion in the as-grown heterostructures with sharp and smooth interfaces. The initial weak oxidation of $SrMoO_3$ with pressure and temperature, observed in Figure 4.35, might be explained by the oxygen deficiency of the capping layers, which were grown in vacuum [69, 77]. These oxygen vacancies are gradually filled until the oxidation of the capping layer is complete. This process is determined by a combination of oxygen pressure, temperature, and annealing time. Once the capping layer is fully oxidized, the oxygen diffuses further towards the interface, causing $Mo^{4+} \rightarrow Mo^{6+}$ oxidation. As a result, a $SrMoO_4$ with a scheelite structure forms at the interface and leads to the degradation of the capping layers, which, in turn, accelerates further oxidation of the underneath $SrMoO_3$. The third important factor is related to the microstructure of thin films, which differs for samples with different capping materials. Among the as-grown samples, the heterostructures with $SrTiO_3$ and $Ba_{0.5}Sr_{0.5}TiO_3$ reveal the smaller R_s and R_{int} roughness as compared to the $BaTiO_3$-capped sample. This fact naturally explains the rapid oxygen diffusion through the compressively strained $BaTiO_3$ capping layer in contrast to theoretical predictions [76].

4.3.1 Effect of the vacuum deposition on stoichiometry

The capping layers on SMO described above are deposited in vacuum. It is well known from literature, that depositions in vacuum lead to oxygen deficiency [69, 77]. In order to confirm this hypothesis, XPS was measured on capping layers different deposited in vacuum and the stoichiometry was determined from the resulting XPS spectra. For reference, a STO substrate was also measured. The chemical formula

were determined by adding the element areas from the XPS spectra of each element, which were corrected by corresponding relative sensitivity factor and normalizing it to five according to the perovskite formula ABO_3. The subscripts of the elements determine the ratio of each element to the normalized entire area. For the fitting of the titanium spectra, the satellite peaks at 471.8 eV and 476.7 eV have been taken into account (see Figure 4.36). These satellites are related to plasmon excitations of the photoelectrons while leaving the sample. Thus, they are related to a higher binding energy, since they lost kinetic energy during the excitation.

Table 4.7: Stoichiometries of different capping layer deposited in vacuum determined by XPS.

Sample	Transfer	Stoichiometry
$SrTiO_3$ substrate	ex situ	$Sr_{1.02}Ti_{1.05}O_{2.93}$
$SrTiO_3$ capping layer	ex situ	$Sr_{1.24}Ti_{0.98}O_{2.78}$
$Ba_{0.5}Sr_{0.5}TiO_3$ capping layer	in situ	$Ba_{0.65}Sr_{0.70}Ti_{0.93}O_{2.72}$

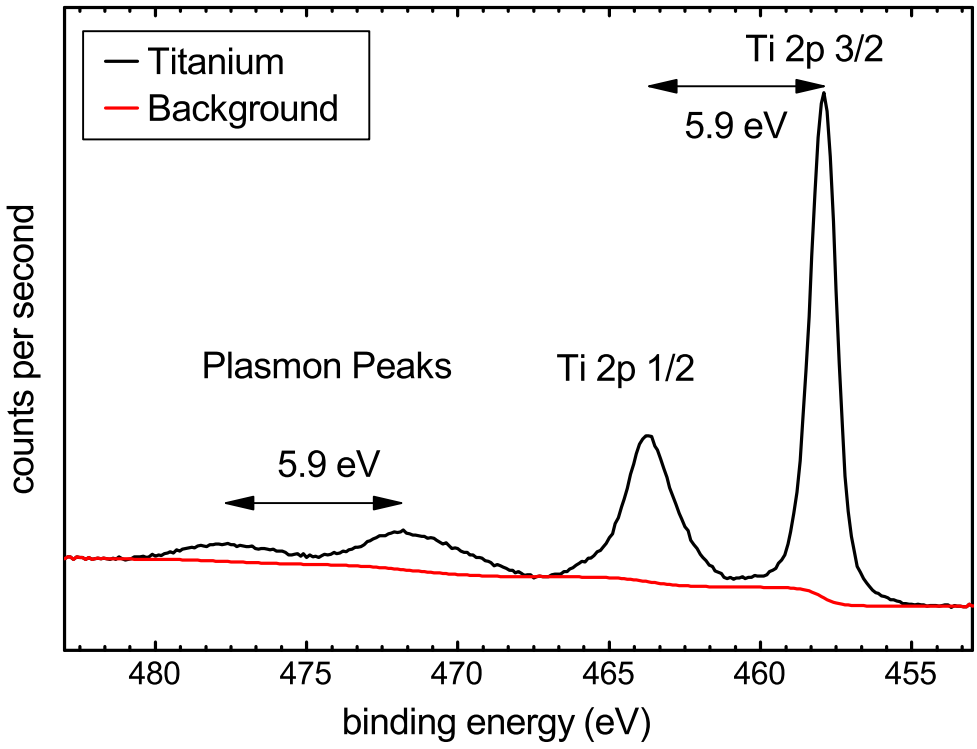

Figure 4.36: XPS spectrum of titanium measured on a STO substrate.

As it can be seen in Table 4.7, this approach leads to matching chemical formula for the STO substrate. The STO capping layer is a 20 nm film on SMO and was measured *ex situ* by XPS. A $Ba_{0.5}Sr_{0.5}TiO_3$ layer was deposited directly on GSO and measured by XPS with *in situ* sample transferring. The resulting stoichiometries reveal an excess in A-site cations for both thin-films deposited in vacuum and, thus, also

oxygen deficiency due to charge neutrality. This coincides with reports from literature. The oxygen deficiency of this interlayer possibly acts as an additional trap for oxygen further preventing SMO oxidation.

4.4 BST composition

During this work, only barium-strontium-titanate with the composition $Ba_{0.5}Sr_{0.5}TiO_3$ was used. As it can be seen in Figure 2.7 (section 2.4.1), this composition is in the paraelectric phase at room temperature. For thin films, this transition can be different due to strain. It is very important to maintain the paraelectric phase in the varactor heterostructure, in order to avoid hysteresis behavior during tuning of the device. For the $Ba_{0.5}Sr_{0.5}TiO_3$ composition, in some samples, small hysteresis behavior could be seen, which might be attributed to local polar regions. Further tuning the composition towards a higher barium content might increase the overall permittivity and, thus, tunability, but comes with the risk of ferroelectric behavior. This requires very fine stoichiometry control of the BST composition but is a possibility for future performance increase.

The correct oxygen stoichiometry and avoidance of oxygen vacancies is also important for the all-oxide varactor performance. Oxygen vacancies are responsible for the bulk conduction mechanism in the dielectric and drastically increase the leakage current of the varactors. A full oxygenation of the dielectric is difficult, since a high oxygen background pressure during BST growth oxidizes the bottom electrode of the heterostructure. However, with the finding of a new oxygen diffusion barrier material, the oxygen background pressure during the BST deposition could be increased.
The oxygen background pressure during BST growth could be optimized to 35 mTorr by lowering the BST growth temperature to 470 °C, which was done by Zeinar *et al.* [131]. This was achieved by mapping the growth temperature and oxygen partial pressure and growing a large set of samples to determine the transition, where the oxygen diffusion barrier can not protect the SMO, thus, $SrMoO_3 \rightarrow SrMoO_4$ oxidation occurs. This oxidation can be observed in situ by a surface roughening. In addition, the leakage current of all samples were compared to verify an improved oxygenation of the dielectric. With these optimized growth parameters, a decrease in leakage current of several orders of magnitude could be achieved.

4.5 Top contacts: Surface mount device

The circular test structure, introduced in section 2.7.1 (Figure 2.16), has been used to characterize all samples shown in this thesis. It also allows to extract the relevant properties of the dielectric layer and bottom electrode.
The future goal is to dice the substrates with the all-oxide heterostructure and patterned top electrodes into individual varactors and mount them onto a circuit board to prove the functionality in a real device. Mounting on a circuit has to be done with low-inductance connections, e.g. with flip-chip bonding, since

wire bonding is not suited for high frequency operation due to high inductances. However, the circular structure does not allow mounting the individual varactors on a circuit via low-inductance flip chip bonding. A novel design for an all-oxide surface mount device (SMD) has been proposed by Walk *et al.* [146]. The processing and a microscope picture can be seen in Figure 4.37. RF front ends in mobile communications deploy capacitance in the low pF regime. The capacitance are described by $C = \varepsilon_0 \varepsilon_r A/d$. Due to the high crystalline quality of the BST resulting in a high permittivity in addition to the very thin layer thickness, the electrode area needs to be small ($< 300\,\mu\text{m}^2$). Thus, separate contact areas are added on the device, which do not contribute to the capacitance. Their purpose is to provide enough surface area for flip-chip bonding. In-depth information for the processing procedure can be found in [146].
The final device can be seen in Figure 4.37 as a schematic in the upper row in step 4 and the real device in the bottom row. The effective area contributing to the capacitance is $200\,\mu\text{m}^2$ and the length/width of the contact pads for bonding are $150/100\,\mu$m. Walk *et al.* have shown the functionality of this design. In the future, integration in a network will prove its application benefits in a real-case scenario [146].

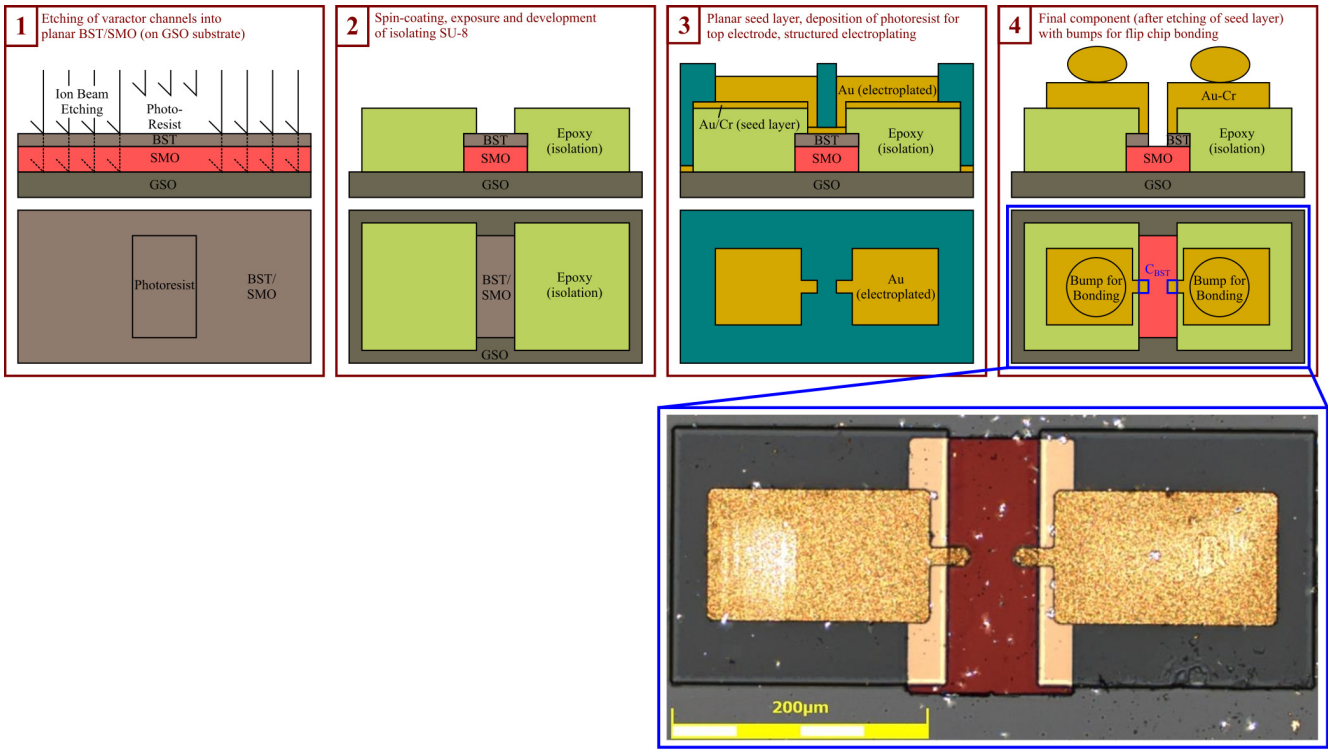

Figure 4.37: Upper Row: Processing steps of the all-oxide SMD component. Side view (top) and top view (bottom). Lower Row: Microscope picture of the SMD component [146].

4.6 Varactor Heterostructures

4.6.1 High performance all-oxide varactors

With the results of section 4.2, namely, an epitaxially grown, atomically sharp and micrometer-thick bottom electrode in combination with an oxygen diffusion capping layer and low leakage BST dielectric, the growth of high performance all-oxide varactors was enabled.
The bottom electrodes have been deposited on $GdScO_3$ substrates with a 2 nm STO buffer layer to ensure smooth layer-by-layer growth of the SMO [92, 93]. More than 300 000 laser pulses with conditions shown in Table 4.1 (see section 4.1.1) yielded a thickness of over 5 μm for the SMO bottom electrode. Figure 6.5 in the Appendix shows a picture of the SMO target after the deposition of the 5 μm thick SMO layer. Two samples will be discussed in this section, both with 5 μm bottom electrodes. One sample has a STO interlayer, to prevent SMO oxidation, and 50 nm dielectric BST layer and the other sample has a BST protective interlayer and 100 nm dielectric BST layer. Top electrodes were applied with a thin Pt and Au seed layer, followed by a thick ($> 4\mu$m) Au layer grown by electroplating. The structuring has been done utilizing photolithography and Ar-based ion-beam etching.

Both heterostructures have a highly coherent crystalline structure as shown by XRD analysis in Figure 4.38 (a) – (c). They exhibit Laue oscillations for BST in the $2\theta - \theta$ XRD scan near the SMO 002 reflex (see Figure 4.38 (a)). The peak position for SMO 002 differs slightly from $SMO_{100\,nm\,BST} = 45.416°$ to $SMO_{50\,nm\,BST} = 45.442°$ by $\Delta = 0.026°$. This corresponds to out-of-plane lattice constants of $SMO_{100\,nm\,BST} = 3.990\,Å$ and $SMO_{50\,nm\,BST} = 3.989\,Å$. BST 002 has a larger peak shift of 0.54° leading to lattice constants of $BST_{100\,nm} = 4.009\,Å$ and $BST_{50\,nm} = 3.968\,Å$. This can be explained by different growth conditions of the two BST layers. $BST_{50\,nm}$ was grown with a relatively low oxygen background pressure of 1.8 mTorr, whereas the $BST_{100\,nm}$ was grown with 15 mTorr. In spite of the difference in BST lattice constant, both films show similar microwave properties. However, the leakage current could be reduced significantly due to a better oxygenation of the dielectric layer, which will be discussed later.
The rocking curves at the 002 reflections of SMO and BST show low diffuse backgrounds and the full width at half maxima (FWHM) of 0.008° is remarkably only limited by the crystallinity of the substrate (see Figure 4.38 (b)) and could only be achieved by measuring with a Ge(220)x2 analyzer crystal at the detector side. Note that the rocking curves are plotted in the linear intensity scaling.
The SMO and BST layers are in-plane locked to the substrates throughout the full stack thickness of several micrometers for both samples as confirmed by the reciprocal space map (see Figure 4.38 (c) and (d)).

It is known that heterostructures with lattice mismatch acquire increasing strain energy with increasing thickness, leading to a strain relaxation by misfit dislocation formation. This occurs at a critical thickness, which is typically in the range of several tens to hundreds of nanometers for perovskites. The RSM in Figure 4.38, however, clearly shows the coherent growth beyond the critical thickness. The in-plane lattice constants are locked to the substrate, which leads to enlarged *c*-axis constant of $SMO_{100\,nm\,BST} = 3.990\,Å$ and $SMO_{50\,nm\,BST} = 3.989\,Å$. Based on this achievement, the functional BST layer can be grown also

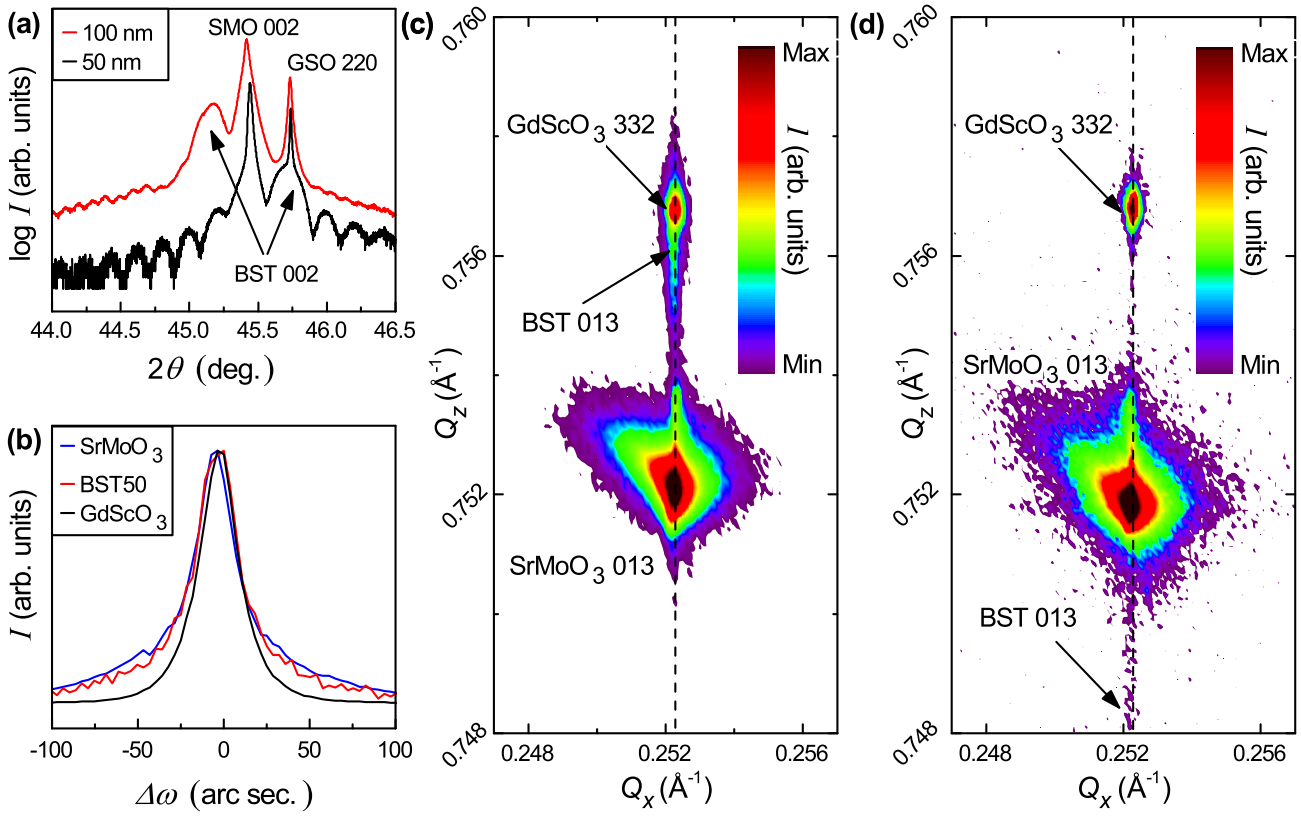

Figure 4.38: (a) $2\theta - \theta$ XRD scan near the SMO 002 reflex for both heterostructures with 50 nm (black) and 100 nm (red) thick BST layer. (b) XRD ω-scan of the following reflections from the heterostructure with 50 nm BST: SMO 002 (FWHM = 0.008°), BST 002 (FWHM = 0.008°), GSO 220 (FWHM = 0.008°) measured with Ge(220)x2 monochromators at source and detector side. (c) and (d) Reciprocal space map of the heterostructure with 50 nm and 100 nm BST, respectively.

in-plane locked with similar crystalline quality as if grown directly onto the substrate.
All layers grow layer-by-layer as indicated by the streaky RHEED patterns (see Figure 4.39 (a)) and intensity oscillations of the specular spot (see Figure 4.39 (b)). To maintain a constant fluence throughout the deposition of 5 μm of SMO, the laser energy has to be checked and adjusted during the deposition. For these particular depositions, 350 000 laser pulses were shot onto the target. The energy was checked after every 50 000 shots and readjusted. Reasons for a decrease in fluence are laser gas exhaustion and coating of the laser entrance windows into the chamber due to the huge amount of ablated material. The RHEED intensity recording was switched on before the restart of the deposition after each energy check. Figure 4.40 shows intensity recordings of the specular spot after the restart of 100 000 and 200 000 pulses respectively. In both cases intensity oscillations arise, proving a layer-by-layer growth.

High-resolution STEM images of the whole heterostructure (see Figure 4.39 (c)) reveal the exceptional high crystalline quality between substrate, STO buffer layer and lower end of the SMO electrode (see Figure 4.39 (d)), as well as the interface between the upper end of the SMO electrode and the subsequent

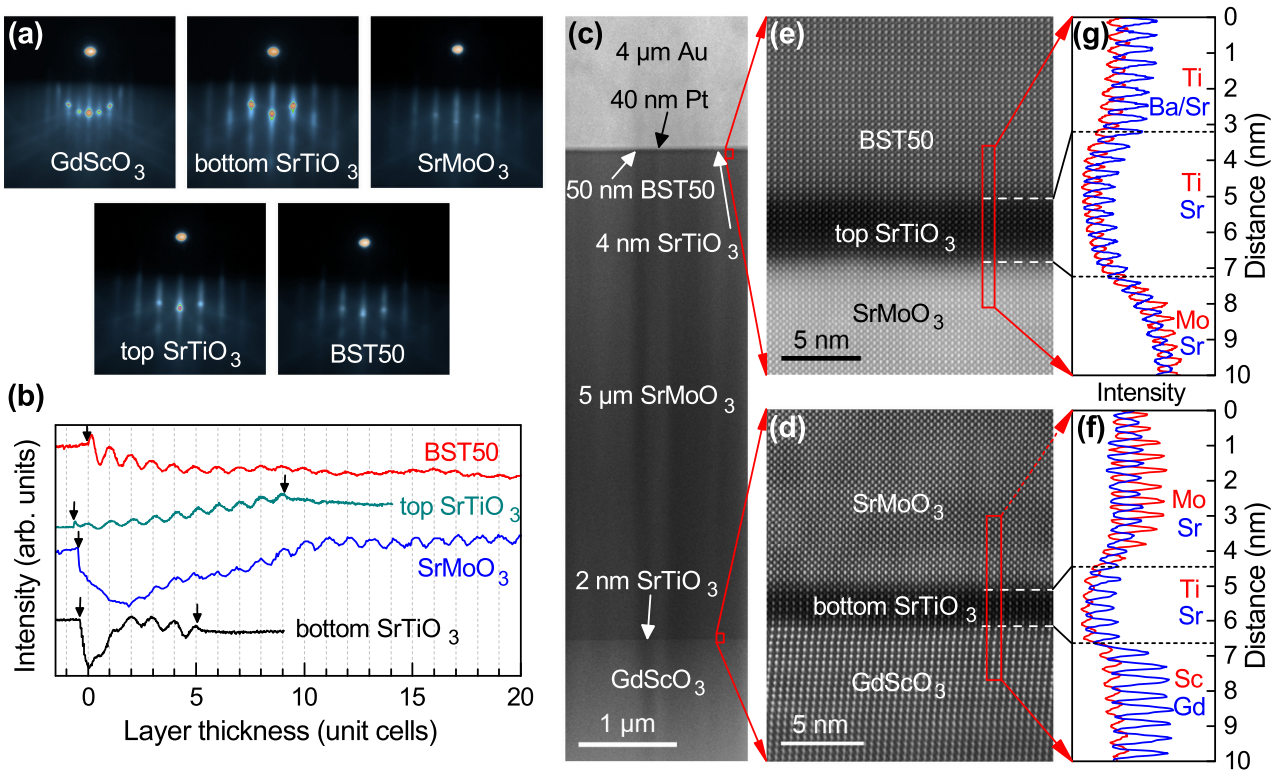

Figure 4.39: RHEED and TEM results for the heterostructure with 50 nm BST (a) RHEED patterns of the GSO substrate, STO buffer layer, SMO, STO capping, and BST layer (b) Intensity oscillations of the specular spot, recorded at the beginning of buffer STO (black), SMO (blue), STO capping (green), and BST layer (red). (c) Low-resolution HAADF-STEM image of the varactor heterostructure. (d) and (e) High-resolution HAADF-STEM image along with (f) and (g) elemental intensity lines of the SMO/STO/GSO and BST/STO/SMO interface, respectively.

STO/BST layer – with 5 μm SMO in between. This shows the close-to-perfect dislocation free atomic layering of the SMO over several micrometer.

As already discussed in section 4.2, the mechanism behind the high-thickness growth of perovskites with atomic control is the ability of perovskites to change their lattice constant as a function of cation ratio. This ratio can be tuned by deposition parameters during thin-film growth. During the PLD deposition, a growth rate of several tens of Hertz provides a constant material flux in the plasma plume, which leads to small, but stable cation off-stoichiometry throughout the electrode growth. This deviation from the ideal stoichiometry allows growing perfectly lattice matched, strain-free "single crystal" films. In order to consolidate this model, the stoichiometry of SMO thin films were determined by XPS measurements. The Sr 3*d*, Mo 3*d*, and O 1*s* core photoelectron spectra were measured for 20 regions of four different films (see Figure 4.41). The Mo 3*d* spectra (Figure 4.41 (b)) exhibits a Mo^{6+} contribution, visible at the appearance of the Mo $3d_{3/2}$ = 236.2 eV peak. This Mo^{6+} contribution occurs as the films were exposed to air prior to the XPS measurements, which indicates that the surface of SMO oxidizes to the scheelite structure $SrMoO_4$.

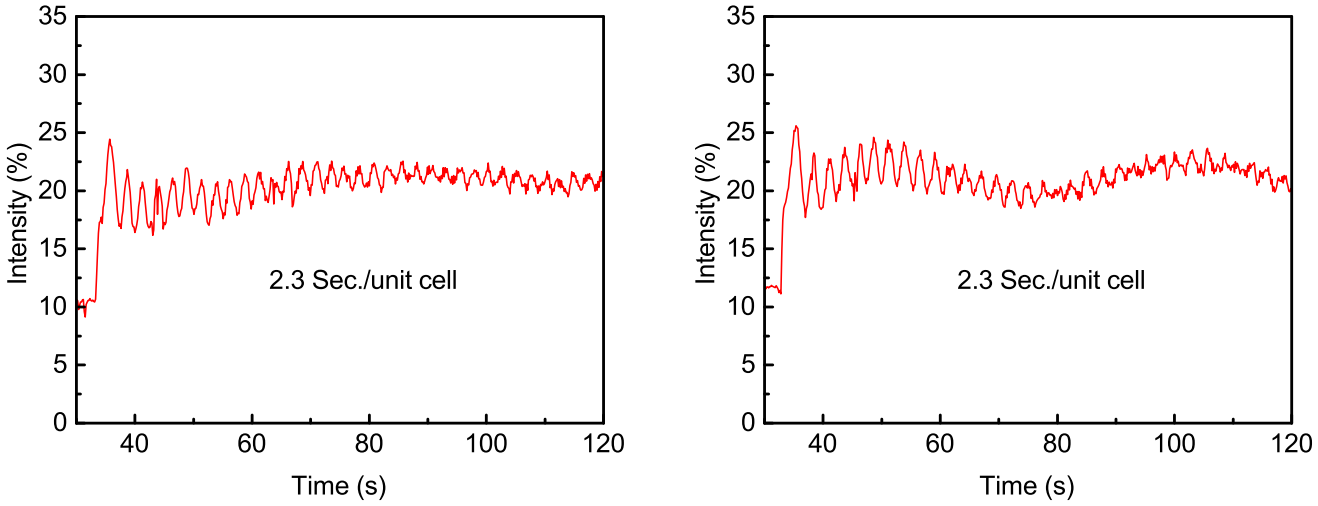

(a) 100 000 laser pulses (b) 200 000 laser pulses

Figure 4.40: RHEED intensity of the specular spot after the energy check of (a) 100 000 and (b) 200 000 laser pulses. After the restart, intensity oscillations arise.

Figure 4.41 (d)) shows the relative atomic concentrations of Sr and Mo in 20 studied regions. The stoichiometries were determined by fitting according to the descriptions in section 4.3. The mean atomic concentration of Sr (51.6 %) and Mo (48.4 %) with the threefold standard deviation of $3\sigma \approx 1.0$ indicate Sr excess in the SMO thin films. This off-stoichiometry is associated with antisite defects act also as additional scattering centers, reducing the conductivity of the SMO thin films as compared to the bulk values.

The thick bottom electrodes with a low resistivity lead to a very low sheet resistance in the varactors. In combination with atomically flat interfaces, proven in Figure 4.39, it is possible to fabricate high-performance varactors utilizing only 50 or 100 nm thick dielectric layers.
The microwave performance is shown in Figure 4.42. The effective relative permittivity $\varepsilon_{r,eff}$ (Figure 4.42 (a)) also including the capping layers at 1 GHz is 325 for the 50 nm BST (black) and 375 for 100 nm BST (red). This effective permittivity includes the non-tunable, low permittivity of the STO interlayer. Assuming a STO permittivity between 100 and 150 and applying a simple model of stacked dielectric capacitors leads to a relative BST permittivity for the 50 nm BST layer between 395 and 440. The resulting capacitance value for these varactors without bias field are around $C(0\,V)_{50\,nm\ BST} = 17\,pF$ and $C(0\,V)_{100\,nm\ BST} = 15\,pF$, both for pad sizes with 20 μm inner diameter. The thin functional layer allows the application field of low tuning voltages in the Li-ion battery regime of 3.7 V, which are not feasible with conventional Pt varactors. This voltage corresponds to a maximum electric field of 74 V/μm (0.74 MV/cm) and 37 V/μm (0.37 MV/cm) for a 50 nm BST and 100 nm BST respectively. At the frequency of 1 GHz, the varactor with 50 nm BST has a high tunability of $n(3.7\,V) = 3.1$, defined as $n(V_{r,eff}) = C(0)/C(V_{r,eff})$. The varactor with 100 nm BST reaches a tunability of $n(3.7\,V) = 2.1$ and for 7.4 V, which leads to the same applied field of 0.74 MV/cm $n(7.4\,V) = 3.3$. For over 100 tuning cycles of applying $\pm 100\,V/\mu m$, the varactor showed no

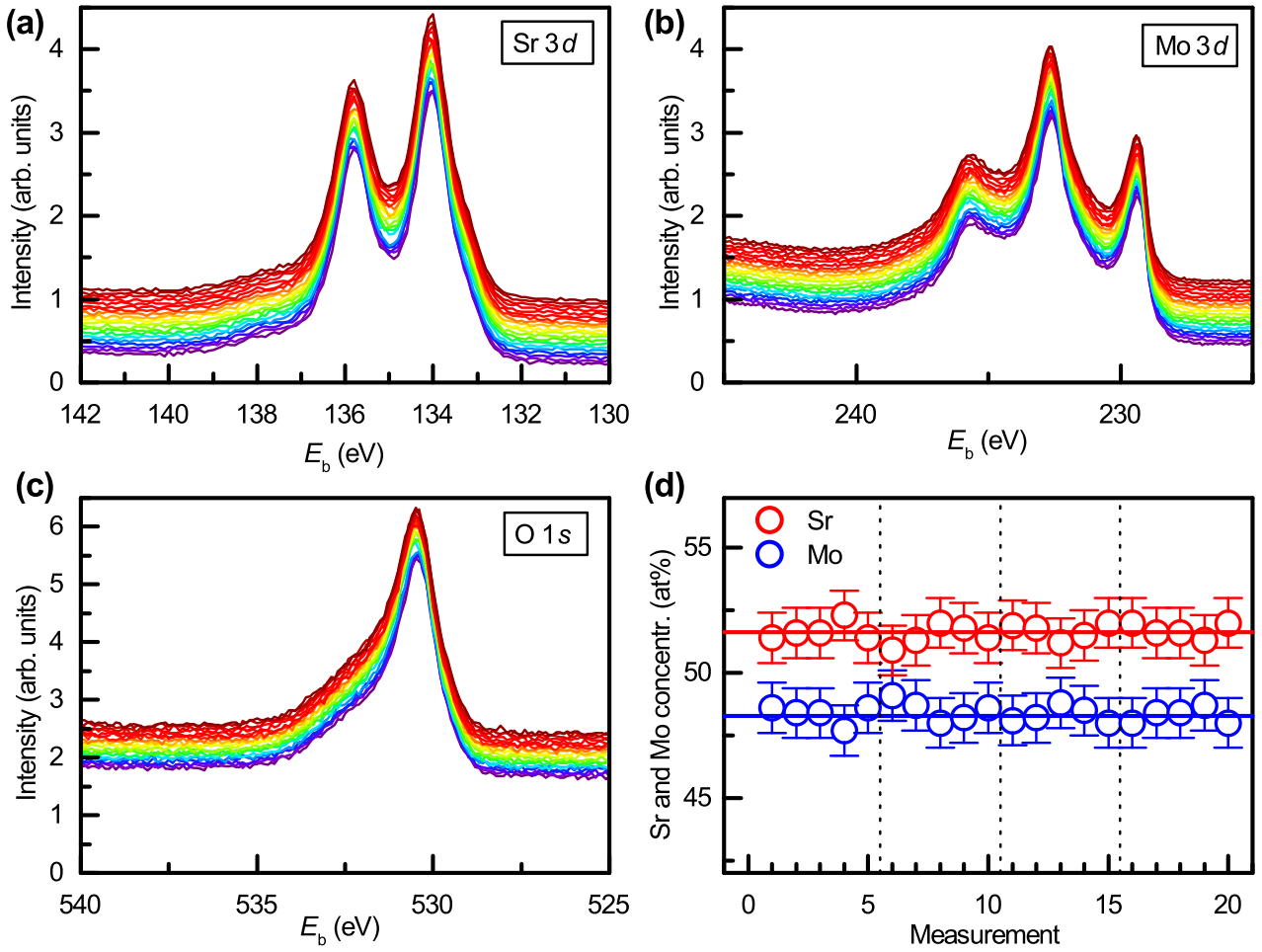

Figure 4.41: XPS spectra for the elements (a) Sr3d, (b) Mo3d, O1s, and (d) relative atomic concentration of Sr and Mo measured for 20 regions of 4 SMO thin films grown by PLD. The threefold standard deviation of $3\sigma \approx 1.0$ is shown for every measured region. Prior to the XPS measurements, the film were exposed to ambient atmosphere for 10 minutes.

signs of degradation and the performance is steady (see Figure 6.6 in the Appendix).

Figure 4.42 (b) displays the quality factors (Q) of the varactors measured up to frequencies of 3 GHz. The zero-bias Q-factors for both samples (50 and 100 nm BST) are quite similar, especially at the electrode dominated frequencies above 500 MHz where both curves are coinciding. The zero-bias values for the sample with 50 nm BST at 1 GHz (3 GHz) are 76 (41). For the sample with 100 nm BST, the zero-bias Q-factors at 1 GHz (3 GHz) are 72 (40). The behavior of the quality factor is dominated by the losses of the dielectric or electrodes, depending on the frequency. For frequencies above a few gigahertz, the quality factor is dominated by the electrode losses. At lower frequencies, it is determined by the losses of the dielectric [4, 97]. The varactor with 100 nm BST reaches a Q-factor of almost 150 at 50 MHz (see red line in Figure 4.42 (b)), showing the high crystallinity and low losses of the epitaxial BST. With applied bias of 4 V, the quality factor of the 50 nm BST varactor decreases below 300 MHz due to an increased leakage current caused by residual oxygen vacancies which occur due to the deposition at a low oxygen pressure

before the optimizations in section 4.4. The 100 nm BST was deposited under optimized growth conditions at a higher oxygen partial pressure, leading to a reduction in oxygen vacancies. This leads to a decrease in leakage current of over four orders of magnitude (Figure 4.42 (c)). The Q-factor of this sample under bias behaves as expected, increasing for low frequencies and reaching values of 200 at 50 MHz.

The performance of varactors are commonly evaluated by the commutation quality factor (CQF), which takes both tunability and losses into account (see equation (2.29) in section 2.7). The combination of excellent tunability at small bias voltage and high quality factor of all-oxide varactors lead to a CQF of 3700 (1200) at 1 GHz (3 GHz) for 3.7 V bias voltage (see Figure 4.42 (d)). The decrease in CQF for the 50 nm BST varactor is caused by the lowered Q(E) due to high leakage current caused by oxygen vacancies, which is not the case for the 100 nm BST varactor grown under the improved higher oxygen growth conditions. The threshold for RF applications suggested in literature [11, 90] of CQF > 2000 is fulfilled by all-oxide varactors up to 2.3 GHz. Although the CQF is often used to compare varactor performances, it originates for switches operating at two defined states with emphasis on the quality factor [147]. In order to take the low-voltage applicability in the performance comparison into account, the voltage performance factor (VPF) was defined [91]:

$$\mathrm{VPF}(V_\mathrm{b}, F) = \frac{n(V_\mathrm{b})}{V_\mathrm{b}} Q(0\,V, f), \tag{4.3}$$

where V_b are the applied tuning voltages. The VPF values of all-oxide varactors in comparison with available literature values are plotted in Figure 4.42 (e). The VPF representation shows clearly that all-oxide varactors stand out due to their unique capability of operation at low voltages and surpass other values in literature.

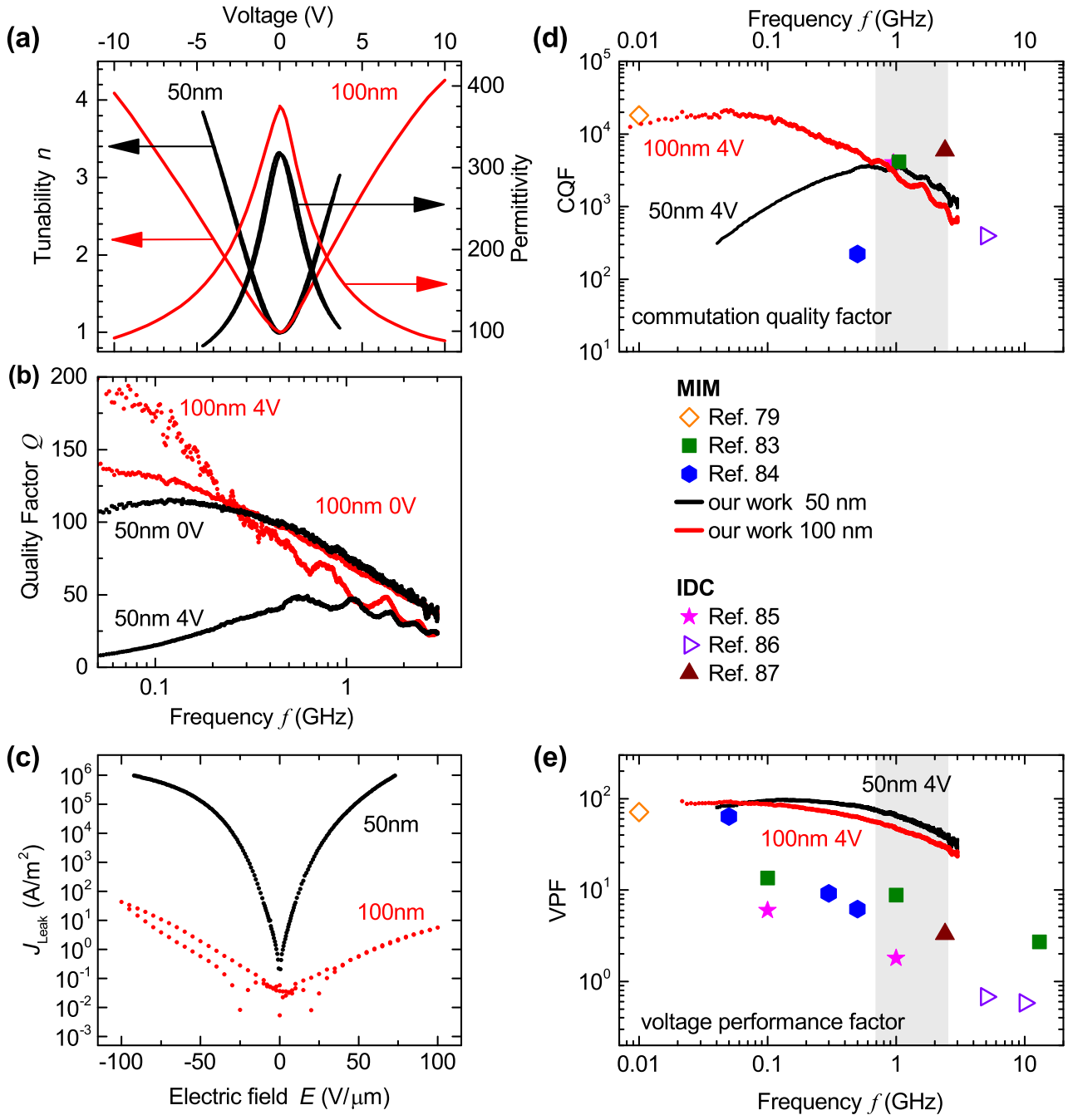

Figure 4.42: (a) Dependences of effective relative permittivity $\varepsilon_{r,eff}$ and tunability n from the applied bias voltage V, (b) frequency dependence of the Q-factor, and (c) leakage current as function of the applied electric field of the MIM varactor heterostructure with 50 nm (black) and 100 nm (red) thick BST layers. Comparison of (d) commutation quality factor (CQF) and (e) voltage performance factor (VPF) of the varactors to literature values of BST-based MIM varactors [79, 83, 84] and, for more completeness, tunable IDCs [85–87]. Note that IDCs intrinsically need considerably higher operation voltages as compared to MIM varactors.

Performance comparison with state-of-the-art commercial varactors

To classify the results of the previously discussed all-oxide varactor with 5 μm SMO bottom electrode in comparison to commercial platinum-based varactors, a varactor from *STMicroelectronics* (STM) was measured and compared to the all-oxide varactors. This commercial varactor from STM is a *Parascan*^{TM} tunable integrated capacitor, developed by *Paratek Microwave*. Table 4.8 shows the electrical characteristics of the *Parascan*^{TM} tunable integrated capacitor. These varactors are grown on sapphire substrates (see Figure 6.7 in the Appendix). In the following, the most important electrical parameters of the all-oxide and commercial *Parascan*^{TM} varactors are compared.

Table 4.8: Electrical characteristics of the Parascan^{TM} tunable integrated capacitor taken from the datasheet of the manufacturer [148].

Parameter	Rating	Rating Min.	Rating Max.	Unit
Bias voltage	25	1	25	V
Operating frequency		700	2700	MHz
Capacitance (1 V)	3.2	2.82	3.58	pF
Capacitance (24 V)	0.57	0.52	0.62	pF
Tuning range	5/1			
Quality factor (700 MHz, 2 V)	65	55		
Quality factor (2700 MHz, 2 V)	50	35		
Leakage current (24 V)			100	nA

Bias voltage

The *Parascan*^{TM} varactor is specified to function in a range of 1 – 24 V and in order to gain optimal performance and tuning, it requires a voltage of 24 V. By contrast, the all-oxide varactors only need voltages in the Li-ion battery regime, due to the low thickness of the dielectric layer. This enables application in mobile devices without the need of DC/DC converters.

Capacitance

The capacitance values of the *Parascan*^{TM} varactor is between C(0 V) = 3.2 pF and C(24 V) = 0.57 pF. These are significantly lower than the capacitance values of the all-oxide varactors reported in the last section between C(0 V) = 10 – 15 pF. A lower capacitance around C(0 V) = 3 pF is desired for integrating the device in an RF front-end. As presented in section 4.5 a new layout of the top contacts will solve this discrepancy in capacitance by decreasing the effective tunable area, while still maintaining a large contact area for flip-chip bonding.

Leakage current

The maximum leakage current for the *Parascan*^{TM} varactors is 100 nA for a bias voltage of 24 V. The leakage current for the all-oxide varactors in the SMO thickness study (see Figure 4.27 in section 4.2) was below 30 nA for bias fields of ± 100 V/μm (≈ 8.5 V). The all-oxide varactor with 5 μm SMO bottom electrode and 100 nm BST layer described in last section has a leakage current for $I_{leak}(10\,V) = 64$ nA. Both leakage current values are measured at a pad with 20 μm inner pad diameter.

Tunability

The tunability of both *Parascan*^{TM} and all-oxide varactors with 5 μm SMO bottom electrode and 100 nm BST layer can be seen in Figure 4.43. Due to the thinner dielectric layer, the tuning requires lower voltages, because the applied field is higher. For the sample in Figure 4.43, at battery voltages of 3.7 V of 54 % can be achieved from the all-oxide varactor, whereas the *Parascan*^{TM} only shows a tunability of 37 % at this voltage. However, if required, the BST thickness can also be lowered, to achieve even higher tunability at lower voltages.

Quality Factor

The quality factor for frequencies between 200 MHz and 3 GHz with and without bias are displayed in Figure 4.43. It is directly evident that the all-oxide varactors with 5 μm SMO bottom electrode surpass the commercial platinum-based varactor over the whole frequency range. However, the Q-factor of the all-oxide varactor exhibit acoustic resonances.

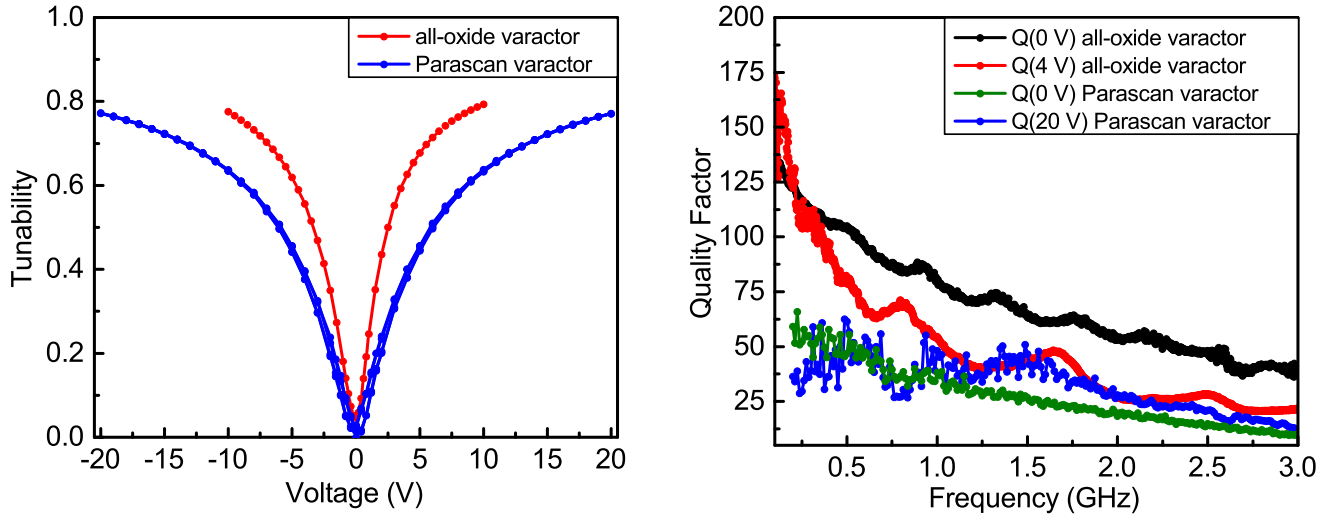

Figure 4.43: Comparison of the all-oxide varactors with 5 μm SMO bottom electrode and 100 nm BST layer with commercial varactors from STMicroelectronics. (Left) Tunability at 1 GHz and (Right) Quality factor over frequency for different bias voltages.

4.6.2 All-oxide varactors on silicon

In order to transfer the all-oxide varactor technology from the lab-scale towards industrial production, a first step is the change of substrate from scandate substrates towards cheap, industrial substrates such as silicon. After preliminary successful depositions of SMO on silicon substrates covered with an STO buffer layer (see section 4.1.3), the varactor heterostructure was grown on these silicon substrates with an STO buffer layer. The growth conditions have been similar to the conditions for heterostructures for GSO (see section 4.6). For further description of the substrates and the preapplied STO buffer layer from the manufacturer, see section 4.1.3.
XRD results of this heterostructure can be seen in Figure 4.44. The full XRD scan in Figure 4.44 (left) confirms the absence of any additional phases. The SMO layer in this heterostructure is $\approx 450\,\text{nm}$ thick, estimated from previous depositions with the same conditions and RHEED intensity oscillations, since this sample does not show Laue oscillations for the SMO layer. The out-of-plane lattice constant determined by Nelson-Riley-Plot has a value of $c(\text{SMO}) = 3.979\,\text{Å}$ and coincides with the value from section 4.1.3. The SMO still provides a good surface and interface for a 60 nm thick BST layer with an out-of-plane lattice constant of $c(\text{BST}) = 3.964\,\text{Å}$. Laue oscillations of this BST layer are visible showing the good crystal quality. RHEED surface images after each layer (see Figure 4.45) confirm a flat 2-dimensional growth for the entire heterostructure.

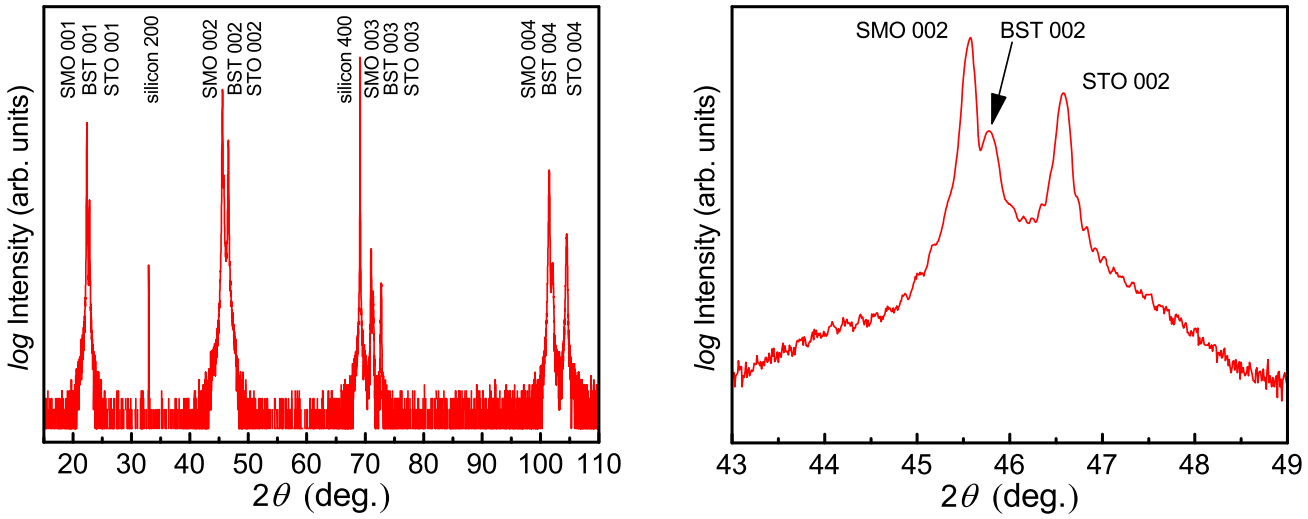

Figure 4.44: (Left) $2\theta - \theta$ scan of a varactor on on silicon substrate covered with an STO layer. (Right) High-resolution $2\theta - \theta$ scan of the SMO, STO and BST 002 peaks of the same sample.

After X-ray characterization, top electrodes were applied by photolithography, sputtering, and lift-off process. The microwave properties of the 36 devices of this sample were measured with the VNA and the results can be seen in Figure 4.46. It has to be noted that this sample was produced during a similar time as the first SMO thickness study (see section 4.2). Therefore, the BST is not sufficiently oxygenated and has oxygen vacancies. This is reflected in the leakage current values, which reach the current compliance

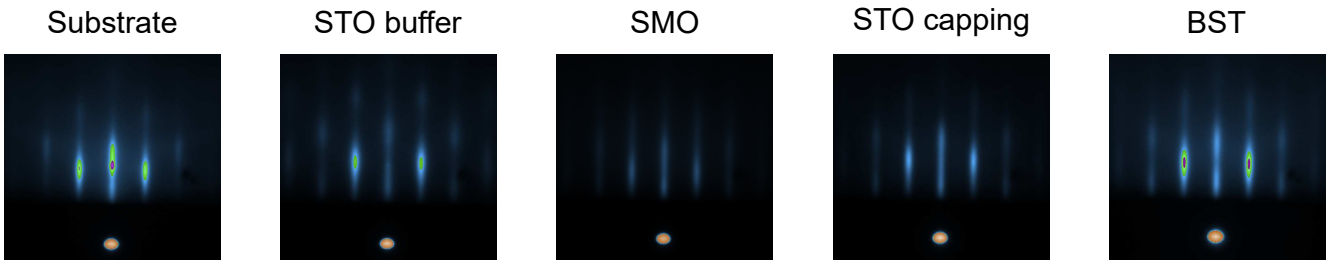

Figure 4.45: RHEED surface images after each layer of the all-oxide heterostructure on a silicon substrate with a preapplied STO buffer layer.

of 1 mA. For negative bias voltages, the device shows a tunability of up to 0.6. However, for positive bias voltages, the measurement aborts already at 3 V, which originates from the leakage current limit of the measurement setup. The shape of the tunability curve is also different for positive bias voltages being much flatter. The overall microwave properties of this sample mirror the results of the first SMO thickness study (see Figure 4.24) quite well. The oxygen vacancies in the dielectric BST layer aggravate the functionality of the device.

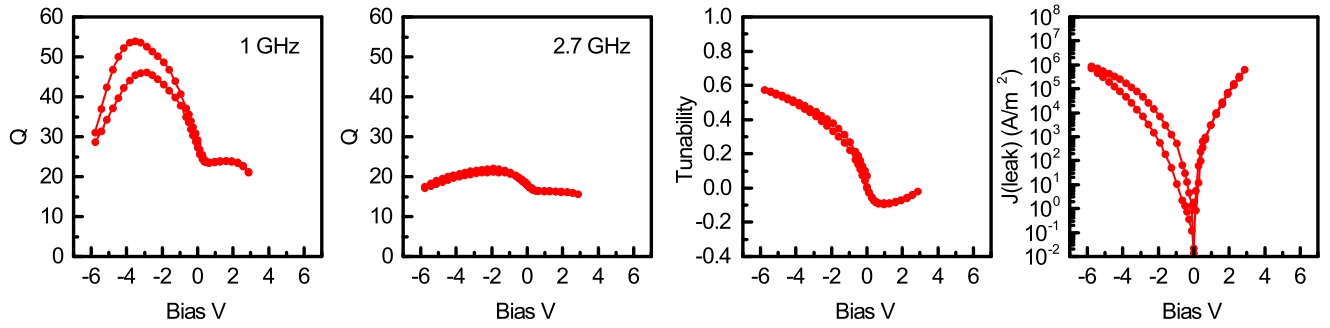

Figure 4.46: Microwave properties of varactors with ≈ 450 nm SMO on a silicon substrate. The values show one pad (A1) with a 20 μm inner pad diameter.

After the problem of the insufficient BST oxygenation was solved, new samples on silicon/STO substrates have been produced to prove the functionality of all-oxide varactors on silicon substrates. The growth conditions for the STO buffer layer and SMO was unchanged, however, the oxygen partial pressure during the BST deposition was increased to 35 mTorr with a flow of 15 sccm. The XRD $2\theta - \theta$ scan (see Figure 4.47 left) shows no additional phases. The scan near the 002 SMO, BST, and STO reflections of SMO and BST shows pronounced, separated peaks, however, no Laue oscillations are visible. The SMO layer has a thickness of ≈ 700 nm estimated by previous depositions and an out-of-plane lattice constant determined by Nelson-Riley-Plot has a value of $c(\mathrm{SMO}) = 3.979$ Å, which is identical to previous SMO films on these substrates.

After the findings from section 4.3, a BST capping layer was deposited subsequently to the SMO layer. The capping layer has a thickness of 12 unit cells and has been deposited in vacuum of $3 \cdot 10^{-8}$ Torr. To ensure a sufficient oxygenated dielectric layer and subsequent lowering the leakage current, the BST was deposited

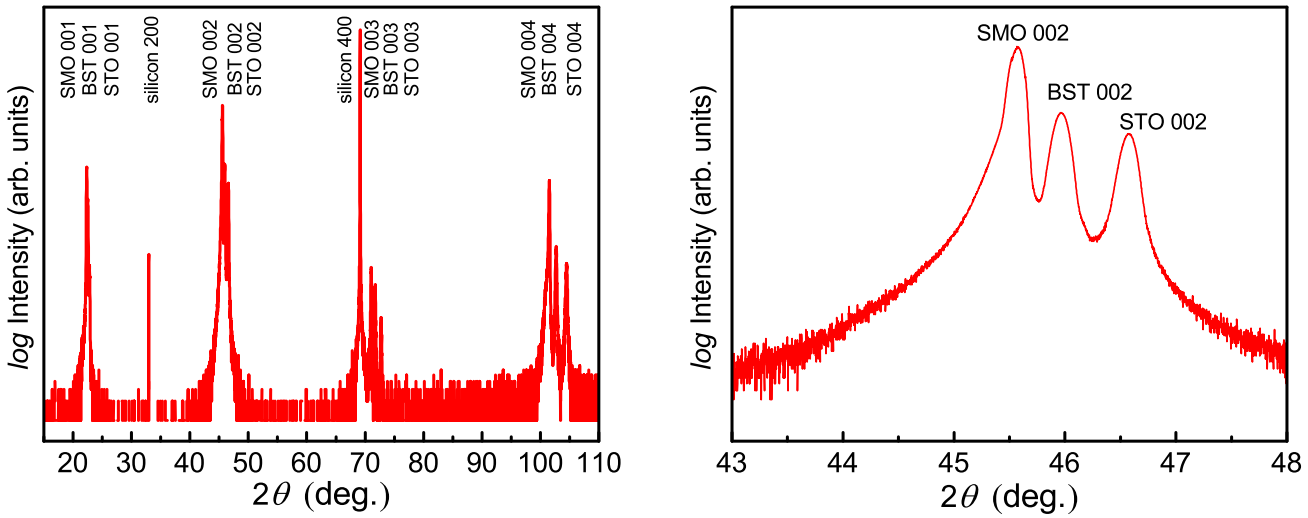

Figure 4.47: (Left) $2\theta - \theta$ scan of a varactor on on silicon substrate covered with an STO layer. (Right) High-resolution $2\theta - \theta$ scan of the SMO, STO and BST 002 peaks of the same sample. Both scans show a sample after the high BST leakage current was solved.

at 35 mTorr, 15 sccm oxygen flow, and has a thickness of 95 ± 3 nm as determined by RHEED oscillations.

Figure 4.48 shows the RHEED surface images after each interface. The streaky pattern of the STO buffer layer on the silicon is the starting point for the deposition of the subsequent layers. The pattern remains consistent through the deposition of the heterostructure, indicating a 2-dimensional layer-by-layer growth. Furthermore, no oxidation of the SMO is visible during the BST deposition with increased background pressure. It has previously been observed that $SrMoO_4$ oxidation caused by a too high oxygen background pressure leads to a roughening of the interface shown by a 3-dimensional islandy RHEED pattern [131].

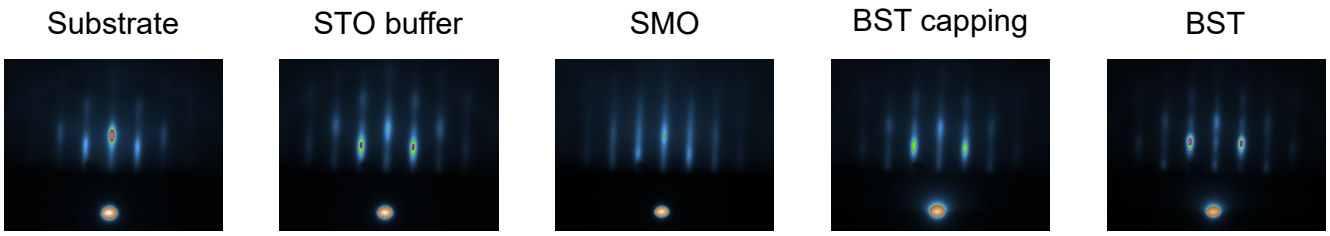

Figure 4.48: RHEED surface images after each layer of the all-oxide heterostructure on a silicon substrate with a preapplied STO buffer layer.

The varactors were patterned with the circular test structure by photolithography, then Pt and Au electrodes were sputtered and structured by a lift-off process. The microwave properties of the 36 devices of this sample were measured with the VNA up to 20 GHz. The results can be seen in Figure 4.49.
It is immediately visible that the devices behave as desired with a symmetrical tunability over the whole bias range. The leakage current is lowered by three orders of magnitude as compared to the previous samples in Figure 4.46. This proves the better oxygenation of the dielectric. However, the I-V curve exhibits

a hysteresis behavior for negative bias voltages, which has also been observed for varactor heterostructures on $GdScO_3$ shown in Figure 4.27 and might be caused by filling of the traps in the BST.
The device is tunable with a value of 0.5 for bias values of ± 10 V. For negative bias voltages, the tunability curve shows a hysteresis, similar to the I-V curve, which might be attributed to local polar regions or caused by filling of the traps in the dielectric. The tunability for this sample is lowered as compared to other samples on $GdScO_3$. This can be explained with the relatively small permittivity value of $\varepsilon = 120$. The origin of this lowered permittivity value was not fully clarified, but might be traced back to non optimal growth conditions. This could be solved by a optimization study on these silicon substrates. The resulting capacitance values are C(0 V) = 3.3 pF and C(10 V) = 1.7 pF for pad sizes of 20 μm inner pad diameter. However, the quality factor $Q(0V) = 45$ at 1 GHz is higher than for previous samples with comparable thickness and is in the same range as for samples with a 2 μm bottom electrode. The reason for this increase in quality factor is the lowered permittivity and, thus, capacitance in this sample, as discussed in detail in section 4.2.

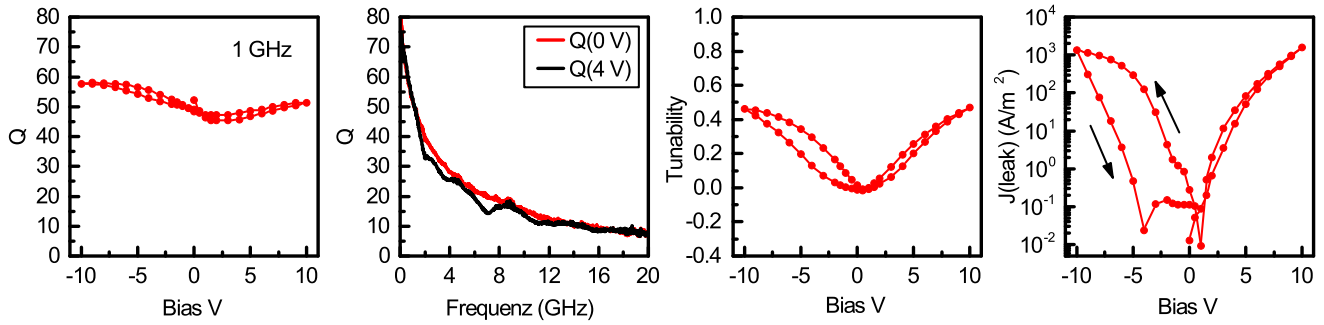

Figure 4.49: Microwave properties of varactors with ≈ 700 nm SMO on a silicon substrate after the high BST leakage current was solved. The values show one pad (B6) with a 20 μm inner pad diameter.

Fitting of the measurement data with an highly accurate analytical model by Walk *et al.* [95] has been performed to extract the resistivity of SMO in this heterostructure. The fitting yielded in a resistivity of 44 $\mu\Omega$·cm. This falls very well in line with previous SMO resistivity measurements and is a very good starting point for further optimizations of the all-oxide heterostructure on silicon substrates.

5 Conclusion and outlook

Conclusion

In the scope of this work, interfaces in all-oxide varactor heterostructures were investigated and deposition on new substrates as well as novel diffusion barrier materials were established. The highly conducting bottom electrode $SrMoO_3$ has been grown by pulsed laser deposition up to a thickness of several micrometer. These thick bottom electrodes in combination with a new oxygen diffusion barrier material enabling oxygenated dielectric layers, significantly improved the performance of all-oxide varactors beyond the level of state-of-the-art platinum-based competitors. By establishing the growth on the industrial popular substrate silicon, the path has been opened for all-oxide varactors to establish as a serious contender in the RF front end market for mobile communication.

In order to achieve thick bottom electrodes in a feasible time frame, the growth has been optimized at a higher laser repetition rate. The optimizations yielded in a laser repetition rate of 20 Hz, while still maintaining a SMO resistivity of only 31 $\mu\Omega$·cm. Thereby, a growth rate of 23 nm/min was established, which allows the growth of 1 μm SMO in only 45 minutes.
In order to gain a deeper understanding in the growth of $SrMoO_3$, especially how strain impacts the growth, $SrMoO_3$ has been grown on a variety of scandates, namely $DyScO_3$, $TbScO_3$, $GdScO_3$, $SmScO_3$ and $NdScO_3$. SMO layers with thicknesses of 650 nm have been grown in-plane locked on $TbScO_3$, $GdScO_3$, $SmScO_3$, confirmed by reciprocal space maps. Growth on $DyScO_3$ and $NdScO_3$ showed a decrease in crystal quality as compared to the other scandates, suggesting that a compressive lattice mismatch of -0.025 Å in case of $DyScO_3$ and tensile lattice mismatch of 0.035 Å in case of $NdScO_3$ are too much strain for high-quality $SrMoO_3$ growth.
Silicon substrates already coated with an $SrTiO_3$ buffer layer from the manufacturer were the base to prove the deposition of the all-oxide heterostructure on the industrially relevant substrate. Phi scans revealed, that the STO is oriented 45° rotated around the Si surface normal [001] axis. On these substrates, SMO has been grown without any additional phases and high crystal quality and visible Laue oscillations. Reciprocal space maps confirmed, that the SMO layer and STO buffer layer are in-plane locked to the substrate.

A first study varying the SMO thickness in varactors, lead to the conclusion that high crystalline quality does not necessarily lead to good microwave performance. The SMO thickness has been successfully scaled up to 2 μm with excellent crystal quality and in-plane locked films. However, it is of huge importance,

to ensure a sufficiently oxygenated dielectric, otherwise a high leakage current can disturb the overall functionality of the varactors and lead to unpredictable microwave properties, which did not follow the predicted trend.
After the leakage current of the varactor devices could be lowered by several orders of magnitude with optimized growth parameter and a higher oxygen partial during the BST deposition, the impact on the SMO thickness on the varactor performance could be measured. By increasing the SMO thickness, the overall quality factor could be improved significantly, following the trend of theoretical predictions. However, the experimental data of the Q-factor remained below the simulated values.

To improve the oxygenation of BST with a higher background pressure during growth, new diffusion barrier materials were investigated with a new approach to study oxygen diffusion in thin-film heterostructures utilizing XPS. By monitoring the Mo valence state in $SrMoO_3$ with XPS, it was possible to quantify the oxygen diffusion through thin-film $SrTiO_3$, $Ba_{0.5}Sr_{0.5}TiO_3$ and $BaTiO_3$ capping layers as a function of oxygen pressure, temperature, and annealing time. The studies in this work revealed $Ba_{0.5}Sr_{0.5}TiO_3$ to be the most efficient oxygen barrier material among the titanates investigated. It was demonstrated that a six-unit-cell-thick capping layer of $Ba_{0.5}Sr_{0.5}TiO_3$ on $SrMoO_3$ is sufficient to maintain over 95 % of Mo^{4+} at 8 mTorr oxygen partial pressure at a temperature of 630 °C for two minutes. The determined pressure, temperature, and time phase-stability window of $SrMoO_3$ allows for the growth of functional, epitaxial heterostructures with highly conducting $SrMoO_3$ electrodes. In effect, a $Ba_xSr_{1-x}TiO_3$ capping layer with a thickness of only 6 unit cells effectively prevents oxidation of $SrMoO_3$ and enables integration of $SrMoO_3$ bottom electrodes with a large range of functional materials in the implementation of all-oxide epitaxial microelectronic devices.

The performance of all-oxide varactors with micrometer-thick bottom electrodes showed, that the all-oxide varactor technology has the potential to enter into the field of electronic devices. Despite the thick bottom electrodes, the growth still maintains the layer-by-layer mode and interfaces are atomically sharp. In a ferroelectric varactor with a five-micrometers-thick low-resistive $SrMoO_3$ bottom electrode and a 50 nm thin tunable dielectric BST layer, the tunability reaches above three at a battery voltage of 3.7 V. The all-oxide varactors have the unique advantage, which allows significant and sufficient tunability at the battery voltage level. Upon further material and device optimization, $SrMoO_3$ based varactors have the potential to drive all-oxide varactors in the emerging 5G frequency range of 3 – 6 GHz.

In order to enable the transition into industrial fabrication, the all-oxide heterostructure was deposited on silicon substrates with a $SrTiO_3$ buffer layer from the manufacturer. The results were very successful and a phase-pure heterostructure grown layer-by-layer was achieved. Microwave properties showed a tunability of 0.5 at 10 V bias and a quality factor of $Q(0\text{V}) = 45$ at 1 GHz with only 700 nm SMO thickness. These results prove, that the advantages of the all-oxide varactors are also achievable on industrially relevant silicon substrates.

Outlook

To gain additional insight in the $SrMoO_3$ growth mechanism, the samples investigated in this work, especially the SMO layers grown on the different scandates, will further be characterized by TEM. This allows to map the SMO stoichiometry through the whole thickness, which can be used to compare possible shifts in SMO stoichiometry to a strain map. The possible occurrence of dislocations can be confirmed and correlated to different strain values. Results can verify the hypothesis of a self-adjusting cation stoichiometry to overcome the critical thickness. In addition, the defects for the films on DSO and NSO can be identified and at what thickness during deposition the SMO on NSO starts to relax.

Several approaches can further increase the performance of all-oxide varactors.

- The composition of the dielectric (Ba:Sr ratio) can be fine tuned, to increase the permittivity at room temperature, while still maintaining the paraelectric phase. This can further increase the tunability or the desired tunability can be achieved at lower bias voltages. In addition, the field of doping the dielectric layer with external elements, such as iron or manganese, is yet still completely unexplored. This is an tremendously huge field and can lead to performance increase of lower leakage current or decreased losses.
- Utilizing the newly-developed experimental measurement technique with XPS can be applied in future investigations of oxygen diffusion through other capping layer materials (e.g. perovskite scandates, hafnates, zirconates) grown onto $SrMoO_3$. With a further improvement in the oxygen diffusion barrier, further increase in oxygen background pressure during BST and, thus, completely oxygenation can be achieved.
- The impact of different interlayer materials on the Schottky barrier has not been investigated. Studies and determination of the Schottky barrier height for the SMO – BST and BST – Pt interface in all-oxide varactors can further clarify the leakage current behavior.
- The deposition of a polar material on top of SMO can increase the work function. With a higher work function, the leakage current can be further decreased lowering the overall power consumption of the varactor device.

After the feasibility of the all-oxide heterostructure on silicon substrates with a $SrTiO_3$ buffer layer from the manufacturer has been shown, the next step is to deposit the heterostructure directly on silicon. Experiments to clean the substrates via flash heating have already been successful. Hence, the STO buffer layer growth on silicon can be attempted by MBE.

For further endeavors to establish an industrial production of the the all-oxide varactor technology the deposition technique has to be changed. The most appealing technique for this use case is sputtering. After a successful transfer to sputtering was done, scaling and endurance studies have to be done. A homogeneous deposition on large scale silicon wafers has to be ensured, in addition to a high endurance of the devices. The already performed studies with 100 bias cycles has to be extended to mimic life cycles

of future application devices such as smartphones. This applies to the number of bias cycles, as well as environmental conditions such as temperature, moisture and vibrations.

6 Appendix

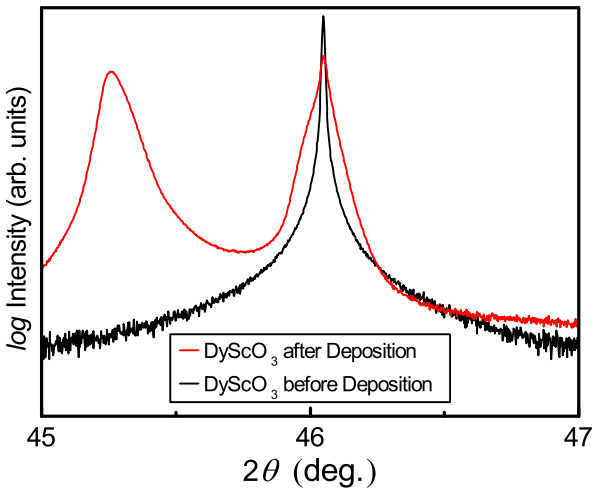

Figure 6.1: DSO Substrate measured before the deposition (black) and afterwards (red). A clear broadening of the substrate peak is visible.

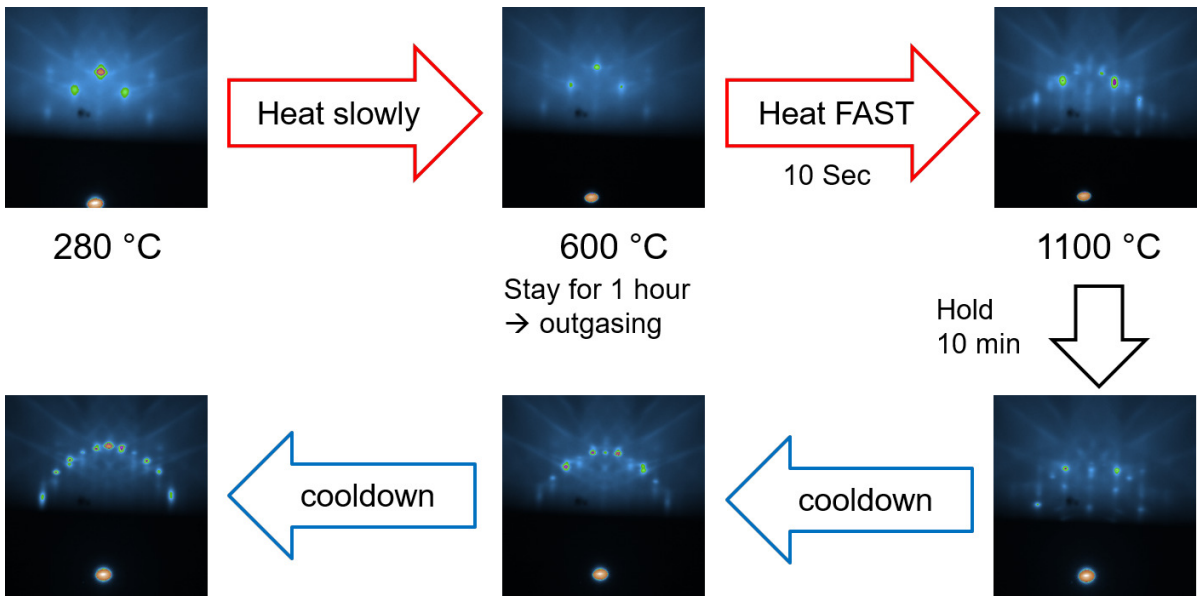

Figure 6.2: Flash Heating procedure in the DCA PLD.

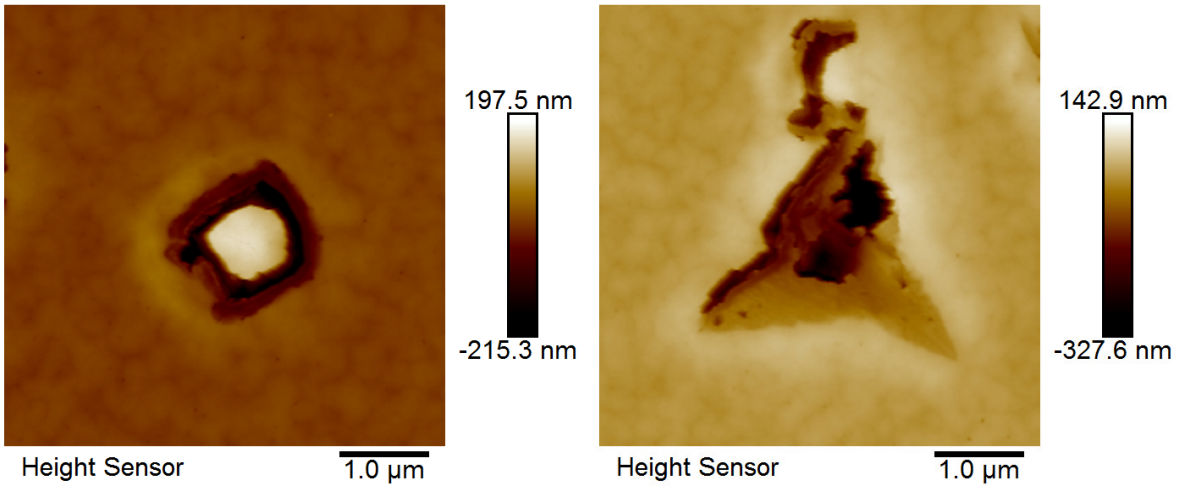

Figure 6.3: (Left) 2D AFM image of the rectangular defect. (Right) 2D AFM image of the star/butterfly shaped defect.

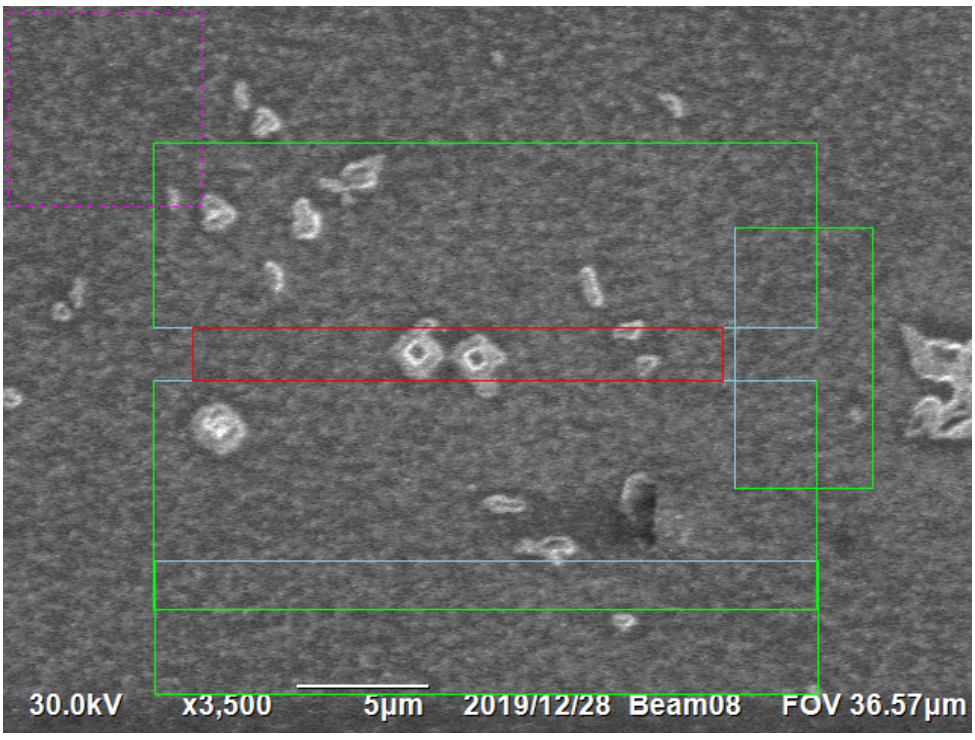

Figure 6.4: Top view of the SMO surface, where the FIB lamalla has been cut to investigate the origin of the SMO defects. The red rectangular indicates the dimensions of the lamella.

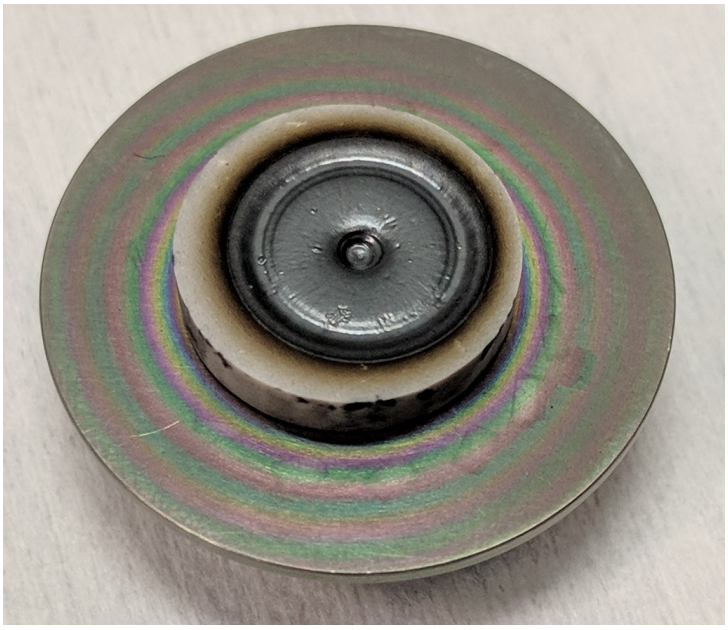

Figure 6.5: SMO target after deposition with 300 000 shots, yielding a layer thickness of 5 μm.

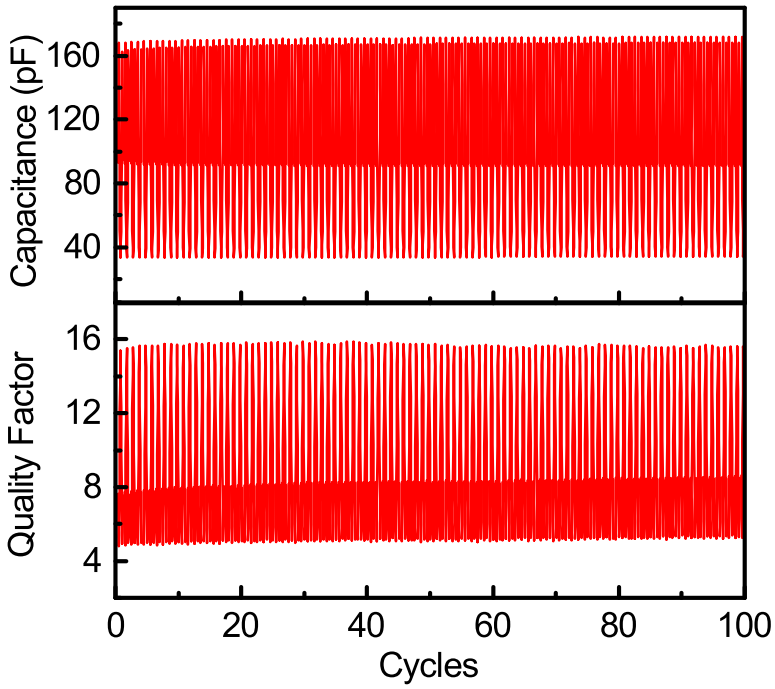

Figure 6.6: Enduarance of a varactor over 100 bias cycles. The low quality factor is due to a bottom electrode thickness of ≈ 500 nm. No breakdown is visible and the performance is steady.

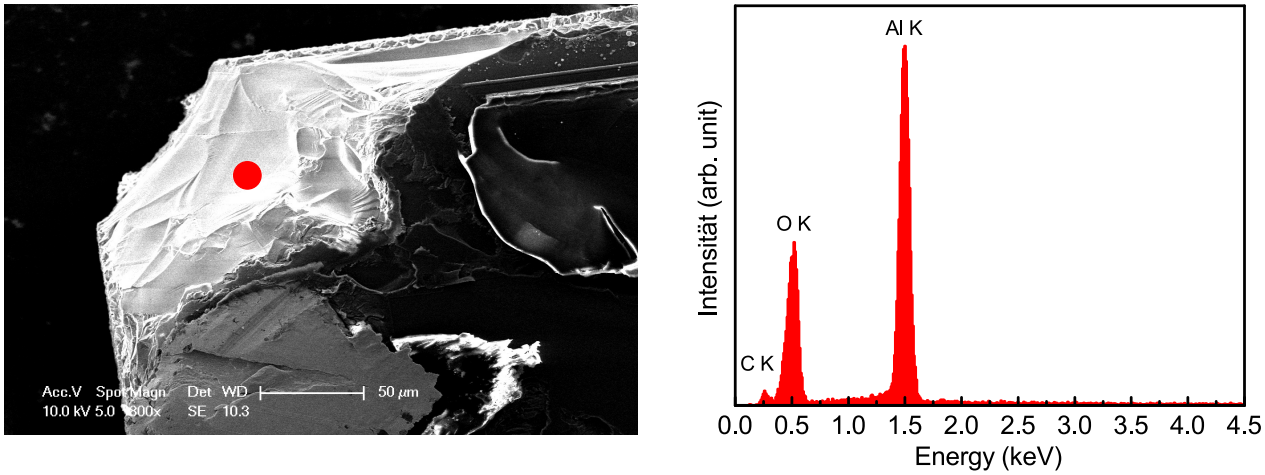

Figure 6.7: To validate the substrate material of the commercial *Parascan*^{TM} varactor, the packaging was removed and the substrate was measured by EDS.
(Left) SEM image of the investigated sample. The red dot shows the measurement location of the EDS spectrum. (Right) EDS spectrum of the substrate of a *Parascan*^{TM} varactor indicating sapphire substrate material.

List of Figures

List of Tables

Bibliography

[1] N. Setter, D. Damjanovic, L. Eng, G. Fox, S. Gevorgian, S. Hong, A. Kingon, H. Kohlstedt, N.Y. Park, G.B. Stephenson, I. Stolitchnov, A.K. Tagantsev, D.V. Taylor, T. Yamada and S. Steiffer. Ferroelectric thin films: Review of materials, properties, and applications. *Journal of Applied Physics*, 100:05106, 2006.

[2] M.D. Domenico, D.A. Johnson and R.H. Pantell. Ferroelectric harmonic generator and the large-signal microwave characteristics of a ferroelectric ceramic. *Journal of Applied Physics*, 33:1697, 1962.

[3] D. Zhou, L.-X. Pang, D.-W. Wang, C. Li, B.-B. Jin and I. M. Reaney. High permittivity and low loss microwave dielectrics suitable for 5G resonators and low temperature co-fired ceramic architecture. *Journal of Materials Chemistry C*, 5:10094–10098, 2017.

[4] A.K. Tagantsev, V.O. Sherman, K.F. Astafiev, J. Venkatesh and N. Setter. Ferroelectric Materials for Microwave Tunable Applications. *Journal of Electroceramics*, 11:5–66, 2003.

[5] Z. Gu et at. Resonant domain-wall-enhanced tunable microwave ferroelectrics. *Nature*, 560:622–626, 2018.

[6] T.S. Rappaport, S. Sun, R. Mayzus, H. Zhao, Y. Azar, K. Wang, G.N. Wong, J. K. Schulz, M. Samimi and F. Gutierrez. Millimeter Wave Mobile Communications for 5G Cellular: It Will Work! *IEEE Access*, 1:335–349, 2013.

[7] Z. Pi and F. Khan. An introduction to millimeter-wave mobile broadband systems. *IEEE Communications Magazine*, 49:101–107, 2011.

[8] H.N. Al-Shareef , K.D. Gifford , S.H. Rou , P.D. Hren , O. Auciello and A.I. Kingon. Electrodes for ferroelectric thin films. *Integrated Ferroelectrics*, 3:321–332, 1993.

[9] P.D. Hren, S.H. Rou, H.N. Al-Shareef, M.S. Ameen, O. Auciello and A. I. Kingon. Bottom electrodes for integrated $Pb(Zr,Ti)O_3$ films. *Integrated Ferroelectrics*, 2:311–325, 1992.

[10] W.W. Jung, S.K. Choi, S.Y. Kweon and S.J. Yeom. Platinum(100) hillock growth in a Pt/Ti electrode stack for ferroelectric random access memory. *Applied Physics Letters*, 83:2160, 2003.

[11] K. Khamchane, A. Vorobiev, T. Claeson and S. Gevorgian. $Ba_{0.25}Sr_{0.75}TiO_3$ thin-film varactors on $SrRuO_3$ bottom electrode. *Journal of Applied Physics*, 96:034103, 2006.

[12] A. Radetinac, A. Mani, S. Melnyk, M. Nikfalazar, J. Ziegler, Y. Zheng, R. Jakoby, L. Alff and P. Komissinskiy. Highly conducting $SrMoO_3$ thin films for microwave applications. *Applied Physics Letters*, 105:114108, 2014.

[13] A.J. Smith, J.C. Burnsa, and J.R. Dahn. High-Precision Differential Capacity Analysis of $LiMn_2O_4$/graphite Cells. *Electrochemical and Solid State Letters*, 14, 2011.

[14] A. Radetinac, J. Zimmermann, K. Hoyer, H.B. Zhang, P. Komissinskiy, and L. Alff. Optical properties of single crystalline $SrMoO_3$ thin films. *Journal of Applied Physics*, 119:055302, 2016.

[15] L. Zhang, Y. Zhou, L. Guo, W. Zhao, A. Barnes, H.-T. Zhang, C. Eaton, Y. Zheng, M. Brahlek, H.F. Haneef, N.J. Podraza, M. H. W. Chan, V. Gopalan, K.M. Rabe, and R. Engel-Herbert. Correlated metals as transparent conductors. *Nature Materials*, 15:204–210, 2016.

[16] M.P. Wells, B. Zou, B.G. Doiron, R. Kilmurray, A.P. Mihai, R.F.M. Oulton, P. Gubeljak, K.L. Ormandy, G. Mallia, N.M. Harrison, L.F. Cohen, S.A. Maier, N. McN. Alford, and P. K. Petrov. Tunable, Low Optical Loss Strontium Molybdate Thin Films for Plasmonic Applications. *Advanced Optical Materials*, 5:1700622, 2017.

[17] A. Radetinac. *Hochleitfähiges $SrMoO_3$: Vom Schichtwachstum zur Anwendungseignung*. PhD thesis, Technische Universität Darmstadt, 2016.

[18] Arzhang Mani. *Thin-film ferroelectric $Ba_xSr_{1-x}TiO_3$ varactors utilizing highly conducting $SrMoO_3$ bottom electrode*. PhD thesis, Technische Universität Darmstadt, 2016.

[19] Rudolf Gross and Achim Marx. *Festkörperphysik*. Oldenbourg Wissenschaftsverlag GmbH, 2012.

[20] Prof. Dr. Siegfried Hunklinger. *Festkörperphysik*. Oldenbourg Wissenschaftsverlag GmbH, 3. edition, 2011.

[21] Christian Gerthsen. *Gerthsen Physik*. Springer, 25. edition, 2015.

[22] G. H. Haertling. Ferroelectric Ceramics: Histroy and Technology. *Journal of the American Ceramic Society*, 82:797–828, 1999.

[23] J. Valasek. Piezo-Electric and Allied Phenomena in Rochelle Salt. *Physical Review*, 17:457–481, 1921.

[24] H. A. Kramers. *La diffusion de la lumière par les atomes*. Atti Cong. Intern. Fisica, Como, 2. edition, 1927.

[25] R. de L. Kronig. On the theory of the dispersion of X-rays. *Journal of the Optical Society of America*, 12:547–557, 1926.

[26] T. J. M. Bayer. *Einfluss injizierter Ladungen auf $Ba_{0.6}Sr_{0.4}TiO_3$-Dünnschichten: Elektrische und dielektrische Charakterisierung und Simulation des Ladungstransports*. PhD thesis, Technische Universität Darmstadt, 2014.

[27] André Moliton. *Applied Electromagnetism and Materials*. Springer, 2007.

[28] Spartak Gevorgian. *Ferroelectrics in Microwave Devices, Ciruits and Systems*. Springer, 2012.

[29] Nava Setter. *Electroceramic-Based MEMS*. Springer, 2005.

[30] V.M. Goldschmidt, T. Barth, G. Lunde and W.H. Zachariasen. Geochemical distribution law of the elements. *Skr. Norske Vidensk. Akad.*, 1, 1926.

[31] A. M. Glazer. The Classification of Tilted Octahedra in Perovskites. *Acta Crystallographica Section B*, 28:3384–3392, 1972.

[32] A. M. Glazer. Simple Ways of Determining Perovskite Structures. *Acta Crystallographica Section A*, 31:756–762, 1975.

[33] S. Sasaki, C. T. Prewitt, J. D. Bass and W. A Schulze. Orthorhombic Perovskite $CaTiO_3$ and $CdTiO_3$: Structure and Space Group. *Acta Crystallographica Section C*, 43:1668–1674, 1987.

[34] O. Bock and U. Müller. Symmetrieverwandtschaften bei Varianten des Perowskit-Typs. *Acta Crystallographica Section B*, 58:594–606, 2002.

[35] A. Ahmed, I.A. Goldthorpe and A.K. Khandani. Electrically tunable materials for microwave applications. *Applied Physics Reviews*, 2:011302, 2015.

[36] Robert A. York. *Tunable Dielectrics for RF Circuits*. Scitech Publishing, 2009.

[37] ICDD. International Center for Diffraction Data (ICDD), Card No. 00-005-0634.

[38] ICDD. International Center for Diffraction Data (ICDD), Card No. 00-005-0626.

[39] A.A. Sirenko, C. Bernhard, A. Golnik, A.M. Clark, J. Hao, W. Si and X.X. Xi. Soft-mode hardening in $SrTiO_3$ thin films. *Nature*, 404:373–376, 2000.

[40] C. Zhou and D.M. Newns. Intrinsic dead layer effect and the performance of ferroelectric thin film capacitors. *Journal of Applied Physics*, 82:3081, 1997.

[41] C. Basceri, S.K. Streiffer, A.I. Kingon and R. Waser. The dielectric response as a function of temperature and film thickness of fibertextured (Ba,Sr)TiO_3 thin films grown by chemical vapor deposition. *Journal of Applied Physics*, 82:2497, 1997.

[42] T.M. Shaw, Z. Suo, M. Huang, E. Liniger, R.B. Laibowitz and J.D. Baniecki. The effect of stress on the dielectric properties of barium strontium titanate thin films. *Applied Physics Letters*, 75:2129–2131, 1999.

[43] Jae-Ho Jeon. Effect of $SrTiO_3$ concentration and sintering temperature on microstructure and dielectric constant of $Ba_{1-x}Sr_xTiO_3$. *Journal of the European Ceramic Society*, 24:1045–1048, 2004.

[44] G. Koster, L. Klein, W. Siemons, G. Rijnders, J.S. Dodge, C.B. Eom, D.H.A. Blank and M.R. Beasley. Structure, physical properties, and applications of $SrRuO_3$ thin films. *Reviews of Modern Physics*, 84:253–298, 2012.

[45] Q.X. Jia, X.D. Wu, S.R. Foltyn and P. Tiwari. Structural and electrical properties of $Ba_{0.5}Sr_{0.5}TiO_3$ thin films with conductive $SrRuO_3$ bottom electrodes. *Applied Physics Letters*, 66:2197–2199, 1995.

[46] M. Izuha, K. Abe, M. Koike, S. Takeno and N. Fukushima. Electrical properties and microstructures of $Pt/Ba_{0.5}Sr_{0.5}TiO_3/SrRuO_3$ capacitors. *Applied Physics Letters*, 70:1405–1407, 1997.

[47] L.J. Sinnamon, R.M. Bowman and J.M. Gregg. Thickness-induced stabilization of ferroelectricity in $SrRuO_3/Ba_{0.5}Sr_{0.5}TiO_3$/Au thin film capacitors. *Applied Physics Letters*, 81:889–891, 2002.

[48] R. Dittmann, R. Plonka, E. Vasco, N.A. Pertsev, J.Q. He, C.L. Jia, S. Hoffmann-Eifert and R. Waser. Sharp ferroelectric phase transition in strained single-crystalline $SrRuO_3/Ba_{0.7}Sr_{0.3}TiO_3/SrRuO_3$ capacitors. *Applied Physics Letters*, 83:5011–5013, 2003.

[49] G.P. Luo, Y.S. Wang, S.Y. Chen, A.K. Heilman, C.L. Chen, C.W. Chu, Y. Liou and N.B. Ming. Electrical and magnetic properties of $La_{0.5}Sr_{0.5}CoO_3$ thin films. *Applied Physics Letters*, 76:1908–1910, 2000.

[50] S. Madhukar, S. Aggarwal, A.M. Dhote, R. Ramesh, A. Krishnan, D. Keeble and E. Poindexter. Effect of oxygen stoichiometry on the electrical properties of $La_{0.5}Sr_{0.5}CoO_3$ electrodes. *Journal of Applied Physics*, 81:3543–3547, 1997.

[51] H. Boschker, M. Huijben, A. Vailionis, J. Verbeeck, S.V. Aert, M. Luysberg, S. Bals, G.V. Tendeloo, E.P. Houwman, G. Koster, D.H.A. Blank and G. Rijnders. Optimized fabrication of high-quality $La_{0.67}Sr_{0.33}MnO_3$ thin films considering all essential characteristics. *Journal of Physics D: Applied Physics*, 44:205001, 2011.

[52] K. Khamchane, Y.A. Boikov and Z.G. Ivanov. Temperature and electric field responseof a dielectric $(Ba,Sr)TiO_3$ layer between perovskite-type manganite electrodes. *Annalen der Physik*, 13:103–105, 2004.

[53] S. Sheng, X.-Y. Zhang, P. Wang and C.K. Ong. Effect of bottom electrodes on dielectric properties of high frequency $Ba_{0.5}Sr_{0.5}TiO_3$ parallel plate varactor. *Thin Solid Films*, 518:2864–2866, 2010.

[54] J. Miao, W. Chen, L. Zhao, B. Chen, H. Yang, W. Peng, X. Zhu, B. Xu, L. Cao, X. Qiu and B. Zhao. Enhanced dielectric properties of $Ba_{1-x}Sr_xTiO_3$ thin film grown on $La_{1-x}Sr_xMnO_3$ bottom layer. *Journal of Applied Physics*, 96:6578–6584, 2004.

[55] M. Zhu, P. Komissinskiy, A. Radetinac, Z. Wang and L. Alff. Joint effect of composition and strain on the anomalous transport properties of $LaNiO_3$ films. *Journal of Applied Physics*, 117:155306, 2015.

[56] C.C. Zhang, J.C. Shi, C.S. Yang and G.F. Ding. Preparation of (100)-oriented $LaNiO_3$ on Si for the textured $Ba_{0.5}Sr_{0.5}TiO_3$ thin films. *Applied Surface Science*, 255:2773–2776, 2008.

[57] P. Bao, T.J. Jackson, X. Wang and M.J. Lancaster. Barium strontium titanate thin film varactors for room-temperature microwave device applications. *Journal of Physics D: Applied Physics*, 41, 2008.

[58] I. Nagai, N. Shirakawa, S. Ikeda, R. Iwasaki, H. Nishimura and M. Kosaka. Highest conductivity oxide $SrMoO_3$ grown by a floating-zone method under ultralow oxygen partial pressure. *Applied Physics Letters*, 87:024105, 2005.

[59] L. Alff, P. Komissinskiy, A. Radetinac, T. Sirman and M. Vafaee. The role of cationic and anionic point defects in pulsed laser deposition of perovskites. *Journal of Physics D: Applied Physics*, 47:034012, 2014.

[60] ICDD. International Center for Diffraction Data (ICDD), Card No. 00-024-1224.

[61] H. Wadati, K. Yoshimatsu, H. Kumigashira, M. Oshima, T. Sugiyama, E. Ilkenaga, A. Fujimori, J. Mravlje, A. Georges, A. Radetinac, K.S. Takahashi, M. Kawasaki and Y. Tokura. Electronic correlations and Hund's coupling effects in $SrMoO_3$ revealed by photoemission spectroscopy. *Physical Review B*, 90:205131, 2014.

[62] R.A. De Souza. Oxygen Diffusion in $SrTiO_3$ and Related Perovskite Oxides. *Advanced Functional Materials*, 25:6326–6342, 2015.

[63] Helmut Mehrer. *Diffusion in Solids*. Springer, 1. edition, 2007.

[64] C. Nivot, C. Legros, B. Lesage, M. Kilo and C. Argirusis. Oxygen diffusion in $SrZrO_3$. *Solid State Ionics*, 180:1040–1044, 2009.

[65] M. Kessel, R. A. De Souza and M. Martin. Oxygen diffusion in single crystal barium titanate. *Physical Chemistry Chemical Physics*, 17:12587–12597, 2015.

[66] R. A. De Souza. Oxygen Diffusion in $SrTiO_3$ and Related Perovskite Oxides. *Advanced Functional Materials*, 25:6326–6342, 2015.

[67] R. Al-Hamadany, J.P. Goss, P.R. Briddon, S.A. Mojarad, A.G. O'Neill and M.J. Rayson. Impact of tensile strain on the oxygen vacancy migration in $SrTiO_3$: Density functional theory calculations. *Journal of Applied Physics*, 113:224108, 2013.

[68] R. Al-Hamadany, J.P. Goss, P.R. Briddon, S.A. Mojarad, M. Al-Hadidi, A.G. O'Neill and M.J. Rayson. Oxygen vacancy migration in compressively strained $SrTiO_3$. *Journal of Applied Physics*, 113:024108, 2013.

[69] Robert Eason. *Pulsed Laser Deposition Of Thin Films*. WILEY, 2007.

[70] Hans Lüth. *Solid Surfaces, Interfaces and Thin Films*. Springer, 4. edition, 2010.

[71] Klaus Wandelt. *Surface and Interface Science*. WILEY, 1. edition, 2014.

[72] T.S. Chow. Wetting of rough surfaces. *Journal of Physics: Condensed Matter*, 10:L445–L451, 1998.

[73] D.G. Schlom, L.-Q. Chen, C.-B. Eom, K.M. Rabe, S.K. Streiffer and J.-M. Triscone. Strain Tuning of Ferroelectric Thin Films. *Annual Review of Materials Research*, 37:89–626, 2007.

[74] A.T. Zayak, X. Huang , J.B. Neaton and K.M. Rabe. Structural, electronic, and magnetic properties of $SrRuO_3$ under epitaxial strain. *Physical Review B*, 74:094104, 2006.

[75] A. Trampert and K.H. Ploog. Heteroepitaxy of Large-Misfit Systems: Role of Coincidence Lattice. *Crystal Research and Technology*, 35:793–806, 2000.

[76] Q. Yang, J.X. Cao, Y. Ma, Y.C. Zhou, L.M. Jiang and X.L. Zhong. Strain effects on formation and migration energies of oxygen vacancy in perovskitee ferroelectrics: A first-principles study. *Journal of Applied Physics*, 113:184110, 2013.

[77] T. Ohnishi, K. Shibuya, T. Yamamoto and M.Lippmaa. Defects and transport in complex oxide thin films. *Journal of Applied Physics*, 103:103703, 2008.

[78] G. Subramanyam, M.W. Cole, N.X. Sun, T.S. Kalkur, N.M. Sbrockey, G.S. Tompa, X. Guo, C. Chen, S.P. Alpay, G.A. Rossetti Jr, K. Dayal, L.-Q. Chen and D.G. Schlom. Challenges and opportunities for multi-functional oxide thin films for voltage tunable radio frequency/microwave components. *Journal of Applied Physics*, 114:191301, 2013.

[79] A. Vorobiev, P. Rundqvist, K. Khamchane and S. Gevorgian. Silicon substrate integrated high Q-factor parallel-plate ferroelectric varactors for microwave/millimeterwave applications. *Applied Physics Letters*, 83:3144, 2003.

[80] P. Rundqvist, T. Liljenfors, A. Vorobiev, E. Olsson and S. Gevorgian. The efffect of SiO_2, Pt and Pt/Au templates on the micrstructure and permittivity of $Ba_xSr_{1-x}TiO_3$ films. *Journal of Applied Physics*, 100:114116, 2006.

[81] P. Rundqvist, A. Vorobiev, E. Kollberg and S. Gevorgian. Large signal circuit model of parallel-plate ferroelectric varactors. *Journal of Applied Physics*, 100:074101, 2006.

[82] E. Mikheev, A.P. Kajdos, A.J. Hauser and S. Stemmer. Electric field-tunable $Ba_xSr_{1-x}TiO_3$ films with high figures of merit grown by molecular beam epitaxy. *Applied Physics Letters*, 101:252906, 2012.

[83] C.R. Freeze and S. Stemmer. Role of film stoichiometry and interface quality in the performance of $(Ba,Sr)TiO_3$ tunable capacitors with high figures of merit. *Applied Physics Letters*, 109:192904, 2016.

[84] A. Tombak, J. Maria, F. Ayguavives, J. Zhang, G.T. Stauf, A.I. Kingon and A. Mortazawi. Tunable Barium Strontium Titanate Thin Film Capacitors for RF and Microwave Applications. *IEEE Microwave and Wireless Components Letters*, 12:3–5, 2002.

[85] C.J.G. Meyers, C.R. Freeze, S. Stemmer and R.A. York. $(Ba,Sr)TiO_3$ tunable capacitors with RF communication factors exceeding 6000. *Applied Physics Letters*, 109:112902, 2016.

[86] C.J.G. Meyers, C.R. Freeze, S. Stemmer and R.A. York. Effect of BST film thickness on the performance of tunable interdigital capacitors grown by MBE. *Applied Physics Letters*, 111:262903, 2017.

[87] Y. Liu, A.S. Nagara, E.G. Erker, P. Periaswarmy, T.R. Taylor, J. Speck and R.A.York. $BaSrTiO_3$ Interdigitated Capacitors for Distributed Phase Shifter Applications. *IEEE Microwave Guided Wave Lett.*, 10:448–450, 2000.

[88] S. Yu, L. Li, W. Zhang, Z. Sun and Haoran Zheng. Fully transparent thin-film varactor: fabrication and performance. *Journal of Materials Chemistry C*, 3:5703–5708, 2015.

[89] S. Gevorgian. Agile Microwave Devices. *Microwave Magazine, IEEE*, 10:93–98, 2009.

[90] S.V. Razumov, A.V. Tumarkin, M.M. Gaidukov, A.G. Gagarin, A.B. Kozyrev, O.G. Vendik, A.V. Ivanov, O.U. Buslov, V.N. Keys, L.C. Sengupta, and X. Zhang. Characterization of quality of $Ba_xSr_{1-x}TiO_3$ thin film by the commutation quality factor measured at microwaves. *Applied Physics Letters*, 81:1675, 2002.

[91] P. Salg, D. Walk, L. Zeinar, A. Radetinac, L. Molina-Luna, A. Zintler, R. Jakoby, H. Maune, P. Komissinskiy and L. Alff. Atomically interface engineered micrometer-thick $SrMoO_3$ oxide electrodes for thin-film $Ba_xSr_{1-x}TiO_3$ ferroelectric varactors tunable at low voltages. *APL Materials*, 7:051107, 2019.

[92] Y. Kozuka, H. Seki, T.C. Fujita, S. Chakraverty, K. Yoshimatsu, H. Kumigashira, M. Oshima, M.S. Bahramy, R. Arita, and M. Kawasaki. Epitaxially Stabilized $EuMoO_3$: A New Itinerant Ferromagnet. *Chemistry of Materials*, 24:3746–3750, 2012.

[93] M. Ito, M. Uchida, Y. Kozuka, K.S. Takahashi, and M. Kawasaki. Effective carrier doping and metallization in $La_xSr_{2-x-y}Ba_yIrO_{4-\delta}$ thin films. *Physical Review B*, 93:045139, 2016.

[94] D. Kan, R. Aso, R. Sato, M. haruta, H. Kurata and Y. Shimakawa. Tuning magnetic anisotropy by interfacially engineering the oxygen coordination environment in a transition metal oxide. *Nature Materials*, 15:432–437, 2016.

[95] D. Walk, D. Kienemund, P. Salg, L. Zeinar, A. Radetinac, L. Molina-Luna, P. Komissinskiy, L. Alff, R. Jakoby and H. Maune. Highly Accurate Analytic Modeling of Dispersive Field Distributions in MIM Capacitances With Electrodes Thinner than Skin Depth. *IEEE Transactions on Microwave Theory and Techniques*, 67:4665–4673, 2019.

[96] D. Walk, D. Kienemund, L. Zeinar, P. Salg, A. Radetinac, P. Komissinskiy, L. Alff, R. Jakoby and H. Maune. Characterization and Deembedding of Negative Series Inductance in On-Wafer Measurements of Thin-Film All-Oxide Varactors. *IEEE Microwave and Wireless Components Letters*, 29:213–215, 2019.

[97] A. Vorobiev, P. Rundqvist, K. Khamchane and S. Gevorgian. Microwave loss mechanisms in $Ba_{0.25}Sr_{0.75}TiO_3$ thin film varactors. *Journal of Applied Physics*, 96:4642–4649, 2004.

[98] F.-C. Chiu. A Review on Conduction Mechanisms in Dielectric Films. *Advances in Materials Science and Engineering*, 2014, 2014.

[99] D.P. Norton. Synthesis and properties of epitaxial electronic oxide thin-film materials. *Materials Science and Engineering*, R 43:139–247, 2004.

[100] P. Komissinskiy L. Alff, A. Klein and J. Kurian. *Vapour phase deposition of oxides in Ceramic science and technology, in I-W. Chen. R. Riedel (Eds.), Synthesis and Processing, vol 3*. Wiley-VCH Verlag GmbH Weinheim Germany, 2011.

[101] G. Koster, M. Huijben, and G. Rijnders. *Epitaxial Growth of Complex Metal Oxides*. Woodhead Publishing, 2015.

[102] G. Koster and G. Rijnders. *In situ characterization of thin film growth*. Woodhead Publishing, 2011.

[103] W. Braun. *Applied RHEED Reflection High-Energy Electron Diffraction During Crystal Growth*, volume 154. Springer, 1. edition, 199.

[104] K. Mae, V.V. Moshchalkov and Y. Bruynseraede. Intensity profiles along the RHEED streaks for various thin film surface morphologies. *Thin Solid Films*, 340:145–152, 1999.

[105] A. Hirsch. *In-situ RHEED-Untersuchungen des PLD-Wachstums von oxidischen Multilagen für die Entwicklung von Bauelementen*. PhD thesis, Technische Universität Braunschweig, 2013.

[106] Katsuhiko Inaba. X-ray thin-film measurement techniques. *The Rigaku Journal 24(1)*, 2008.

[107] Toru Mitsunaga. X-ray thin-film measurement techniques. *The Rigaku Journal 25(1)*, 2009.

[108] J. B. Nelson and D. P. Riley. An Experimental Investigation of Extrapolation Methods in the Derivation of Accurate Unit-Cell Dimensions of Crystals. *Proceedings of the Physical Society of London*, 57:160–177, 1945.

[109] M. Maul, B. Schulte, P. Häussler, G. Frank, T. Steinborn, H. Fuess and H. Adrian. Epitaxial CeO_2 buffer layers for $YBa_2Cu_3O_{7-\delta}$. *Journal of Applied Physics*, 74:2942–2944, 1993.

[110] Miho Yasaka. X-ray thin-film measurement techniques. *The Rigaku Journal 26(2)*, 2010.

[111] A. Wachau. *Sauerstoffaustausch polykristalliner kathodenzerstäubter Indiumoxid-Dünnschichten*. PhD thesis, Technische Universität Darmstadt, 2015.

[112] D. A. Shirley. High-Resolution X-Ray Photoemission Spectrum of the Valence Bands of Gold. *Physical Review B*, 5:4709–4714, 1972.

[113] S. Tougaard. Practical Algorithm For Background Subtraction. *Surface Science*, 216:343–360, 1989.

[114] G. Friedbacher and H. Bubert. *Surface and Thin Film Analysis: A Compendium of Principles, Instrumentation, and Applications*. Wiley-VCH Verlag GmbH Weinheim Germany, 2011.

[115] S. Wicklein, A. Sambri, S. Amoruso, X. Wang, R. Bruzzese, A. Koehl and R. Dittmann. Pulsed laser ablation of complex oxides: The role of congruent ablation and preferential scattering for the film stoichiometry. *Applied Physics Letters*, 11:131601, 2012.

[116] S.A. Lee, H. Jeong, S. Woo, J.-Y. Hwang, S.-Y. Choi, S.-D. Kim, M. Choi, S. Roh, H. Yu, Ju. Hwang, S. W. Kim and W. S. Choi. Phase transitions via selective elemental vacancy engineering in complex oxide thin films. *Scientific Reports*, 6:23649, 2016.

[117] H.N. Lee, S.S.A. Seo, W.S. Choi and C.M. Rouleau. Growth control of oxygen stoichiometry in homoepitaxial $SrTiO_3$ films by pulsed laser epitaxy in high vacuum. *Scientific reports*, 6:19941, 2016.

[118] R. Uecker, B. Velickov, D. Klimm, R. Bertram, M. Bernhagen, M. Rabe, M. Albrecht, R. Fornari and D.G. Schlom. Properties of rare-earth scandate single crystals (Re = Nd - Dy). *Journal of Crystal Growth*, 310:12649–2658, 2008.

[119] A. Vailionis and H. Boschker and W. Siemons and E.P. Houwman and D.H.A. Blank and G. Rijnders and G. Koster. Misfit strain accommodation in epitaxial ABO_3 perovskites: Lattice rotations and lattice modulations. *Physical Review B*, 83:064101, 2011.

[120] N. Kaur, R. Mohan, N.K. Gaur, R.K. Singh. Influence of La doping on elastic and thermodynamic properties of $SrMoO_3$. *Journal of Alloys and Compounds*, 509:6077–6082, 2011.

[121] R.I. Barabash, W. Donner and H. Dosch. X-ray scattering from misfit dislocations in heteroepitaxial films: The case of Nb(110) on Al_2O_3. *Applied Physics Letters*, 78:443, 2001.

[122] A.R. Wildes, R.A. Cowley, R.C.C. Ward, M. R. Wells, C. Jansen, L. Wireen and J.P. Hill. The structure of epitaxially grown thin films: a study of niobium on sapphire. *Journal of Physics: Condensed Matter*, 10:L631–L637, 1998.

[123] D. Reisinger, M. Schonecke, T. Brenninger, M. Opel, A. Erb, L. Alff and R. Gross. Epitaxy of Fe_3O_4 on Si(001) by pulsed laser deposition using a TiN/MgO buffer layer. *Journal of Applied Physics*, 94:1857–1863, 2003.

[124] ICDD. International Center for Diffraction Data (ICDD), Card No. 00-005-0565.

[125] Z. Yu, J. Ramdani, J.A. Curless, J.M. Finder, C.D. Overgaard, R. Droopad, K.W. Eisenbeiser, J.A. Hallmark, and W.J. Ooms. Epitaxial perovskite thin films grown on silicon by molecular beam epitaxy. *Journal of Vacuum Science & Technology B*, 18:1653, 2000.

[126] P. Zaumseil, A. Giussani and T. Schroeder. Laboratory-based characterization of heteroepitaxial structures: Advanced experiments not needing synchrotron radiation. *Powder Diffraction*, 25:92–98, 2010.

[127] Y. Lu, D. Jia, F. Gao, T, Chen, T. Hu. First-principles study on the elastic properties of Sr-Ti-O ceramics. *Solid State Communications*, 182:43–46, 2014.

[128] S. Gevorgian. *Surface Impedance of Silicon Substrates and Films*. Wiley, 1998.

[129] D. Walk, P. Salg, D. Kienemund, A. Radetinac, L. Zeinar, C. Schuster, P. Komissinskiy, L. Alff, R. Jakoby and H. Maune. Characterization and Modeling of Epitaxially Grown BST on a Conducting Oxide Electrode. *2018 48th European Microwave Conference (EuMC)*, pages 563–566, 2018.

[130] M. Schmidt. *Abstimmbare Anpassnetzwerke auf Basis ferroelektrischer Varaktoren für Mobilfunanwendungen*. PhD thesis, Universität Erlangen-Nürnberg, 2007.

[131] L. Zeinar, P. Salg, D. Walk, S. Petzold, A. Arzumanov, R. Jakoby, H. Maune, L. Alff and P. Komissinskiy. Effect of oxidation and lattice distortion of the tunable dielectric BST films on the electric performance of MIM epitaxial ferroelectric varactors with $SrMoO_3$ oxide electrodes. *Journal of Applied Physics*, under preperation, 2020.

[132] J. Robertson and C.W. Chen. Schottky barrier heights of tantalum oxide, barium strontium titanate, lead titanate, and strontium bismuth tantalate. *Applied Physics Letters*, 74:1168–1170, 1999.

[133] H.L. Skriver and N.M. Rosengaard. Surface energy and work function of elemental metals. *Physical Review B*, 46:7157, 1992.

[134] R. Schafranek, S. Payan, M. Maglione and A. Klein. Barrier height at (Ba,Sr)TiO_3/Pt interfaces studied by photoemission. *Physical Review B*, 77:195310, 2008.

[135] R.G. Schafranek. *Kathodenzerstäubte (Ba,Sr)TiO_3-Dünnschichten für steuerbare Mikrowellenkomponenten*. PhD thesis, Technische Universität Darmstadt, 2009.

[136] A.L. Campbell, R.R. Biggers, G. Subramanyam, G. Kozlowski, R.A. Kleismit, H.N. Zate, S.C. Hopkins, B.A. Glowacki, B.D. Riehl and T.L. Peterson. Microwave characterization of nanostructured ferroelectric $Ba_{0.6}Sr_{0.4}TiO_3$ thin films fabricated by pulsed laser deposition. *Nanotechnology*, 19:485704, 2008.

[137] A. Uedono, K. Shimoyama, M. Kiyohara, Z.Q. Chen, K. Yamabe, T. Ohdaira, R. Suzuki and T. Mikado. Vacancy-type defects in $BaTiO_3$/$SrTiO_3$ structures probed by monoenergetic positron beams. *Journal of Applied Physics*, 105:5307–5312, 2002.

[138] A. Uedono, M. Kiyohara, N. Yasui and K. Yamabe. Suppressing of oxygen diffusion by thin Al_2O_3 films grown on $SrTiO_3$ studied using a monoenergetic positron beam. *Journal of Applied Physics*, 97:033508, 2005.

[139] G.L. Yuan and A. Uedono. Behavior of oxygen vacancies in $BiFeO_3$/$SrRuO_3$/$SrTiO_3$(110) and $DyScO_3$(110) heterostructures. *Applied Physics Letters*, 94:132905, 2009.

[140] G.L. Yuan, K. Nishio, M. Lippmaa and A. Uedono. Epitaxial $DyScO_3$ films as passivation layers suppress the diffusion of oxygen vacancies in $SrTiO_3$. *Journal of Physics D: Applied Physics*, 43:025301, 2010.

[141] G.L. Yuan, C. Li, J. Yin, Z. Liu, D. Wu and A. Uedono. Positron annihilation studies on the behaviour of vacancies in $LaAlO_3/SrTiO_3$ heterostructures. *Journal of Physics D: Applied Physics*, 45:445305, 2012.

[142] A. Radetinac, J. Ziegler, M. Vafaee, L. Alff and P. Komissinskiy. Growth and interface engineering in thin-film $Ba_{0.6}Sr_{0.4}TiO_3$ $SrMoO_3$ heterostructures. *Journalf of Crystal Growth*, 463:134–138, 2017.

[143] P. Salg, L. Zeinar, A. Radetinac, D. Walk, H. Maune, R. Jakoby, L. Alff, and P. Komissinskiy. Oxygen diffusion barriers for epitaxial thin-film heterostructures with highly conducting $SrMoO_3$ electrodes. *Journal of Applied Physics*, 127:065302, 2020.

[144] ICDD. International Center for Diffraction Data (ICDD), Card No. 00-039-1395.

[145] D.O. Scanlon, G.W. Watson, D.J. Payne, G.R. Atkinson, R.G. Egdell and D.S.L. Law. Theoretical and Experimental Study of the Electronic Structures of MoO_3 and MoO_2. *The Journal of Physical Chemistry C*, 114:4636–4645, 2010.

[146] D. Walk, D. Kienemund, P. Salg, L. Zeinar, A. Radetinac, P. Komissinskiy, L. Alff, R. Jakoby and H. Maune. All-Oxide Thin Film Varactor: From Test Structure to SMD Component. *2019 49th European Microwave Conference (EuMC)*, pages 184–187, 2019.

[147] I.B. Vendik, O.G. Vendik and E.L. Kollberg. Commutation Quality Factor of Two-State Switchable Devices. *IEEE Transactions on Microwave Theory and Techniques*, 48:802, 2000.

[148] STMicroelectrinics, 2015. Parascan^{TM} STPTIC-27G2 tunable integrated capacitor `https://www.st.com/resource/en/datasheet/stptic-27g2.pdf`; accessed at 06. April 2020.

List of publications and conference contributions

Publications

The compilation of this thesis was done solely by the author. Most results have been published or are available as preprints under the following references:

[91] *Atomically interface engineered micrometer-thick $SrMoO_3$ oxide electrodes for thin-film $Ba_xSr_{1-x}TiO_3$ ferroelectric varactors tunable at low voltages*
Patrick Salg, Dominik Walk, Lukas Zeinar, Aldin Radetinac, Leopoldo Molina-Luna, Alexander Zintler, Rolf Jakoby, Holger Maune, Philipp Komissinskiy and Lambert Alff
Published in APL Materials **7**, 051107 (2019)
This paper was selected as Editor's pick and was awarded with the APL Materials Excellence in Research Award.

[143] *Oxygen diffusion barriers for epitaxial thin-film heterostructures with highly conducting $SrMoO_3$ electrodes*
Patrick Salg, Lukas Zeinar, Aldin Radetinac, Dominik Walk, Holger Maune, Rolf Jakoby, Lambert Alff and Philipp Komissinskiy
Published in Journal of Applied Physics **127**, 065302 (2020)
This paper was selected as Editor's pick.

[131] *Effect of oxidation and lattice distortion of the tunable dielectric BST films on the electric performance of MIM epitaxial ferroelectric varactors with $SrMoO_3$ oxide electrodes*
Lukas Zeinar, **Patrick Salg**, Dominik Walk, Stefan Petzold, Alexey Arzumanov, Rolf Jakoby, Holger Maune, Lambert Alff and Philipp Komissinskiy
under preperation for Journal of Applied Physics

[129] *Characterization and Modeling of Epitaxially Grown BST on a Conducting Oxide Electrode*
Dominik Walk, **Patrick Salg**, Daniel Kienemund, Aldin Radetinac, Lukas Zeinar, Christian Schuster, Philipp Komissinskiy, Lambert Alff, Rolf Jakoby and Holger Maune
Published in 2018 48th European Microwave Conference (EuMC), 563 – 566 (2018)

[96] *Characterization and Deembedding of Negative Series Inductance in On-Wafer Measurements of Thin-Film All-Oxide Varactors*
Dominik Walk, Daniel Kienemund, Lukas Zeinar, **Patrick Salg**, Aldin Radetinac, Philipp Komissinskiy, Lambert Alff, Rolf Jakoby and Holger Maune
Published in IEEE Microwave and Wireless Components Letters **29**, 213 – 215 (2019)

[146] *All-Oxide Thin Film Varactor: From Test Structure to SMD Component*
Dominik Walk, Daniel Kienemund, **Patrick Salg**, Lukas Zeinar, Aldin Radetinac, Philipp Komissinskiy, Lambert Alff, Rolf Jakoby and Holger Maune
Published in 2019 48th European Microwave Conference (EuMC), 184 – 187 (2019)

[95] *Highly Accurate Analytic Modeling of Dispersive Field Distributions in MIM Capacitances With Electrodes Thinner than Skin Depth*
Dominik Walk, Daniel Kienemund, **Patrick Salg**, Lukas Zeinar, Aldin Radetinac, Leopoldo Molina-Luna, Philipp Komissinskiy, Lambert Alff, Rolf Jakoby and Holger Maune
Published in IEEE Transactions on Microwave Theory and Techniques **67**, 4665 – 4673 (2019)

Awards

APL Materials Excellence in Research Award
from AIP publishing for the publication: *Atomically interface engineered micrometer-thick $SrMoO_3$ oxide electrodes for thin-film $Ba_xSr_{1-x}TiO_3$ ferroelectric varactors tunable at low voltages*
November 2019

Winner of the Science4Life Venture Cup - Ideenphase
for the idea of all-oxide varactor based 5G applications
November 2019

Winner of the Science4Life Venture Cup - Konzeptphase
for the concept and business development of all-oxide varactor based 5G applications
March 2020

Conference Contributions

Interface engineering in all-oxide $Ba_xSr_{1-x}TiO_3$ thin-film varactors with highly conducting $SrMoO_3$ electrodes
Patrick Salg, Aldin Radetinac, Dominik Walk, Leopoldo Molina-Luna, R. Egoavil, Philipp Komissinskiy, Holger Maune, Rolf Jakoby and Lambert Alff
DPG-Spring Meeting 2017, Dresden, Germany, 19. – 24. March 2017.

All-oxide epitaxial ferroelectric varactors for low-voltage microwave applications
Patrick Salg, Aldin Radetinac, Lukas Zeinar, Dominik Walk, Holger Maune, Rolf Jakoby, Philipp Komissinskiy and Lambert Alff
International Workshop on Oxide Electronics 2017, Chicago, USA, 24. – 27. September 2017.

Oxygen diffusion in epitaxial oxide heterostructures with $SrMoO_3$ thin films
Patrick Salg, Lukas Zeinar, Dominik Walk, Holger Maune, Rolf Jakoby, Philipp Komissinskiy and Lambert Alff
European Materials Research Society Fall Meeting 2018, Warsaw, Poland, 17. – 20. September 2018.

Oxygen diffusion in epitaxial oxide heterostructures with $SrMoO_3$ thin films
Patrick Salg, Lukas Zeinar, Dominik Walk, Aldin Radetinac, Holger Maune, Rolf Jakoby, Philipp Komissinskiy and Lambert Alff
International Workshop on Oxide Electronics 2018, Les Diablerets, Switzerland, 1. – 3. October 2018.

Interface Engineering Of All-Oxide Epitaxial Ferroelectric Varactors
Patrick Salg
GraFOx Summer School on Oxide Semiconductors for Smart Electronic Devices 2019, Menaggio, Italy, 03. – 09. June 2019.

Highly conducting $SrMoO_3$ as a substitution for metal electrodes
Patrick Salg
Internationale Ressourcenchemie-Konferenz 2019, Darmstadt, Germany, 23. – 24. March 2020.

Danksagung

Zuerst möchte ich mich bei Herrn **Prof. Dr. Lambert Alff** für die Möglichkeit der Promotion im Fachgebiet Dünne Schichten bedanken.

Weiterer Dank gebührt Herrn **Dr.-Ing. Holger Maune** für die freundliche Übernahme der Position des Zweitgutachters.

Herrn **Dr. rer. nat. Leopoldo Molina-Luna** und Herrn **Prof. Dr. Wolfgang Ensinger** für die freundliche Übernahme der weiteren Prüfungsverantwortung.

Herrn **Dr. Philipp Komissinskiy** für die Unterstützung während meiner Promotion, sowie Einführung in die wundervolle Welt der gepulsten Laserdeposition.

Herrn **Jürgen Schreeck**, Frau **Gabi Haindl** und der **mechanischen und elektronischen Werkstatt** des Fachbereichs Materialwissenschaft für stete Hilfsbereitschaft und tatkräftige Unterstützung in allen technischen Angelegenheiten.

Allen Leuten, die Teil am Varaktorprojekt ALOVA waren. Herr **Prof. Dr. Rolf Jakoby** für die Unterstützung, **Dominik Walk** zum einen für die Mikrowellencharakterisierung der Proben und zum anderen für die Ruhe immer wieder die gleichen elektrotechnischen Diskussionen mit unwissenden Materialwisseschaftlern zu führen. **Oscar Recalde** sowie **Alexander Zintler** für die TEM Aufnahmen.

Lukas Zeinar, der neben einem Kollegen auch ein sehr guter Freund geworden ist und mit der Skate Banana nicht nur im Labor Höchstleistung bringt. Dem resistive switching Guru **Dr. Stefan Petzold**, der mich vom ersten Tag als Schreibtischnachbar begleitet hat. **Dr. Shalini Sharma** für die Fortsetzung einer entspannten Schreibtischnachbarschaft. **Dr. Vikas Shabadi** für die Butter Chicken Ausflüge, sowie der gesamten **Arbeitsgruppe Dünne Schichten** und allen **Doktoranden der Materialwissenschaft** die hier

nicht namentlich erwähnt sind.

Allen meinen Freunden, die mich während der Promotionszeit unterstüzt und begleitet haben. **Philipp** und **Sabrina Klos**, die immer ein offenes Ohr für mich hatten. **Noah Strobel**, mit dem ich mich in Darmstadt eingelebt habe und die besten PowPow Abfahrten gemacht habe. **Julian Weis** für die Fortführung der Hochstraßen-Ära. **Christian Appel** als Teil der alten LBS Crew und meinen Lieblingsösterreicher **Lukas Rammelmüller**, für die besten Schnitzel Darmstadts. **Magdalena Nadenau** für die Laufeinheiten und Haarschnitte während der Corona Zeit und meiner **Doppelkopf Crew** für die lustigen Abende.

Frederic Hummel und **Karin Ibe**, mit denen ich, trotz Entferung nach Hamburg, die Extremsportarten Wakeboarden, sowie Bigwave Surfen für mich entdeckt habe.

Meinen **Großeltern**, die jetzt endlich nicht mehr fragen müssen, wie lange ihr Enkel noch für sein Studium braucht.

Und zuletzt meinen **Eltern** für die Unterstützung während der Schulzeit, Studium, sowie Promotion und mir so eine entspannte, unbefangene Studienzeit hier ermöglicht haben und mir immer Rückhalt gegeben haben.